

I. ASPECTS OF LITHOSPHERIC EVOLUTION ON VENUS
II. THERMAL AND COLLISIONAL HISTORIES OF CHONDRITE PARENT BODIES

by

Robert E. Grimm

B.A., University of Tennessee
(1983)

SUBMITTED TO THE DEPARTMENT OF
EARTH, ATMOSPHERIC, AND PLANETARY SCIENCES
IN PARTIAL FULFILLMENT
OF THE REQUIREMENTS
FOR THE DEGREE OF

DOCTOR OF PHILOSOPHY

at the

MASSACHUSETTS INSTITUTE OF TECHNOLOGY

October 1988

© Massachusetts Institute of Technology 1988

ACCESSIONING, REPRODUCTION AND DISTRIBUTION
BY OR FOR NASA PERMITTED

Signature of Author _____
Department of Earth, Atmospheric, and Planetary Sciences

Certified by _____
Sean C. Solomon
Thesis Supervisor

Accepted by _____
Theodore R. Madden
Chairman, Department Committee

(NASA-CR-184588) PART 1: ASPECTS OF
LITHOSPHERIC EVOLUTION ON VENUS. PART 2:
THERMAL AND COLLISIONAL HISTORIES OF
CHONDRITE PARENT BODIES Ph.D. Thesis
(Massachusetts Inst. of Tech.) 329 p

N89-15844

Unclas
G3/91 0178596

I. ASPECTS OF LITHOSPHERIC EVOLUTION ON VENUS

II. THERMAL AND COLLISIONAL HISTORIES OF CHONDRITE PARENT BODIES

by

Robert E. Grimm

Submitted to the Department of Earth, Atmospheric, and Planetary Sciences on
October 25, 1988, in partial fulfillment of the requirements of the Degree of
Doctor of Philosophy in Geophysics

ABSTRACT

This thesis consists of two principal sections which address the geological evolution of distinctly different kinds of solar system objects. Venus, the second largest of the terrestrial planets, has been observed over the past decade by orbital radars on both American and Soviet spacecraft. These surface measurements provide clues to the structure and evolution of the lithosphere. The parent bodies of chondritic meteorites, thought to resemble asteroids, represent the other end of the size spectrum of terrestrial objects. Their early thermal and collisional histories may be constrained by the chemical and textural record preserved in meteorite samples.

Impact craters on Venus have been observed by the Soviet Venera 15/16 spacecraft. We present a formalism by which the size-frequency distribution of impact craters may be used to estimate upper bounds on the mean global rates of volcanic resurfacing and lithospheric recycling on that planet over the past several hundred million years. The principal assumptions are that an upper bound on the rate of crater production on Venus may be estimated, that craters are volcanically obliterated only when flows completely cover their rims, and that the mean rate of lithospheric recycling is inversely proportional to the surface age. The impact crater density reported from Venera 15/16 observations, if valid for the entire Venus surface, then indicates a mean volcanic flux no greater than $2 \text{ km}^3/\text{y}$, corresponding to a maximum average rate of resurfacing of about $4 \text{ km}/\text{b.y.}$ The fraction of global heat loss due to such a rate of volcanic resurfacing is negligible. For the lowest estimated mean crater retention age of the surface of Venus imaged by Venera 15/16, the rate of lithospheric recycling on Venus does not exceed $1.5 \text{ km}^2/\text{y}$, corresponding to 25% of the global heat loss. More likely estimates of the mean surface age limit the contribution to global heat loss of any lithospheric recycling to be less than 10%. These results support the hypothesis that simple conduction dominates heat transport at lithospheric levels in the Venus interior.

Changes in the morphology of impact craters with time may also be used to investigate the interior. Because of the high surface temperature on Venus and the strong temperature dependence of strain rate in silicates, solid state creep may be an important mechanism for the reduction of topographic relief on that planet. On

the basis of models for the viscous relaxation of impact crater topography we derive constraints on the thickness of the crust and the mean lithospheric thermal gradient beneath craters observed by Venera 15/16. From the mean and variance of observed crater depth as a function of crater diameter on Venus and from estimates of the initial depths of fresh impact craters on Venus obtained by scaling from lunar observations, we formulate a statistical test for the maximum amount of viscous relaxation that is consistent with the observations at a specified confidence level. We develop a general formulation for gravity-driven flow in a linearly viscous fluid, incorporating the densities and temperature-dependent effective viscosities of distinct crust and mantle layers. The statistical comparison of predicted and observed depths yields linked upper limits to crustal thickness H and thermal gradient dT/dz . Since dT/dz can be estimated from global heat loss arguments or thermal models, an upper bound to H may be derived. The preserved relief of the largest craters constrains H to be less than or equal to 10-20 km. Because the craters with measured depths appear to be representative of a larger population of impact structures in terms of regional elevation, geological unit, and degree of preservation of morphological detail, extrapolation of this result to lowlands and rolling plains regions on a global basis is not unreasonable. Such an extrapolation, together with isostatic considerations, yields an upper limit to the crustal volume of Venus of 10^{10} km³. This value is an order of magnitude less than the time-integrated volume of crust produced on Earth and implies either that the average rate of crustal generation has been much smaller on Venus than on Earth or that some form of crustal recycling has occurred on Venus.

Aphrodite Terra, the largest highland region of Venus, is a likely site of mantle upwelling and active volcanism and extensional tectonics. Crumpler and Head have proposed that Aphrodite is a divergent plate boundary and cite as support of this model an organized system of lineaments held to be analogs to oceanic fracture zones; small-scale bilateral symmetry of topographic elements, hypothesized to be rifted and separated relief analogous to some terrestrial oceanic plateaus; and subsidence of topography proportional to the square root of distance, consistent with that expected for a divergent thermal boundary layer. We undertake quantitative tests of each of these assertions, and we compare the results to similar tests of the Mid-Atlantic Ridge. We find that, apart from the long-wavelength symmetry of broadly elevated regions, there is no evidence for regional bilateral symmetry of features several hundred kilometers in size on either planet. The fit of the topography of Aphrodite to a that of a thermal boundary layer is in general much poorer than for the Earth, and so other mechanisms such as dynamic uplift or crustal thickness variations must dominate the topography. The broad saddle-shaped region between Thetis and Atla Regiones shows the best fit to the root-distance relation, yielding apparent spreading half-rates of a few centimeters per year, but the statistics are quite sensitive to the distance range analyzed. Calculation of a single pole of relative motion for the entire postulated system of transform faults shows that the inferred fracture zone traces are not consistent with a simple two-plate model, regardless of past pole motions. A multiple-plate geometry is required, and one or more of the lineaments must be a plate boundary if the plate-divergence hypothesis is correct. Such a boundary would be discernable by

geological evidence for non-transform motion in forthcoming *Magellan* radar images. If, however, in the absence of such evidence, the lineaments themselves are nevertheless verified, then rigid-plate rotations are invalid, and a nonrigid model must be adopted in which deformation is broadly accommodated and the lineaments are surface traces of mantle convective flow. A model dominated by vertical tectonics, wherein horizontal mantle divergence is largely decoupled from the surface, is possible only if the lineaments are unconfirmed by *Magellan*.

Ordinary chondrite meteorites show textural and chemical patterns indicative of varying intensities of thermal metamorphism. The conventional "onion-shell" model, which envisions highly metamorphosed material in the core and less intensely heated rocks near the surface, predicts an inverse relation between peak temperature and cooling rate, but none has been observed. Scott and Rajan devised a "metamorphosed-planetesimal" model to explain this discrepancy, whereby heating occurs in planetesimals a few kilometers in radius which then accrete to form 100-km-radius parent bodies. Cooling rates are then randomly controlled by burial depth. Thermal and collisional constraints on the metamorphosed-planetesimal are examined here, and the model is found to be applicable only to highly insulating, ^{26}Al -rich planetesimals that remain closely aggregated upon accretion. An alternative model is presented here, in which onion-shell parent bodies are collisionally fragmented during metamorphism and then gravitationally reassembled. If reassembly times are short, then cooling rates would be determined by burial depth in the reaccreted parent body. This model, unlike previous ones, can explain both coherent and incoherent cooling of breccia clasts, by collisions during or after metamorphism, respectively.

Carbonaceous chondrites have, in general, not experienced the thermal metamorphism seen in ordinary chondrites but have been aqueously altered within their parent bodies. From chemical and textural data on these meteorites, and from studies of collision mechanics, we pose two hypotheses for the aqueous alteration environment. In the first model, alteration occurs uniformly throughout the parent body interior; in the second, alteration occurs in a post-accretional surface regolith. Both models are based on the assumptions of an initially homogeneous mixture of ice and rock and heating by decay of ^{26}Al . Under the interior-alteration model, linked bounds on the initial ice-to-rock ratio and ^{26}Al abundance may be found that satisfy peak temperatures derived from oxygen isotope studies. Additional constraints imposed by the inferred water volume consumed by the alteration reaction and the total water volume that exchanged oxygen isotopes with host rocks are best explained if alteration occurred in a regolith. We show quantitatively how liquid water may be introduced there by hydrothermal circulation, by diffusion of vapor from below, or by venting due to fracture when interior pore pressures exceed the parent body strength. Retention of primordial ice is probably not limited by sublimation or by collisional comminution, but by shock vaporization. If large, C-type asteroids are representative of carbonaceous chondrite parent bodies, they may contain significant quantities of ice.

Thesis Supervisor: Sean C. Solomon, Professor of Geophysics

ACKNOWLEDGEMENTS

I am grateful to Sean Solomon for his exemplary standard of scientific excellence, and for the freedom to pursue my interests wherever they wandered across the solar system. I also thank Hap McSween for advice and encouragement over the years.

To all my friends and colleagues -- I would rather share a smile and a simple "thank you" with each of you than attempt to inscribe it here in awkward words.

Finally, thanks to family for unending confidence and support.

This work was supported by the National Aeronautics and Space Administration under grant NSG-7297 and by a National Science Foundation Graduate Fellowship.

CONTENTS

	Page
Abstract.....	2
Acknowledgements.....	5
Chapter 1: Introduction.....	10
Chapter 2: Limits on Modes of Lithospheric Heat Transport on Venus from Impact Crater Density.....	15
Introduction.....	16
Cratering.....	16
Volcanic Resurfacing.....	19
Lithospheric Recycling.....	22
Conclusions.....	23
Appendix 2.A: Effect of Geographic Variations in Crater Density on the Estimated Rate of Lithospheric Recycling.....	24
References.....	26
Tables.....	29
Figure Captions.....	30
Figures.....	31
Chapter 3: Viscous Relaxation of Impact Crater Relief on Venus: Constraints on Crustal Thickness and Thermal Gradient.....	35
Introduction.....	36
Impact Craters on Venus.....	37
Approach.....	40
Depths of Observed and Fresh Craters on Venus.....	41
Statistical Interpretation of Viscous Relaxation Models.....	44
Viscous Relaxation Model.....	46
Application to Venus.....	51
Initially Uncompensated Craters.....	53
Initially Compensated Craters.....	56

Finite Lithospheric Strength.....	57
Discussion.....	58
Conclusions.....	62
Appendix A: Numerical Treatment of the Viscous Relaxation of Topography.....	64
Appendix B: Support of Crater Relief by Lithospheric Strength.....	75
References.....	79
Tables.....	85
Figure Captions.....	90
Figures.....	96
 Chapter 4: Tests of Crustal Divergence Models for Aphrodite Terra, Venus.....	 119
Introduction.....	120
Characteristics of Aphrodite Terra.....	121
Tectonic Models for Aphrodite Terra.....	125
Vertical Tectonics.....	125
Plate Divergence.....	126
Distributed Deformation.....	128
Tests of Tectonic Models.....	129
Plate Kinematic Tests.....	130
Selection and Processing of Topographic Data.....	134
Tests for Thermal Boundary Layer Topography.....	136
Tests for Bilateral Symmetry.....	145
Discussion.....	155
Conclusions.....	157
References.....	159
Tables.....	164
Figure Captions.....	169
Figures.....	176

Chapter 5: Penecontemporaneous Metamorphism, Fragmentation, and Reassembly of Ordinary Chondrite Parent Bodies.....	209
Introduction.....	210
Thermal History of Ordinary Chondrites.....	210
Onion-Shell Model.....	213
Metamorphosed-Planetesimal Model.....	214
Collision Dynamics.....	217
Fragmentation-and-Reassembly Model.....	219
Discussion.....	221
Conclusions.....	223
References.....	224
Figure Captions.....	227
Figures.....	229
 Chapter 6: Water and the Thermal History of Carbonaceous Chondrite Parent Bodies.....	 234
Introduction.....	235
Alteration in Carbonaceous Chondrite Parent Bodies.....	236
Constraints on Thermal Models.....	240
Peak Temperatures.....	240
Timing and Extent of Aqueous Alteration.....	242
Water:Rock Ratio.....	242
Formulation of Thermal History Models.....	243
Nebular Condensation.....	244
Accretion.....	246
Parent Body Compaction.....	247
Heat Sources.....	248
H ₂ O Transport.....	251
Rate of Aqueous Alteration.....	253
Results for Interior-Alteration Model.....	254
Effect of H ₂ O on Peak Temperature and Limits on ²⁶ Al Abundance.....	254
Thermal Effect of Aqueous Alteration.....	258
Results for Regolith-Alteration Model.....	260

Internal Heating.....	261
Impact Heating.....	262
Retention of H ₂ O in Chondrite Parent Bodies.....	263
Discussion.....	266
Conclusions.....	268
Appendix A: Mathematical Formulation of the Carbonaceous Chondrite Thermal Model.....	270
Heat Flow.....	270
Ice-Water Phase Transition.....	272
Hydrothermal Convection.....	273
Gas Diffusion.....	276
Venting of H ₂ O.....	279
Hydration and Dehydration Reactions.....	281
Temperature-Dependent Material Properties.....	283
Nomenclature.....	285
Appendix B: Degassing and Secular Retention of H ₂ O.....	288
References.....	291
Figure Captions.....	301
Figures.....	306
Chapter 7: Concluding Remarks.....	325

CHAPTER 1:

INTRODUCTION

The solar system is a motley family. Its members vary vastly in size, from Jupiter, the glaring master of the night sky, to the countless dust particles which comprise the hazy zodiacal light. Between these extremes are those solid bodies which have undergone distinct structural and chemical changes with time, that is, they have *geological* histories. These objects range in size from Earth and Venus, with diameters of several thousand kilometers, to meteorite parent bodies, whose diameters are inferred to have been several hundred kilometers or less. This thesis investigates several aspects of the physical evolution of objects at both boundaries of geological inquiry, the planet Venus and the parent bodies of chondritic meteorites.

The surface geological histories of terrestrial objects are determined principally by the competition between endogenic processes, manifested by volcanism and tectonism, and the exogenic imprint of impact cratering (erosion plays a secondary role). The earliest geological evolution of terrestrial objects was dominated by collisions during their accretion. Continued impact cratering, with decreasing intensity over solar system history, has affected all planetary surfaces. The ubiquity of impact craters makes them not only the products of an easily studied geological process in themselves, but variations in their areal density are excellent measures of the relative ages of different regions of a planetary surface, although absolute ages are more difficult to assign. Moreover, detailed examination of the size-frequency distribution and morphology of impact craters can be used to infer mechanisms and rates of endogenic modification, which can in turn yield clues on the state of the interior.

Heating of a planetary interior drives volcanism and tectonism at the surface. For the planets and larger moons, the main heat source is radioactive decay. Heating is proportional to the planetary volume for such an internal heat source. However, radiation is proportional to the surface area, which leads to the so-called "square-cube law": since the volume-to-area ratio increases linearly with planetary

size, larger planets will retain heat better and have more vigorous and longer-lasting geologic histories. This simple and perhaps well-worn rule nevertheless explains the approximate correlation between size and surface age inferred from impact crater density: the Moon and Mercury, heavily cratered, have been largely inactive for billions of years; Mars, partially cratered but marked with enormous shield volcanoes and deep rifts, attests to activity within the past few billion years; Earth, with only a smattering of craters largely on old continental shields, remains strongly volcanically and tectonically active today. Using size as a guide to thermal longevity leads to predictions that Venus should be presently volcanically and tectonically active, whereas small meteorite parent bodies should be long dead. The active early histories of these objects are nonetheless preserved in the chemistry and texture of meteorites. Understanding the earliest geological processes of the solar system and the different geological histories of the two largest terrestrial objects are important goals in planetary science.

The relationship between impact and thermal histories is explored along several avenues in this thesis. In the first two investigations, impact craters are used as tools to probe the outer tens of kilometers of Venus. Chapter Two combines the size-frequency distribution of impact craters on Venus with estimates of the recent cratering rate to calculate the maximum rates at which impact craters can be obliterated by volcanism or lithospheric recycling. The heat loss by each mechanism may be derived from the crater obliteration rate, therefore leading to identification of the dominant mode of heat loss at lithospheric levels on Venus.

Chapter Three analyzes the endogenic modification of impact craters on Venus by viscous relaxation and derives constraints on the rheological and thermal structure of the interior imposed by observed crater morphology. Viscous relaxation, a process analogous to terrestrial postglacial rebound wherein gravity-driven flow gradually eradicates topographic relief, is expected to more important on

Venus because of the high surface temperature. The viscous relaxation model developed in this thesis depends principally on the local crustal thickness and thermal gradient. Statistical comparison of the observed depths of craters against model predictions of the depth of partially relaxed craters is used to establish linked bounds on these parameters.

The tectonic styles resulting from specified modes of heat transport are investigated in Chapter 4 for Aphrodite Terra, the largest highland region on Venus. Three alternative models for the interaction of mantle convection with the surface are considered (vertical tectonics, rigid-plate divergence, and distributed deformation). These models differ in the strength of coupling of interior flow to the surface and the response of the surface to these stresses. A rigid-plate model is the most straightforward to test, as the associated topography and tectonics have been well studied for terrestrial ocean basins. Departures from the predictions of this model may be used to assess the alternative hypotheses. Further predictions necessary to discriminate between these models may be resolved by forthcoming high-resolution radar imaging by the Magellan spacecraft.

Impact and thermal processes are again linked in Chapter 5, which examines the metamorphic and collisional history of ordinary chondrite parent bodies. Chemical and textural properties of meteorites yield information both on the peak temperatures during metamorphism and subsequent cooling rates. Because no simple relation has been observed between these parameters for ordinary chondrites, some workers have suggested that metamorphic signatures were fixed in small planetesimals, and that cooling was randomly controlled by the timing and location of accretion into the final parent bodies. Some implicit thermal and collisional assumptions in this model are clarified here. These considerations also suggest a new model in which parent bodies are collisionally fragmented and gravitationally reassembled during the metamorphic interval.

The thermal history of carbonaceous chondrite parent bodies has heretofore been largely ignored because these primitive meteorites have not been thermally metamorphosed. However, aqueous alteration has profoundly affected their chemistry and texture, and some heat source must be responsible for these effects. In Chapter 6, thermal models for carbonaceous chondrites are tested under the alternative assumptions that aqueous alteration occurred in the interiors of parent bodies or within surficial regoliths. The principal constraints on these models derive from oxygen isotope systematics. The thermodynamic and transport properties of H₂O bear strongly on the thermal evolution of interior-alteration models. Several specific mechanisms for introducing water to the regolith are suggested and quantitatively supported. The secular retention of ice on asteroids is also discussed, and the implications for exploration are assessed.

Chapters Two and Three were cowritten with S.C. Solomon and appeared in *Geophys. Res. Lett.*, 14, 538-541, 1987 and *J. Geophys. Res.*, 93, 11911-11929, 1988, respectively. Chapter Four, also written with Solomon, will be submitted to the *Journal of Geophysical Research*. Chapter Five was published in *J. Geophys. Res.*, 90, 2022- 2028, 1985. Chapter Six, cowritten with H.Y. McSween, will be submitted to *Icarus*.

CHAPTER 2:

**LIMITS ON MODES OF LITHOSPHERIC HEAT TRANSPORT
ON VENUS FROM IMPACT CRATER DENSITY**

INTRODUCTION

Characterization of the dominant mode of lithospheric heat transport on Venus remains an important step in understanding the internal evolution of the planet [Solomon and Head, 1982]. Among the other solid planets and satellites of the solar system are examples of bodies on which lithospheric heat transport is dominated by conduction (Moon, Mercury, Mars), volcanism (Io), and lithospheric recycling (Earth). Figure 2.1 is a schematic ternary diagram showing the estimated relative contribution of each of these heat loss mechanisms for these bodies. Images of the Venus surface from Earth-based radar [Campbell *et al.*, 1983, 1984] and Venera 15/16 [Barsukov *et al.*, 1986; Basilevsky *et al.*, 1986] have revealed evidence for widespread volcanism and tectonism but also a significant number of impact craters [Campbell and Burns, 1980; Ivanov *et al.*, 1986]. On the basis of simple models of impact crater production and obliteration, we present a formalism to estimate upper bounds on the contributions to lithospheric heat transport by volcanism and lithospheric recycling from the observed density of impact craters on the Venus surface.

CRATERING

Impact crater densities and crater retention ages are usually expressed relative to a reference surface, typically the lunar maria [BVSP, 1981]. Under the assumption that the same population of planetesimals has been responsible for cratering throughout the inner solar system, surfaces of the same age on the Moon and Venus should have crater density distributions differing only by a multiplicative scaling factor derivable in principle from the relative impact probabilities and velocities of planet-crossing asteroids and comets [Hartmann, 1977; BVSP, 1981]. Of course, the atmosphere of Venus will act to reduce the production of impact craters, particularly at smaller diameters, because of the deceleration and break-up

of incident meteors [*Tauber and Kirk, 1976; Kahn, 1982*]. Assuming that the cratering rate on each body has been constant since emplacement of the lunar reference surface, the expected number of craters per area produced in the diameter increment D to $\sqrt{2}D$ per time on an atmosphere-free Venus can be expressed by

$$F_v(D) = (f N_m/t_m)D^{-b} \quad (2.1)$$

where f is the ratio of the crater production rate on Venus to that on the Moon, t_m and N_m are the age and incremental crater density at unit diameter, respectively, of the lunar reference surface, and b is a constant. Similarly, the average crater retention age t_v of the Venus surface is [*Hartmann, 1977*]

$$t_v = t_m N_v / (f N_m) \quad (2.2)$$

where N_v is the incremental crater density at unit diameter for Venus.

Given the uncertainties in the lunar cratering record and particularly in the scaling of crater production from the Moon to Venus, it is appropriate to consider a range of plausible cratering rates on Venus. Several rates are presented in Table 2.1. For each estimate, the lunar mare regions surrounding the Apollo 12 and 15 landing sites are taken as the reference surface. Mare basalts from Apollo 12 and 15 are among the youngest dated lunar rocks, and the assumption of a near-constant cratering flux since the emplacement of these mare units is a reasonable one [*BVSP, 1981*]. Uncertainties in both crater density and mare emplacement age [*BVSP, 1981*] are represented. We consider two independent estimates, with associated uncertainties, in the crater production scaling factor f . The first estimate, $f = 0.8 - 2.0$ [*Hartmann, 1977; BVSP, 1981*], has been applied to the cratering

record of Venus by a number of other workers [*Masursky et al.*, 1980; *Campbell and Burns*, 1980; *Ivanov et al.*, 1986]. The second and more recent estimate, $f = 1.2 - 4.2$, is derived from *Schaber et al.* [1987], who recalculated impact probabilities and concluded that impact rates on Earth and Venus are nearly identical. In particular, they considered that the estimate of *Grieve* [1984] for the cumulative production function for craters with $D > 20$ km during the past 120 m.y. on Earth, $(5.4 \pm 2.7) \times 10^{-15} \text{ km}^{-2}\text{y}^{-1}$, is valid for Venus. We compare this value to the cumulative cratering rate for $D > 4$ km at the Apollo 12 and 15 sites, correcting for the difference in cutoff diameter using $b = 1.8$ [*BVSP*, 1981]. The equivalent f is then the ratio of crater production on the Earth to that on the Moon. For both sets of estimates of f , we take the unit diameter to be 1 km. This choice is largely for ease of evaluation of equation (2.1) when D is expressed in kilometers; we recognize that N_m and N_v have meaning only as values extrapolated from crater densities at diameters sufficiently large so that the effects of secondary craters on the Moon and of atmospheric shielding on Venus are unimportant. The range in incremental crater production rate on Venus so extrapolated to $D = 1$ km, $F_v(1) = f N_m/t_m$, is then as given in Table 2.1.

A mean crater retention age for Venus can be calculated from equation (2.2) for a given density of impact craters on the Venus surface. Different assumptions have been made in the literature as to which surface features visible in radar images are likely to be of impact origin. Impact craters have been identified by *Campbell and Burns* [1980] in Earth-based radar images as circular areas of low backscatter surrounded by an annular region of high contrast terrain; such features sometimes display a central bright spot. *Masursky et al.* [1980] drew attention to a number of large, circular, radar-dark depressions and suggested they may also be impact features. The 1-4 km resolution of *Venera* 15/16 images allows more confident identification of such classic characteristics of impact craters as elevated rims,

central peaks, and ejecta blankets [*Ivanov et al.*, 1986], although there remain numerous approximately circular features of uncertain origin [*Barsukov et al.*, 1986]. The Venera 15/16 images thus provide the best current estimate of crater density statistics for the northern quarter of the planet [*Ivanov et al.*, 1986]. We note, however, that the crater density distribution reported by *Campbell and Burns* [1980] for a different but overlapping region is similar for craters in the diameter range 80-140 km.

We have estimated N_v from a linear regression on the Venera 15/16 incremental crater density data (log-log plot) of *Ivanov et al.* [1986] for $D > 23$ km, with b fixed at 1.8. This estimate, with associated uncertainties, can be substituted into equation (2.2) to define a range of possible crater retention ages (Table 2.1). A crater retention age of about 1 b.y. is obtained if $f = 1$, in agreement with the mean ages reported by *Campbell and Burns* [1980] and *Ivanov et al.* [1986] under similar assumptions. When all uncertainties are considered, however, the range in possible mean surface ages is quite large, from about 100 m.y. to over 2 b.y.

VOLCANIC RESURFACING

Impact craters, of course, can be obliterated by many processes, including erosion, sedimentation, viscous relaxation, and tectonic disruption, as well as volcanic resurfacing and lithospheric recycling. Several studies [*Garvin et al.*, 1984; *Head et al.*, 1985; *Barsukov et al.*, 1986] suggest that the effects of erosion and sedimentation on Venus are unimportant at the scale of features considered here. As a working hypothesis, we first assume that volcanism is the major resurfacing process and is equally likely anywhere on the Venus surface. This hypothesis is at least partly supported by the widespread occurrence of smooth plains, flow features, and volcanic cones, domes, and calderas [*Campbell et al.*, 1984; *Barsukov et al.*, 1986]. The combined effects of other obliteration processes

serve only to decrease the contribution of volcanism required, which ensures that our estimate of volcanic flux will be an upper bound.

To maintain a conservative approach, we assume that a crater must be buried by volcanic flows to the top of its rim in order that it not be observable in a radar image. We estimate the rim height h of fresh craters on Venus by applying a gravity scaling factor to the power-law relation between h and diameter D for lunar craters [Pike, 1977]. Two different scaling rules are possible, following suggestions that either the depth (and, by inference, the rim height) of complex craters or the transition diameter between simple and complex crater morphology varies inversely with gravity [Grieve and Robertson, 1979; Pike, 1980]. We choose the latter scaling rule here because it predicts higher rims and hence requires a greater amount of volcanic resurfacing to achieve crater obliteration. The prediction for Venus rim heights, in km, is then $h = 0.085 D^{0.4}$.

For a specified time t since initiation of resurfacing at a constant rate of volcanic burial ds/dt , there exists a critical crater diameter D_c at which the rim height is equal to the total thickness of volcanic flows: $h(D_c) = t (ds/dt)$. Craters with $D > D_c$ are unaffected by the resurfacing process and reflect the crater density prior to resurfacing; craters with $D < D_c$ are continually obliterated and replaced. The crater density in the latter state is in equilibrium and depends on the ratio of the rate of cratering to that of obliteration [Jones, 1974]

$$N(D) = F(D) h(D)/(ds/dt) \quad (2.3)$$

where N is the number of preserved craters per area in the diameter interval D to $\sqrt{2}D$. The volcanic resurfacing model is schematically illustrated in Figure 2.2. For a specified crater density, a larger volcanic flux is allowed for a larger crater production rate. For $F(1) = 1.4 \times 10^{-12} \text{ km}^{-2}\text{y}^{-1}$, the largest value in Table 2.1, the

predicted equilibrium crater densities for steady volcanic fluxes of 1, 2, and 4 km³/y are as shown in Figure 2.3. If we take the diameter of the largest reported crater in the Venera images (140 km) as the critical diameter D_c , the minimum periods of resurfacing so that equation (2.3) is valid over the diameter range spanned by the Venera data are 280, 140, and 70 m.y., respectively.

On the basis of Figure 2.3, an upper limit to the mean volcanic flux consistent with the Venera observations, if representative of the entire planet, is 2 km³/y. This is equivalent to an average volcanic resurfacing rate ds/dt of 4 km/b.y. Of course, volcanic extrusion has not been steady but has likely fluctuated about a gradually decreasing function of time. The inferred upper bound on the rate of resurfacing on Venus remains valid, however, as such a volcanic history would have eliminated more craters than in a constant-flux model.

An independent geochemical test of this result has been obtained by *Fegley and Prinn* [1988], who concluded that a volcanic eruption rate of 0.4 to 11 km³/y is required to replenish atmospheric SO₂ lost to chemical weathering of surface rocks. Their best estimate, using surface compositions reported by Venera and Vega landers, is 1 km³/y, quite consistent with the value reported here.

The rate of heat Q_v delivered to the surface by a volcanic flux dV/dt is

$$Q_v = \rho(C_p\Delta T + H_f) (dV/dt) \quad (2.4)$$

where C_p is the heat capacity, ρ is the density, H_f is the heat of fusion, and ΔT is the temperature drop across the lithosphere. Using $\Delta T = 1015$ K [*Kaula and Phillips*, 1981], $\rho = 2.8$ g/cm³, $C_p = 1.2$ J/g K, and $H_f = 400$ J/g, the rate of heat loss due to a volcanic flux of 2 km³/y is 2.9×10^{11} W, or less than 1% of the nominal rate of global heat loss of 3.4×10^{13} W [*Solomon and Head*, 1982]. This rate of heat transport is negligible on a planetary scale, though such a result does not preclude

the possibility of a significant component of heat transport by shallow conduction above igneous intrusions [*Head and Wilson, 1986*]. Volcanism on Earth, principally associated with lithospheric divergence, delivers an order of magnitude more heat per time than inferred here for Venus. However, the terrestrial volcanic contribution to heat loss is still nearly an order of magnitude smaller than that lost due to creation and cooling of the lithosphere [*Sclater et al., 1980*], which distinguishes plate recycling as a separate mode of heat loss (Figure 2.1).

LITHOSPHERIC RECYCLING

We next consider as an alternative working hypothesis that the principal mechanism of impact crater obliteration is tectonic disruption due to lithospheric recycling. Such recycling may be considered to occur either by foundering or by subduction, though we recognize that evidence for neither process has yet been observed in images of the Venus surface [*Barsukov et al., 1986; Basilevsky et al., 1986*]. If the regions imaged by *Venera 15/16* are globally representative, then the lowest estimate of the mean crater retention age (130 m.y.) in Table 2.1 can be converted into an upper bound on the rate of lithospheric recycling. If we assume that there are no preferentially preserved "islands" of more ancient terrain, the rate of lithospheric recycling is inversely proportional to the mean age of the surface. The mean age of oceanic lithosphere on Earth is approximately 60 m.y. [*Sclater et al., 1980*], which would imply under the above assumptions that any lithospheric recycling on Venus is at least a factor of 2 slower than on Earth. The terrestrial rate of creation of new lithosphere is $3 \text{ km}^2/\text{y}$ [*Parsons, 1981*]; the maximum rate on Venus would thus be $1.5 \text{ km}^2/\text{y}$. The presence of ancient terrain uninvolved in the recycling process would seriously bias this estimate; for instance, the mean age of the Earth's surface including the continents is about 400 m.y. [*Sclater et al., 1980*]. However, no systematic large scale variations in crater density are evident in the

Venera images [*Barsukov et al.*, 1986]. In particular, no regions of heavily cratered terrain have been identified in the portions of the Venus surface well imaged by Arecibo and Venera.

The rate of heat loss due to lithospheric recycling is approximately

$$Q = 0.5 \rho C_p L \Delta T (dA/dt) \quad (2.5)$$

where L is the thickness of the thermal lithosphere and dA/dt is the areal rate of creation of new lithosphere. With $dA/dt = 1.5 \text{ km}^2/\text{y}$, C_p and ΔT as above, $\rho = 3.3 \text{ g/cm}^3$ and $L = 94 \text{ km}$ [*Kaula and Phillips*, 1981], $Q = 9 \times 10^{12} \text{ W}$, or 25% of the nominal Venus heat loss. The fractional heat loss corresponding to the more likely estimates of cratering rate and mean crater retention age in Table 2.1 are only 3-9%, a small fraction of the Venus heat budget. These estimates of the rate of Venus heat loss contributed by lithospheric recycling are comparable to the upper bound (15%) derived by *Kaula and Phillips* [1981] using different arguments. It is evident that the situation on Venus is in strong contrast to the Earth, where plate recycling accounts for approximately 65% of the heat loss from the interior [*Sclater et al.*, 1980].

CONCLUSIONS

The density of impact craters in Venera 15/16 radar images of the Venus surface, if representative of the entire planet, limits the average rate of volcanic resurfacing to be less than $2 \text{ km}^3/\text{y}$, corresponding to less than 1% of the global heat loss. On similar grounds the rate of lithospheric recycling on Venus is less than $1.5 \text{ km}^2/\text{y}$ and probably less than $0.5 \text{ km}^2/\text{y}$; these figures correspond to 25% and 9% of the global heat loss, respectively. The position of Venus on the ternary diagram of heat loss mechanisms as estimated by this work is given in Figure 2.4.

These results suggest that heat loss at lithospheric levels in Venus is dominated by conduction. Substantial lateral variation in vertical thermal gradients, associated with lithospheric thinning [*Morgan and Phillips, 1983*] or magmatic intrusions [*Head and Wilson, 1986*], may nonetheless be present. Detailed characterization of volcanic, tectonic, and impact processes on Venus must await the improved resolution and coverage of radar images to be obtained during the Magellan mission and will provide tests of the simple models and arguments presented here.

APPENDIX 2.A: Effect of geographic variations in crater density on the estimated rate of lithospheric recycling.

Both of the approaches discussed above require that there be no significant heterogeneity in crater density with geographic location. On the basis of a χ^2 test of distribution, *Basilevsky et al. [1987]* found no reason to reject the null hypothesis that impact craters are randomly distributed over the area imaged by Venera 15/16. However, *Head et al. [1988]* concluded that crater density over this portion of the Venus surface increases as a function of latitude. They took this variation as supportive of a model of equatorial crustal spreading [*Head and Crumpler, 1988*; see Chapter 4 of this thesis]. We have confirmed this latitudinal trend in the Venera data [*Basilevsky et al., 1987*] with a χ^2 test, although craters identified from the Arecibo data [*Campbell and Burns, 1980*] in a different region of Venus do not support a similar result.

If such a zonal variation in surface age is present and is due to creation of young surface near the equator, its effect on the mean surface age and contribution to heat loss by lithospheric recycling may be estimated. Under the simplest assumption that impact crater density increases linearly with latitude from a value of zero near the equator, the crater density N over a latitudinal band θ_1 to θ_2 is proportional to

$$N = \frac{\int_{\theta_1}^{\theta_2} \theta \cos \theta \, d\theta}{\int_{\theta_1}^{\theta_2} \cos \theta \, d\theta} = \frac{[\cos \theta + \theta \sin \theta]_{\theta_1}^{\theta_2}}{[\sin \theta]_{\theta_1}^{\theta_2}} \quad (2.6)$$

From equation (2.6), we find that the mean crater density over the portion of the surface imaged by the Venera orbiters (approximately 30°-90°N) would be 1.6 times larger than that of the entire northern hemisphere if crater density increases linearly with latitude. Assuming a symmetrical crater distribution for the southern hemisphere leads to a corresponding upper limit to the fractional heat loss of ~35%. More likely estimates of the cratering rate given in Table 2.1 still limit this contribution to less than 15%, however.

REFERENCES

- Barsukov, V. L., and 29 others, The geology and geomorphology of the Venus surface as revealed by the radar images obtained by Veneras 15 and 16, *Proc. Lunar Planet. Sci. Conf. 16th, J. Geophys. Res.*, 91, D378-D398, 1986.
- Basilevsky, A. T., A. A. Pronin, L. B. Ronca, V. P. Kryuchkov, A. L. Sukhanov, and M. S. Markov, Styles of tectonic deformations on Venus: Analysis of Venera 15 and 16 data, *Proc. Lunar Planet. Sci. Conf. 16th, J. Geophys. Res.*, 91, D399-D411, 1986.
- BVSP (Basaltic Volcanism Study Project), *Basaltic Volcanism on the Terrestrial Planets*, 1286 pp., Pergamon, New York, 1981.
- Campbell, D. B., and B. A. Burns, Earth-based radar imagery of Venus, *J. Geophys. Res.*, 85, 8271-8281, 1980.
- Campbell, D. B., J. W. Head, J. K. Harmon, and A. A. Hine, Venus: Identification of banded terrain in the mountains of Ishtar Terra, *Science*, 221, 644-647, 1983.
- Campbell, D. B., J. W. Head, J. K. Harmon, and A. A. Hine, Venus: Volcanism and rift formation in Beta Regio, *Science*, 226, 167-170, 1984.
- Fegley, B., and R.G. Prinn, The rate of volcanism on Venus, *Nature*, in press, 1988.
- Garvin, J. B., J. W. Head, M. T. Zuber, and P. Helfenstein, Venus: The nature of the surface from Venera panoramas, *J. Geophys. Res.*, 89, 3381-3399, 1984.
- Grieve, R. A. F., The impact cratering rate in recent time, *Proc. Lunar Planet. Sci. Conf. 4th, J. Geophys. Res.*, 89, B403-B408, 1984.
- Grieve, R. A. F., and P. B. Robertson, The terrestrial cratering record, 1, Current status of observations, *Icarus*, 38, 212-229, 1979.
- Hartmann, W. K., Relative crater production rates on planets, *Icarus*, 31, 260-276, 1977.
- Head, J. W., and L. Wilson, Volcanic processes and landforms on Venus: Theory, predictions, and observations, *J. Geophys. Res.*, 91, 9407-9446, 1986.

- Head, J.W., and L.S. Crumpler, Evidence for divergent plate-boundary characteristics and crustal spreading on Venus, *Science*, 238, 1380-1385, 1987.
- Head, J. W., A. R. Peterfreund, J. B. Garvin, and S. H. Zisk, Surface characteristics of Venus derived from Pioneer Venus altimetry, roughness, and reflectivity measurements, *J. Geophys. Res.*, 90, 6873-6885, 1985.
- Head, J.W., L.S. Crumpler, and S. Frank, Regional trends in crater density on Venus: Implications for surface processes (abstract), *Lunar Planet. Sci. XIX*, 473-474, 1988.
- Ivanov, B. A., A. T. Basilevsky, V. P. Kryuchkov, and I. M. Chernaya, Impact craters of Venus: Analysis of Venera 15 and 16 data, *Proc. Lunar Planet Sci. Conf. 16th*, *J. Geophys. Res.*, 91, D413-D430, 1986.
- Jones, K. L., Evidence for an episode of crater obliteration intermediate in Martian history, *J. Geophys. Res.*, 79, 3917-3931, 1974.
- Kahn, R., Deducing the age of the dense Venus atmosphere, *Icarus*, 49, 71-85, 1982.
- Kaula, W. M., and R. J. Phillips, Quantitative tests for plate tectonics on Venus, *Geophys. Res. Lett.*, 8, 1187-1190, 1981.
- Masursky, H., E. Eliason, P. G. Ford, G. E. McGill, G. H. Pettengill, G. G. Schaber, and G. Schubert, Pioneer Venus radar results: Geology from images and altimetry, *J. Geophys. Res.*, 85, 8232-8260, 1980.
- Morgan, P., and R. J. Phillips, Hot spot heat transfer: Its application to Venus and implications to Venus and Earth, *J. Geophys. Res.*, 88, 8305-8317, 1983.
- Parsons, B., The rates of plate creation and consumption, *Geophys. J. R. Astron. Soc.*, 67, 437-448, 1981.
- Pike, R. J., Size-dependence in the shape of fresh impact craters on the Moon, in *Impact and Explosion Cratering*, edited by D. J. Roddy, R. O. Pepin, and R. B. Merrill, pp. 489-509, Pergamon, New York, 1977.

- Pike, R. J., *Formation of complex impact craters: Evidence from Mars and other planets*, *Icarus*, 43, 1-19, 1980.
- Schaber, G. G., E. M. Shoemaker, and R. C. Kozak, *The surface age of Venus: Use of the terrestrial cratering record*, *Solar System Res.*, 21, 89-93, 1987.
- Sclater, J. G., C. Jaupart, and D. Galston, *The heat flow through oceanic and continental crust and the heat loss of the Earth*, *Rev. Geophys. Space Phys.*, 18, 269-311, 1980.
- Solomon, S. C., and J. W. Head, *Mechanisms for lithospheric heat transport on Venus: Implications for tectonic style and volcanism*, *J. Geophys. Res.*, 87, 9236-9246, 1982.
- Tauber, M. E., and D. B. Kirk, *Impact craters on Venus*, *Icarus*, 28, 351-357, 1976.

TABLE 2.1. Incremental crater production function $F_V(D)$ at $D = 1$ km
and implied crater retention age t_V for Venus

f	t_m 10^9 y	N_m 10^{-4} km $^{-2}$	$F_V(1)$, 10^{-13} km $^{-2}$ y $^{-1}$	N_V , 10^{-4} km $^{-2}$	t 10^9 y
Scaling factor f from <i>Hartmann</i> [1977] and <i>BVSP</i> [1981]					
0.8 ^a	3.4 ^b	4.4 ^a	1.1 ^a	2.4 ^b	2.3 ^b
1.0	3.2	7.2	2.2	2.1	0.94
2.0 ^b	3.1 ^a	11. ^b	6.8 ^b	1.9 ^a	0.27 ^a
Scaling factor f from <i>Grieve</i> [1984] and <i>Schaber et al.</i> [1987]					
1.4 ^a	3.4 ^b	4.4 ^a	1.9 ^a	2.4 ^b	1.3 ^b
2.8	3.2	7.2	6.3	2.1	0.34
4.2 ^b	3.1 ^a	11. ^b	14. ^b	1.9 ^a	0.13 ^a

^a Approximate lower bound for this quantity.

^b Approximate upper bound for this quantity.

Figure 2.1. Schematic ternary diagram showing the relative contributions of each mechanism of lithospheric heat transfer toward global heat loss on solid planets and satellites, after *Solomon and Head* [1982]. For the Moon, Mercury, and Mars, thermal conduction carries all of the lithospheric heat flow. The position of Earth, on which the majority of lithospheric heat transport occurs by plate recycling, does not include the contribution to global heat loss from continental crustal radioactivity. Hot-spot volcanism dominated heat loss on Io, but the relative fraction contributed by conduction is not well known; at the position shown, the conductive heat flow on Io is equal to the Earth's average heat flux. The placement of Venus on this diagram is uncertain.

Figure 2.2. Schematic view of how impact crater density limits the rate of volcanic resurfacing. The crater density $N(D)$ is in equilibrium for $D > D_c$ (see text). The crater-production function $F(D)$ is the expected number of craters within a given diameter increment produced per area per time. For assumed values of $F(D)$ and $h(D)$, the observed crater distribution limits ds/dt .

Figure 2.3. Incremental crater density versus diameter obtained from Venera 15/16 observations [*Ivanov et al.*, 1986] compared with equilibrium crater densities for constant assumed global volcanic fluxes of 1, 2, and 4 km^3/y (solid lines).

Figure 2.4. Position of Venus on the ternary diagram for mechanisms of lithospheric heat transport, as constrained by impact crater density on the portion of the Venus surface imaged by Venera 15/16.

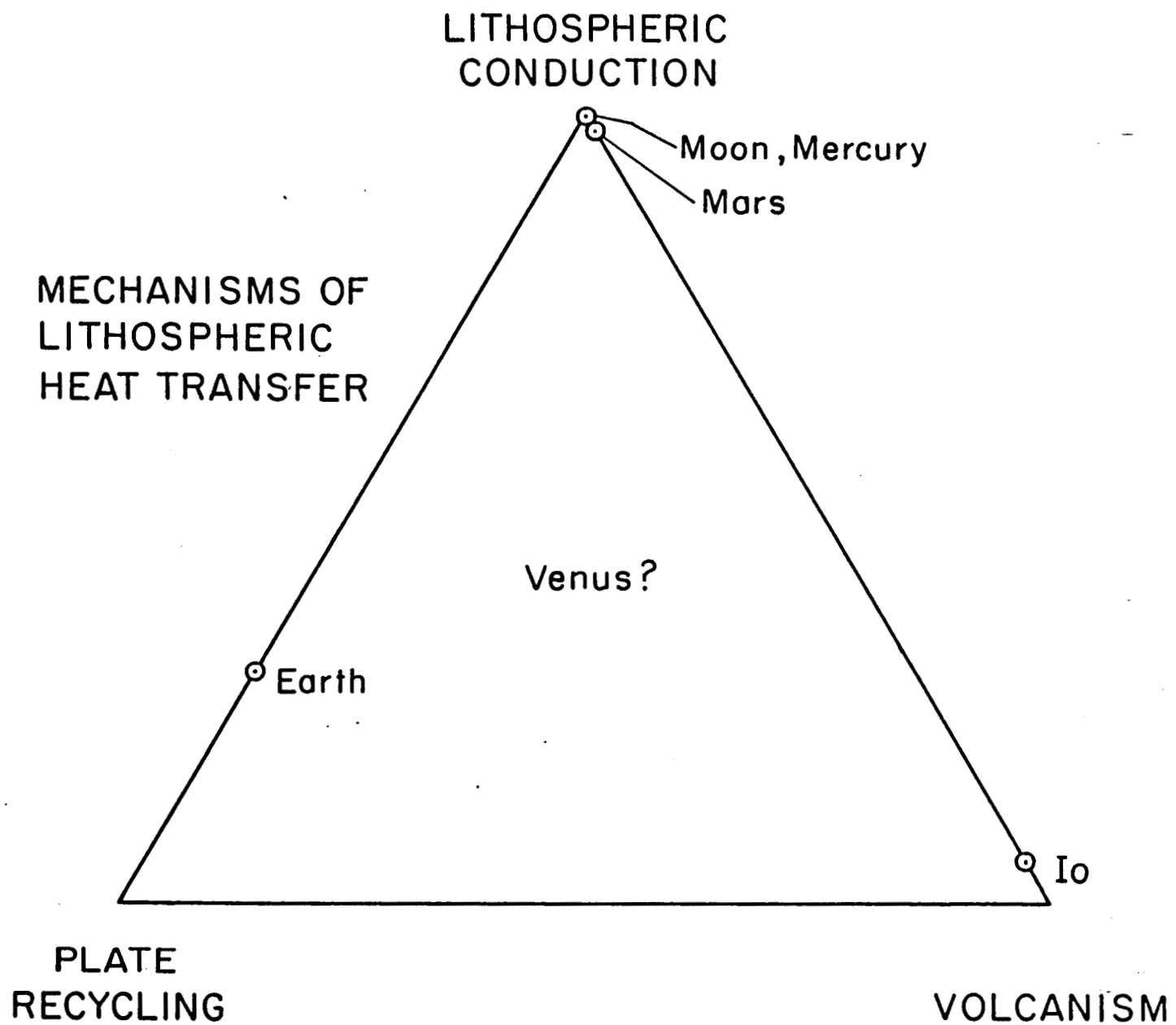
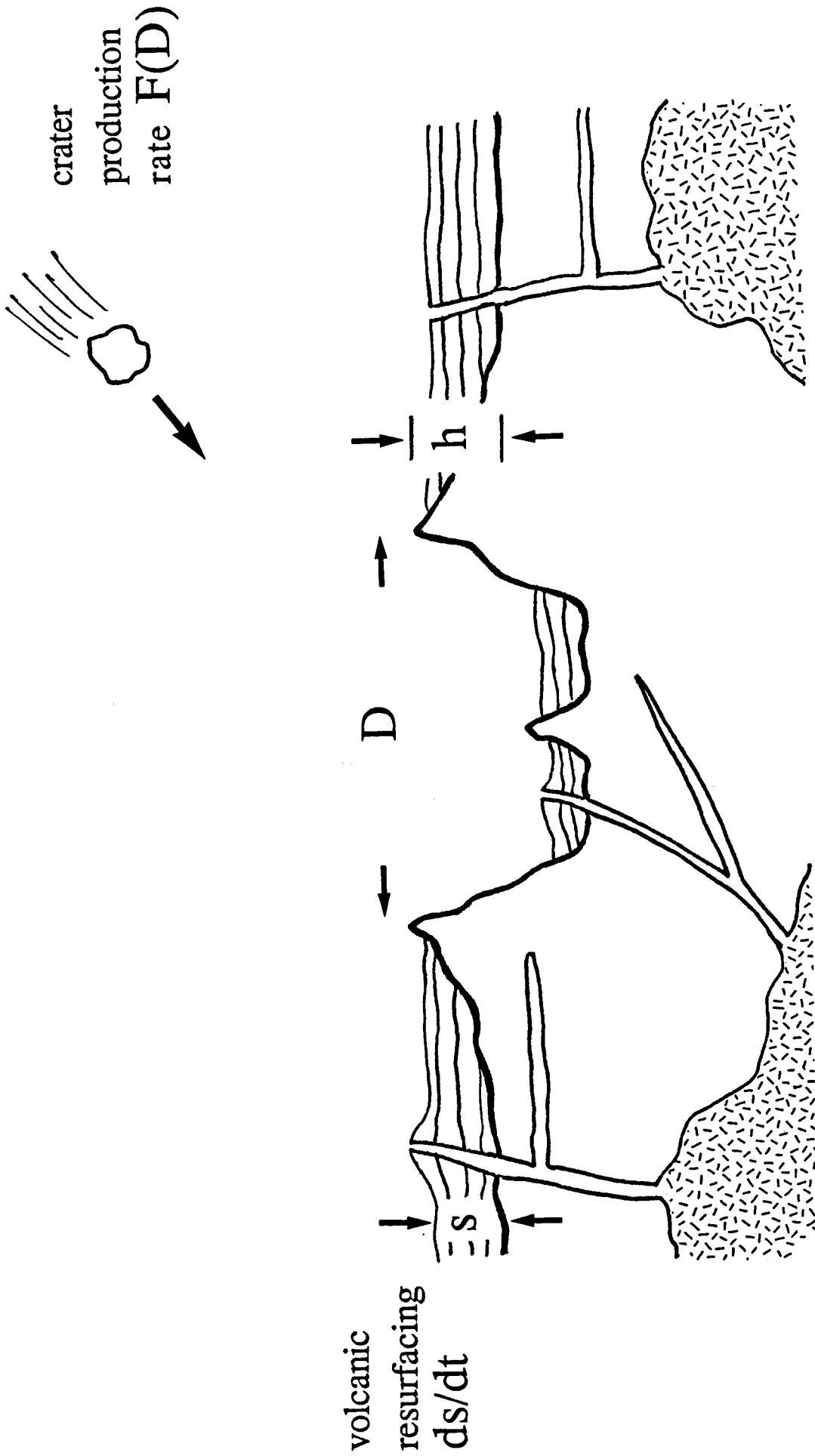


Figure 2.1



equilibrium crater density $N(D) = F(D) h(D) / (ds/dt)$

Figure 2.2

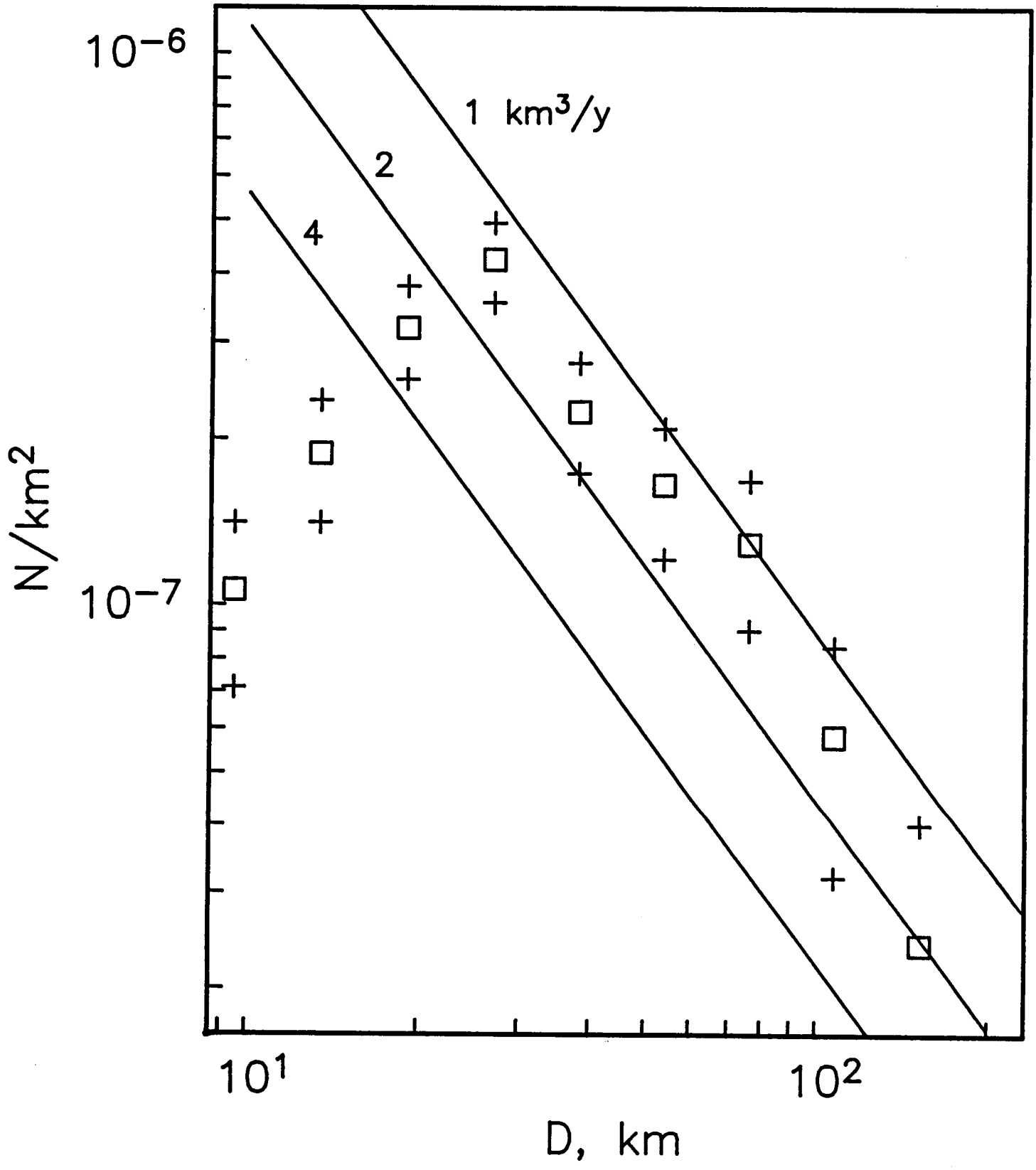


Figure 2.3

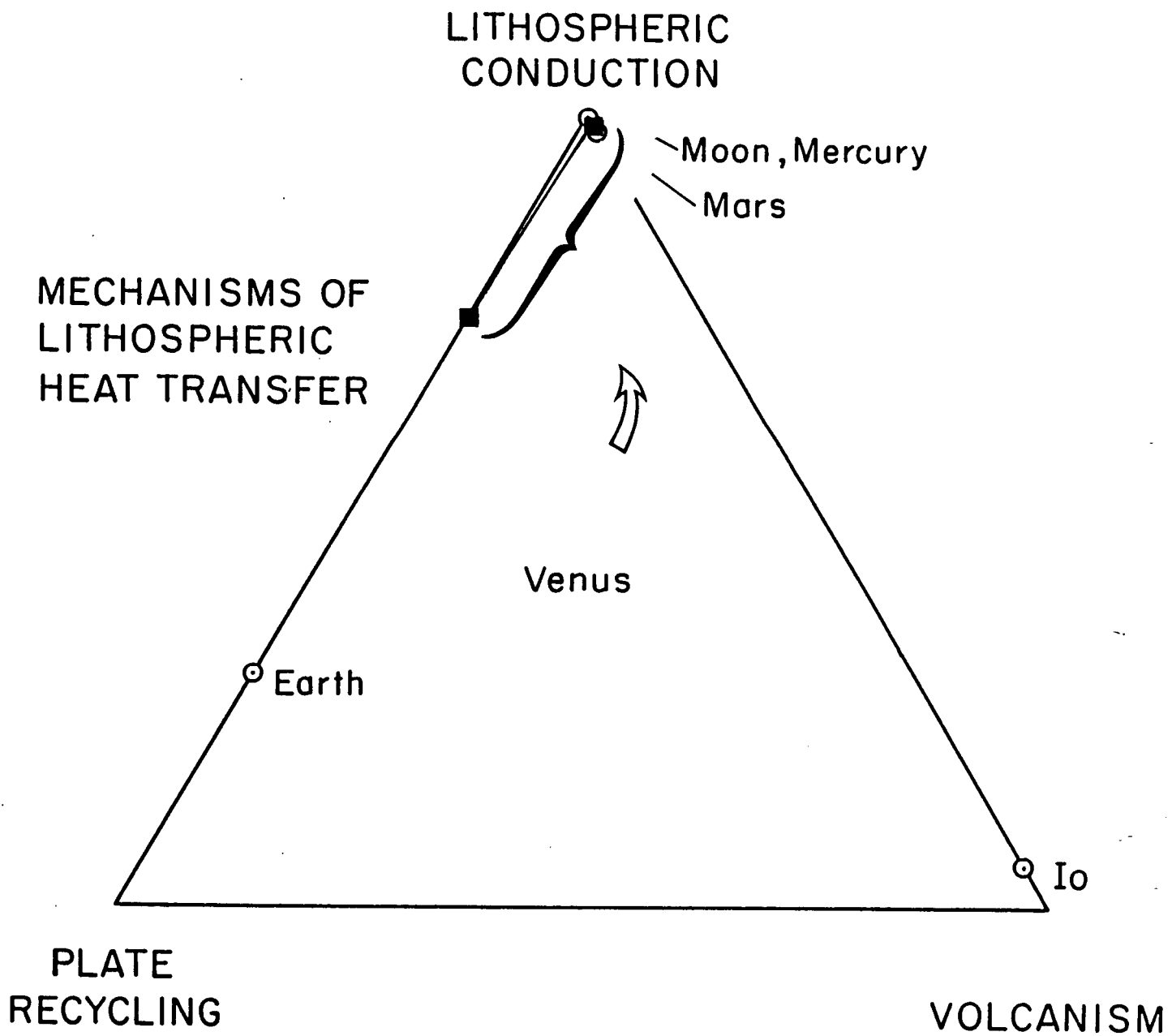


Figure 2.4

CHAPTER 3:

**VISCOUS RELAXATION OF IMPACT CRATER
RELIEF ON VENUS: CONSTRAINTS ON CRUSTAL
THICKNESS AND THERMAL GRADIENT**

INTRODUCTION

Radar images of Venus have revealed a planet with a variety of tectonic and volcanic features [*Campbell et al.*, 1983, 1984; *Barsukov et al.*, 1986]. The Venus surface has also preserved a number of large impact craters [*Campbell and Burns*, 1980; *Ivanov et al.*, 1986; *Basilevsky et al.*, 1987]. The density and distribution of these craters provide crucial information for understanding the geological evolution of the planet [*Ivanov et al.*, 1986; *Schaber et al.*, 1987a; *Grimm and Solomon*, 1987]. The endogenic modification of impact craters can also yield key constraints on internal planetary processes. One such modification mechanism is the viscous relaxation of crater topography. This process is thought to have been important for the Moon [*Danes*, 1965; *Hall et al.*, 1981; *Solomon et al.*, 1982a; *Baldwin*, 1987] and the Galilean satellites [*Parmentier and Head*, 1981; *Passey and Shoemaker*, 1982; *Thomas and Schubert*, 1986, 1987]. On Venus, considerable viscous relaxation of topography has been anticipated because of the high surface temperature and the strong temperature dependence of strain rate [*Weertman*, 1979; *Solomon et al.*, 1982b, *Stephens et al.*, 1983]. Venera 15/16 radar altimetric profiles across impact craters 30 - 140 km in diameter, however, show crater depths in excess of several hundred meters, suggesting that the extent of relaxation of relief for these features has been small [*Ivanov et al.*, 1986; *Basilevsky et al.*, 1987].

In this paper we employ the observed depths of impact craters to test models for the viscous relaxation of surface topography on Venus. We utilize a general numerical formulation of gravity-driven flow in a linearly viscous fluid, and we incorporate distinct densities and temperature-dependent flow laws for crustal and mantle material. Given an estimate for the initial topography of impact craters on Venus, we compare the observed topography with that predicted by viscous relaxation for a range of possible values for crater age, crater diameter, crustal

thickness, and mean lithospheric thermal gradient. On the basis of a statistical approach, we determine confidence levels for rejecting combinations of these parameters. These calculations suggest that the mean thickness of the crust over a substantial fraction of the planet is probably about 10-20 km. We consider several possible implications of this result for the evolution of Venus.

IMPACT CRATERS ON VENUS

Impact craters on Venus were first identified in Earth-based radar images of the surface as circular areas of low backscatter surrounded by an annular region of high reflectivity; the circular radar-dark regions sometimes contained a central bright spot [*Campbell and Burns*, 1980]. The orbital radar images obtained by Venera 15 and 16, with a resolution of 1-2 km, currently allow the best identification of impact craters over the imaged portion of the planet [*Ivanov et al.*, 1986; *Basilevsky et al.*, 1987]. Distinct characteristics diagnostic of impact craters, such as elevated rims, central peaks, and ejecta blankets, can be resolved for many craters, although there are also many approximately circular features of uncertain origin [*Barsukov et al.*, 1986]. A total of 146 features on the northernmost 25% of the Venus surface have been classified as impact craters [*Basilevsky et al.*, 1987]. These features range in diameter from approximately 10 to 140 km. A Venera image of the largest identified impact crater, Klenova, is shown in Figure 3.1.

The density of impact craters observed by Venera 15/16 may be used to estimate the mean crater retention age of the northern quarter of the Venus surface. A key and highly uncertain parameter in such estimates is the crater production rate on Venus and its variation with time. Different assumptions regarding this parameter can lead to quite different values for the mean surface age. *Ivanov et al.* [1986], following *Hartmann* [1977], assumed that the cratering flux on Venus has

been equal to that for the Moon since the end of lunar mare emplacement. With such an assumption the mean crater retention age is about 1 b.y. *Schaber et al.* [1987a], in contrast, suggested that the cratering flux for Venus is closer to that of the Earth, which is nearly triple the lunar cratering flux [*Grieve*, 1984]. A crater retention age of only a few hundred million years results.

Topographic profiles of a number of impact craters were obtained by the Venera 15/16 radar altimeters [*Ivanov et al.*, 1986]. *Basilevsky et al.* [1987] give apparent depths (measured from rim crest to crater floor) for 20 craters. These features, with diameter D ranging from about 25 to 140 km and depth varying from 200 to 2400 m, are depicted on a depth-diameter plot in Figure 3.2.

The crater topographic data are subject to several sources of error. The first is the uncertainty in the measurement of the average elevation over the altimeter footprint. At ± 50 m this uncertainty is small compared with the relief of large impact craters on Venus [*Barsukov et al.*, 1986]. A second source of error is the smoothing effect of the 50-km-diameter footprint of the altimeter [*Barsukov et al.*, 1986]; this smoothing yields an underestimate of topographic relief. Examination of the apparent depth of the 20 craters in Figure 3.2 suggests that depths are significantly underestimated only for craters with diameters less than or equal to about 30 km. We do not consider further the topography of craters less than about 30 km in diameter in order to avoid this source of bias. A third potential error is the misidentification of features as impact craters in the tabulation of *Basilevsky et al.* [1987]. We do not include Cleopatra Patera in our analysis, because its deep inner floor, breached rim, and associated infilling by plains materials suggest a volcanic origin for this feature [*Schaber et al.*, 1987b]. Yablochkina and Tsvetaeva are noticeably noncircular in map view [*Basilevsky et al.*, 1987], and the possibility of a volcanic origin for these two features has been raised [G. G. Schaber, personal

communication, 1987]; without further information, however, we include them in our analysis. After eliminating Cleopatra and smaller features with significantly under-sampled depths, there are 15 craters of probable impact origin with topographic profiles measured by Venera 15 and 16; these craters are listed in Table 3.1.

The geographical distribution of the craters in Table 3.1 appears to be non-random (Figure 3.3). Two-thirds of these craters fall within a region extending over the pole and covering only about 10% of the Venera 15/16 survey area, or 2-3% of the Venus surface. A nearest-neighbor test of intercrater distances [Davis, 1973] indicates that a random distribution of crater locations may be rejected with greater than 90% confidence in favor of a clustered distribution. This result suggests that there is some systematic experimental bias in the locations of impact craters with measured depths. These craters are only a small subset of the total observed to date, however, and the overall distribution of craters imaged by Venera 15 and 16 appears to be random [Basilevsky *et al.*, 1987]. These observations raise the question of whether the craters with known topography are globally representative. Available Pioneer Venus elevation data [Pettengill *et al.*, 1980], referenced to the mean radius of 6051.9 km [Ford, 1986], show that the distribution of elevations of the regions surrounding the craters in Table 3.1 spans the range -1.5 to 1.2 km and is given approximately by a normal distribution with mean -0.2 km and standard deviation 0.7 km (Figure 3.4). Further, 13 of the 15 craters occur on smooth or rolling plains (Figure 3.4), units widespread on the northern quarter of the Venus surface [Barsukov *et al.*, 1986; Basilevsky *et al.*, 1987]. We therefore assume that the crater relief measurements are representative of other plains units at similar elevations elsewhere on Venus.

APPROACH

There are several possible procedures for testing viscous relaxation models against the preserved topography of impact craters. One approach would be to separate the craters with measured topography into candidate fresh and relaxed craters and seek viscous relaxation models that map the topography of a fresh crater into that of a relaxed crater of the same or similar diameter. Such a methodology was adopted by *Hall et al.* [1981] in their study of the importance of viscous relaxation as a crater modification process on the Moon. Unfortunately, the combined effects of limited horizontal resolution and the small number of craters with measured topography preclude such a treatment for Venus at present.

Instead, we adopt the following approach. We employ apparent depth as the sole measure of crater relief on Venus, because estimates of depth are likely to be more robust than are the details of crater topographic profiles. From Venera data we calculate the mean and variance of observed crater relief on Venus as a function of crater diameter. From observations of lunar craters and scaling arguments, we then estimate the mean and variance of the apparent depth that fresh impact craters would display on Venus as a function of crater diameter. Support for this estimation procedure comes from the observation of *Ivanov et al.* [1986] that large craters on Venus are morphologically similar to impact features of comparable size on other planetary bodies. In particular, all of the observed impact craters on Venus with $D > 30$ km are morphologically complex, with terraced inner walls and central peaks on a flat floor [*Basilevsky et al.*, 1987]. Given the two relations for observed and fresh crater populations we test theoretical models of viscous relaxation. For specific model parameters and crater diameter, we compare the crater depth predicted by the viscous relaxation model with the observed distribution of crater depths. We establish a formal statistical criterion for

the rejection of specific viscous relaxation models as being inconsistent with the observations.

Depths of Observed and Fresh Craters on Venus

A relationship between depth and diameter of craters on Venus may be obtained from the data in Table 3.1. Linear regression of log diameter D versus log depth d_v yields the relation

$$\log d_v = (-0.83 \pm 0.03) + (0.34 \pm 0.17) \log D \quad (3.1)$$

where both D and d_v are expressed in kilometers.

Because of the dependence of crater characteristics on the surface gravitational acceleration g [Melosh, 1980] and the similarity in g for Earth and Venus, terrestrial data are the natural choice from which to estimate initial depths of fresh craters on Venus. There may be systematic differences between craters on the Earth and Venus due to increased fallback into the crater of atmospherically decelerated ejecta [Settle, 1980] and increased volume of impact melt [Grieve and Head, 1982] on Venus, but such differences have not been detected at Venera resolution and appear to be minor contributions to overall relief. The relationship between diameter and apparent depth for complex terrestrial craters was examined by Grieve and Robertson [1979], who derived $\log d = -0.85 + 0.31 \log D$ for craters in sedimentary targets. No regression was performed on the widely scattered data from craters in crystalline targets, but such craters were reported to be approximately twice as deep as structures of the same diameter in sedimentary targets, a result that would be consistent with the approximate relation $\log d \cong -0.55 + 0.31 \log D$. The principal source of error in estimates of apparent depth for

terrestrial craters is the correction for rim erosion. Examination of the available information on the geometry of the complex craters included by *Grieve and Robertson* [1979] suggests that initial depths are well known for no more than about five such structures.

On account of the large uncertainties in the initial depths of complex terrestrial impact craters, we have elected to utilize the depths of 52 comparatively fresh lunar craters of Copernican and Eratosthenian age. The significantly larger number of observations will ensure that our predictions of crater depth, scaled to Venus conditions, will have small variance. Stereophotogrammetric and shadow-measurement data from *Pike* [1980a] and maps from the Lunar Topographic Orthophotomap (LTO) and Lunar Aeronautical Chart (LAC) series were used to obtain depths. Errors in depth measurements are tens of meters for LTOs and 100-200 m for LACs.

We assume that the initial topographic profile of a large crater on Venus differs from that of a fresh lunar crater of the same diameter by a simple multiplicative scaling factor. Observations of crater dimensions on the terrestrial planets and satellites have been invoked to suggest two possible scaling rules: that either the depth of complex craters or the crater diameter D_t marking the transition from simple to complex crater morphology varies inversely with the surface gravitational acceleration g [*Pike*, 1977, 1980b; *Grieve and Robertson*, 1979; *Basilevsky and Ivanov*, 1982]. These two relations are mutually exclusive. If the depth of complex craters scales inversely with gravity, then $d_v = (g_m / g_v) d_m$, where the subscripts m and v refer to the Moon and Venus, respectively. Under the alternative assumption that transition diameter D_t scales inversely with gravity, a relation describing the depth of complex craters on Venus has been derived graphically from lunar data by *Ivanov et al.* [1986]. Such a relation may be given in analytic form, $d_v = (g_m / g_v)$

$(1-a_1) d_m$, under the assumptions that the ratio d/D for simple craters is independent of g and that the parameter a_1 in the relation $\log d = a_0 + a_1 \log D$ for complex craters is similar on all of the terrestrial planets. The factors for scaling the topography of complex craters from the Moon to Venus under the assumptions that d or D_t scales inversely with g are 0.183 and 0.305, respectively. Regression analysis of the lunar data can then be used to predict the initial depth of a complex crater of diameter D on Venus

$$\log d_i = (a_0 \pm 0.01) + (0.31 \pm 0.04) \log D \quad (3.2)$$

where a_0 is -0.74 under depth scaling or -0.52 under transition-diameter scaling and both D and d_i are expressed in kilometers. The means and 95% confidence intervals for the mean for observed and fresh crater depths are shown in Figure 3.2; the fresh crater depths are those given by the depth-scaling rule. We note that the depth interval spanned by the two scaling rules is similar to the range of depths inferred by *Grieve and Robertson* [1979] for complex terrestrial craters in sedimentary and crystalline targets, although as noted above the errors in the initial depths of such terrestrial craters may be large.

In addition to crater depth, we need an estimate of the complete topographic profile of a fresh complex crater on Venus in order to evaluate the change in apparent depth associated with a particular model for viscous relaxation. We used the profiles of three comparatively young lunar impact craters having diameters that approximately span the diameter range of the Venera observations: Langrenus ($D = 132$ km), Eratosthenes ($D = 58$ km), and Timocharis ($D = 34$ km). The topography for Langrenus was derived from Earth-based radar [S. Zisk, personal communication, 1986], that for Eratosthenes was obtained from LAC 58, and that

for Timocharis was obtained from LTO 40B3. For all three craters, an azimuthally averaged profile was calculated. These profiles were stretched uniformly in the radial direction to match specific crater diameters in the Venera data [Ivanov *et al.*, 1986; Basilevsky *et al.*, 1987]. The elevations were adjusted in the radial stretch using the empirical relations of Pike [1977] expressing the variation of key crater morphological parameters with diameter. For example, Pike showed that rim height is proportional to $D^{0.4}$, so the rim height at $D + \Delta D$ is multiplied by $(1 + \Delta D/D)^{0.4} \simeq 1 + 0.4 \Delta D/D$. The profiles were then multiplied by the factor appropriate to depth or transition-diameter scaling derived above to convert the lunar profiles to initial topographic profiles for Venus craters.

Statistical Interpretation of Viscous Relaxation Models

Given the regression curves and confidence intervals for the depths of both fresh and observed impact craters on Venus, we may estimate from Figure 3.2 the extent of viscous relaxation at each diameter such that the mean depth of partially relaxed craters is no longer consistent with the observations. For example, the predicted average depth of a fresh crater 140 km in diameter, from Figure 3.2, is 0.8 km. The estimated lower bound at 95% confidence for the mean depth of observed craters on Venus at $D = 140$ km is 0.5 km. Therefore viscous relaxation could reduce the mean depth of craters at this diameter to as little as 0.5 km without making this datum inconsistent with the observations at the given confidence level. In other words, any viscous relaxation model that produced more than about a 35% decrease in the apparent depth of craters of this diameter for the given initial depth would yield craters significantly shallower than are observed.

We may formalize this approach as follows. For a fixed D , we assume that all craters are of the same age, equal to half the mean crater retention age. We further

assume that the initial crater depths at fixed diameter are log-normally distributed, with mean $\log d_i$ and variance of the mean s_i^2 given by linear regression on the scaled lunar data. Note that s_i^2 is also a function of D , with the smallest values near the center of the data field. Viscous relaxation will reduce the mean depth to $\delta(D)$ (Figure 3.5), which we compare with the observed crater population, taken also to be log-normally distributed with mean $\log d_v$ and variance of the mean s_v^2 at the same diameter. We test the null hypothesis, $H_0: d_v = \delta$, by forming the Smith-Satterthwaite T statistic [Devore, 1982, p. 292]

$$T = (d_v - \delta) / (s_v^2 + s_i^2)^{1/2} \quad (3.3)$$

with v degrees of freedom given by

$$v = (s_v^2 + s_i^2)^2 / [s_v^4 / (n_v - 1) + s_i^4 / (n_i - 1)] \quad (3.4)$$

In the limit where the variance of scaled lunar crater depths is negligible compared with the variance in observed crater depths on Venus, the one-sample t test may be used, although in practice we use the Smith-Satterthwaite test in all cases. The null hypothesis is rejected at the significance level α in favor of the alternative hypothesis, $H_1: d_v > \delta$, if $T \geq t_{\alpha,v}$, where $t_{\alpha,v}$ is the 100(1- α) cumulative percentile of the t distribution with v degrees of freedom. For a value of T fixed by a specified amount of viscous relaxation, we can solve for the confidence level 1- α at which the null hypothesis may be rejected by integrating the t distribution [Selby, 1967]

$$1 - \alpha = \int_0^{\Gamma} \frac{\Gamma\left(\frac{\nu + 1}{2}\right)}{(\nu\pi)^{1/2} \Gamma\left(\frac{\nu}{2}\right)} \left(1 + \frac{x^2}{\nu}\right)^{-\left(\frac{\nu+1}{2}\right)} dx \quad (3.5)$$

where Γ is the gamma function. The parameter α varies from 0 to 0.5 in the one-tailed test; here it provides a measure of the likelihood of a particular viscous relaxation model given depths of observed and fresh craters.

VISCOUS RELAXATION MODEL

We assume that the crust and upper mantle of Venus behave as linearly viscous fluids. This simple rheology has successfully described the response of the terrestrial mantle to deglaciation [e.g., *Cathles, 1975*] and should be applicable to most of the Venus interior because of the high surface temperature and long time scales involved. Laboratory measurements of high-temperature creep in rocks typically show a nonlinear relationship between stress and strain rate [e.g., *Ashby and Verrall, 1977*], which we incorporate in an approximate fashion by means of an effective viscosity. Near-surface frictional sliding [*Brace and Kohlstedt, 1980*] is also parameterized by an effective viscosity. We consider below the possible modifying effects if portions of the crust or upper mantle of Venus display elastic behavior on long time scales.

By direct numerical integration of the equations of motion of a linearly viscous fluid [*Cathles, 1975*], relaxation of topography can be evaluated for a medium with an arbitrary depth dependence of viscosity. Different densities in the crust and mantle are accommodated by solving the equations of motion in the two regions subject to appropriate boundary conditions. A detailed presentation of this treatment is given in Appendix 3.A. This method is an improvement over most

previous planetary applications of viscous relaxation models. In simple formulations involving a layer over a halfspace that include approximately the effects of both depth-dependent viscosity and isostatic compensation of surface topography [e.g., *Solomon et al.*, 1982b], discontinuities in density (crust) and viscosity (lithosphere) must occur at the same subsurface horizon; this restriction is not required here. Further, the dependence of viscosity on thermal gradient can be explicitly included rather than resorting to isoviscous halfspace models [*Passey and Shoemaker*, 1981] or invoking an exponential variation with depth [*Parmentier and Head*, 1981].

On Earth, the differences in creep behavior between crustal and mantle materials can result in a weak lower crust separating stronger crustal and upper mantle layers. This situation arises for certain combinations of crustal thickness and thermal gradient, including those appropriate to many continental regions. Evidence supporting this view includes the aseismic nature of the lower continental crust [*Chen and Molnar*, 1983], the narrowness of the zone of strain accumulation across major strike-slip faults [*Turcotte et al.*, 1984], and the two scales of deformation in zones of continental extension [*Zuber et al.*, 1986]. The crust-mantle boundary, therefore, is a major mechanical discontinuity within the lithosphere. By analogy with terrestrial behavior, we consider a model for Venus consisting of a chemically and mineralogically uniform crust overlying an ultramafic mantle to describe the principal compositionally-induced variation in rheology within the upper few tens of kilometers.

The effective viscosity in the crust and mantle depends strongly on temperature. High-temperature deformation of planetary materials, in general, can be described by a flow law of the form

$$\dot{\epsilon} = A \sigma^n \exp(-Q/RT) \quad (3.6)$$

where $\dot{\epsilon}$ is a strain rate, σ is a corresponding deviatoric stress, R is the gas constant, T is the absolute temperature, and A , n , and Q are empirically derived constants. For linearly viscous flow under uniaxial compression (the state of stress under which creep measurements are typically made), the constitutive relation is $\sigma = 2 \eta \dot{\epsilon}$, where η is the dynamic viscosity. Substituting from (6), the effective viscosity has the form

$$\eta(T) = [\sigma^{(1-n)}/2A] \exp(Q/RT) \quad (3.7)$$

For the mantle, we use the flow law for polycrystalline olivine (Fo_{91}) determined by *Goetze* [1978]. For the crustal layer we use the flow law for Frederick diabase given by *Caristan* [1982]. *Shelton* [1981] also reported a flow law for this material; the predicted strain rate is about an order of magnitude lower than that given by the relation of *Caristan* [1982] over the range of temperatures and stress differences relevant to the viscous relaxation problem. The difference may be the result of different experimental procedures (particularly the nature of the confining medium) or a greater proportion of pyroxene and a lesser proportion of weaker feldspar in the particular samples used by Shelton. The composition of the Venus surface measured at the Venera 13 and 14 landing sites [*Surkov et al.*, 1983] is closer to that of the diabase samples of *Caristan* than that of *Shelton's* samples, so *Caristan's* flow law is preferable for our application. However, viscous relaxation calculations were also carried out using *Shelton's* results as a test of sensitivity to variations in crustal rheology.

Creep rates in rock can be strongly affected by the presence of water,

particularly in the form of thin films between silicate grains [e.g. , *Ashby and Verrall*, 1977]. Both *Caristan* [1982] and *Shelton* [1981] endeavored to dry their diabase samples prior to measurement of strain rate, and the olivine analyzed by *Goetze* [1978] contained only a small (0.3 %) weight fraction of water. Nonetheless, neither the relative water contents of the laboratory samples and the Venus interior nor whether any differences significantly affect the flow laws are known.

We assume that the temperature increases linearly with depth from an average surface value, equal to the surface temperature at the mean planetary elevation [*Seiff et al.*, 1980]. Because the dependence on stress observed in laboratory samples is nonlinear, the effective viscosity must be evaluated at some characteristic stress difference $\bar{\sigma}$, which we take to be the average initial stress difference within a cylindrical volume of radius D and depth $D/2$ centered beneath the crater. These dimensions are somewhat arbitrary but approximately reflect the volume within which significant deviatoric stress occurs. In practice, the characteristic stress is solved iteratively by specifying an initial value for $\bar{\sigma}$, calculating the average initial viscous stress deviator within the designated volume, substituting this new value for $\bar{\sigma}$, and repeating the calculation until convergence occurs. Because such calculations would be extremely time consuming if conducted for every model, we determine $\bar{\sigma}$ in this fashion at each crater diameter only for a single reference model with representative parameter values. We discuss this approximation further below.

Near the Venus surface rock strength is likely limited by frictional sliding on faults rather than by ductile flow. This effect can be parameterized by specifying a brittle-ductile transition depth above which the effective viscosity increases linearly with depth. The viscosity in both the brittle and ductile regions is then proportional to lithospheric strength as defined by *Brace and Kohlstedt* [1980]. Values of the

characteristic stress $\bar{\sigma}$ and the depths of the brittle-ductile transitions in the crust and mantle are determined simultaneously for the reference model. Adopted model parameters are given in Table 3.2.

Largely for numerical convenience, we impose a lower bound of 10^{20} Pa s on the effective viscosity in either the crust or the mantle. Substantially lower values are not likely to be characteristic of long-term bulk deformation of the Venus lithosphere. The results reported below are not sensitive to the value selected for this lower limit.

As an illustrative comparison, we have applied the viscous relaxation model to a large impact crater on the stable interior of a terrestrial continent. On Earth, erosion modifies crater topography at rates of order 10 m/m.y. [*Grieve and Robertson, 1979*], and a primary issue is whether viscous relaxation of relief occurs at comparable or greater rates and can therefore be resolved. We take $D = 140$ km as the largest preserved terrestrial impact structure [*Grieve and Robertson, 1979*], and we assume that the initial topography may be obtained from that of the lunar crater Langrenus under the scaling that crater depth varies as g^{-1} . In this test case, we select parameters so as to maximize the rate of relaxation. We adopt $H = 35$ km and $dT/dz = 20$ K/km, and we assume that the flow law for the continental crust is that for quartz [*Brace and Kohlstedt, 1980*]. We also decrease the volume over which the characteristic stress $\bar{\sigma}$ is obtained to that contained within the cylinder of radius $D/2$ and depth $D/4$, giving $\bar{\sigma} = 15$ MPa and a depth of 15 km for the brittle-ductile transition in the crust. We find rates of relaxation of topography of a few meters per m.y., which result in relaxation of 45% of the crater relief in 200 m.y. These rates are an order of magnitude smaller than the rate of removal of relief by erosion. We conclude that viscous relaxation has not been an important modification process for impact craters on stable terrestrial continents.

APPLICATION TO VENUS

The key parameters in the viscous relaxation model that are of geological and geophysical interest are the crustal thickness H and the average lithospheric thermal gradient dT/dz (see Appendix 3.A). Comparison of the observed relief of impact craters with that predicted from the model can be used to derive upper bounds on these parameters. Since viscosity decreases with increasing temperature, relaxation will occur more rapidly at higher temperature, or at a higher value of dT/dz for a fixed surface temperature. Because the crust is less viscous than the mantle at a comparable temperature, topographic decay will be more rapid for a thicker crust. We can therefore anticipate that a trade-off exists between dT/dz and H when other parameters are fixed: a given amount of topographic relaxation in a specified time can be accommodated by a low thermal gradient and a thick crust or alternatively by a higher thermal gradient and a thinner crust. In terms of the statistical approach discussed in the last section, models with higher thermal gradients and thicker crusts can be rejected more easily than models with lower thermal gradients and thinner crusts. We adopt the $\alpha = 0.05$ significance (95% confidence) level for the statistical test of upper limits to dT/dz and H . The risk of incorrectly rejecting a $(dT/dz, H)$ combination (type I error) is therefore only 5%. The corresponding probability of incorrectly accepting a $(dT/dz, H)$ pair (type II error) is about 20% [Devore, 1982, p. 246]. Since we seek upper limits to dT/dz and H , the possibility of a type I error is more serious and should be minimized in spite of the higher probability of the alternative type of error.

To ensure that the derived upper bounds on dT/dz and H are valid, we should utilize observations and adopt modeling approaches such that errors are likely to lead to overestimates of these parameters. For instance, observed crater depths are likely to be underestimates of the true depths because of the smoothing effect

of the altimeter footprint (see above), and because such additional processes that degrade crater relief as volcanism or erosion have been neglected. Under these conditions the amount of viscous relaxation will be overestimated, which will raise the upper bounds on dT/dz and H . The possibility that young impact craters on Venus are systematically shallower than terrestrial or scaled lunar craters because of enhanced ejecta fallback [Settle, 1980], increased impact melt production [Grieve and Head, 1982], or more rapid initial strain rates during the transient decay of impact heat [O'Keefe and Ahrens, 1977] from a target at higher ambient temperatures, will also yield overestimates of the extent of any long-term viscous relaxation. The characteristic stress, described in the previous section, is also deliberately underestimated in order to overestimate the effective viscosity for a specified material and temperature; this in turn yields larger upper bounds on dT/dz and H .

Beyond crustal thickness and average thermal gradient the remaining parameters in the viscous relaxation problem are the crater age t , the initial state of isostatic compensation c (see Appendix 3.A), and the choice of a scaling rule to estimate the depths of fresh impact craters from the depths of lunar craters. We will consider average crater ages of 50 m.y. and 500 m.y., corresponding to mean crater retention ages of 100 m.y. and 1 b.y., respectively; these values approximately span the range in reported values for the northern 25% of the Venus surface [Ivanov *et al.*, 1986; Schaber *et al.*, 1987a; Grimm and Solomon, 1987]. The parameter c is taken to be 0 or 1, corresponding to zero or complete initial local compensation of crater topography. For all calculations described below we shall assume that crater depth scales as g^{-1} . The alternative scaling law in which transition diameter scales as g^{-1} yields greater depths for fresh craters at each diameter. This greater relief results in a greater effective stress beneath the crater,

which in turn drives more rapid viscous relaxation. However, the accumulated fractional change in relief before the depth of a partially relaxed crater becomes inconsistent with observed depths is also larger for this scaling law (about 60% at 140 km diameter instead of 35%). These two effects tend to offset one another, so that the final distribution of confidence levels is not very different from those derived under the adopted scaling rule.

Initially Uncompensated Craters

The viscous relaxation of a crater 140 km in diameter is depicted in Figure 3.6. This diameter corresponds to the largest crater on Venus with a measured depth (Table 3.1 and Figure 3.2). Relaxation is shown for two sets of values of thermal gradient and crustal thickness; for both sets of calculations the crater is assumed to be initially uncompensated. With a low thermal gradient (10 K/km) and a thin crust (10 km) there is relatively little relaxation of relief even in 500 m.y. (Figure 3.6a), whereas with a somewhat higher thermal gradient (15 K/km) and a somewhat thicker crust (15 km) relaxation is nearly complete after only a few tens of millions of years (Figure 3.6b).

A similar set of calculations for a crater 32 km in diameter is shown in Figure 3.7. This diameter corresponds to the smallest Venus crater for which the measurement of depth is likely to be reliable (Table 3.1 and Figure 3.2). Compared with the case for $D = 140$ km, there is a comparable relaxation of relief for a thin crust and low thermal gradient but substantially less relaxation for a thicker crust and higher gradient.

This behavior may be understood by consideration of the constant τ governing the exponential decay with time of surface topographic relief; these time constants are shown in Figure 3.8 for the four models in Figures 3.6 and 3.7. (Formally, there

are two time constants τ_1 and τ_2 for each model, but the term corresponding to the larger time constant τ_1 makes only a small contribution to the topography in this case; see equation A40 in Appendix 3.A). For given dT/dz and H , values of τ at different D differ by a multiplicative constant; the lower stress difference beneath a smaller crater results in a higher effective viscosity, which in turn leads to a longer relaxation time. The largest contributions to the Hankel transform of the crater topographic profile are at wavelengths between 0.5 and 3 D . For models with $dT/dz = 15$ K/km and $H = 15$ km, the time constants at these wavelengths for a crater with $D = 32$ km are of order 10^8 yr, whereas those for a crater with $D = 140$ km are of order $10^5 - 10^7$ yr. Much of the relief of the smaller crater therefore remains after 500 m.y. (Figure 3.7b) while the larger crater relaxes completely over the same time (Figure 3.6b).

The situation differs for models with $dT/dz = 10$ K/km and $H = 10$ km. The time constants at the relevant wavelengths for the crater with $D = 32$ km are near a local minimum in τ controlled by the low viscosity zone in the lower crust. The important time constants for the crater 140 km in diameter, however, are near a local maximum in τ controlled by the high viscosity upper mantle. Because of the stress-dependence of effective viscosity, the values of τ near the respective extrema are similar and of order 10^9 yr. At a given time after crater formation, the fractional relaxation for craters of both diameters is similar under these circumstances (Figures 3.6a and 3.7a).

We have conducted calculations of the sort shown in Figures 3.6 and 3.7 for a wide range of values of both dT/dz and H . For a crater 140 km in diameter, the fractional relief remaining after 50 m.y. is shown as a function of these two parameters in Figure 3.9a. The trade-off between dT/dz and H is apparent. Corresponding confidence intervals for rejecting parameter values are given in Figure

3.9b. Figure 3.10 shows the remaining relief and the associated confidence levels for parameter rejection for a crater 140 km in diameter and 500 m.y. in age. For given values of dT/dz and H , the confidence level for model rejection is higher at a 500 m.y. age than a 50 m.y. age, because the larger predicted amount of relaxation of topographic relief is more difficult to reconcile with the observed crater depths. The results for a similar suite of calculations for a crater 32 km in diameter are shown in Figures 3.11 and 3.12. At this crater diameter the fractional relief remaining is insensitive to crustal thickness for $H > 20$ km because the upper mantle does not play a significant role in the flow accommodating relaxation of shorter wavelengths.

A summary of 95% confidence limits to paired values of dT/dz and H as constrained by these models with initially uncompensated crater relief is given in Figure 3.13. For $D = 140$ km, lithospheric thermal gradients in excess of 20 K/km are possible only when the crust is thinner than 10 km and then only if most craters are young (of order 50 m.y.). If the average lithospheric thermal gradient is as low as 10 K/km, then a 15-20 km thick crust is possible, again only if most craters are young. However, if the age of the Venus surface is comparable to the largest current estimates (mean crater ages of order 500 m.y.), then acceptable models are restricted to $H \leq 10$ km and $dT/dz \leq 10$ K/km. The range of possible combinations of H and dT/dz is larger for $D = 32$ km, since relaxation is generally slower for shorter wavelengths. For such features, the crustal thickness is unconstrained provided that the observed craters at this diameter are young and that $dT/dz < 20$ K/km. For a 500 m.y. mean crater age, similar behavior independent of H requires $dT/dz < 10$ K/km.

We have also examined viscous relaxation for a Venus crater with $D = 50$ km, a value near the median diameter of craters in Table 3.1. Although the relaxation of

a 50-km-diameter crater is somewhat closer to that for $D = 32$ km than that for $D = 140$ km, the inferred limits to crustal thickness and thermal gradient are closer to those imposed by the relief of the largest craters, with upper limits to H of 20, 10, and 5 km for $dT/dz = 10, 20,$ and 30 K/km respectively (Figure 3.13). This result is because the constraint on the mean depth of observed craters is strongest in the center of the diameter distribution than at either extreme (Figure 3.2) and so less viscous relaxation is allowed at a specified confidence interval.

For a diabase crust that deforms according to the flow law derived by *Shelton* [1981], limits on dT/dz and H are less restrictive than those using *Caristan's* [1982] flow law, probably because of the greater proportion of stronger pyroxene in *Shelton's* samples. In general, the range in allowable H is 5-10 km greater at fixed dT/dz than shown here.

Initially Compensated Craters

We have repeated these calculations under different assumptions concerning the initial state of isostatic compensation of crater topography. Initial compensation will lessen the relaxation rate, principally because of lesser stress differences to drive flow. Partial to complete initial compensation of relief, therefore, is permissive of a broader range of acceptable combinations of H and dT/dz . Curves showing 95% confidence limits for rejecting combinations of values for dT/dz and H for initially compensated craters are shown in Figure 3.13. If the characteristic stress difference σ is taken to be equal to that for the initially uncompensated crater of the same diameter (Table 3.2), then the solutions at $dT/dz < 20$ K/km are similar for compensated and uncompensated cases because relaxation is limited by the large viscosity of the upper mantle. At $dT/dz > 20$ K/km, H is still restricted to be less than about 10 km.

Calculation of the characteristic stress difference $\bar{\sigma}$ is much more sensitive to variation of dT/dz and H for initially compensated relief ($c = 1$) than for the situation with $c = 0$. For an initially uncompensated crater 140 km in diameter, $\bar{\sigma}$ varies over the narrow interval 2.5 - 5 MPa for the ranges of dT/dz and H shown in Figure 3.13, whereas for $c = 1$, $\bar{\sigma}$ varies over the interval 0.1 - 3.5 MPa. For a reference model given by $dT/dz = 13$ K/km and $H = 13$ km, $\bar{\sigma}$ is 4 MPa and 0.5 MPa for $c = 0$ and $c = 1$, respectively. The latter value for the characteristic stress difference is probably artificially low, because of the large averaging volume, yielding a high effective viscosity and conservative upper limits to H and dT/dz for initially compensated large craters. For this situation, thermal gradients in excess of 20 K/km and a thick crust ($H > 30$ km) are permissible parameters if the crater is young (50 m.y.). For an older crater H must be less than about 20 km at $dT/dz = 25$ K/km. The difference in $\bar{\sigma}$ between initially compensated and uncompensated cases is minor at 32 km diameter, because the surface and crust-mantle boundary are effectively decoupled at the relevant wavenumbers for $H > 10$ km.

Finite Lithospheric Strength

We have also considered the support of crater relief by an elastic-plastic lithosphere; see Appendix 3.B. Because the strength in the lower portion of the lithosphere is limited by temperature-dependent ductile flow, a lower bound on the extent of flexural support of relief may be converted to an upper bound on mean lithospheric thermal gradient. For craters 140 km in diameter the limits on dT/dz if relief is supported flexurally (Table 3.B1) are similar to those from viscous relaxation models with no initial isostatic compensation and with comparatively young crater ages (of order 50 m.y.) for the cases of both thick and thin crust. The topography of smaller craters, however, can be supported elastically in a

lithosphere having a crust of arbitrary thickness for dT/dz up to 30 K/km at $D = 32$ km and dT/dz up to 18 K/km at $D = 50$ km (Table 3.B1). If an elastic-plastic model is appropriate to the lithosphere of Venus, the depths of smaller craters do not provide useful information on crustal thickness or thermal gradient.

DISCUSSION

The results of the viscous relaxation models presented in the previous section, and summarized in Figure 3.13, provide limiting values for crustal thickness and lithospheric thermal gradient consistent with the preservation of topographic relief in large impact craters on Venus. In this section we compare these limiting values to estimates derived independently by others, and we explore the implications of these results for the evolution of Venus.

As noted above any finite strength of the Venus lithosphere can contribute significantly to the support of topographic relief for craters with $D \leq 50$ km. The largest ($D > 100$ km) craters, therefore, provide the most stringent and robust constraints on crustal thickness and lithospheric thermal gradient. The small number of such craters with measured relief makes uncertain any extrapolation to regional or global conditions. It should be recognized, however, that the limits on the extent of relaxation are derived from the entire data set depicted in Figure 3.2; i.e., the variance in the mean depth at large diameter is a function of the variance in the data at all diameters. Because of the possibility of partial elastic support for even the largest craters, and to maintain a conservative approach, we shall use the limiting values obtained under the assumption of a young mean surface age (Figure 3.13a) in the following discussion.

According to Figure 3.13a, the crustal thickness beneath the largest ($D > 100$ km) craters with measured depths on Venus and, by inference, beneath geologically similar plains units at comparable elevations, is less than about 10 km for

a mean lithospheric thermal gradient of 20 K/km and less than about 20 km for a mean lithospheric thermal gradient of 10 K/km. These values may be compared with other estimates of lithospheric thermal gradient and crustal thickness on Venus. Assuming that Venus loses heat at the same rate per unit mass as the Earth, the global rate of heat loss is 3.4×10^{13} W and the average heat flux is 74 mW/m² [Solomon and Head, 1982]. Alternatively, if radioactive heat sources are present in Venus at chondritic abundances, then the average heat flux may be as low as 50 mW/m² [Phillips and Malin, 1984]. If all of this heat flow is transported through the lithosphere by conduction and if the thermal conductivity of the lithosphere is similar to that on Earth (3.1 W/m-K, [Parsons and Sclater, 1977]), then the mean lithospheric thermal gradient is 16-24 K/km. Locally the thermal gradient may be as low as that in terrestrial continental shields and old ocean basins, about 10 K/km [Sclater et al., 1980]; in areas of active rifting and volcanism, of course, the local gradient may be considerably greater than 25 K/km.

Upper bounds to the crustal thickness on Venus of one hundred to several hundred kilometers have been suggested on the basis of the projected depth of the basalt-eclogite stability field [Anderson, 1980] or the apparent depth of isostatic compensation of long-wavelength topography [Phillips et al., 1981; Phillips and Malin, 1984]. These bounds may greatly exceed the actual crustal thickness if the crust does not fill the volume of the interior lying within the basalt stability field or if mantle dynamical effects contribute significantly to the support of long-wavelength topography. Much lower values of maximum crustal thickness were derived by Zuber [1987] and by Banerdt and Golombek [1988] from the observation that there are often two characteristic wavelengths of tectonic features in extensional and compressive terrains on Venus. These workers interpret this observation as evidence for a layered lithosphere: strong upper crustal and mantle layers

separated by a weak lower crust. These layers arise from the different temperatures at which ductile flow limits strength in crustal and mantle material (see Appendix 3.B for a related discussion); the observed scales of deformation can be quantitatively related to crustal thickness and lithospheric thermal gradient. *Zuber* [1987] found that the crustal thickness is less than about 15 km if $dT/dz = 25$ K/km and less than about 30 km if $dT/dz = 10$ K/km. These values are quite similar to those obtained in this study (Figure 3.13a).

There are two scenarios that would invalidate the constraints on crustal thickness and thermal gradient implied by Figure 3.13, but both of these possibilities are unlikely. First, the largest craters on Venus with measured relief could be very young, i.e., considerably younger than 50 m.y., so that viscous relaxation would be minimal for any plausible model. The ages of 40-2000 m.y. for the largest ($D = 100$ to 140 km) terrestrial craters [*Grieve and Robertson*, 1979] do not support this view, however. Further, the distribution of crater morphological types, or states of preservation, appears to be independent of crater diameter [*Basilevsky et al.*, 1987]. In particular, the largest craters with measured relief have intermediate states of preservation (Table 3.1) and therefore are inferred not to be substantially younger than the overall crater population. In a second scenario, the topographic relief of large impact craters could be completely compensated by variations in crustal thickness; as noted above, a crustal thickness of 30 km or more would then be compatible with the observed relief and inferred surface age even in the presence of a lithospheric gradient in excess of 20 K/km. Variations in the Bouguer gravity anomaly across large ($D \sim 100$ km) terrestrial impact structures in continental crust, however, are modest (~ 10 mgal) and do not indicate significant Moho relief [*Masaitas et al.*, 1976; *Sweeney*, 1978]. It is doubtful that in crust of comparable thickness on Venus the craters in this size range should be completely

compensated.

We conclude that the thickness of the crust beneath the largest ($D > 100$ km) craters, and possibly beneath plains units over at least the northern quarter of the Venus surface, is no more than 10-20 km thick. If this result holds for plains units at similar elevations elsewhere on the planet, we may obtain a simple estimate of the total crustal volume from the hypsometry of the Venus surface by assuming that long-wavelength topographic variations are locally compensated by crustal thickness variations. Measured gravity anomalies indicate that other compensation mechanisms also operate [Phillips *et al.*, 1979; Phillips and Malin, 1984], so that the crustal volume estimated under this assumption is an upper bound. If H_0 is the crustal thickness beneath plains units of elevation z_0 , then the crustal volume is given by

$$V = \int_{z_{\min}}^{z_{\max}} [H_0 + (z - z_0) (1 + \rho_c/\Delta\rho)] dA(z) \quad (3.8)$$

where $dA(z)$ is the area with elevation between z and $z + dz$, and where z_{\min} and z_{\max} are the minimum and maximum elevation. If the Pioneer Venus hypsometry curve [Masursky *et al.*, 1980; Ford, 1986] is representative of the planet, and taking $\rho_c = 2.9$ Mg/m³, $\Delta\rho = 0.5$ Mg/m³, and $z_0 = 6051.5$ km (the elevation of the crater Cochran), we calculate $V = 0.5 - 1.2 \times 10^{10}$ km³ for H_0 equal to 10-20 km. Such a volume is equivalent to a global mean crustal thickness of 10-25 km, and is comparable to the Earth's present crustal volume.

Whether this volume of crust represents the total volume of crustal material produced on Venus is uncertain. Assuming that the present terrestrial rate of plate creation [Parsons, 1982] is approximately representative of the past 4 b.y., the total

volume of crust generated on Earth has been $\sim 10^{11}$ km³. If Venus has produced a comparable crustal volume, then recycling of older crust, by subduction, foundering or remelting, must have occurred. If 10^{10} km³ is the full time-integrated volume of crustal material on Venus, then the average rate of crustal generation over the last 4 b.y would be 2 km³/yr. This value coincides with the upper bound on the global rate of volcanic resurfacing obtained from the density of preserved impact craters [*Grimm and Solomon, 1987*]. It should be noted that the latter figure is insensitive to the contribution to crustal generation by igneous intrusions. Since the rate of intrusion of new crustal volume may be several times the rate of extrusion of new material, a value of 10^{10} km³ would for the crustal volume would suggest that the average volcanic flux on Venus in the absence of crustal recycling could be considerably less than 2 km³/y.

CONCLUSION

The depths of large ($D > 100$ km) impact craters on Venus limit the extent of viscous relaxation of topographic relief that has occurred since crater formation. Under the assumption that the crust-mantle boundary is the principal mechanical discontinuity of compositional origin within the lithosphere, we have developed a new solution to the viscous relaxation problem that incorporates a density contrast at that boundary and an arbitrary vertical variation in viscosity. By means of a statistical formalism for testing relaxation models against observed crater depths, we have derived trade-off curves for acceptable combinations of crustal thickness and lithospheric thermal gradient beneath such craters. The preservation of significant crater topographic relief may be achieved by a low thermal gradient or a thin crust. Because average thermal gradients are not likely to be less than 10 K/km on a regional basis, a thin (10-20 km) crust is the most plausible explanation

for the degree of preservation of relief of large impact craters on Venus. This is a conservative estimate, as we have consistently assigned limits to mean crater age, apparent crater depth, amount of viscous relaxation, effective stress, and finite lithospheric strength in such a manner as to yield upper bounds on local crustal thickness and lithospheric thermal gradient.

The large craters on Venus with measured depths, although few in number, are representative of a larger number of imaged craters in terms of regional elevation, geological unit, and state of preservation of morphological detail. It is therefore not unreasonable to infer that the crust does not exceed 10-20 km beneath much of the lowlands and rolling plains throughout the northern quarter of the Venus surface. Global extrapolation of this result yields a total volume of crust on Venus of about 10^{10} km³, comparable to the present crustal volume on Earth. This similarity, despite the role of plate tectonics in recycling terrestrial crust, suggests either that the rate of crustal generation on Venus over the past 4 b.y. has been an order of magnitude less than on Earth or that some form of crustal recycling has occurred on Venus.

The conclusions reached in this work are sensitive principally to the accuracy of experimentally derived flow laws and their applicability to crustal and mantle material on Venus and to the small number of measurements to date of the topography of Venus impact craters. With further measurements of rock deformation and the improved coverage and resolution of altimetry and imaging of the surface of Venus to be obtained by the Magellan mission, the approach followed in this paper should lead to better constraints on the structure of the crust and upper mantle of Venus.

**APPENDIX 3.A:
Numerical Treatment of the Viscous Relaxation of Topography**

In this appendix we derive a numerical formulation for the gravity-driven relaxation of a topographic load at the surface of a density-stratified fluid having an arbitrary vertical variation of viscosity. In principle a fluid having any number of constant-density layers can be treated by this method; the present analysis is confined to a two-layer model with distinct crust and mantle.

The model is illustrated in Figure 3.A1. The vertical coordinate z is positive downward. The crustal thickness is H , the crustal density is ρ_c , the mantle density is $\rho_c + \Delta\rho$, and the viscosity is $\eta(z)$.

Let the surface topography h_s be azimuthally symmetric, that is, a function of horizontal distance r and time t only. In the wavenumber domain the topography can be represented by the zero-order Hankel transform

$$h_s^{(0)}(k,t) = \int_0^{\infty} h_s(r,t) J_0(kr) r dr \quad (3.A1)$$

where J_0 is the zero-order Bessel function and k is the wavenumber. The corresponding inverse transform is

$$h_s(r,t) = \int_0^{\infty} h_s^{(0)}(k,t) J_0(kr) k dk \quad (3.A2)$$

A similar relation exists for relief $h_m(r,t)$ on the crust-mantle interface. The initial relief at $z = H$ can be obtained from the initial surface relief by an assumption

regarding the initial state of local isostatic compensation

$$h_m^{(0)}(k,0) = -\frac{c \rho_c}{\Delta \rho} h_s^{(0)}(k, 0)$$

where c is the initial degree of isostatic compensation ($c = 0$ corresponds to uncompensated topography; $c = 1$ corresponds to complete Airy isostasy).

The rest of this discussion treats the relaxation of a single harmonic component of relief h_s at the surface and h_m on the crust-mantle boundary, and the wave-number dependence is implicit. The complete solution for the decay of arbitrary surface topography is obtained by integrating over all wavenumbers via (3.A2).

Consider the interior of an incompressible fluid away from any density discontinuities, and assume that inertial stresses are much smaller than viscous stresses. Then the equation of static equilibrium

$$\nabla \cdot \boldsymbol{\sigma} + \mathbf{f} = 0 \tag{3.A3}$$

applies, where $\boldsymbol{\sigma}$ is the stress tensor and \mathbf{f} is the body force per unit volume. Normal stress is taken to be positive in extension. The continuity condition is

$$\nabla \cdot \mathbf{v} = 0 \tag{3.A4}$$

where \mathbf{v} is the fluid velocity. With the assumption of circular symmetry, expressions (3.A3) and (3.A4) in cylindrical polar coordinates are [Fung, 1977]

$$\partial_r \sigma_{rr} + \frac{1}{r} (\sigma_{rr} - \sigma_{\theta\theta}) + \partial_z \sigma_{rz} = 0 \quad (3.A5)$$

$$\partial_z \sigma_{zz} + \partial_r \sigma_{rz} + \frac{1}{r} \sigma_{rz} + \rho g = 0 \quad (3.A6)$$

$$\partial_r v_r + \frac{1}{r} v_r + \partial_z v_z = 0 \quad (3.A7)$$

where we have assumed that $f(r, \theta, z) = (0, 0, \rho g)$ and where ∂_r and ∂_z denote the operators $\partial/\partial r$ and $\partial/\partial z$, respectively. The constitutive relation for an incompressible viscous fluid is

$$\boldsymbol{\sigma} = -p \mathbf{I} + 2\eta \mathbf{D} \quad (3.A8)$$

where \mathbf{I} is the identity matrix, p is the total pressure, and \mathbf{D} is the strain-rate tensor.

Under azimuthal symmetry (3.A8) becomes

$$\sigma_{rr} = -p + 2\eta \partial_r v_r \quad (3.A9)$$

$$\sigma_{\theta\theta} = -p + 2\eta \frac{v_r}{r} \quad (3.A10)$$

$$\sigma_{zz} = -p + 2\eta \partial_z v_z \quad (3.A11)$$

$$\sigma_{rz} = \eta (\partial_r v_z + \partial_z v_r) \quad (3.A12)$$

$$\sigma_{r\theta} = \sigma_{z\theta} = 0 \quad (3.A13)$$

Boundary conditions require that σ_{rz} and σ_{zz} vanish at the free surface; that v_r , v_z , σ_{rz} , and σ_{zz} are all continuous across the crust-mantle boundary; and that v_r and v_z vanish at large depth. Since the radial variation of these quantities will be given by a superposition of Bessel functions, we seek a system of equations which describes their vertical variation. We therefore must transform the equilibrium equations and constitutive relation so that the only derivatives appearing are with respect to z . We make use of the following properties of Hankel transforms (denoting zero- and first-order transforms by the superscripts (0) and (1) , respectively):

$$[\partial_r f(k)]^{(0)} = k f^{(1)} - \left(\frac{f}{r}\right)^{(0)} \quad (3.A14)$$

$$[\partial_r f(k)]^{(1)} = -k f^{(0)} \quad (3.A15)$$

$$\int_0^{\infty} \left(\partial_{rr} f + \frac{1}{r} \partial_r f - \frac{1}{r^2} f \right) J_1(kr) r dr = -k^2 f^{(1)} \quad (3.A16)$$

where J_1 is the Bessel function of order one. Transformed versions of equations (3.A12) and (3.A7) can be written, respectively, as

$$\partial_z v_r^{(1)} = \sigma_{rz}^{(1)}/\eta + k v_z^{(0)} \quad (3.A17)$$

$$\partial_z v_z^{(0)} = -k v_r^{(1)} \quad (3.A18)$$

Using (3.A7) to solve (3.A11) for p , and substituting into (3.A9) and (3.A10), we can express the remaining nonzero stress components in terms of v_r and σ_{zz} :

$$\sigma_{rr} = \sigma_{zz} + 4\eta \partial_r v_r + 2\eta \frac{v_r}{r} \quad (3.A19)$$

$$\sigma_{\theta\theta} = \sigma_{zz} + 2\eta \partial_r v_r + 4\eta \frac{v_r}{r} \quad (3.A20)$$

Substituting (3.A19) and (3.A20) into (3.A5) gives

$$\partial_r \sigma_{zz} + 4\eta \left(\partial_{rr} v_r + \frac{1}{r} \partial_r v_r - \frac{v_r}{r^2} \right) + \partial_z \sigma_{rz} = 0 \quad (3.A21)$$

which, from (3.A15-3.A16), becomes

$$\partial_z \sigma_{rz}^{(1)} = k \sigma_{zz}^{(0)} + 4\eta k^2 v_r^{(1)} \quad (3.A22)$$

in the wavenumber domain.

The incorporation of an equation for $\partial_z \sigma_{zz}$ requires a modification of the definition of stress. Since the hydrostatic component of pressure makes no contribution to the flow, we can express the viscous stresses relative to this state.

Write the total pressure as

$$p = p_0 + p_1 \quad (3.A23)$$

where $p_0 = \rho g z$ and p_1 is the perturbation due to flow. Then (3.A11) becomes

$$\sigma_{zz} = \sigma'_{zz} - \rho g z \quad (3.A24)$$

where $\sigma'_{zz} = -p_1 + 2\eta \partial_z v_z$ is the vertical normal stress relative to the hydrostatic pressure. The shear stress is unaffected, so $\sigma'_{rz} = \sigma_{rz}$, and (3.A6) becomes

$$\partial_z \sigma'_{zz} + \partial_r \sigma'_{rz} + \frac{1}{r} \sigma'_{rz} = 0 \quad (3.A25)$$

For convenience, we drop the primes, and measure all stresses relative to the hydrostatic state unless otherwise noted. In the wavenumber domain, (3.A25) is

$$\partial_z \sigma_{zz}^{(0)} = -k \sigma_{rz}^{(1)} \quad (3.A26)$$

We may combine (3.A17), (3.A18), (3.A22), and (3.A26) into the system of equations

$$\partial_z \begin{bmatrix} v_r^{(1)} \\ v_z^{(0)} \\ \sigma_{rz}^{(1)} \\ \sigma_{zz}^{(0)} \end{bmatrix} = \begin{bmatrix} 0 & k & 1/\eta & 0 \\ -k & 0 & 0 & 0 \\ 4\eta k^2 & 0 & 0 & k \\ 0 & 0 & -k & 0 \end{bmatrix} \begin{bmatrix} v_r^{(1)} \\ v_z^{(0)} \\ \sigma_{rz}^{(1)} \\ \sigma_{zz}^{(0)} \end{bmatrix} \quad (3.A27)$$

We will call $\omega = [v_r^{(1)}, v_z^{(0)}, \sigma_{rz}^{(1)}, \sigma_{zz}^{(0)}]^T$ the velocity-stress vector, and we drop the Hankel transform superscripts for convenience. An analog to equation (3.A27) holds in two-dimensional cartesian coordinates with $\omega = [iv_x, v_z, i\sigma_{xz}, \sigma_{zz}]^T$, where

all quantities are Fourier transformed [*Cathles, 1975*].

Equation (3.A27) satisfies continuity of velocity and stress everywhere in the fluid away from density discontinuities. At such boundaries, continuity of velocity and stress must be ensured on the deformed interface. However, if the boundary relief h is small compared with the wavelength and the layer thickness, then to first order the boundary conditions may be applied on the undeformed interface, requiring only a correction $\Delta\rho g h$ to σ_{zz} [*Solomon et al., 1982a; Richards and Hager, 1984*].

The boundary conditions at the surface are

$$\sigma_{rz}(0) = 0 \quad (3.A28)$$

$$\sigma_{zz}(0) = \rho_c g h_s \quad (3.A29)$$

The boundary conditions at the crust-mantle interface are implicitly satisfied by (3.A27), with the exception of the correction to normal stress

$$\Delta\sigma_{zz}(H) = -\Delta\rho g h_m \quad (3.A30)$$

The final two boundary conditions, that the velocity components vanish at large depth, are also implicitly satisfied by (3.A27).

Evaluation of (3.A27-30) is more convenient if these equations are expressed in nondimensional form, which is achieved by dividing each dimensional quantity by an appropriate reference value. We choose H as the reference length, ρ_c as the reference density, and $\eta_0 = \eta(0)$ as the reference viscosity. It follows that the reference values for time, velocity, and stress are $t_0 = \eta_0 / (\rho_c g H)$, $v_0 = \rho_c g H^2 / \eta_0$,

and $\sigma_o = \rho_c g H$, respectively. Equations (3.A27) and (3.A28) are unchanged with nondimensional quantities, whereas (3.A29) and 3.A30) become $\sigma_{zz}(0) = h_s$ and $\Delta\sigma_{zz}(H) = -\Delta\rho h_m$, respectively.

A linear combination of three independent solutions to (3.A27) is required to satisfy the three conditions (3.A28-A30). Let these three solutions, in nondimensional form, be $\omega^{(i)}$, $i = 1, 2, 3$. Two of these solutions, $\omega^{(1)}$ and $\omega^{(2)}$, are specified at depth $d_0 \gg H$, and (3.A27) is numerically integrated to $z = 0$ using a fourth-order Runge-Kutta method [*Shampine et al.*, 1976]. Although any two independent vectors are sufficient, the most accurate results ensue when the specified values of these vectors have the form $[A, B, A, B]^T$, where A and B are constants [*Cathles*, 1975]. Accordingly, we set $\omega^{(1)}(d_0) = [1, 0, 1, 0]^T$ and $\omega^{(2)}(d_0) = [0, 1, 0, 1]^T$. The effect of the crust-mantle discontinuity is ignored in the integration of (3.A27) with these vectors, so the third solution must represent the apparent normal stress discontinuity at $z = H$. This requires that $\omega^{(3)}(H) = [0, 0, 0, 1]^T$. Again, the upper limit of integration is $z = 0$.

We now form linear combinations of these solutions to match the boundary conditions. Denoting ω_{ij} as the j^{th} component of the nondimensional velocity-stress vector $\omega^{(i)}$, the boundary conditions (3.A28)-(3.A30) become

$$\sigma_{rz}(0) = \sum_{i=1}^3 \alpha_i \omega_{i3}(0) = 0 \quad (3.A31)$$

$$\sigma_{zz}(0) = \sum_{i=1}^3 \alpha_i \omega_{i4}(0) = h_s \quad (3.A32)$$

$$\Delta\sigma_{zz}(H) = \alpha_3 \omega_{34}(H) = -\Delta\rho h_m \quad (3.A33)$$

Equation (3.A33) allows immediate solution for $\alpha_3 = -\Delta\rho h_m$, since $\omega_{34}(H) = 1$.

We are left with a 2 x 2 system for α_1 and α_2 :

$$\begin{bmatrix} \omega_{13}(0) & \omega_{23}(0) \\ \omega_{14}(0) & \omega_{24}(0) \end{bmatrix} \begin{bmatrix} \alpha_1 \\ \alpha_2 \end{bmatrix} = \begin{bmatrix} \Delta\rho h_m \omega_{33}(0) \\ h_s + \Delta\rho h_s \omega_{34}(0) \end{bmatrix} \quad (3.A34)$$

The solution is

$$\begin{bmatrix} \alpha_1 \\ \alpha_2 \end{bmatrix} = \begin{bmatrix} a & b \\ c & d \end{bmatrix} \begin{bmatrix} h_s \\ h_m \end{bmatrix} \quad (3.A35)$$

where

$$\begin{aligned} a &= -\omega_{23}/\det \Omega \\ b &= \Delta\rho [\omega_{33} \omega_{24} - \omega_{34} \omega_{23}]/\det \Omega \\ c &= \omega_{13}/\det \Omega \\ d &= \Delta\rho [-\omega_{33} \omega_{14} + \omega_{34} \omega_{13}]/\det \Omega \\ \det \Omega &= \omega_{13} \omega_{24} - \omega_{14} \omega_{23} \end{aligned}$$

and all ω_{ij} are evaluated at $z = 0$.

We can now calculate the time-dependent motion of relief on the surface and crust-mantle boundary by using the kinematic constraints

$$\begin{aligned} \frac{d h_s}{dt} &= v_z(0) = \sum_{i=1}^3 \alpha_i \omega_{i2}(0) \\ \frac{d h_m}{dt} &= v_z(H) = \sum_{i=1}^3 \alpha_i \omega_{i2}(H) \end{aligned} \quad (A36)$$

Using (3.A35), we write (3.A36) as a system of first-order differential equations

$$\frac{d}{dt} \begin{bmatrix} h_s \\ h_m \end{bmatrix} = \begin{bmatrix} s_1 & m_1 \\ s_2 & m_2 \end{bmatrix} \begin{bmatrix} h_s \\ h_m \end{bmatrix} \quad (3.A37)$$

where

$$s_1 = a \omega_{12}(0) + c \omega_{22}(0)$$

$$m_1 = b \omega_{12}(0) + d \omega_{22}(0) - \Delta \rho \omega_{32}(0)$$

$$s_2 = a \omega_{12}(H) + c \omega_{22}(H)$$

$$m_2 = b \omega_{12}(H) + d \omega_{22}(H).$$

The eigenvalues of the 2 x 2 matrix in (3.A37) are

$$\lambda_{1,2} = \frac{1}{2} [s_1 + m_2 \pm (s_1^2 + m_2^2 - 2s_1 m_2 + 4s_2 m_1)^{1/2}] \quad (3.A38)$$

Corresponding eigenvectors are

$$\mathbf{x}_i = (\zeta_i, 1)^T \quad i = 1, 2$$

where

$$\zeta_i = \frac{\lambda_i - m_2}{s_2} \quad (3.A39)$$

The time-dependent solution to coupled topographic decay on the surface and crust-mantle boundary may be written

$$\begin{bmatrix} h_s \\ h_m \end{bmatrix} = a_1 \mathbf{x}_1 e^{-t\tau_1} + a_2 \mathbf{x}_2 e^{-t\tau_2} \quad (3.A40)$$

where $\tau_i = -1/\lambda_i$. From the initial conditions, the coefficients a_1 and a_2 in (3.A40) are given by

$$a_1 = h_{m0} - a_2 \tag{3.A41}$$

$$a_2 = (h_{s0} - \zeta_1 h_{m0}) / (\zeta_2 - \zeta_1)$$

where h_{s0} and h_{m0} are the initial relief at the surface and crust-mantle boundary, respectively. The time constants τ_i may be expressed in dimensional form by multiplying by $\eta_0/(\rho_c g H)$, and the amplitude coefficients a_i may be redimensionalized by multiplying by H .

APPENDIX 3.B:

Support of Crater Relief by Lithospheric Strength

In Appendix 3.A, the interior of Venus is taken to be a layered viscous fluid without finite elastic strength. A simple and commonly adopted alternative representation for the mechanical properties of a planetary interior is a uniform thin elastic plate overlying an inviscid fluid. With this representation a portion of the topographic relief of an impact crater can be supported by bending moments and shear stresses within the plate and by buoyancy forces due to displacement of the fluid substrate. A lower bound on flexural rigidity or, equivalently, elastic plate thickness may be obtained by requiring the flexurally supported relief to be consistent with the observed crater depths. The bending stress predicted by this elastic plate model, however, exceeds the probable strength in the upper and lower portions of the lithosphere. Taking this strength into account, we employ an elastic-plastic plate with the same bending moment as the elastic plate to convert the lower bound on plate thickness to an upper bound on lithospheric thermal gradient. This bound on thermal gradient may then be compared with those derived from viscous relaxation models.

Elastic plate model

If the topographic relief is small compared with the dominant horizontal wavelengths and with the thickness L of the elastic plate, then a crater topographic profile $h(r)$ can be considered as a surface load on the plate and the resulting vertical deflection $w(r)$ satisfies

$$D \nabla^4 w(r) + \rho_m g w(r) = \rho g h(r) \quad (3.B1)$$

where D is the flexural rigidity, ρ_m is the density of the fluid substrate (taken equal to the density of the mantle), ρ is the density at the surface, g is the gravitational acceleration, and w is positive downward. The flexural rigidity is related to the plate thickness L by $D = E L^3/[12(1 - \nu^2)]$, where E and ν are Young's modulus and Poisson's ratio in the plate, respectively. The final surface topography is given by $h - w$.

For a given initial crater profile, we seek a minimum flexural rigidity such that the crater relief after lithospheric flexure remains consistent with observed crater depths. We utilize the same statistical approach to testing the plausibility of elastic plate models as for viscous models. Specifically we reject any model that predicts a crater depth shallower than the 95% confidence lower bound on mean observed crater depth. This criterion is equivalent to a change in relief of no more than 30-35% for craters with diameters between 30 and 140 km.

We solve (3.B1), following *Solomon and Head* [1979], by representing the topography as a set of concentric cylinders and utilizing the analytical solution for w for a uniform cylindrical load. Because the resulting solution is for the flexure of a uniform elastic plate, we must take crustal thickness H to be effectively zero ($H \ll L$) or infinite ($H \gg L$); the corresponding values for ρ are 3.4 and 2.9 Mg/m³, respectively. We solve (3.B1) with both $E = 10^{10}$ and 10^{11} Pa; this range for Young's modulus probably spans that of the mean value for the Venus lithosphere, with the lower value more likely [*Solomon and Head*, 1984]. Poisson's ratio for the elastic plate is taken to be 0.25.

Minimum values for elastic plate thickness L for different combinations of crater size, lithospheric elastic modulus, and crustal thickness are given in Table 3.B1. The areal mean M of the bending moment beneath the crater is also given. An

example of the effect of the maximum permitted flexural deformation at 95% confidence on a crater topographic profile is shown in Figure 3.B1.

Elastic-plastic plate model

Laboratory measurements of the strength of rock suggest that a uniform elastic plate is generally a poor model for the mechanical lithosphere. Crustal and mantle materials display a finite strength that varies with depth; this strength is controlled by frictional sliding on faults at shallow depths and by ductile flow at greater depths [Goetze and Evans, 1979; Brace and Kohlstedt, 1980]. In the ductile regime, an approximate strength may be estimated by solving equation (3.6) at a specified strain rate. The strength depends strongly on temperature (and hence on thermal gradient) but only weakly on strain rate. We adopt $\dot{\epsilon} = 3 \times 10^{-17} \text{ s}^{-1}$ (corresponding to unit strain in 10^9 yr); a tenfold increase in $\dot{\epsilon}$ results in a change of only a few K/km for dT/dz less than 40 K/km. The flow laws for diabase and olivine cited in the text are assumed to govern ductile flow in the Venus crust and mantle, respectively.

In a purely elastic plate, the bending stress varies linearly with depth and is antisymmetric about the neutral surface at a depth $L/2$. For the elastic-plastic plate the stress distribution will be modified where the predicted elastic stress exceeds the local strength. From the lower bound on elastic plate thickness we obtain an upper bound on thermal gradient dT/dz with the elastic-plastic plate model under the assumptions that the bending moment of the elastic-plastic plate equals the moment M for the purely elastic plate and that the vertical integral of bending stress is zero. These conditions lead to two equations that may be solved numerically for dT/dz and for the depth z_n of the neutral surface:

$$M - \int_0^{\infty} \sigma (z - z_n) dz = 0 \quad (3.B2)$$

$$\int_0^{\infty} \sigma dz = 0 \quad (3.B3)$$

where σ is the lesser of the strength and the radial horizontal bending stress given by the elastic plate model.

An example of the flexural stress distribution for the elastic-plastic plate corresponding to the model in Figure 3.B1 is shown in Figure 3.B2. The upper bounds on thermal gradient are given in Table 3.B1.

REFERENCES

- Anderson, D. L., Tectonics and composition of Venus, *Geophys. Res. Lett.*, 7, 101-102, 1980.
- Ashby, M. F., and R. A. Verrall, Micromechanisms of flow and fracture, and their relevance to the rheology of the upper mantle, *Phil. Trans. R. Soc. Lond.*, A288, 59-95, 1977.
- Baldwin, R. B., On the relative and absolute ages of seven lunar front face basins, I. From viscosity arguments, *Icarus*, 71, 1-18, 1987.
- Banerdt, W. B., and M. P. Golombek, Deformational models of rifting and folding on Venus, *J. Geophys. Res.*, 93, 4759-4772, 1988.
- Barsukov, V. L., and 29 others, The geology and geomorphology of the Venus surface as revealed by the radar images obtained by Veneras 15 and 16, *Proc. Lunar Planet. Sci. Conf. 16th*, *J. Geophys. Res.*, 91, D378-D398, 1986.
- Basilevsky, A. T., and B. A. Ivanov, Impact cratering on stony and icy bodies: Different mechanisms of central peak formation (abstract), *Lunar Planet. Sci.*, 13, 27-28, 1982.
- Basilevsky, A. T., B. A. Ivanov, G. A. Burba, I. M. Chernaya, V. P. Kryuchkov, O. V. Nikolaeva, D. B. Campbell, and L. B. Ronca, Impact craters of Venus: A continuation of the analysis of data from the Venera 15 and 16 spacecraft, *J. Geophys. Res.*, 92, 12869-12901, 1987.
- Brace, W. F., and D. H. Kohlstedt, Limits on lithospheric stress imposed by laboratory experiments, *J. Geophys. Res.*, 85, 6248-6252, 1980.
- Campbell, D. B., and B. A. Burns, Earth-based radar imagery of Venus, *J. Geophys. Res.*, 85, 8271-8281, 1980.
- Campbell, D. B., J. W. Head, J. K. Harmon, and A. A. Hine, Venus: Identification of banded terrain in the mountains of Ishtar Terra, *Science*, 221, 644-647, 1983.
- Campbell, D. B., J. W. Head, J. K. Harmon, and A. A. Hine, Venus: Volcanism and

- rift formation in Beta Regio, *Science*, 226, 167-170, 1984.
- Caristan, Y., The transition from high temperature creep to fracture in Maryland diabase, *J. Geophys. Res.*, 87, 6781-6790, 1982.
- Cathles, L. M., *The Viscosity of the Earth's Mantle*, 386 pp., Princeton Univ. Press, 1975.
- Chen, W.-P., and P. Molnar, Focal depths of intracontinental and intraplate earthquakes and their implications for the thermal and mechanical properties of the lithosphere, *J. Geophys. Res.*, 88, 4183-4214, 1983.
- Danes, Z. F., Rebound processes in large craters, in *Astrogeologic Studies*, Ann. Prog. Rep., part A, U.S. Geological Survey, Washington, D.C., 81-100, 1965.
- Davis, J. C., *Statistics and Data Analysis in Geology*, 550 pp., J. Wiley, New York, 1973.
- Devore, J. L., *Probability and Statistics for Engineering and the Sciences*, 640 pp., Brooks/Cole, Monterey, Calif., 1982.
- Ford, P. G., Pioneer Venus hypsometry, Center for Space Research, M.I.T., Cambridge, Mass., 12 pp., 1986.
- Fung, Y. C., *A First Course in Continuum Mechanics*, 340 pp., Prentice-Hall, Englewood Cliffs, N.J., 1977.
- Goetze, C., The mechanisms of creep in olivine, *Phil Trans. R. Soc. Lond. A288*, 99-119, 1978.
- Goetze, C., and B. Evans, Stress and temperature in the bending lithosphere as constrained by experimental rock mechanics, *Geophys. J. R. Astr. Soc.*, 59, 463-478, 1979.
- Grieve, R. A. F., The impact of cratering rate in recent time, *Proc. Lunar Planet. Sci. Conf. 14th*, *J. Geophys. Res.*, 89, B403-B408, 1984.
- Grieve, R. A. F., and J. W. Head, The impact cratering process on Venus (abstract), *Lunar Planet. Sci.*, 13, 285-286, 1982.

- Grieve, R. A. F., and P. B. Robertson, The terrestrial cratering record, 1, Current status of observations, *Icarus*, 38, 212-229, 1979.
- Grimm, R. E., and S. C. Solomon, Limits on modes of lithospheric heat transport on Venus from impact crater density, *Geophys. Res. Lett.*, 14, 538-541, 1987.
- Hall, J. L., S. C. Solomon, and J. W. Head, Lunar floor-fractured craters: Evidence for viscous relaxation of topography, *J. Geophys. Res.*, 86, 9537-9552, 1981.
- Hartmann, W. K., Relative crater production rates on planets, *Icarus*, 31, 260-276, 1977.
- Ivanov, B. A., A. T. Basilevsky, V. P. Kryuchkov, and I. M. Chernaya, Impact craters of Venus: Analysis of Venera 15 and 16 data, *Proc. Lunar Planet Sci. Conf. 16th*, *J. Geophys. Res.*, 91, D413-D430, 1986.
- Masaitas, V. L., M. V. Mikhailov, and T. V. Selivanovskaya, The Popigai meteorite crater, *NASA Technical Translation, F-1900*, 1976.
- Masursky, H., E. Eliason, P. G. Ford, G. E. McGill, G. H. Pettengill, G. G. Schaber, and G. Schubert, Pioneer Venus radar results: Geology from images and altimetry, *J. Geophys. Res.*, 85, 8232-8260, 1980.
- Melosh, H. J., Cratering mechanics – observational, experimental, and theoretical, *Ann. Rev. Earth Planet. Sci.*, 8, 65-93, 1980.
- O'Keefe, J. D., and T. J. Ahrens, Impact-induced energy partitioning, melting, and vaporization on terrestrial planets, *Proc. Lunar Sci. Conf. 8th*, 3357-3374, 1977.
- Parmentier, E. M., and J. W. Head, Viscous relaxation of impact craters on icy planetary surfaces: Determination of viscosity variation with depth, *Icarus*, 47, 100-111, 1981.
- Parsons, B., The rates of plate creation and consumption, *Geophys. J. R. Astron. Soc.*, 67, 437-448, 1981.
- Parsons, B., and J. G. Sclater, An analysis of the variation of ocean floor bathymetry and heat flow with age, *J. Geophys. Res.*, 82, 803-827, 1977.

- Passey, Q. R., and E. M. Shoemaker, Craters and basins on Ganymede and Callisto: Morphological indicators of crustal evolution, in *Satellites of Jupiter*, edited by D. Morrison, Univ. Ariz. Press, Tucson, 379-434, 1982.
- Pettengill, G. H., E. Eliason, P. G. Ford, G. B. Loriot, H. Masursky, and G. E. McGill, Pioneer Venus radar results: Altimetry and surface properties, *J. Geophys. Res.*, **85**, 8261-8270, 1980.
- Phillips, R.J., W.M. Kaula, G.E. McGill, and M.C. Malin, Tectonics and evolution of Venus, *Science*, **212**, 879-887, 1981.
- Phillips, R.J., and M.C. Malin, Tectonics of Venus, *Ann. Rev. Earth Planet. Sci.*, **12**, 411-443, 1984.
- Pike, R. J., Size-dependence in the shape of fresh impact craters on the Moon, in *Impact and Explosion Cratering*, edited by D. J. Roddy, R. O. Pepin, and R. B. Merrill, pp. 489-509, Pergamon, New York, 1977.
- Pike, R. J., Geometric interpretation of lunar craters, *Prof. Paper 1046-C*, 77 pp., U. S. Geol. Survey, Reston, Va., 1980a.
- Pike, R. J., Formation of complex impact craters: Evidence from Mars and other planets, *Icarus*, **43**, 1-19, 1980b.
- Richards, M. A., and B. H. Hager, Geoid anomalies in a dynamic Earth, *J. Geophys. Res.*, **89**, 5987-6002, 1984.
- Schaber, G. G., E. M. Shoemaker, and R. C. Kozak, The surface age of Venus: Use of the terrestrial cratering record, *Solar System Res.*, **21**, 89-93, 1987a.
- Schaber, G.G., R.C. Kozak, and H. Masursky, Cleopatra Patera on Venus: Venera 15/16 evidence for a volcanic origin, *Geophys. Res. Lett.*, **14**, 41-44, 1987b.
- Sclater, J. G., C. Jaupart, and D. Galson, The heat flow through oceanic and continental crust and the heat loss of the Earth, *Rev. Geophys. Space Phys.*, **18**, 269-312, 1980.
- Seiff, A., D. B. Kirk, R. E. Young, R. C. Blanchard, J. T. Findlay, G. M. Kelley, and S.

- C. Sommer, Measurements of thermal structure and thermal contrasts in the atmosphere of Venus and related dynamical observations: Results from the four Pioneer Venus probes, *J. Geophys. Res.*, **85**, 7903-7933, 1980.
- Selby, S.M., editor, *Standard Mathematical Tables, 15th ed.*, p. 516, Chemical Rubber Co., Cleveland, Ohio, 1967.
- Settle, M., The role of fallback ejecta in the modification of impact craters, *Icarus*, **42**, 1-19, 1980.
- Shampine, L F., H. A. Watts, and S. M. Davenport, Solving non-stiff ordinary differential equations - the state of the art, *Soc. Indust. Appl. Math. Rev.*, **18**, 376-441, 1976.
- Shelton, G., Experimental deformation of single phase and polyphase crustal rocks at high pressures and temperatures, Ph.D. thesis, 146 pp., Brown University, Providence, R.I., 1981.
- Solomon, S. C., and J. W. Head, Vertical movement in mare basins: Relation to mare emplacement, basin tectonics, and lunar thermal history, *J. Geophys. Res.*, **84**, 1667-1682, 1979.
- Solomon, S. C., and J. W. Head, Mechanisms for lithospheric heat transport on Venus: Implications for tectonic style and volcanism, *J. Geophys. Res.*, **87**, 9236-9246, 1982.
- Solomon, S. C., and J. W. Head, Venus banded terrain: Tectonic models for band formation and their relationship to lithospheric thermal structure, *J. Geophys. Res.*, **89**, 6885-6897, 1984.
- Solomon, S. C., R. P. Comer, and J. W. Head, The evolution of impact basins: Viscous relaxation of topographic relief, *J. Geophys. Res.*, **87**, 3975-3992, 1982a.
- Solomon, S. C., S. K. Stephens, and J. W. Head, On Venus impact basins: Viscous relaxation of topographic relief, *J. Geophys. Res.*, **87**, 7763-7771, 1982b.
- Stephens, S. K., S. C. Solomon, and J. W. Head, On the age of Venus highland

- topography: Constraints from the viscous relaxation of relief (abstract), *Lunar Planet. Sci.*, 14, 747-748, 1983.
- Surkov, Yu. A., L. P. Moskalyeva, O. P. Shcheglov, V. P. Kharyukova, O. S. Manvelyan, V. S. Kirichenko, and A. D. Dudin, Determination of the elemental composition of rocks on Venus by Venera 13 and 14 (preliminary results), *Proc. Lunar Planet. Sci. Conf. 13th, J. Geophys. Res.*, 88, A481-A493, 1983.
- Sweeney, J.F., Gravity study of great impact, *J. Geophys. Res.*, 83, 2809-2815, 1978.
- Thomas, P. J., and G. Schubert, Crater relaxation as a probe of Europa's interior, *Proc. Lunar Planet. Sci. Conf. 16th, J. Geophys. Res.*, 91, D453-D459, 1986.
- Thomas, P. J., and G. Schubert, Finite element models of non-Newtonian crater relaxation, *Proc. Lunar Planet. Sci. Conf. 17th, J. Geophys. Res.*, 92, E749-E758, 1987.
- Turcotte, D. L., J. Y. Liu, and F. H. Kulhawy, The role of an intracrustal asthenosphere on the behavior of major strike-slip faults, *J. Geophys. Res.*, 89, 5801-5816, 1984.
- Weertman, J., Height of mountains on Venus and the creep properties of rock, *Phys. Earth Planet. Inter.*, 19, 197-207, 1979.
- Zuber, M. T., Constraints on the lithospheric structure of Venus from mechanical models and tectonic surface features, *Proc. Lunar Planet. Sci. Conf. 17th, J. Geophys. Res.*, 92, E541-E551, 1987.
- Zuber, M. T., E. M. Parmentier, and R. C. Fletcher, Extension of continental lithosphere: A model for two scales of Basin and Range deformation, *J. Geophys. Res.*, 91, 4826-4838, 1986.

TABLE 3.1. Large impact craters on Venus with measured depths [Basilevsky *et al.*, 1987]

Name	Latitude, °N	Longitude, °E	Diameter, km	Depth, km	Elevation ^a , km	Geological Unit ^b	Crater Class ^c
Klenova	78	104	144	0.78 ^d	N/A	rp	2
Cochran	52	143	104	0.7	- 0.4 ± 0.4	sp	2
Zhilova	66.5	126	60	0.62	0.7 ± 0.3	rp	2
Lagerlöf	81	289.5	58	0.62	N/A	rp	3
Fedosova	45	172	56	0.75	- 1.5 ± 0.3	sp	3
Voynich	35.5	56	56	0.44	- 0.5 ± 0.3	sp	1
Yablochkina	48	194.5	55. ^e	0.7	- 0.4 ± 0.2	rp	2
Cotton	71	300	52	0.7 ^d	1.2 ± 0.5	b	1
Fedorets	59.5	65.5	52	0.55 ^d	- 0.4 ± 0.3	sp	1
Duncan	68	292	46	0.44	- 0.4 ± 0.2	rp	1
Tsvetaeva	65	147	45. ^e	0.9	- 0.8 ± 0.3	sp	1
Obukhova	71	290	44	0.53 ^d	0.2 ± 0.3	b	2
Ruslanova	84	15	44	0.4	N/A	rp	2
Akhmatova	61	308	42. ^e	0.4	- 0.2 ± 0.4	rp	3
Deledda	76	128	32	0.5	N/A	rp	2

^a Mean and standard deviation of the elevation measurements obtained by the Pioneer Venus altimeter [Pettengill *et al.*, 1980; Ford, 1986] within a circle 2° in diameter centered on the crater, excluding the crater interior. The elevation datum is a sphere of radius 6051.9 km. N/A signifies no data available.

^b "Terrain type" of Barsukov *et al.* [1986] and Basilevsky *et al.* [1987]: sp - smooth plains, rp - rolling plains, b - ridge and groove belts.

^c Morphological class [*Basilevsky et al.*, 1987]: class 1 craters, inferred to be the freshest, have a prominent rim and a radar-bright halo; class 2 craters have morphological features similar to class 1 but lack a radar-bright halo; for class 3 craters all or most diagnostic morphological features are present but degraded.

^d Mean value where two measurements were reported.

^e Geometric mean of two principal diameters.

TABLE 3.2. Adopted model parameters

Crater diameter	32 km	50 km	140 km
Wavenumber band	0.060-1.137 km ⁻¹	0.042-1.215 km ⁻¹	0.011-0.325 km ⁻¹
Number of wavenumbers	20	30	30
Average stress difference $\bar{\sigma}$	2 MPa	2 MPa	4 MPa
Crustal density	2.9 Mg/m ³		
Mantle density	3.4 Mg/m ³		
Surface temperature	738 K		
Depth of brittle-ductile transition, crust	1 km		
Depth of brittle-ductile transition, mantle	10 km		

Stress evaluated under the assumption that crater depth scales as g^{-1} for a reference model with crustal thickness $H = 13$ km and mean lithospheric thermal gradient $dT/dz = 13$ K/km.

TABLE 3.B1. Limits on plate thickness and thermal gradient beneath Venus impact craters
from elastic and elastic-plastic models for lithospheric flexure

	Elastic Plate			Elastic-Plastic Plate
H	$E,$ Pa	$L,$ km	$M,$ 10^{11} N	$dT/dz,$ K/km
$D = 140$ km				
0	10^{10}	20	4.2	19
	10^{11}	9	9.0	29
$H \gg L$	10^{10}	22	4.8	5
	10^{11}	10	10.3	6
$D = 50$ km				
H	$E,$ Pa	$L,$ km	$M,$ 10^{11} N	$dT/dz,$ K/km
0	10^{10}	7.7	2.0	49
	10^{11}	3.5	1.9	68
$H \gg L$	10^{10}	7.9	2.1	18
	10^{11}	3.7	2.1	18

$D = 32 \text{ km}$

H	$E,$ Pa	$L,$ km	$M,$ 10^{11} N	$dT/dz,$ K/km
0	10^{10}	3.3	1.1	96
	10^{11}	1.5	2.3	110
$H \gg L$	10^{10}	3.5	1.2	31
	10^{11}	1.6	2.6	30

FIGURE CAPTIONS

- Figure 3.1 Venera 16 radar image of Klenova, an impact structure 144 km in diameter [*Barsukov et al.*, 1986]. Klenova has a complex morphology, including a scalloped rim crest, a flat inner floor, and a peak ring. The width of the image is 520 km; white lines denote meridians spaced at 5° intervals; the 80° parallel is also shown.
- Figure 3.2 Depth versus diameter for impact craters on Venus, from *Basilevsky et al.* [1987]. Solid circles denote craters included in this study (Table 3.1); crosses denote other craters not included here, for reasons given in the text. The cross at upper right represents Cleopatra Patera. Also shown are the mean and 95% confidence limits for the mean depths of observed (solid lines) and predicted fresh (dashed lines) impact craters. Depths of fresh craters are estimated from the depths of lunar Copernican and Eratosthenian craters under the assumption that relief scales inversely with surface gravitational acceleration (see text).
- Figure 3.3 Locations of the 15 impact craters used in this study (filled circles). Topographic provinces, following *Masursky et al.* [1980], are outlined; highlands are cross-hatched and lowlands are shaded. Most of the craters depicted lie at intermediate elevations.
- Figure 3.4 Distribution of impact craters with depths measured by Venera 15 and 16 (from Table 3.1). (a) Distribution by regional elevation as indicated

by Pioneer Venus altimetric data (where available). (b) Distribution by geological unit [Basilevsky *et al.*, 1987], where *sp* denotes smooth plains, *rp* rolling plains, and *b* ridge and groove belts. (c) Distribution by crater morphological class [Basilevsky *et al.*, 1987], where class 1 craters are most pristine and class 3 are significantly degraded. The craters used in this study are fairly typical in terms of elevation, geological terrain, and state of preservation.

Figure 3.5 The statistical approach to viscous relaxation adopted in this paper. Assuming that at a fixed crater diameter D the crater depths follow a log-normal distribution, and that all craters at diameter D have an age given by half the mean crater retention age, then a particular viscous relaxation scenario will reduce the mean depth of fresh craters from d_i to δ . If δ is much smaller than d_v , the observed mean depth of craters of diameter D , then that viscous relaxation model is not plausible. A t test may be used to quantify this relationship by calculating the significance level α at which the null hypothesis $d_v = \delta$ can be rejected in favor of $d_v > \delta$; larger values of α are associated with more plausible viscous relaxation models.

Figure 3.6 Two models for the viscous relaxation of a Venus impact crater 140 km in diameter, illustrating the combined effects of thermal gradient (dT/dz) and crustal thickness (H) on the extent of relaxation versus crater age t . The initial topography is scaled from that of the lunar crater Langrenus and is assumed to be initially uncompensated ($c = 0$). (a) A model with $dT/dz = 10$ K/km and $H = 10$ km. There is little

change in relief after 50 m.y., but some decrease has occurred by 500 m.y. The latter change could be marginally resolved at 95% confidence (see text). (b) A model with $dT/dz = 15$ K/km and $H = 15$ km. Substantial topographic relaxation occurs in 50 m.y., and the crater relief is effectively removed by 500 m.y.

Figure 3.7 Two models for the viscous relaxation of a Venus impact crater 32 km in diameter. Except for crater diameter and initial topography (scaled from that of the lunar crater Timocharis), parameters are identical to those of the models depicted in Figure 3.6. (a) A model with $dT/dz = 10$ K/km and $H = 10$ km. The change in relief is small, even after 500 m.y. (b) A model with $dT/dz = 15$ K/km and $H = 15$ km. The extent of viscous relaxation is greater than in (a) but the change in relief is not proportionally nearly as great as for the crater with $D = 140$ km, in part because the relaxation of larger features is sensitive to the generally lower viscosity at greater depth.

Figure 3.8 Relaxation time constants τ versus wavenumber k for the models in Figures 3.6 and 3.7. The solid portions of each curve delimit the wavenumber range corresponding to the largest values of the crater topographic spectra ($2\pi/k = 0.5 - 3 D$). At $dT/dz = 15$ K/km and $H = 15$ km, the relevant time constants for $D = 32$ km exceed those for $D = 140$ km. At $dT/dz = 10$ K/km and $H = 10$ km, however, the relevant time constants for both diameters are comparable because the sensitivity of the smaller crater to the viscosity of the weak lower crust is largely offset by an increase in effective viscosity due to lower

Figure 3.13 Summary of 95% confidence levels for rejecting combinations of dT/dz and H from Figures 3.9-12 (solid lines) for craters 50 m.y. (a) or 500 m.y. (b) in age. A similar curve is shown for a crater 50 km in diameter; the initial topography is scaled from that of the lunar crater Eratosthenes. Dashed extensions of several of these curves show similar calculations for initially compensated craters where these solutions differ from those for initially uncompensated craters; the characteristic stress difference $\bar{\sigma}$ and thus the effective viscosity at each temperature are taken to be identical to those for the initially uncompensated cases. The dashed curve at upper right gives the 95% confidence level for rejecting combinations of dT/dz and H for an initially compensated crater 140 km in diameter and a characteristic stress difference of 0.5 MPa. Such a low value of $\bar{\sigma}$ is unlikely but gives conservative upper limits to dT/dz and H for initially compensated large craters.

Figure 3.A1. Sketch of the viscous relaxation problem as applied to Venus in this paper. A crust with density ρ_c and thickness H overlies a mantle with density $\rho_c + \Delta\rho$. Given an average lithospheric thermal gradient dT/dz and specified flow laws for ductile deformation of crustal and mantle rocks, the effective viscosity as a function of depth may be constructed.

Figure 3.B1. Flexural deformation of a 140-km-diameter impact crater on an elastic plate overlying an inviscid fluid. The portion of the original crater

differential stress.

Figure 3.9 Effect of viscous relaxation for an initially uncompensated crater 140 km in diameter after 50 m.y., shown as a function of dT/dz and H . (a) Fractional relief remaining. (b) Confidence levels for rejecting combinations of dT/dz and H . At a specified confidence level, models to the right of each curve may be rejected.

Figure 3.10 Effect of viscous relaxation for an initially uncompensated crater 140 km in diameter after 500 m.y., shown as a function of dT/dz and H . (a) Fractional relief remaining. The small shift in the 0.1 contour is due to a change in the radial position of the point of greatest depth on the crater floor. (b) Confidence levels for rejecting combinations of dT/dz and H .

Figure 3.11 Effect of viscous relaxation for an initially uncompensated crater 32 km in diameter after 50 m.y., shown as a function of dT/dz and H . (a) Fractional relief remaining. (b) Confidence levels for rejecting combinations of dT/dz and H . A greater proportional relief remains than under the same conditions with $D = 140$ km (Figure 3.9).

Figure 3.12 Effect of viscous relaxation for an initially uncompensated crater 32 km in diameter after 500 m.y., shown as a function of dT/dz and H . (a) Fractional relief remaining. (b) Confidence levels for rejecting combinations of dT/dz and H . Note that the extent of relaxation is insensitive to crustal thickness for H greater than about 20 km.

relief (solid line) that can be elastically supported increases with the plate thickness. The dashed profile corresponding to an elastic plate thickness of 20 km for $E = 10^{10}$ Pa matches the 95% confidence lower bound on the mean observed depth of craters of this size.

Figure 3.B2. The distribution with depth of the average radial horizontal stress beneath the crater in the example shown in Figure 3.B1 for an elastic-plastic plate model. The crustal thickness is taken to be zero, so the bending stresses are limited by the strength envelope for olivine (long dashed line). An upper bound on the thermal gradient for this model is 19 K/km.

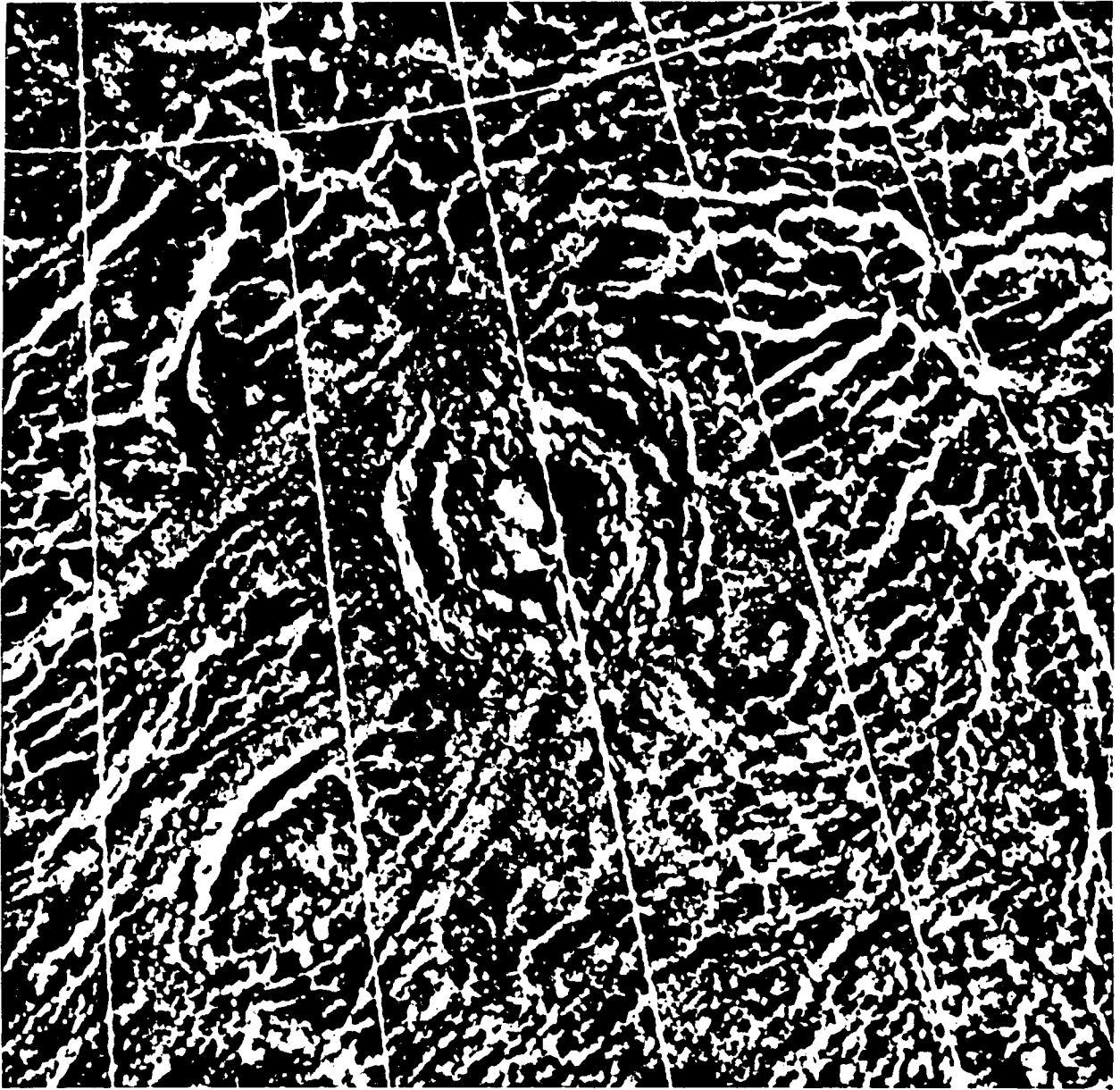


Figure 3.1

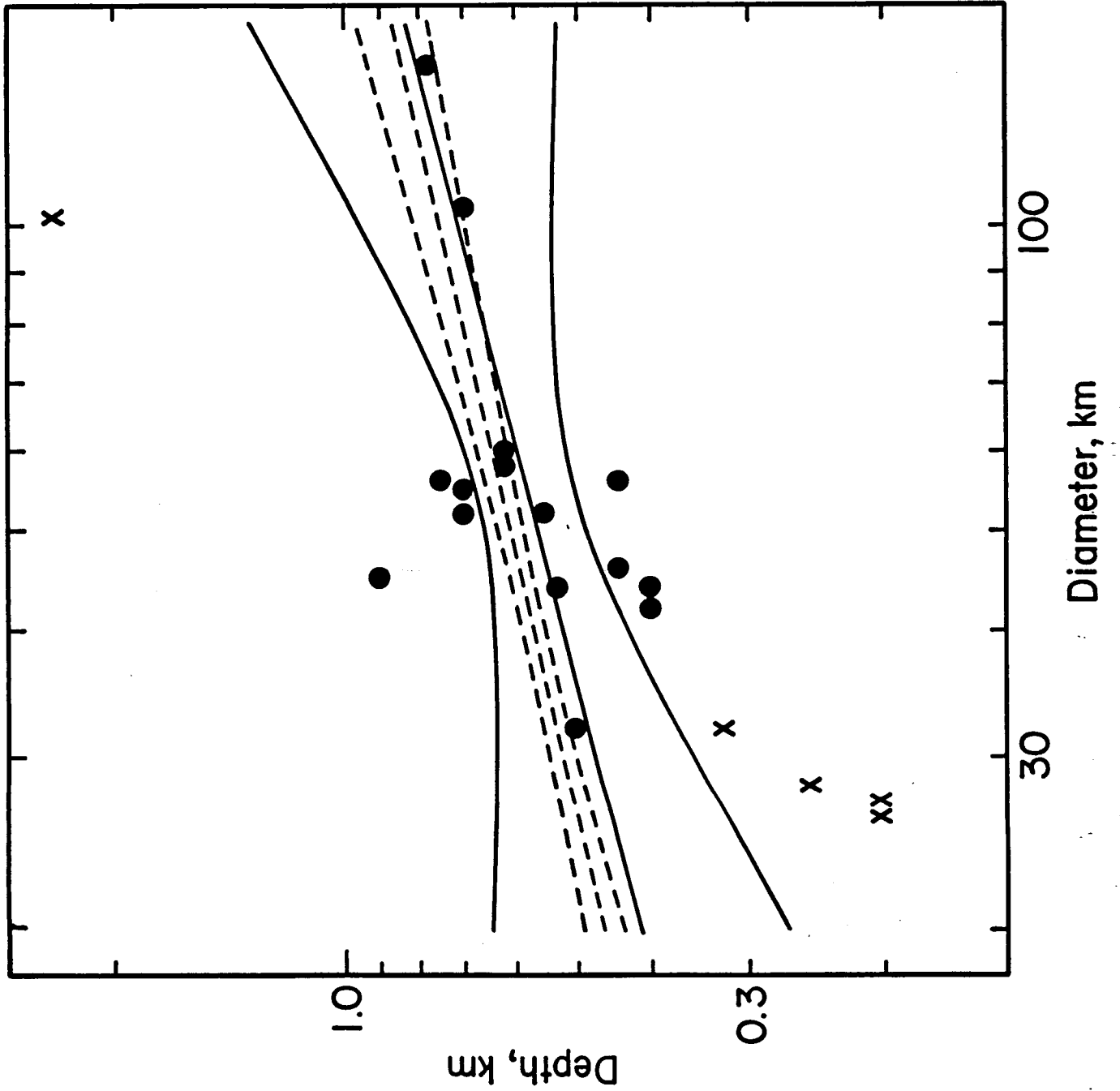


Figure 3.2

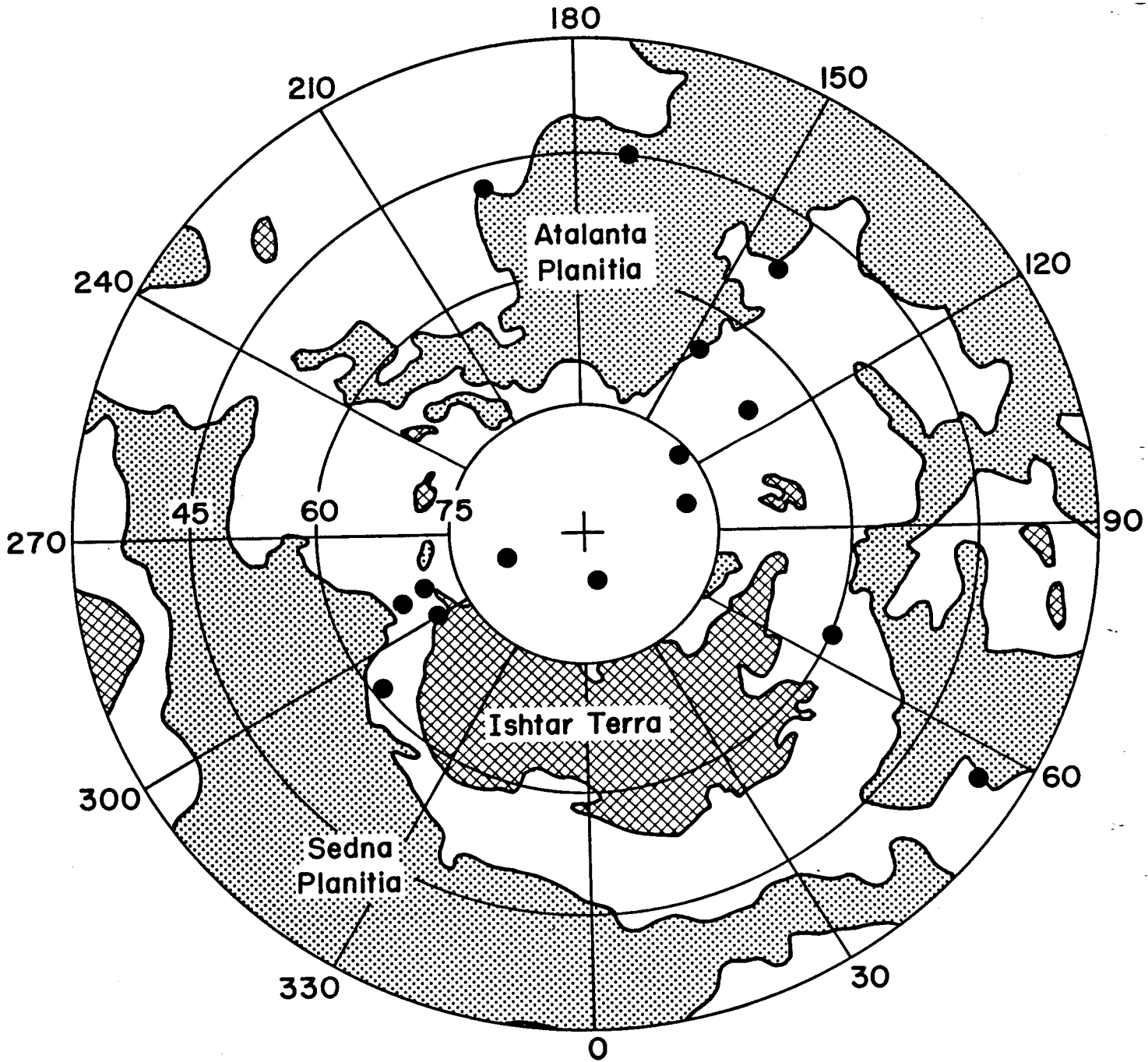


Figure 3.3

C-2

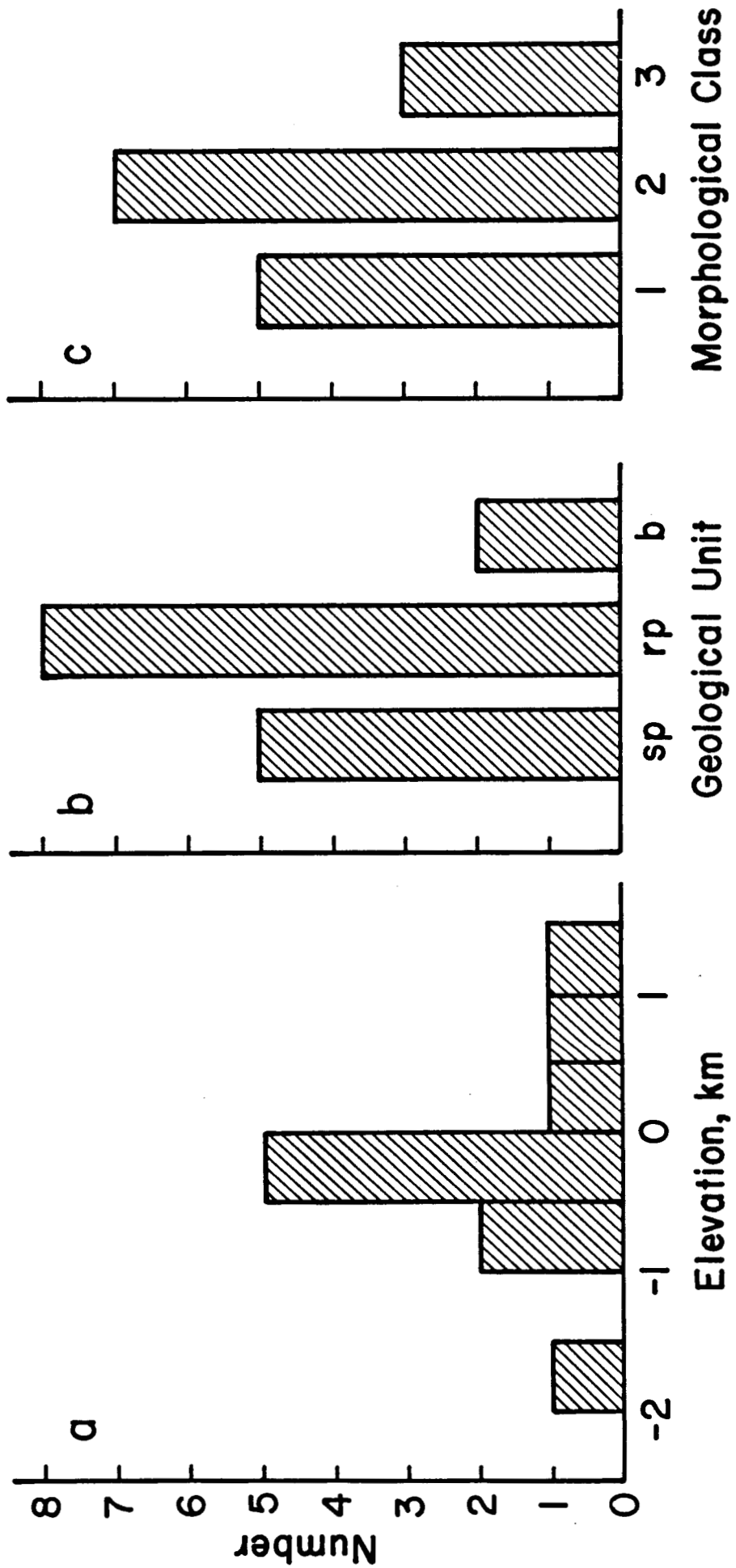


Figure 3.4

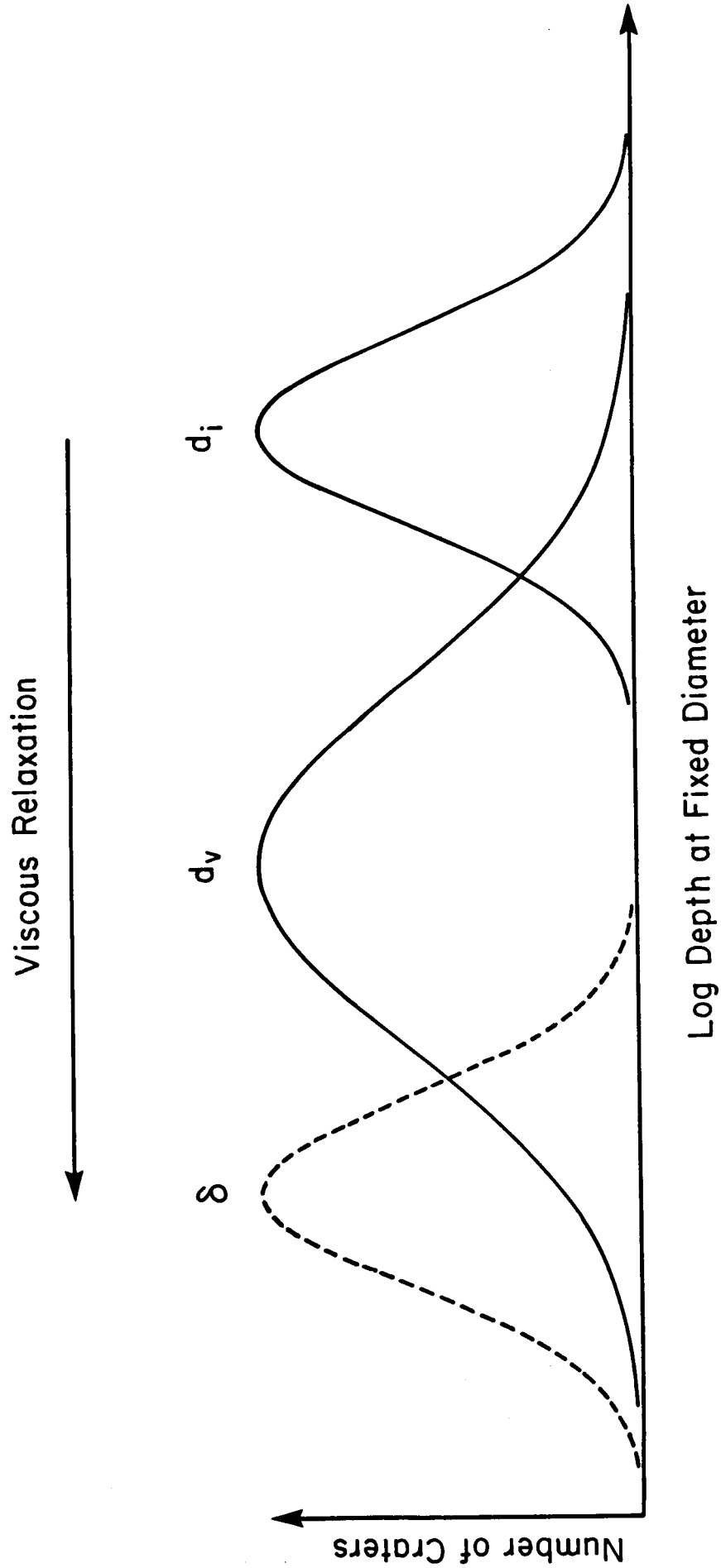


Figure 3.5

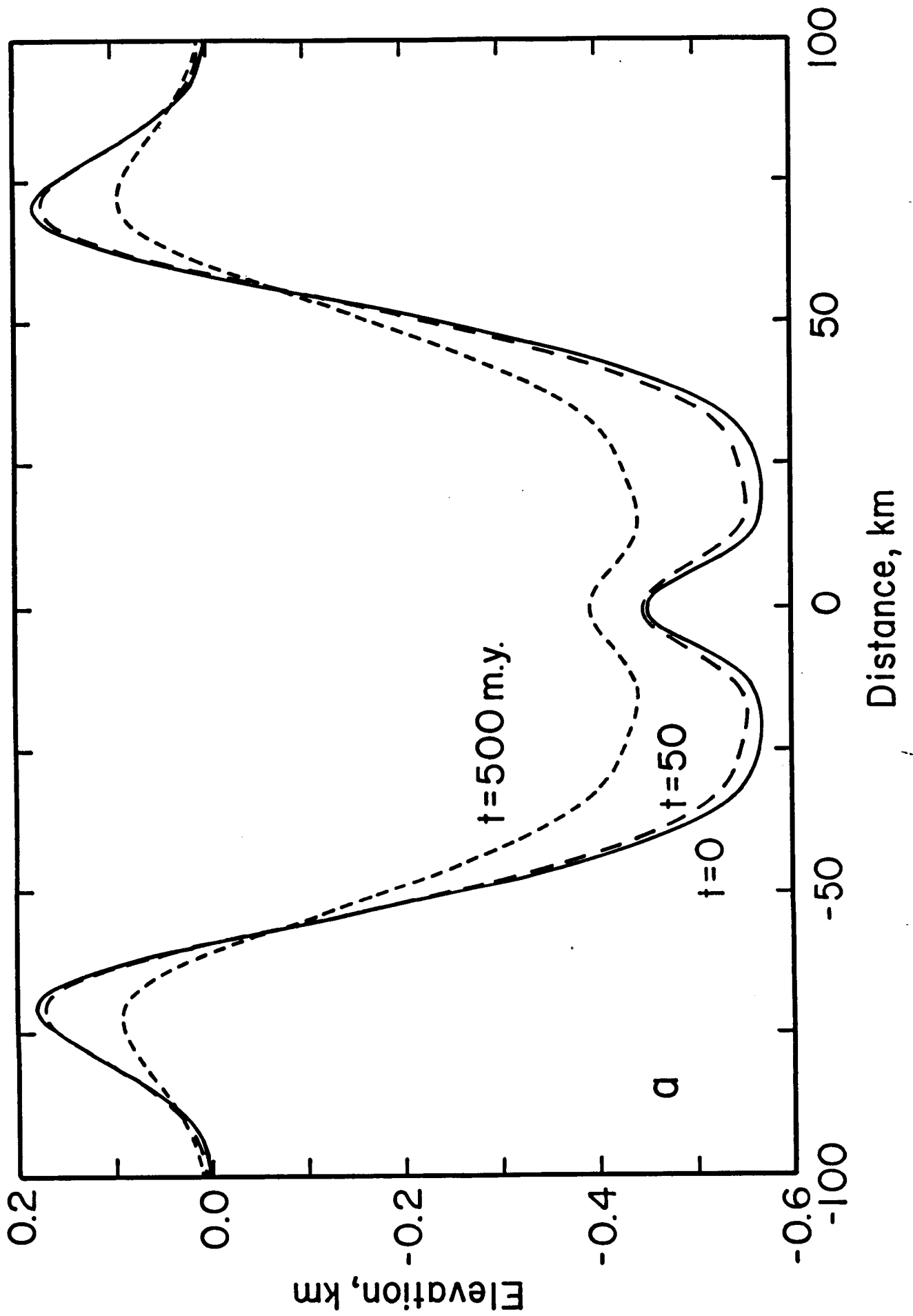


Figure 3.6a

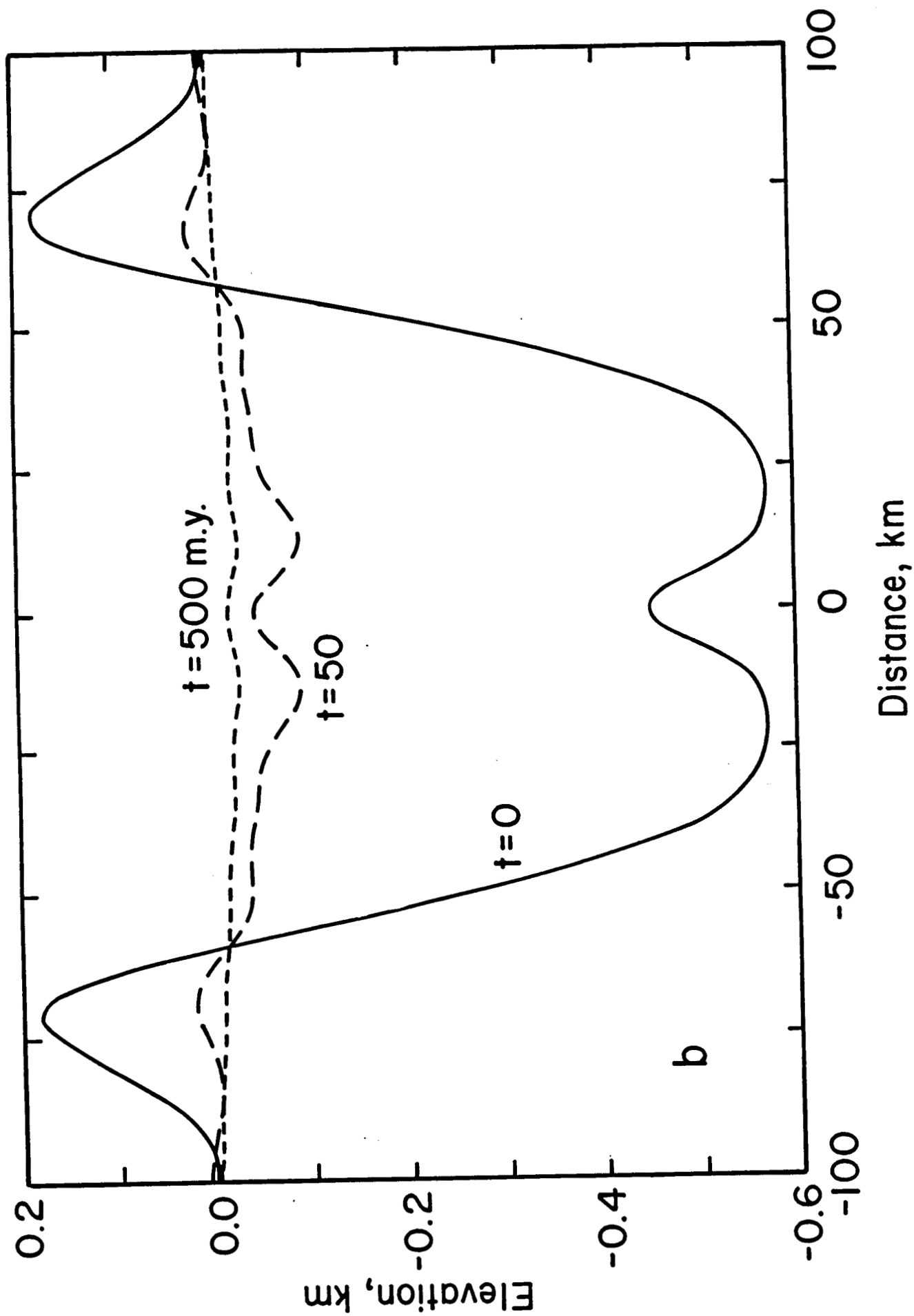


Figure 3.6b

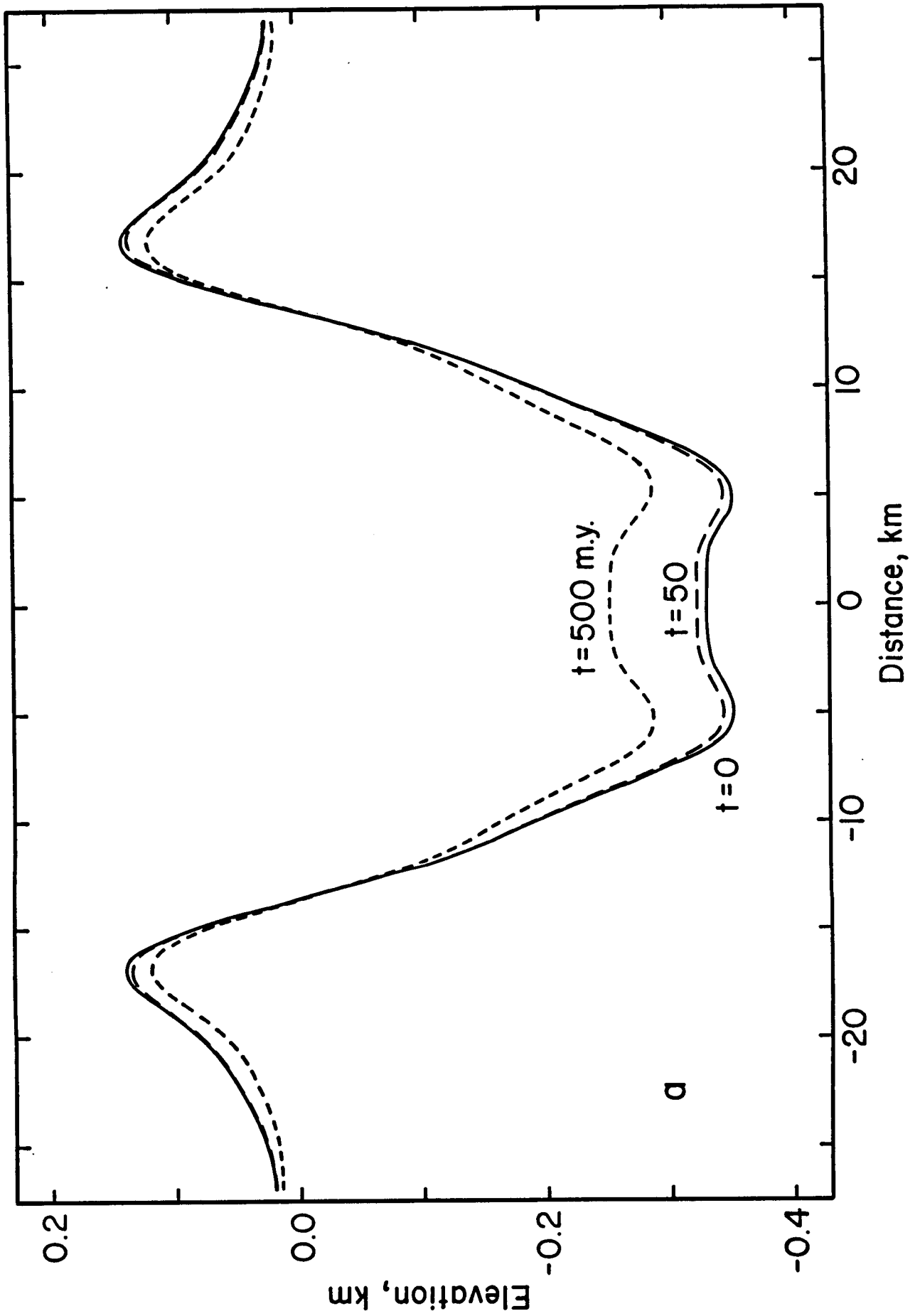


Figure 3.7a

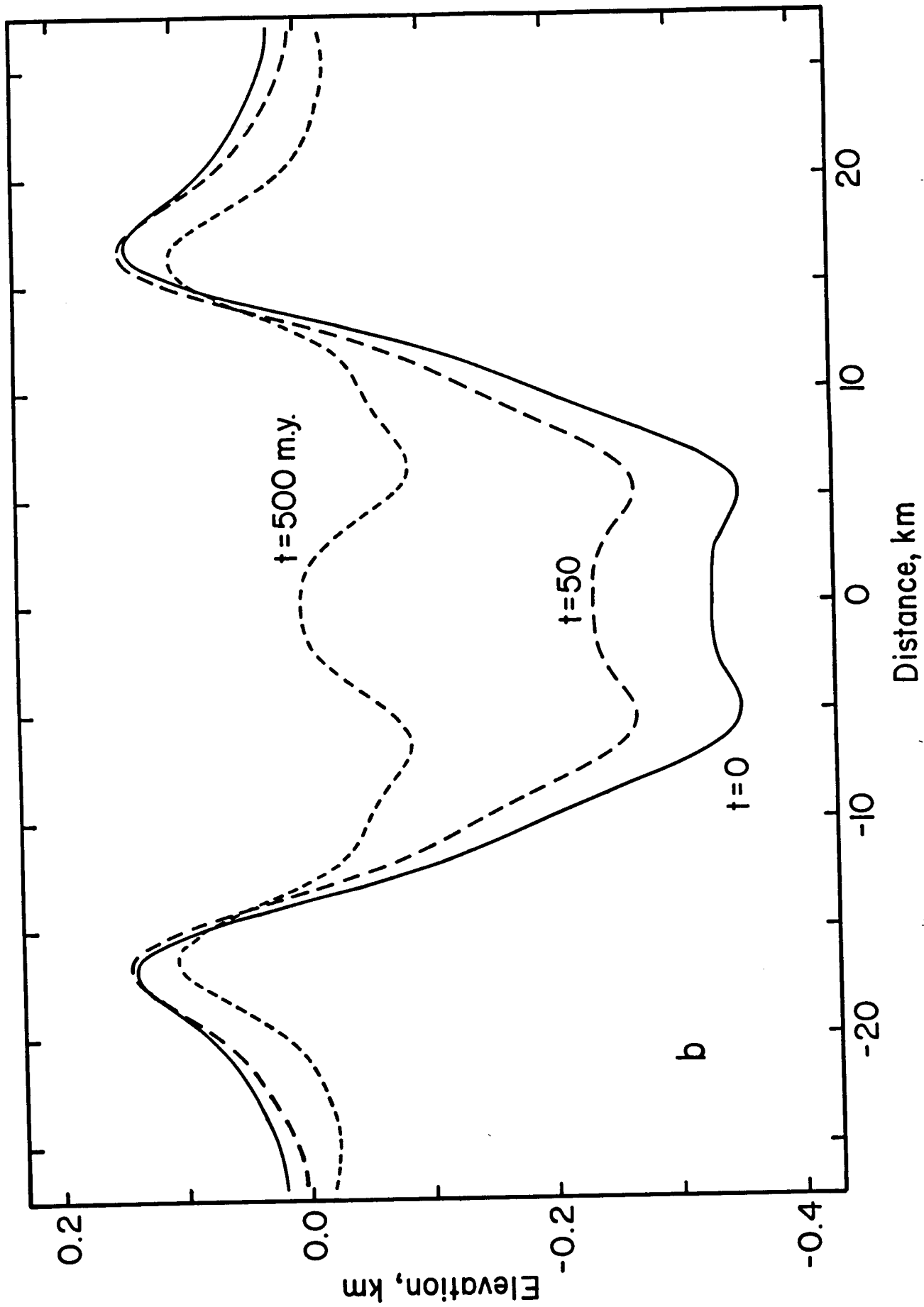


Figure 3.7b

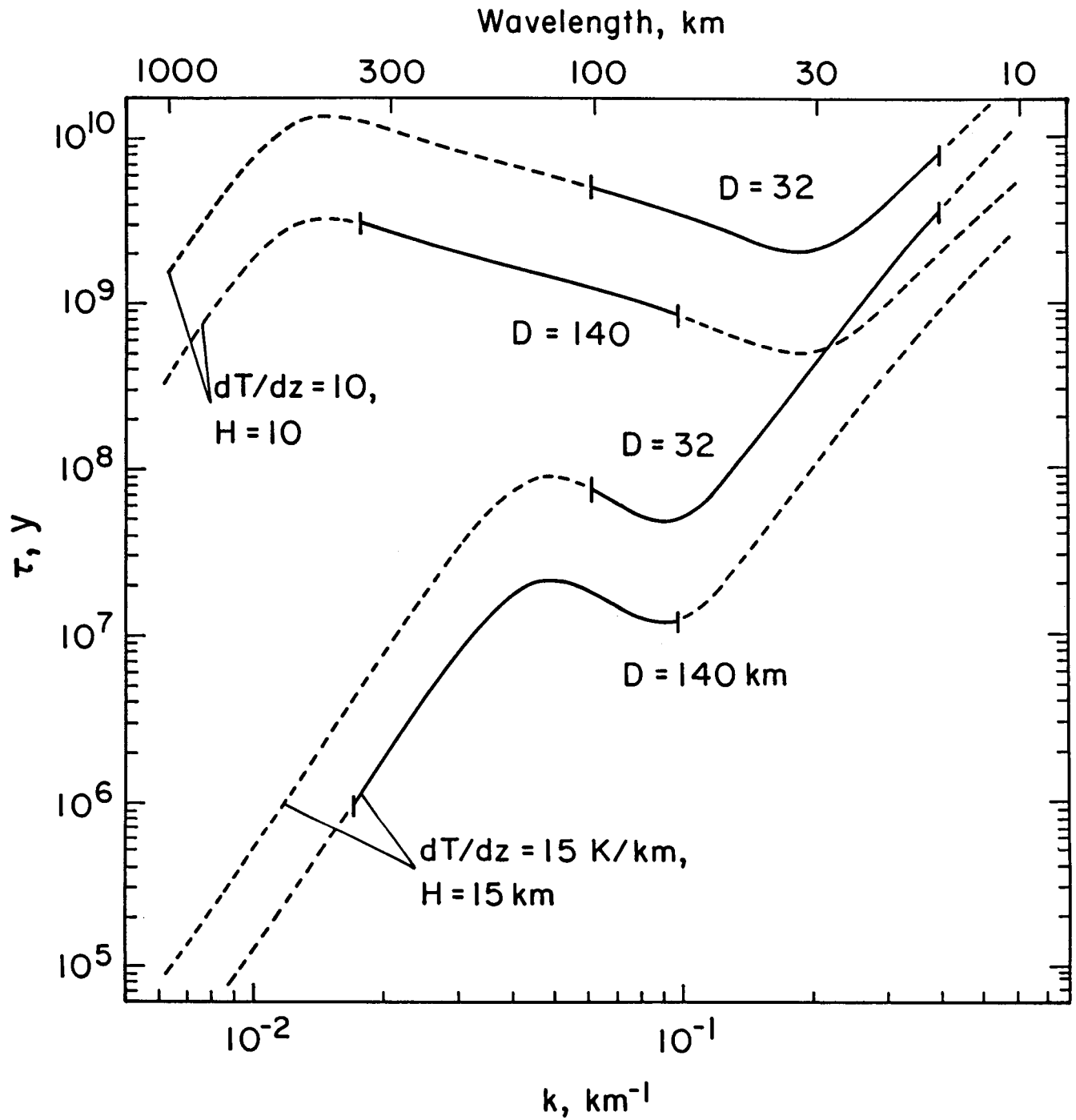


Figure 3.8

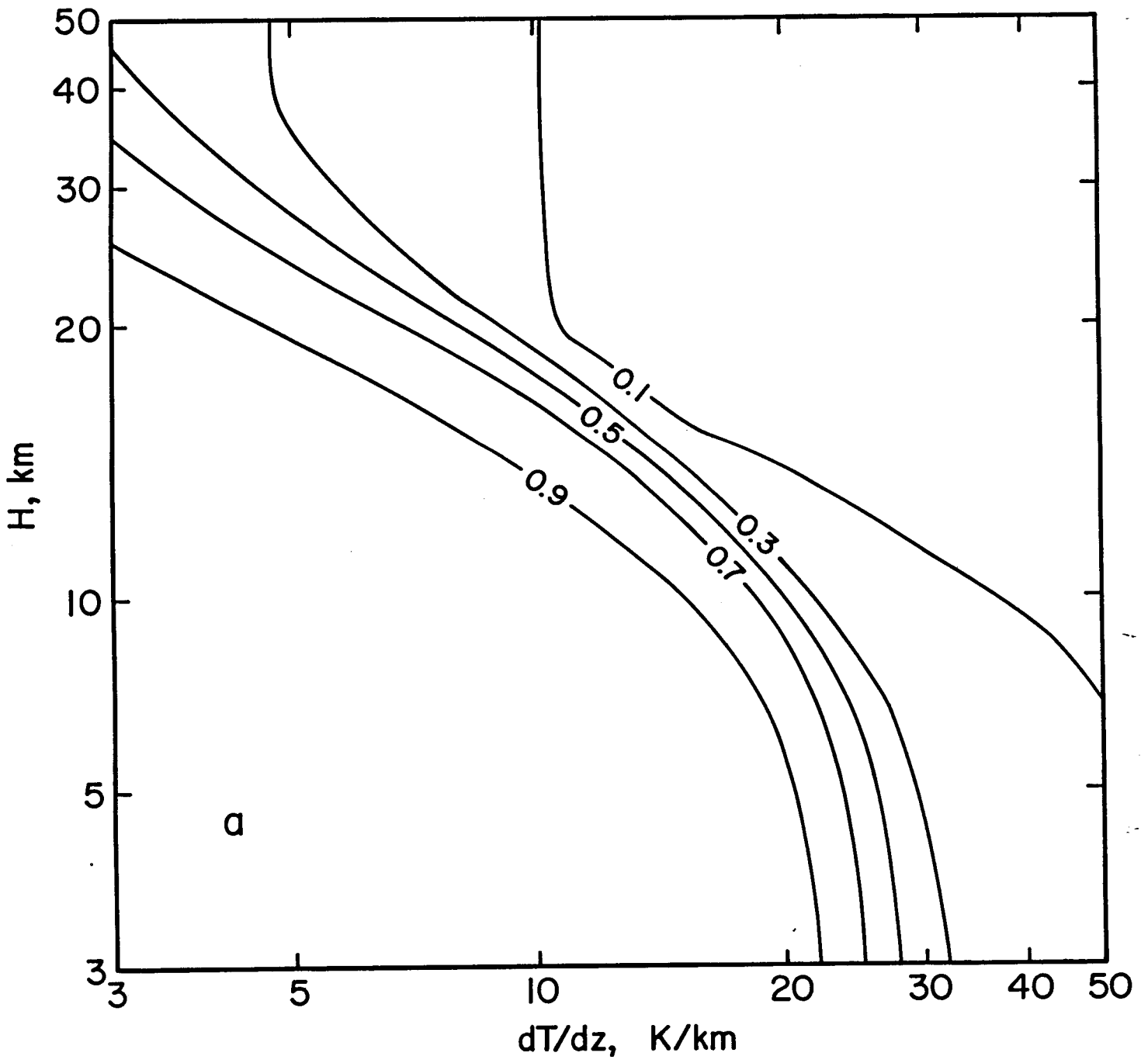


Figure 3.9a

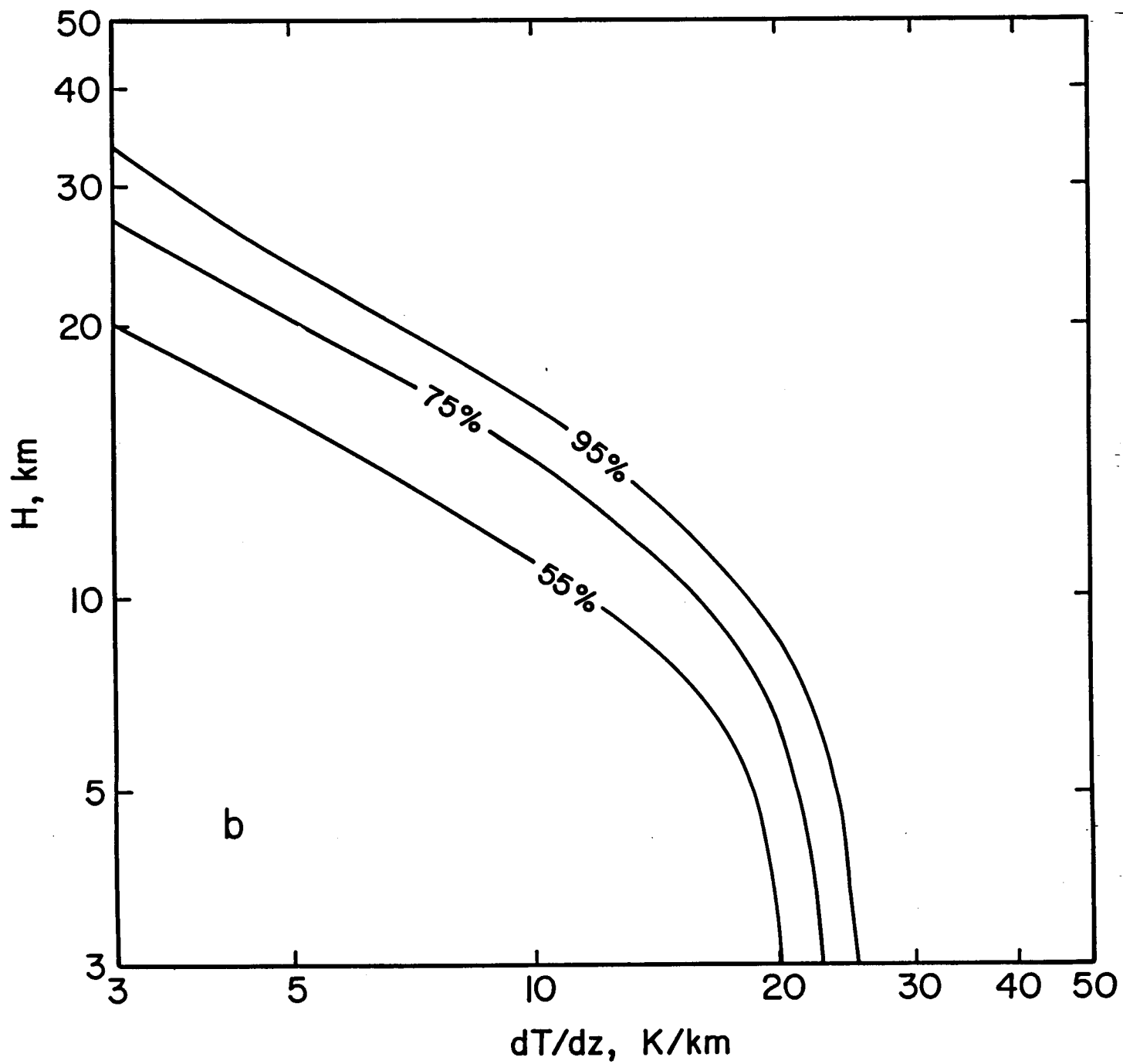


Figure 3.9b

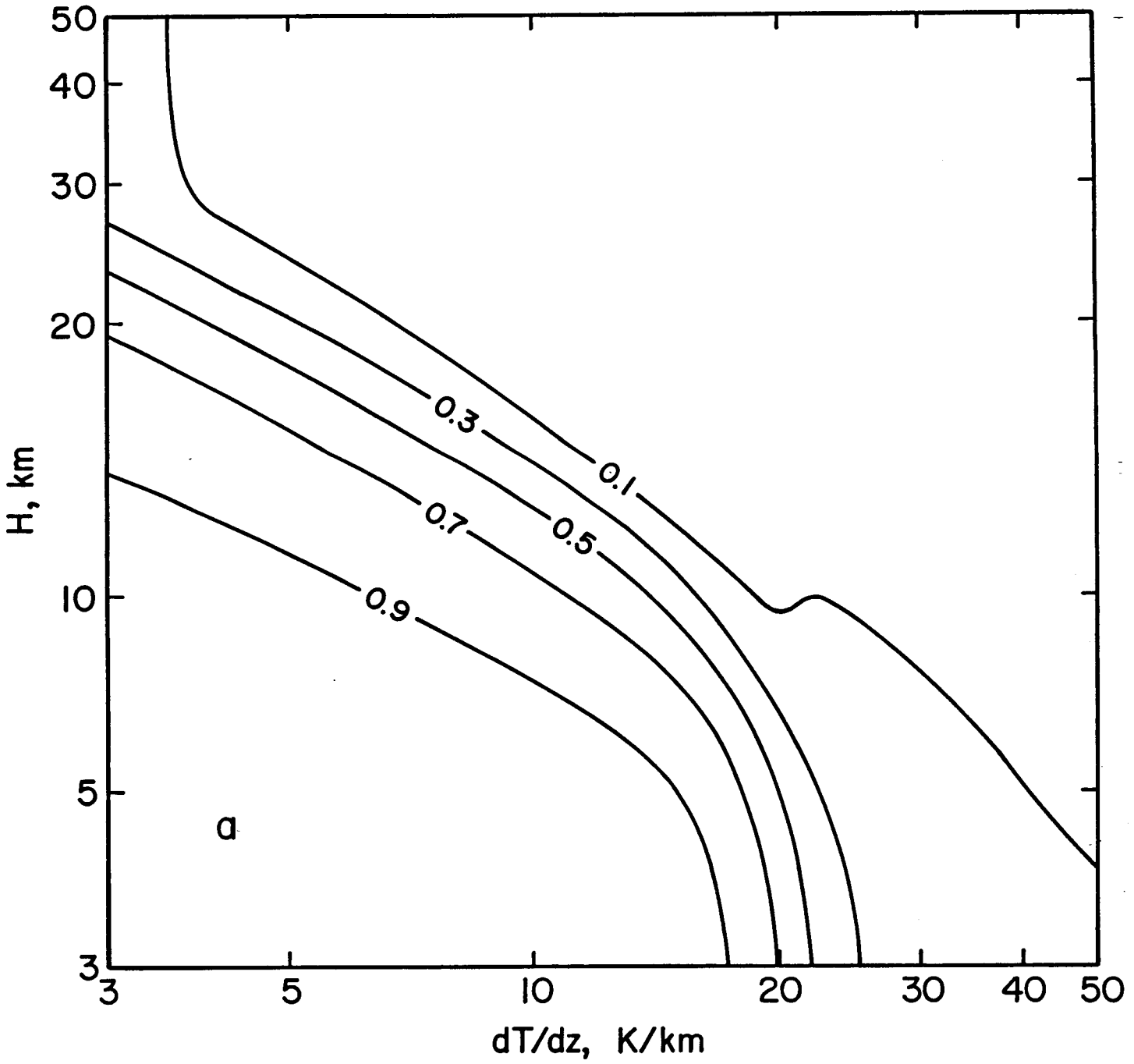


Figure 3.10a

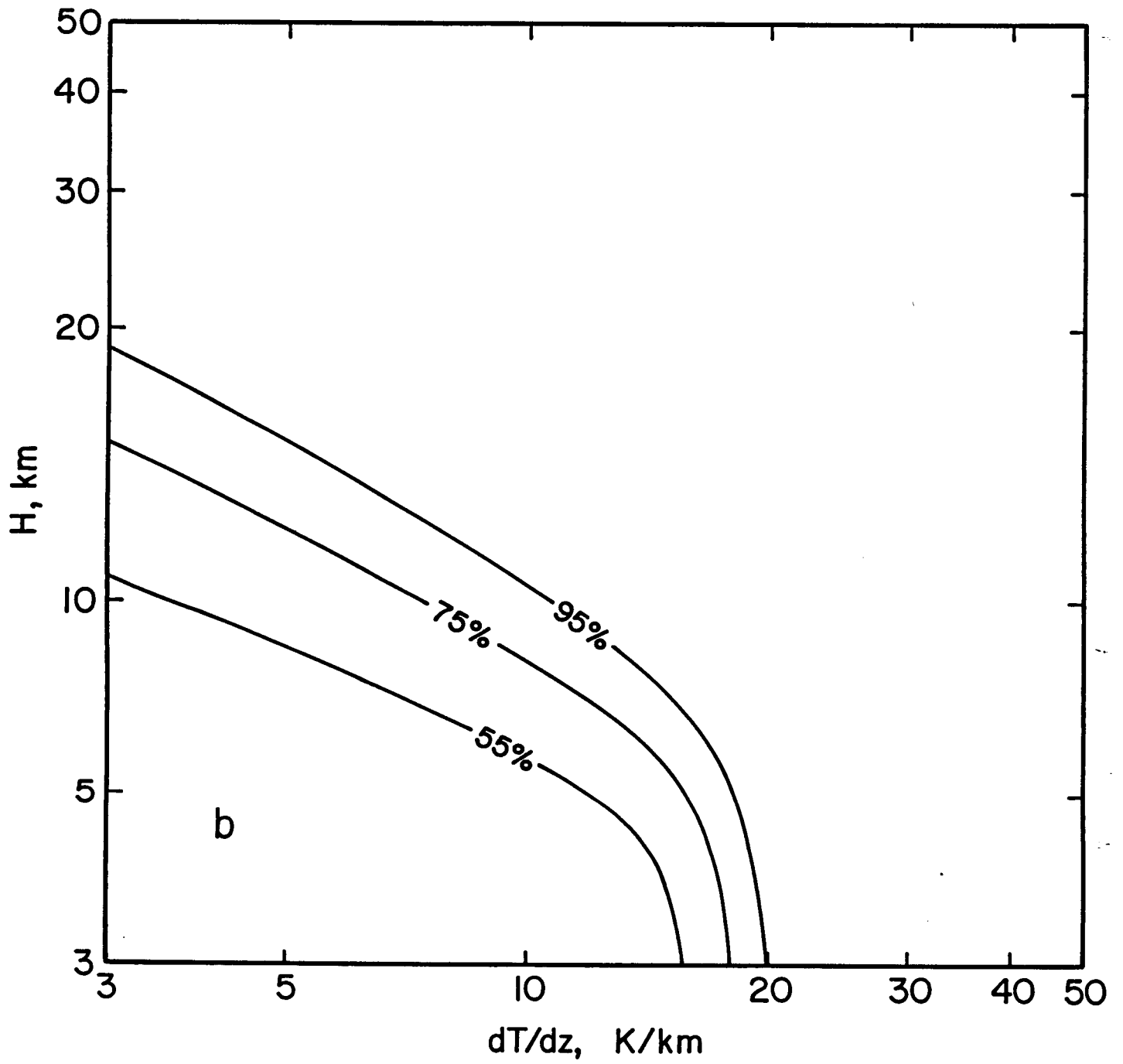


Figure 3.10b

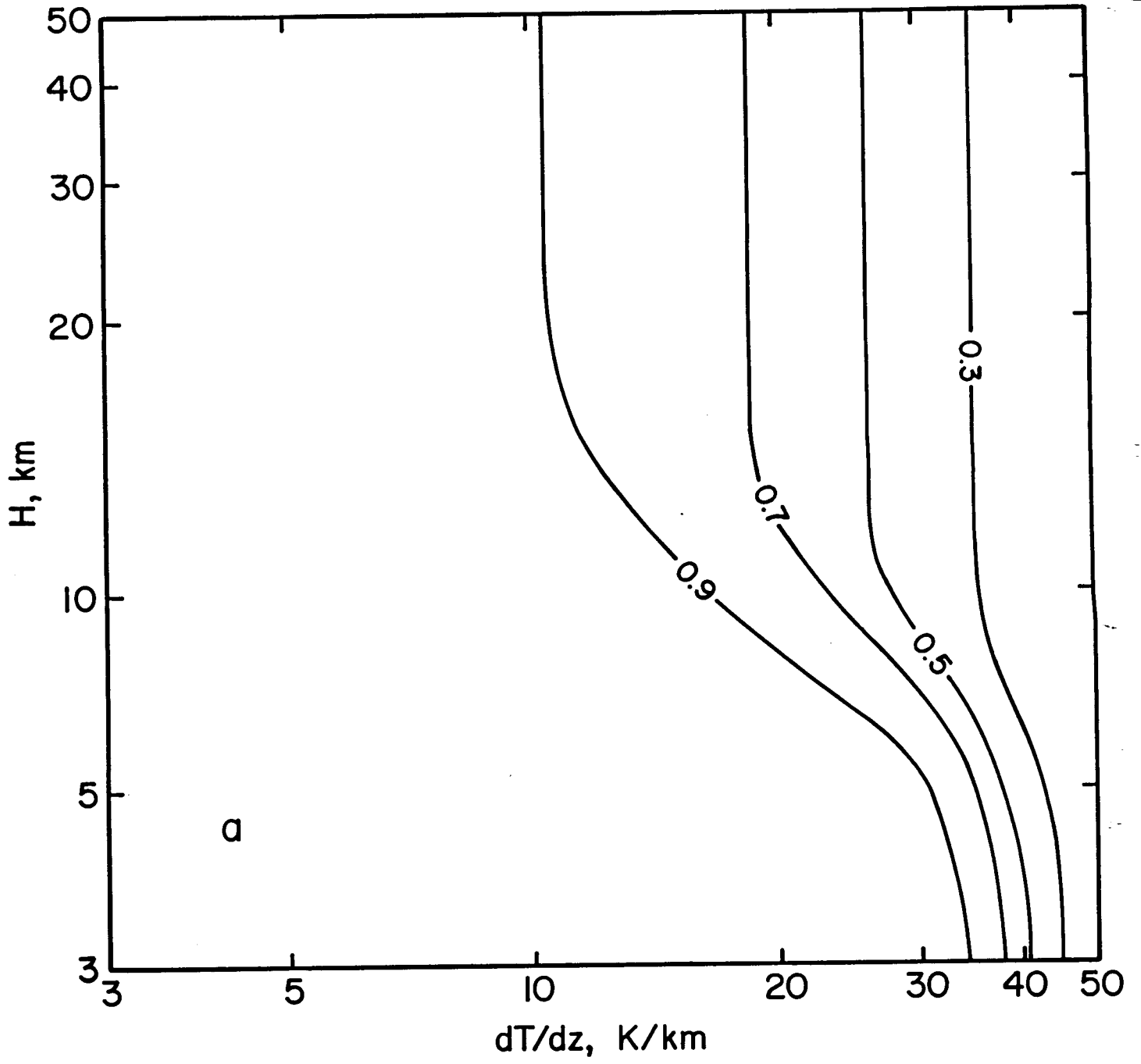


Figure 3.11a

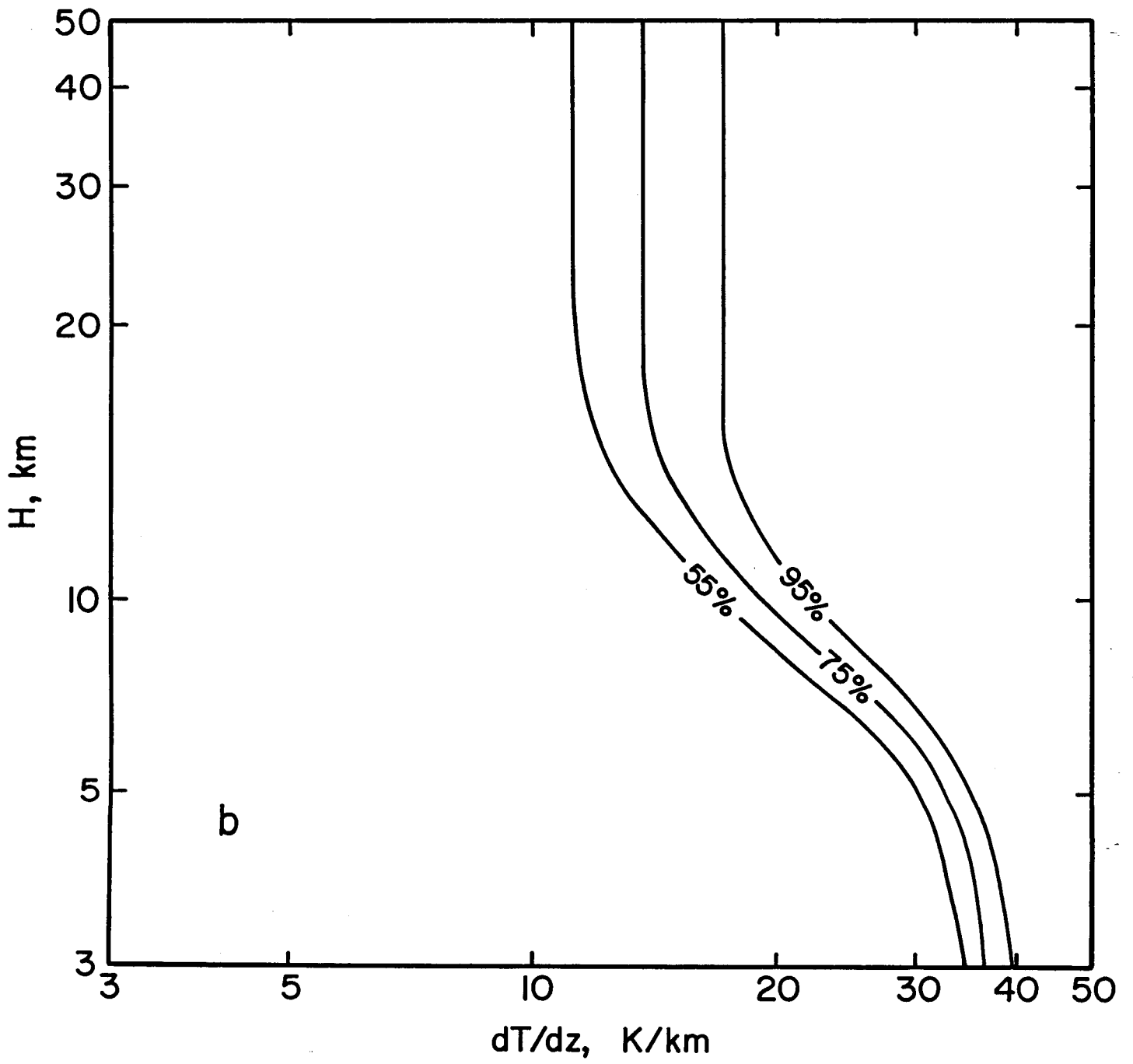


Figure 3.11b

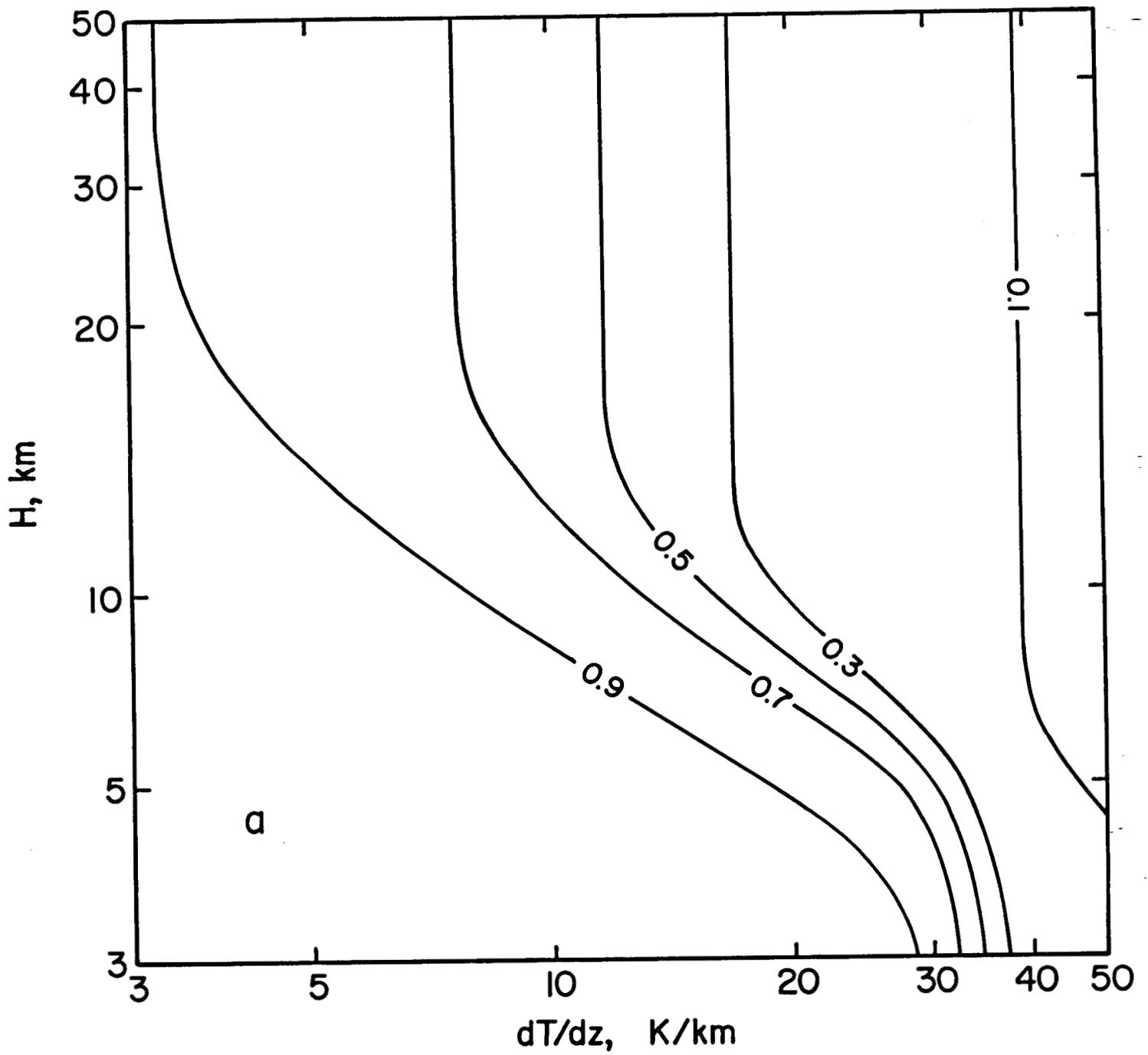


Figure 3.12a

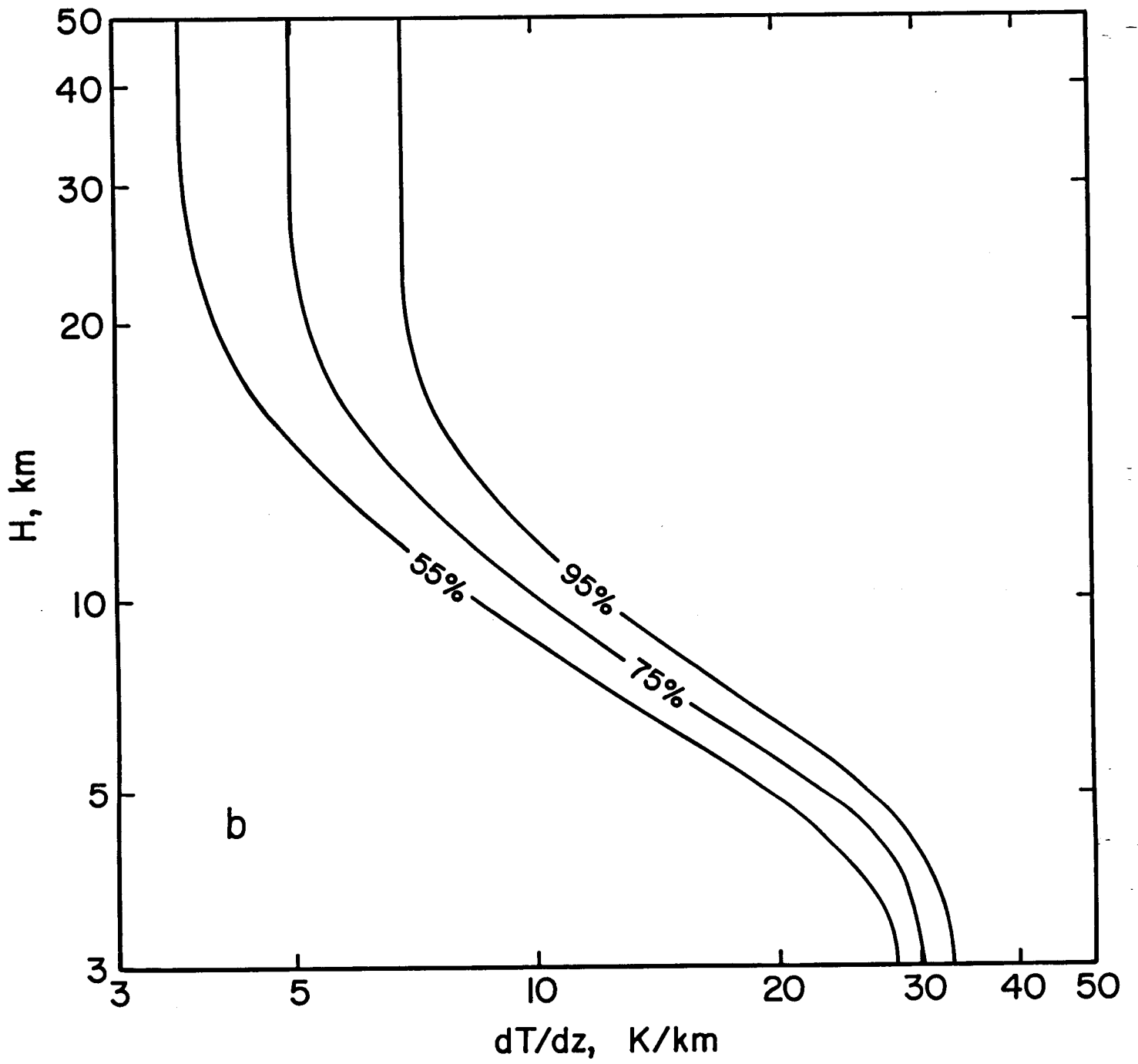


Figure 3.12b

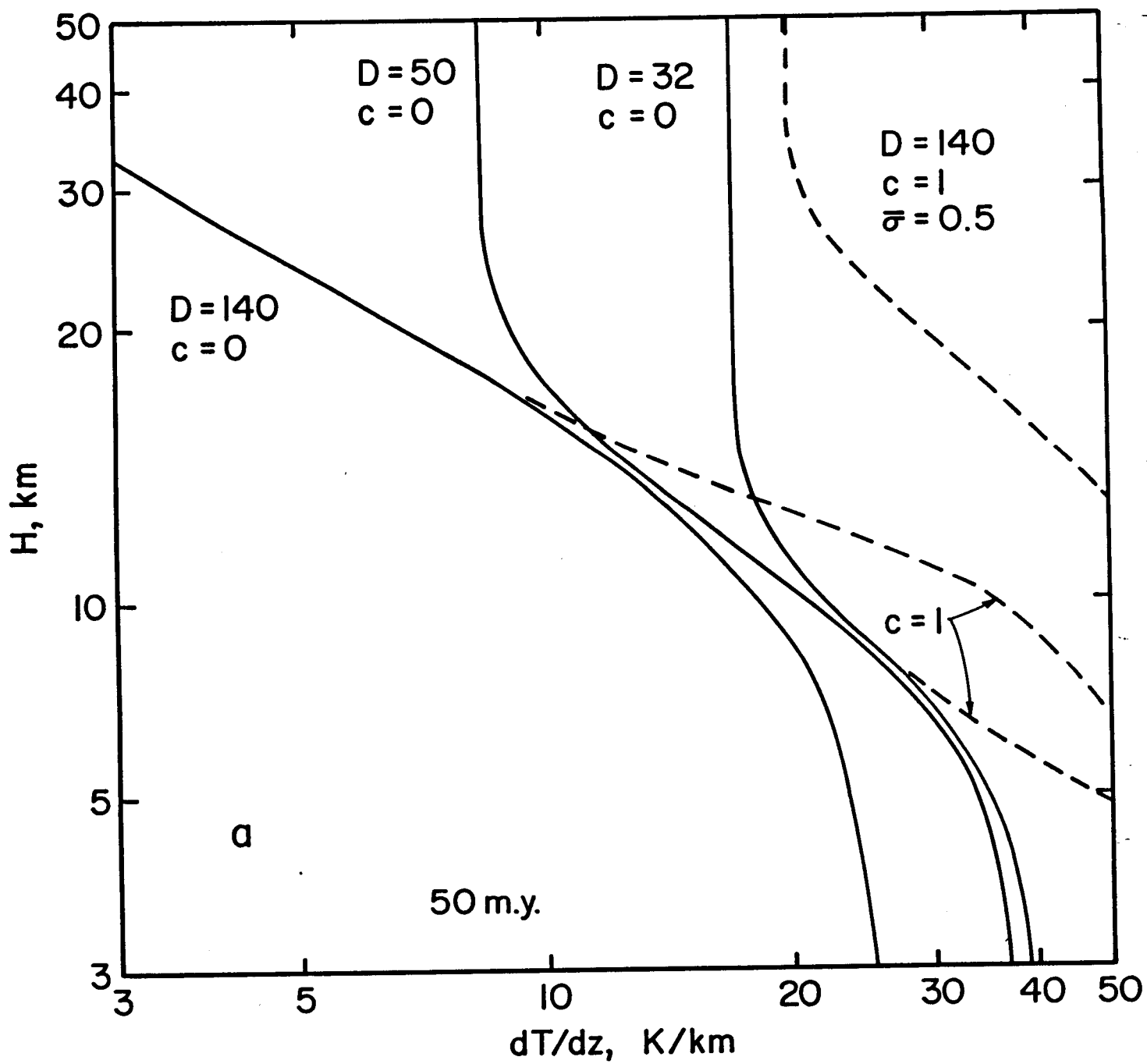


Figure 3.13a

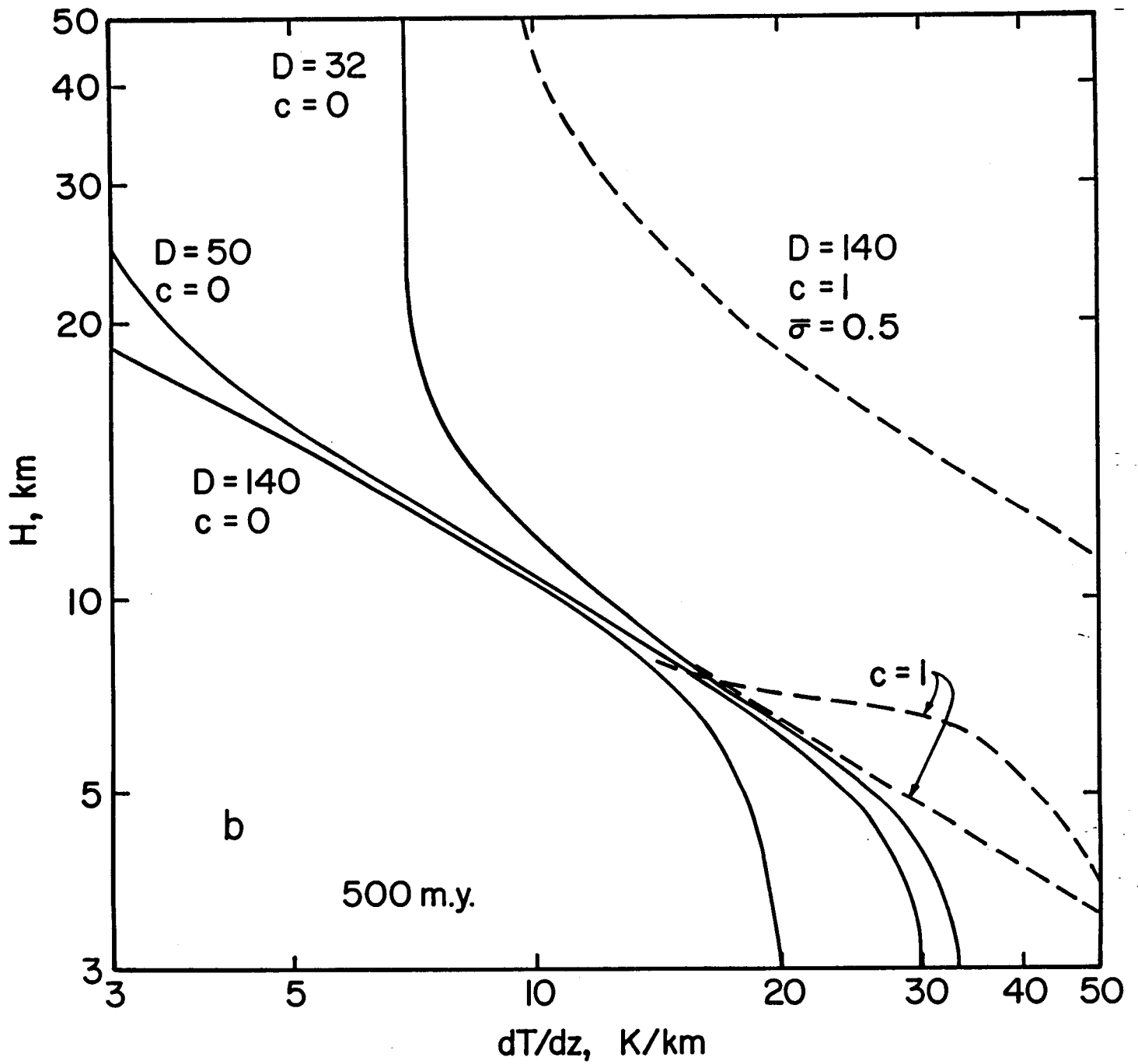


Figure 3.13b

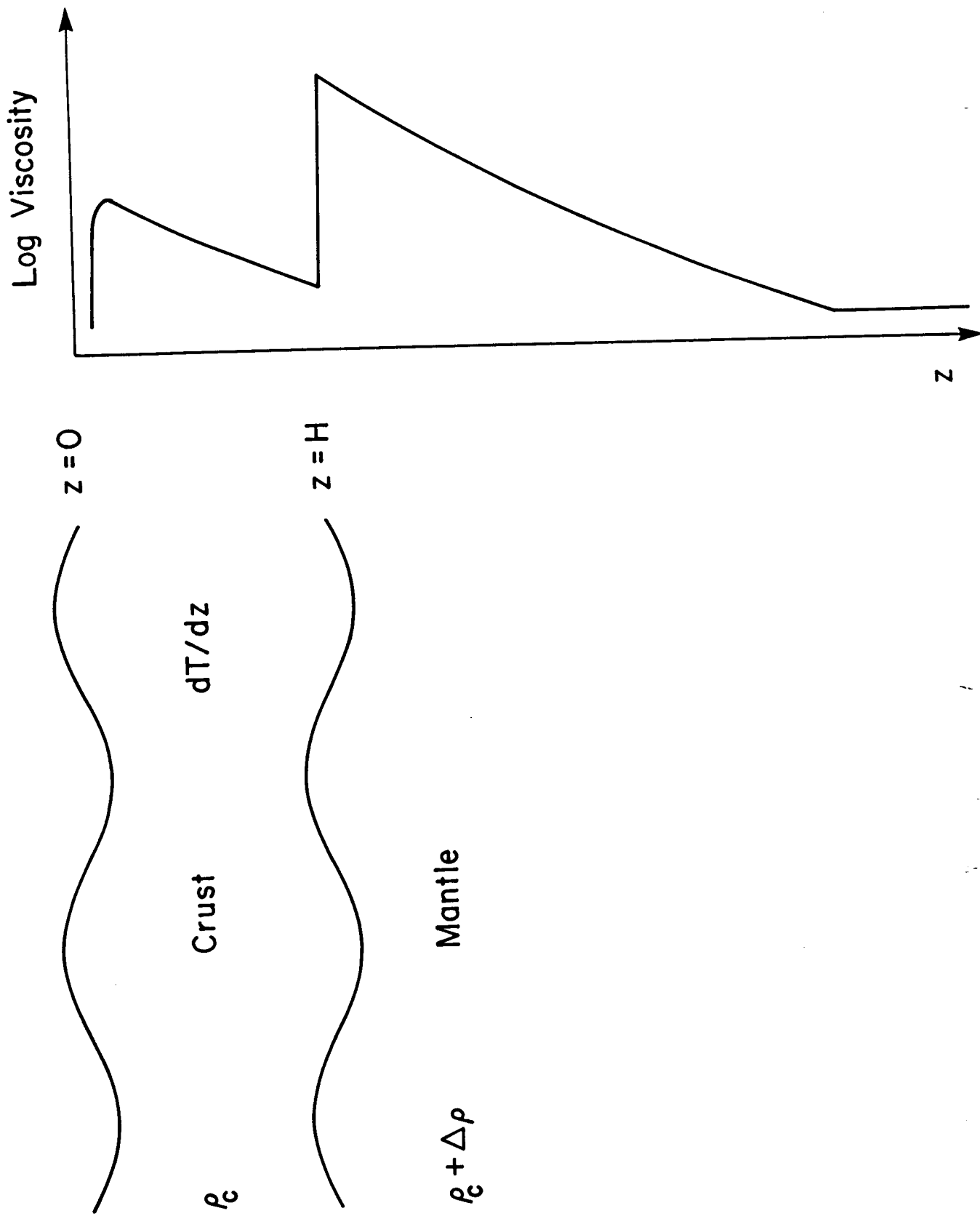


Figure 3.A1

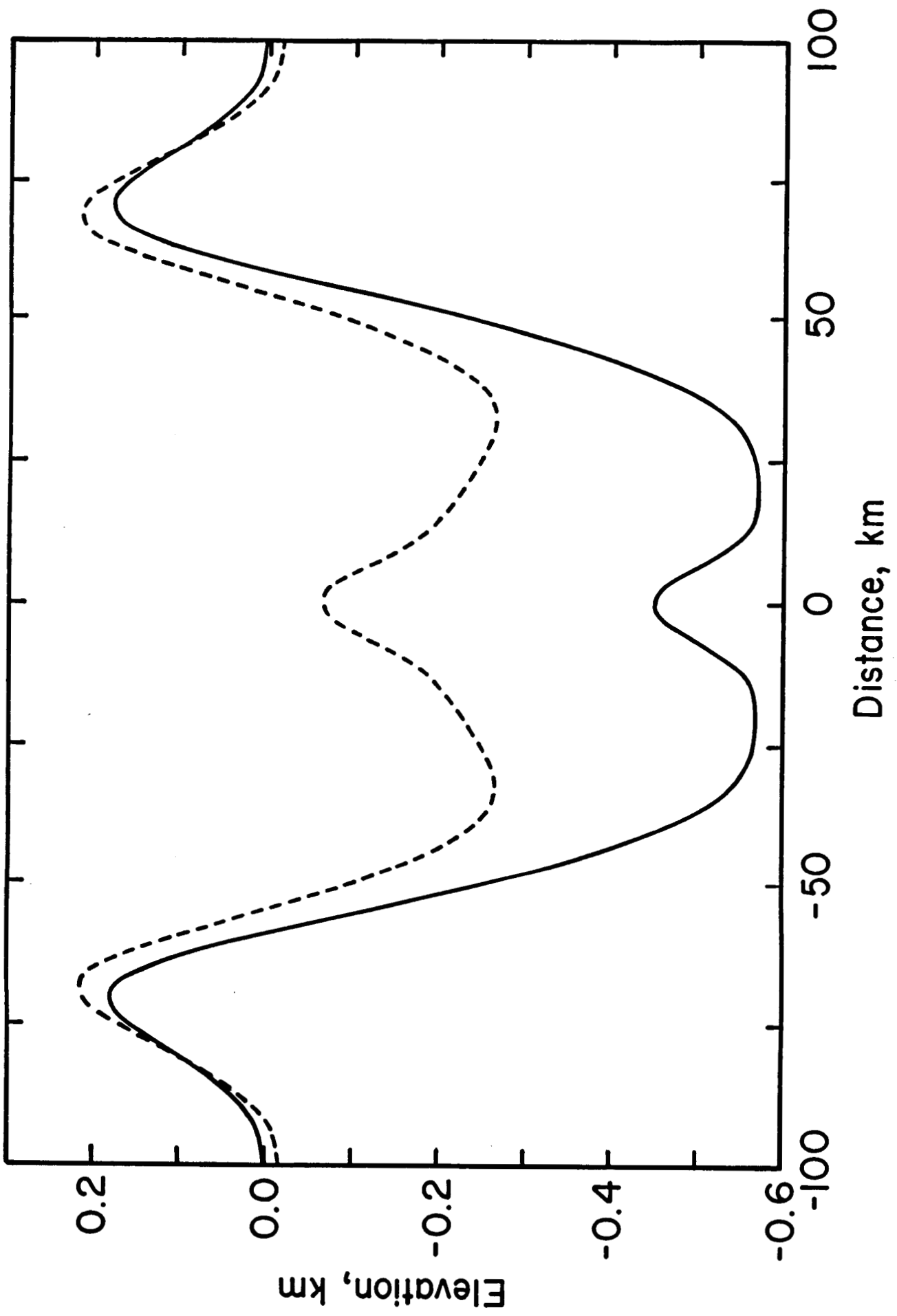


Figure 3.B1

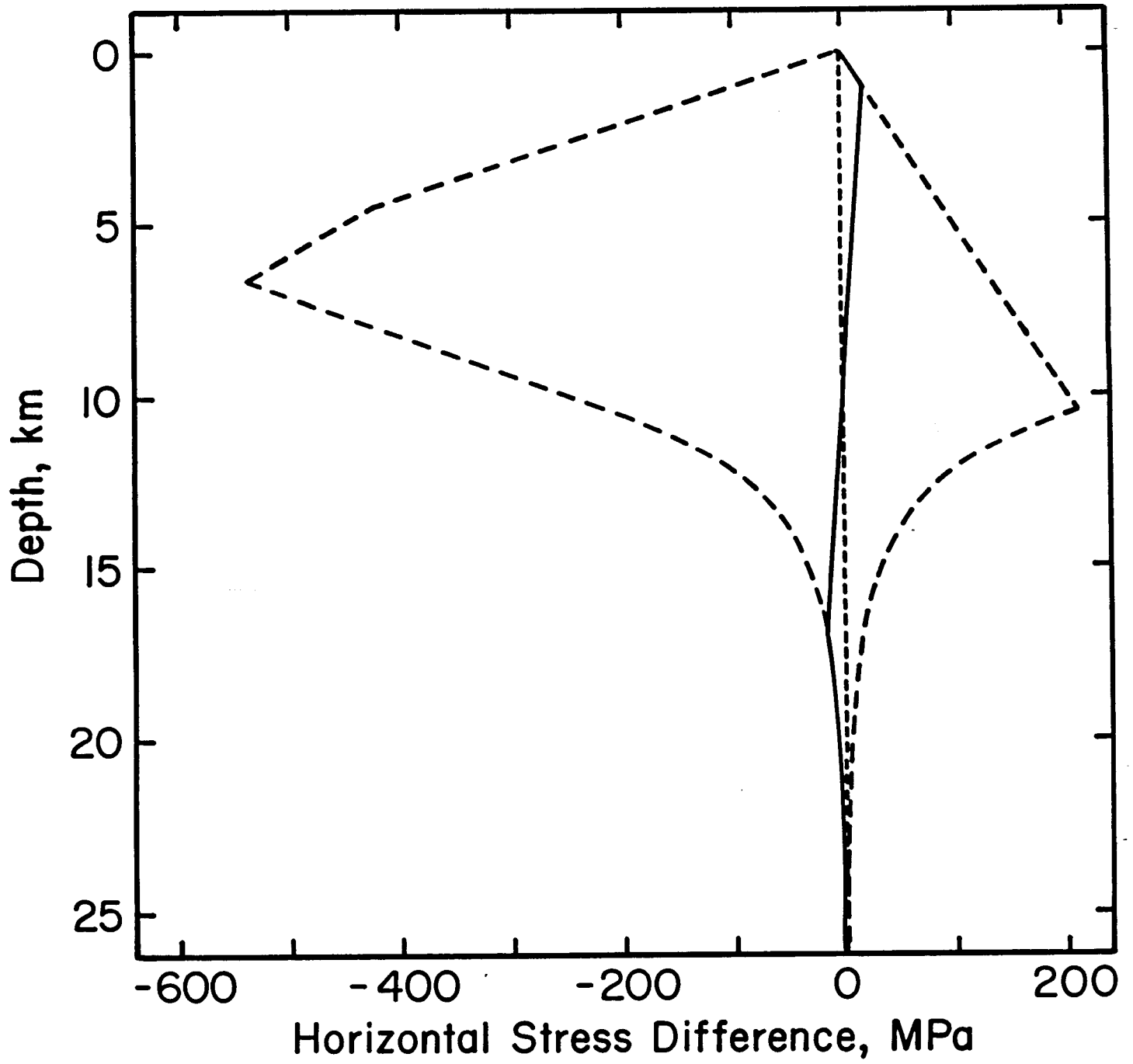


Figure 3.B2

CHAPTER 4:

**TESTS OF CRUSTAL DIVERGENCE MODELS
FOR APHRODITE TERRA, VENUS**

INTRODUCTION

Aphrodite Terra plays a key role in the geology of Venus. It is the largest highland region on the planet, stretching nearly 15,000 km in length [Pettengill *et al.*, 1980]. Aphrodite Terra together with Beta Regio and its extensions constitute the equatorial highlands, which stand out on the basis of their rough, elevated topography, large free air gravity anomalies, and volcanic and rift structures inferred from radar observations [Masursky *et al.*, 1980; Phillips *et al.*, 1981]. Recently-mapped features in Aphrodite include an organized pattern of lineaments [Crumpler *et al.*, 1987] and elements of topographic bilateral symmetry [Crumpler and Head, 1988a] in a direction parallel to these lineaments.

Upwelling of mantle convective flow is a likely explanation for most of these observations, but the planform of this convection and its interaction with the surface is unresolved. Many workers [Phillips and Malin, 1983; Morgan and Phillips, 1983; Banerdt, 1986; Kiefer *et al.*, 1986] have proposed mantle-plume and hotspot models, from inferences that topography is maintained by mantle convection and that regional tectonics are largely vertical with little lateral strain. Head and Crumpler [1987], however, have suggested that Aphrodite is a divergent plate boundary, on the basis of geological evidence for horizontal displacements over several thousand kilometers.

In this paper, we first review the characteristics of Aphrodite Terra and their relation to these tectonic models. We suggest an additional model in which linear upwelling and divergence of mantle flow is accommodated at the surface by distributed, nonrigid deformation. We undertake several quantitative tests of evidence proposed to support the rigid-plate model, namely, that the lineaments, inferred to be fracture zone traces, are organized in a geometrical pattern that may

be interpreted in terms of plate kinematics, that the topography is consistent with a diverging, cooling thermal boundary layer, and that a regional topographic bilateral symmetry exists. Since terrestrial analogy is an important part of the plate-divergence hypothesis, we perform the same tests on the Mid-Atlantic Ridge, restricting our information to a level comparable to that for Venus. We examine the implications of these tests for the other models as well, and we suggest observations from the planned Magellan mission that will lead to the resolution of these competing hypotheses.

CHARACTERISTICS OF APHRODITE TERRA

Regional elevations exceeding 2 km above the mean planetary radius are restricted to the three principal highlands of Venus: Ishtar Terra, Beta Regio, and Aphrodite Terra [*Masursky et al.*, 1980]. Aphrodite and Beta may be distinguished from Ishtar on the basis of their smoother overall topography, larger free-air gravity anomalies, and a predominance of tectonic features of inferred extensional origin (see below).

Aphrodite Terra consists of three mountainous plateaus (Ovda, Thetis, and Atla Regiones) and intervening equatorial terrain between longitudes 50° and 210° (Figure 4.1). Thetis and Atla are connected by a broad saddle which is dissected by numerous troughs and ridges; we refer to this region as east-central Aphrodite. The principal tectonic elements of Aphrodite are linear to arcuate troughs, or chasmata, often flanked by asymmetric ridges, which broadly resemble terrestrial rift valleys. Groups of aligned paired troughs and ridges become clearly resolvable in Pioneer Venus (PV) altimetry over length scales of several hundred kilometers, and arcuate troughs and ridges range up to several thousand kilometers in length

and several kilometers in depth [McGill *et al.*, 1983]. The largest of these features occur on the southern flanks of Ovda and Thetis Regiones and in east-central Aphrodite. The single largest trough, Artemis Chasma, is perhaps the most anomalous, in that it is strongly curved, extending over 210° of arc. Chasmata are also observed in the Beta-Phoebe region; detailed analysis of this area from Pioneer Venus [McGill *et al.*, 1981], Arecibo [Campbell *et al.*, 1984] and limited Venera 15/16 data [Stofan *et al.*, 1987] suggests that these features are graben and therefore the result of extensional stresses.

In addition to the ridge-and-trough systems, two other classes of potential tectonic features that may be related to the evolution of the equatorial highlands have been described by Masursky *et al.* [1980]. The first includes lineaments and scarps associated with highlands that may indicate terraced block faulting, such as a series of radar-bright and dark bands on the northwest margin of Ovda. The second consists of linear "disturbed zones" of modest topographic relief (several hundred meters) that are rough at radar wavelengths; such zones link Atla Regio to Beta Regio and Themis Regio. The association of these disturbed zones with troughs lead Schaber [1982] to infer an extensional origin for them as well. Schaber further proposed that elevated regions (Beta, Phoebe, Atla) are located at sites of weakened lithosphere at the intersections of major zones of lithospheric disruption.

Long-wavelength gravity and topography are correlated on Venus [Phillips *et al.*, 1979]. This correlation is strongest for Atla and Beta Regiones, and weaker for Ovda and Thetis Regiones [Sjogren *et al.*, 1983]. Indeed, there appears to be a progressive variation in the gravity signature from Ovda to Atla, manifested by an increasing apparent depth of isostatic compensation across this region [Herrick

and Bills, 1988].

Phillips et al. [1981] analyzed the trade-off between flexural and crustal (Airy) compensation in western Aphrodite and found that static support of relief requires either an elastic lithosphere several hundred kilometers thick or a crustal thickness compensation depth of about 100 km. If heat production in the Venus interior is comparable to that of Earth, high temperatures at these depths lead to solid-state creep and relaxation of stress and topography for both cases. *Phillips et al.* [1981] concluded either that the crust and upper mantle of Venus are depleted in heat-producing elements or that the topography is young or maintained by interior convective flow.

Others have sought to explain the observed topography by density variations within the mantle. *Morgan and Phillips* [1983] found that 99% of the topography of Venus could be explained by a hotspot model in which relief is primarily generated by thermal uplift due to lithospheric thinning, supplemented by volcanic construction. *Banerdt* [1986] presented a model that matches topography by variations in upper mantle density and crustal thickness and which explicitly satisfies the observed gravity field. He concluded that uplift by low-density mantle is generally required to produce tensional stresses normal to the strike of troughs in Aphrodite and the disturbed zones joining Aphrodite to Beta and Themis Regiones. *Banerdt* [1988] also argued that these density differences are too deep to be statically maintained and therefore must be caused by temperature variations associated with mantle convection. Within Aphrodite itself, a thicker crust and lesser mantle density anomaly (presumably the result of a cooler upper mantle) are required under this model for Ovda Regio than elsewhere.

The dynamic support of topography (i.e., including a component of support by

normal stresses induced by upward mantle flow) by mantle plumes on Venus has been investigated by *Kiefer et al.* [1986] and *Kiefer and Hager* [1987]. They found that models without an upper-mantle low-viscosity zone allowed stronger coupling of convective stresses to the lithosphere, producing geoid anomalies and topography comparable to those observed in the equatorial highlands. *Kiefer and Hager* [1987] further suggested that the comparatively smaller geoid anomaly at Ovda Regio is due to a hotter upper mantle and a better-developed low-viscosity zone, leading to a smaller admittance and apparent depth of compensation. *Robinson et al.* [1986] described a similar effect for terrestrial mid-plate swells, wherein an upper-mantle low-viscosity zone could explain apparent depths of compensation within the lithosphere. These analyses suggest both that the mantle actively contributes to topographic support and that lateral variations in the style of support exist across Aphrodite.

Recent detailed geological mapping of Aphrodite Terra has suggested two new classes of tectonic features. From Pioneer Venus orbital radar altimetric and imaging maps and from Arecibo radar altimetric profiles, *Crumpler et al.* [1987] mapped a series of parallel linear structural discontinuities in Ovda and Thetis Regiones, termed "cross-strike discontinuities", or CSDs, which are up to several thousand kilometers in length and show an approximately constant NNW strike, at high angles to the general trend of Aphrodite. Mapping of additional CSDs, extending through east-central Aphrodite, was reported by *Crumpler and Head* [1988b]. A strong bilateral symmetry across Aphrodite Terra parallel to the strike of the CSDs was noted by *Crumpler and Head* [1988a], not only in the broad shape of the highland but also in individual topographic elements to the north and south. Assembling the centers of symmetry over many profiles, *Crumpler and Head*

argued that these centers were organized along a series of linear, offset segments. The system of CSDs and linear centers of topographic bilateral symmetry as suggested by these authors is shown in Figure 4.2.

TECTONIC MODELS FOR APHRODITE TERRA

We describe three models for the tectonics of Aphrodite Terra and its interaction with mantle convection. Vertical tectonics will dominate if little horizontal surface displacement results from an upwelling mantle flow. Rigid-plate divergence is the appropriate description if shear strain from large horizontal displacements is accommodated only in narrow deformation zones. Alternatively, such strain could be broadly accommodated if the lithosphere is thin and easily deformed. We refer to these models as vertical tectonics, plate divergence, and distributed deformation, respectively (Figure 4.3). Specific predictions of these models are given below.

Vertical Tectonics

If divergence of upward mantle flow is not strongly coupled to the surface, predominantly vertical tectonics will result. Individual mantle plumes beneath Ovda, Thetis, and Atla Regiones can account for their approximately circular topographic plan [Kiefer *et al.*, 1986], and no link to global tectonics is required. Axisymmetric plumes do not adequately account for the east-west orientation of chasmata, however, unless individual plumes are contemporaneous, so that a regionally coherent north-south orientation of extensional stress may develop. In this situation, there may be little difference between a chain of simultaneous, linearly aligned plumes and a linear zone of upwelling appropriate to the alternative models.

The consistent orientation of the CSDs (nearly normal to the trend of Aphrodite) also cannot be explained by widely separated plumes. Even for a linear upwelling, the great lateral extent of the CSDs implies that horizontal strains exist to distances of several thousand kilometers from the topographic axis of Aphrodite Terra. Although it is possible that topographically-induced stresses may be transmitted to such distances [e.g., *Bindschadler and Parmentier, 1987*], such stresses should produce compressional features oriented approximately parallel to the highland trend and not nearly perpendicular features, as observed for the CSDs.

If upwelling occurs along linear zones, then the divergence and cooling of new lithosphere can lead to subsidence of topography. Because the surface is decoupled from the interior in the vertical-tectonics model, however, the thermal structure will differ from that in cases where the surface is part of a plate, e.g., terrestrial oceanic lithosphere. This in turn will lead to large departures from the form of topography expected from a thermal boundary layer (see below).

Plate Divergence

The CSDs are the principal geological indicator of large-scale horizontal motion in Aphrodite. *Crumpler et al. [1987]* found that the pattern of CSDs was consistent with either regional strike-slip faults or oceanic fracture zones, but they favored the latter interpretation on the basis of the parallelism and great length of the CSDs. *Crumpler and Head [1988a]* mapped individual elements of topographic bilateral symmetry along profiles parallel to the CSDs, and they suggested that these smaller topographic features were created at the divergent plate boundary and subsequently rifted and separated.

As additional support of the plate-divergence hypothesis, *Head and Crumpler*

[1987] argued that the long-wavelength relief of Aphrodite Terra is consistent with divergence, cooling and subsidence of newly created lithosphere. For a constant rate of divergence, topographic subsidence away from the rise crest should be proportional to the square root of distance x [e.g., *Parsons and Sclater*, 1977]. Evidence for such thermal boundary layer topography on Venus was examined by *Kaula and Phillips* [1981]. On a broader scale, they found that the equatorial highlands satisfied two out of four important criteria for plate tectonics; namely, that the rises were predominantly concave upward and rose above a broad reference plain of little topographic variation. However, Kaula and Phillips concluded that these highlands do not have a well-defined maximum elevation, nor do they form a globally interconnected system, in contrast to Earth's mid-ocean ridges. The first of these results may not be a valid argument against the plate-divergence hypothesis if there are variable contributions to topography from dynamic support or crustal thickness variations. The second argument, however, remains a serious objection to the model, as other plate boundaries integrating Aphrodite into a global system have not been identified. On the basis of thermal boundary-layer scaling arguments, *Kaula and Phillips* [1981] predicted that topographic relief at divergent margins on Venus should be about 40% that of Earth's mid-ocean ridge elevations. The equatorial highlands have relief in excess of 4 km with respect to the mean elevation, in disagreement with this prediction by a factor of two or more. In addition to the possible variations in relief just mentioned, this result depends on the proportionate scaling between Earth and Venus of heat sources that limit the thickness of the boundary layer and amount of subsidence. Greater relative cooling and thickening of the thermal boundary layer on Venus, and greater relief than that predicted by Kaula and Phillips, cannot be ruled out. We return to these

issues in the discussion of thermal boundary layer topography below.

The chasmata do not play an important role in the plate-tectonic model outlined by *Crumpler and Head* [1988a], in spite of the great size and geographic extent of these features. The linear centers of crustal divergence defined by these workers generally do not coincide with the principal chasmata. However, this is not necessarily evidence against the model, as the orientation of the chasmata is generally perpendicular to the inferred direction of plate divergence, and horizontal extensional stresses may be expected for this high-standing region.

Distributed Deformation

Phillips [1986] analyzed the coupling of convective tractions to a thin lithosphere and concluded that such stresses could reach .1 kbar and lead to tectonic deformation. Under the distributed-deformation model, then, CSDs may represent flowlines indicating the planform of underlying mantle convection. As in the plate model, the east-west orientations of the chasmata are consistent with a linear axis of upwelling and divergence, but topographic stresses may also contribute to their formation. A thermal boundary-layer component of topography should also be present, although the apparent rate of spreading would apply largely to the underlying mantle and not necessarily to the spreading rate, if any, of the surface. Moreover, near-surface thermal structure differing from a simple cooling boundary layer could also lead to departures from the \sqrt{x} subsidence of topography. Because surface deformation is not required to be spatially coherent, the global interconnection of tectonic features need not be as strongly developed as under the plate-tectonic model.

TESTS OF TECTONIC MODELS

If the CSDs are analogs of terrestrial fracture zones, then they provide strong geometrical constraints on plate motion. The portions of CSDs offsetting adjacent linear centers of bilateral symmetry represent transform faults under the plate-tectonic hypothesis and must follow small circles about an appropriate rotation pole, and the distal traces of CSDs, representing inactive fracture zones, can yield information on past motions. If more than two plates exist, then one or more triple junctions must also be present, and additional plate boundaries must be identified. Because there is no evidence to support a ridge or trench intersection with Aphrodite proper, the most likely such boundary would be a fault zone, presumably one of the mapped CSDs. Transform motion would probably dominate, although some extension or compression most likely would also occur across the boundary. Under nonrigid divergence, CSDs need not satisfy the same criteria as do fracture zones. Our first test then, is to examine the CSDs from the perspective of plate kinematics.

Provided that thermal contributions to isostasy dominate at wavelengths of less than a few thousand kilometers, the plate-divergence model should show relief that falls off approximately with the square root of age. Furthermore, rigid-plate rotations constrain these velocities to vary regularly with position along the plate-boundary distance.

The thermal boundary-layer tests of *Kaula and Phillips* [1981] centered on the differences in the distribution of apparent rise heights on Earth and Venus; they calculated apparent spreading rates as a function of the deviation of individual rise crests from the modal rise height under varying definitions. The variation of apparent spreading rate with distance from the rise crest and under conditions of

restricted uncertainty in the topography were also tabulated. As mentioned above, however, and discussed in detail below, rise height may not be a particularly diagnostic guide to the thermal boundary layer contribution to topography. Given the specific plate-divergence scenario proffered by *Head and Crumpler* [1987], it is appropriate to extend the analysis of Kaula and Phillips. Our second test is to perform least-squares fits of topography versus the square root of distance along the spreading direction indicated by *Crumpler and Head* [1988a]. We test the goodness of fit by geographic location, both as a function of distance away from the rise axis and position along the axis. These tests follow from suggestions by Crumpler and Head that regions away from the Ovda and Thetis plateaus, such as the rolling plains to the north and south or the saddle-shaped region of east-central Aphrodite, may show a stronger thermal boundary layer signature.

Lastly, we test the bilateral symmetry of topography at short wavelengths by a cross-correlation technique, as such relief could support a plate-divergence model [*Crumpler and Head*, 1988a]. On Earth, magnetic lineations have been the primary signature of symmetric spreading [e.g., *Vine*, 1966], although a preliminary catalog of potentially rifted and separated topography has been compiled by *Crumpler and Head* [1988c]. It is important, therefore, to examine this question for the terrestrial seafloor as well.

PLATE KINEMATIC TESTS

By Euler's theorem, the relative motion of two rigid plates on the surface of a sphere may be described by a rotation about an axis passing through the center of the sphere [*Bullard et al.*, 1965]. The intersection of the axis of instantaneous relative angular velocity with the planetary surface is known as the Euler pole.

Because transform faults follow small circles about this pole, a single best-fitting Euler pole may be calculated by minimizing χ^2 [LePichon, 1968]:

$$\chi^2 = \sum_{i=1}^N \frac{(\zeta_i - \zeta_{oi})^2}{\sigma_i^2} \quad (4.1)$$

where ζ_i and σ_i^2 are the azimuth and its uncertainty for the i^{th} transform fault, and ζ_{oi} is the azimuth of a small circle about an Euler pole at latitude λ_0 and longitude ϕ_0 . In practice, a search over all (λ_0, ϕ_0) is used to find the minimum value of χ^2 , and formal errors corresponding to different values of χ^2 may be assigned following standard statistical methods [e.g., Press *et al.*, 1986].

If the relative position of the Euler pole and the plate boundary does not change with time, then fracture zones should follow the same small circles as do transform faults. On Earth, however, it is well documented that Euler poles do migrate relative to the plate boundary over time scales of millions of years. We therefore compute an instantaneous Euler pole using only the segments of CSDs located between offset linear centers of bilateral symmetry (Table 4.1). The calculated Euler pole lies at $20 \pm 3^\circ\text{N}$, $204 \pm 17^\circ\text{E}$. Because of the fewer number of CSDs in east-central Aphrodite and their larger location errors, the Euler pole position is fixed largely by the CSDs in Ovda and Thetis Regiones. Figure 4.4 shows the location of this Euler pole in relation to the Aphrodite system of CSDs and symmetry centers, along with level curves for one and two standard deviations. Small circles about the Euler pole are concave to the northeast in eastern Aphrodite and to the southwest in western Aphrodite. This is a consequence of a pole location approximately 90° from the center of the CSD system, which in turn is

due to the fact that the CSD traces are all nearly parallel in Mercator projection.

The geometry of the CSDs in relation to the best-fitting Euler pole is further elucidated by examining CSD geometry in a spherical coordinate system about the Euler pole (Figure 4.5). Small circles about the Euler pole now appear as lines of latitude in this projection, and lines of longitude are great circles passing through the Euler pole. The linear centers of topographic bilateral symmetry fall approximately along lines of longitude for Euler latitudes 40°S to 35°N. Within this latitude range, CSD segments within about 30° of the axes of topographic symmetry tend to follow parallels. The CSDs display increasing curvature, however, at larger Euler latitudes. The opposing curvature of CSDs on the same side of the axis of topographic symmetry is evidence against a single, fixed Euler pole, as movement of rigid lithosphere cannot be geometrically accommodated at increasing distances from the rise axis. A single Euler pole fixed with respect to the plate boundary over the age of the CSDs may therefore be rejected. We examined the effect of uncertainties in CSD strikes on this result by posing a *t* test for the deviations of CSD azimuths from lines of latitude in the Euler-pole projection. For CSD segments greater than 20° distant from both the Euler equator and from the nearest linear center of topographic bilateral symmetry, the inward curvature may be resolved at greater than 95% confidence. This conclusion may not be valid, however, if there is some systematic, rather than random, measurement error.

It is not unreasonable that a single, fixed Euler pole should not match the observed CSD traces, simply given their size and probable age. The Aphrodite system of linear centers of topographic bilateral symmetry is over 12,000 km in length. By comparison, the longest plate boundaries on Earth are less than 10,000 km long. In particular, $\chi^2 = 0.07$ for the best-fitting Euler pole above; a similar test

on the Atlantic Ocean basin using 13 transform faults between latitudes 52°N and 30°S with offsets exceeding 1° yielded a pole at $55 \pm 12^\circ$ N, $328 \pm 2^\circ$ E, and $\chi^2 = 0.08$, assuming measurement errors comparable to those found for the CSDs. In reality, the Atlantic system includes four major plates whose speed and direction of movement have varied over time.

The next simplest model is a single rotation pole, but with time-dependent motion with respect to the plate boundary. On Earth, for example, migration of the pole with respect to the Mid-Atlantic Ridge (MAR) in the late Mesozoic and early Cenozoic has imparted a broad sigmoidal shape to fracture zones on either side of the MAR [e.g., *Klitgord and Schouten, 1986*]. If changes in the location of the pole for a two-plate system in Aphrodite have occurred, then all fracture zones on one side of the ridge system should show a shift in azimuth in the same sense, and the shifts on the opposite side should be in the opposite sense. The opposing curvature of CSDs on the same side of the axis of topographic symmetry in Figure 4.5 argues against a single Euler pole, regardless of whether it migrates with respect to the plate boundary over time or not.

The lack of Pioneer Venus radar images further to the east (in Euler coordinates) precludes consideration of more complicated multiple-pole, time-dependent models. Although such models cannot be tested quantitatively on the basis of the data considered here, any scenario would require a separate pole for each few CSDs, or else poles in a system of several plates would have to be adjusted continuously with time in order to maintain the fairly constant strike of the CSDs as portrayed in Mercator projection. The former scenario may probably be ruled out because it implies that each CSD is a plate boundary and would lead to plates that are very long in the spreading direction compared with the length of the

divergent boundary; stresses on such a "ribbon" plate would most likely break it into smaller, more equidimensional pieces, leading to more distributed deformation. Therefore, if the plate-divergence model holds, the Aphrodite system must be limited to only a few plates and Euler poles must move with respect to plate boundaries over time to maintain the nearly-linear traces of the CSDs. We predict additional features of such a geometry in a later section.

SELECTION AND PROCESSING OF TOPOGRAPHIC DATA

Some preliminary processing of topographic data is necessary prior to conducting tests for thermal boundary layer topography and bilateral symmetry. Each test of topographic characteristics of Aphrodite Terra is matched by an equivalent test of the MAR; the latter data are restricted to Pioneer Venus resolution by the following approach. There are nearly 20,000 individual PV radar altimetric measurements over the greater Aphrodite area (approximately 130×10^6 km²) depicted in Figure 4.1 [*Pettengill et al.*, 1980; *Ford*, 1986], corresponding to a mean spacing of ~ 80 km. The geometric mean of the along- and cross-track dimensions of PV altimeter footprints at typical altitudes over Aphrodite is ~ 25 km. The terrestrial DBDB5 data set [*U.S. Naval Oceanographic Office*, 1985] consists of topographic and bathymetric data interpolated every 5' of arc, which may be considered equivalent to an 8 km footprint and spacing at 30° latitude. It is appropriate, therefore, to decimate these data by sampling one 15'x15' square out of each square degree to simulate the coverage and resolution of Pioneer Venus.

We examined the elevations along 38 profiles across Aphrodite and 35 profiles across the MAR. For Aphrodite, the traces of these profiles are taken perpendicular to the linear centers of topographic bilateral symmetry and follow great-circle paths

approximately parallel to the CSDs (Figure 4.6). Profile centers are spaced approximately 200 km apart (Table 4.2) and are taken no closer than about 150 km to CSDs. All data within 100 km of the profile trace are used; therefore near-contiguous coverage of Aphrodite Terra away from CSDs is afforded. For the Atlantic, profile centers were also spaced at approximately 200 km intervals along the mid-ocean ridge (Table 4.3) and were taken no closer than about 150 km from large-offset ($>1^\circ$) transform faults. This offset length was chosen on the grounds that such transforms might be recognized at a resolution for Earth comparable to that available on Venus. The terrestrial profiles approximately follow fracture zone traces [Klitgord and Schouten, 1986; Cande et al., 1988] and appear curved because of changes in plate motion (Figure 4.7). A few short profiles in the equatorial and northern Atlantic follow small circles about the instantaneous two-plate rotation pole [Minster and Jordan, 1978]. The mean length of the MAR profiles is 1500 km in each direction from the ridge.

The Venus profiles are taken to a distance of 3600 km in each direction, comparable to those shown by Crumpler and Head [1988a] and extending slightly beyond the mapped length of the CSDs. Because continents play no role in the plate-divergence model for Aphrodite Terra, terrestrial profiles are truncated where they intersect continental rises or oceanic plateaus with continental basement. No such constraints are imposed on any profiles crossing seamounts or mid-plate swells, for which plausible analogs may exist on Venus, regardless of any plate-tectonic environment.

For the analysis of boundary-layer topographic characteristics, all data within the 200-km-wide profile swath are taken to correspond to the distance of the nearest point on the profile trace. For the cross-correlation approaches used to test

bilateral symmetry, data gridded at regular intervals are required. We used a 100-km grid spacing, comparable to the typical measurement spacing of the PV altimeter. For each grid point, elevation measurements within 100 km were averaged after weighting by the inverse squared distance. The inverse square form is appropriate for the case of sample (footprint) sizes smaller than the observation spacing because it strongly favors nearby observations but will include distant observations if no nearby observations are available. The topographic profiles so constructed for Venus are shown in Figure 4.8, and those for Earth are given in Figure 4.9.

TESTS FOR THERMAL BOUNDARY-LAYER TOPOGRAPHY

A divergent thermal boundary layer may contribute to relief under any of the models discussed here, but its form is best known for the plate-divergence model. On Earth, the variation of seafloor depth with age has been attributed to the cooling of spreading oceanic lithosphere. Two alternative models exist for the form of this cooling and differ in their predictions for the depth of old seafloor. *Turcotte and Oxburgh* [1967] described the thickening of the lithosphere as the thermal boundary layer of a mantle convective system. Since this boundary layer is formulated in terms of a conductively cooling halfspace, it grows in proportion to the square root of distance x until a zone of downwelling is reached. Subsidence is also proportional to \sqrt{x} . In the alternative plate model [*McKenzie*, 1967; *Parsons and Sclater*, 1977] the thickness of mature lithosphere is limited by some constant upper mantle temperature; the plate grows asymptotically to a maximum thickness determined by this temperature. Since early cooling resembles that of a halfspace, subsidence is initially proportional to \sqrt{x} , but older seafloor subsides more slowly,

decaying exponentially to a constant depth [*Parsons and Sclater, 1977*]. This depth is about 6400 m, and terrestrial seafloor elevations e given herein are measured relative to this datum. Where seafloor age is known as a function of distance, the variation of seafloor depth may be predicted to well within the 300-400 m accuracy of regional bathymetric measurements, after correcting for any sediments and their isostatic adjustment [*Parsons and Sclater, 1977*].

We use elevation-distance measurements to infer average apparent spreading rates, employing the inner asymptotic solution for the \sqrt{x} subsidence of diverging, cooling lithosphere given by *Parsons and Sclater* [1977]. Where this approximation is valid, it may apply to either the thermal boundary layer or plate models, and so the limits to this form when applied to Venus, if any, must be evaluated. There are two potential reasons for deviation from this relation: a limiting plate thickness and other sources of topography.

On Earth, the exact cause of a limiting plate thickness is not completely understood. *Parsons and McKenzie* [1978] interpreted the departure from a \sqrt{x} relation at approximately 70 m.y. in terms of convective instability at the base of the lithosphere, leading to small-scale convection and to the supply of additional heat. However, *Buck* [1985] has concluded from temperature-dependent viscosity models that small-scale convection may develop much earlier than inferred by *Parsons and McKenzie* from constant-viscosity models. An implication of this result is that the flattening of the depth-age curve must have another cause. Other mechanisms have been proposed, such as internal heating [*Forsyth, 1975; Jarvis and Peltier, 1982*] or shear heating [*Schubert et al., 1976*]; indeed, *Heestand and Crough* [1981] contend that the depth-age flattening is an artifact of including hotspot traces in averages of seafloor depth at large age.

Nevertheless, if the age at which such flattening occurs decreases as the thickness of the lithosphere decreases, then the thinner lithosphere expected for Venus [Kaula and Phillips, 1981] should lead to departures from a \sqrt{x} subsidence at a younger age than on Earth. Deviations of terrestrial seafloor depth from the \sqrt{x} prediction that exceed the measurement errors do not occur until ~ 100 m.y. If comparable deviations occur for Venus at earlier ages, then this value will be an upper limit to the validity of the \sqrt{x} relation. The distance corresponding to 100 m.y. age is just 100 times the apparent spreading rate in mm/y. We emphasize that this limit is only a guide, as there is no firm evidence to reject the notion that the Venus lithosphere could cool and thicken beyond this age. Moreover, even if a flattening of depth versus age is observed over some interval to which a \sqrt{x} fit is applied, there is no reason to reject the thermal boundary layer model. Instead, we know only that a nonlinear inversion of height versus distance using the the full plate model or its exponential outer asymptotic solution will lead to a *smaller* spreading velocity. We conclude that, at worst, the \sqrt{x} fit will lead to an overestimate of the spreading rate if a finite plate thickness is achieved over the length of the profile.

For convenience, we measure elevations relative to the mean radius of Venus, although this may yield underestimates of the thermal boundary-layer relief if lowland regions with elevations of 1 km or more below the mean represent lithosphere that has further cooled and subsided. Any such discrepancy between the predicted maximum rise elevation of 1.5 km [Kaula and Phillips, 1981] and a greater observed relief using this datum therefore will be a minimum value.

The second and potentially more serious source of error is the contribution to topography from sources other than the boundary-layer form of thermal isostasy. Two such causes of topography are crustal thickness variations and dynamic uplift.

Another possibility which could lead to large departures from a \sqrt{x} relation is one in which thermal isostasy is the dominant mechanism of support, but the thermal structure is different from that expected for a simple boundary layer. Such situations could arise for both the vertical-tectonics and distributed-deformation models, wherein an overlying lid is largely decoupled from underlying flow or the lid moves at a velocity differing from that of the convective cell. Any of these factors could lead to the rejection of the hypothesis that a thermal boundary layer dominates the topography.

Assuming that the spreading half-rate v is constant, the model equation relating distance x to elevation e for a spreading thermal boundary layer is

$$e = e_0 - \delta (x/v)^{1/2} \quad (4.2)$$

where $\delta = 350 \text{ m (m.y.)}^{-1/2}$ for Earth [Parsons and Sclater, 1977] and is expected to be about $180 \text{ m (m.y.)}^{-1/2}$ for Venus [Kaula and Phillips, 1981]. For Earth, we have performed least-squares fits to distances of 600 km and to the maximum length of individual profiles, solving for both e_0 and v . The former distance is chosen to lie within the known validity of the \sqrt{x} subsidence for the MAR. For Venus, 600, 1500, and 3600 km intervals are used. The first two are chosen for comparison with Earth, where the 1500 km length corresponds to the mean length of the terrestrial profiles. The 3600 km interval spans the full topographic profiles across Aphrodite.

Figure 4.10 shows several examples of such fits to terrestrial and venusian elevations. The fit to 600 km distance in Figure 4.10a, for profile 18 in the central north Atlantic, yields a good fit (the coefficient r of linear correlation is -0.8), and the rms residual topography σ is modest (400 m). The spreading rate inferred from this

model is 16 ± 2 mm/y, in good agreement with the observed range of values over the past 80 m.y., 14 - 24 mm/y [Klitgord and Schouten, 1986]. When the fit is taken to 2000 km, a higher σ (500 m) and v (38 ± 3 mm/y) are found, because of the departure of subsidence from the \sqrt{x} form for old seafloor and from contributions to topography from processes unrelated to the divergent thermal boundary layer (here, the Bermuda and Cape Verde rises). The residuals are uncorrelated with distance, except where the ends of the profile cross these rises.

Similar fits to profile 30 in the South Atlantic are given in Figure 4.10b. The regression to 600 km distance yields $v = 27 \pm 3$ mm/y with $r = -0.82$, and $\sigma = 300$ m, and at 1600 km distance $v = 17 \pm 1$ mm/y, with $r = -0.88$, and $\sigma = 400$ m. In this example the apparent velocity decreases as the fit is taken farther, and the residuals are also uncorrelated with distance.

Several linear regressions for e (\sqrt{x}) are given in Figure 4.10c for profile 9 across central Ovda Regio in Aphrodite Terra. The correlation is poor to 600 km distance ($r = -0.45$), but better fits ($r = -0.84$ to -0.86) are found for $x = 1500$ and 3600 km. The large residual topography (800 m) and strong correlation of residual topography with distance indicates, however, that other processes contribute to the relief. This is not a surprising result, as several authors [e.g., Morgan and Phillips, 1983; Banerdt, 1986; Head and Crumpler, 1987] invoke crustal thickening for Ovda Regio. The apparent spreading velocities are small, 1.5 ± 0.2 and 4 ± 0.3 mm/y for the distance intervals 0-1500 and 0-3600 km, respectively. The corresponding ages of the lithosphere at the profile extrema are 1000 and 900 m.y., respectively; these ages so greatly exceed our 100 m.y. rule of thumb that the \sqrt{x} model certainly may be rejected. Inferred velocities less than 1-4 mm/y raise the question of just how slowly spreading can occur and still be considered plate divergence. A

large apparent velocity (72 ± 49 mm/y) is found for topography off of the plateau (1500-3600 km), and the inferred age of the lithosphere there (~20-50 m.y.) is within the scope of the asymptotic solution used. However, the correlation coefficient is very poor (-0.24) and the residuals are still correlated with x ; the latter effect is due to the dorsae approximately perpendicular to the profile at this distance (see discussion of bilateral symmetry below). Such a correlation suggests that unmodeled processes dominate the topography, for example, crustal thickness anomalies [Crumpler and Head, 1988a] or local thermal basin-and-swell relief [Morgan and Phillips, 1983]. Moreover, it is difficult to reconcile the large differences in apparent spreading rate between the full profile and the distal segment only.

Figure 4.10d displays several fits to profile 29, across Dali Chasma. This region has been suggested by Crumpler and Head [1988a] to be more analogous to a typical mid-ocean ridge than the Ovda and Thetis plateaus. The data are more widely scattered near $x = 0$, yielding poor fits for both 600 and 1500 km distances. A reasonable fit ($r = -0.66$) is found over 3600 km distance, with $v = 41 \pm 6$ mm/y (consistent with model assumptions) and $\sigma = 500$ m. As in the previous example, however, residual topography is strongly correlated with distance. There also appears to be a break in slope at ~ 1500 km distance. Taking just the interval beyond this break (1500-3600 km), small residuals (300 m) are found that are uncorrelated with distance, and $r = -0.79$. However, the apparent velocity is also small (10 ± 1 mm/y), which leads to rejection of a \sqrt{x} relation.

The rms residual topography σ and coefficient of linear correlation r are given in Figure 4.11 for each profile as a function of regression distance interval. Figure 4.11a shows the results of all fits to 600 km distance. The terrestrial data are tightly

grouped with high (negative) r and $\sigma < 400$ m; this interval near the rise crest most clearly shows the characteristic divergent thermal boundary topography. The Venus data, in contrast, are widely scattered at higher residual relief, and many profiles show a *positive* correlation of elevation with distance. In Figure 4.11b, the regressions are extended to 1500 km for Venus, and to the full length of terrestrial profiles, which average 1500 km. The terrestrial data are more scattered than in Figure 4.11a, but most values of σ are less than 500 m and the magnitude of r exceeds 0.5. The Venus points are somewhat less scattered than in Figure 4.11a but still indicate a poorer fit than for Earth.

Figure 4.11c shows the fits to Venus only for distance intervals 0-3600 km and 1500-3600 km. The regressions for distant topography only are nearly as poor as those of Figure 4.11a, so there is no evidence that only the central portions of Aphrodite are dominated by non-thermal boundary layer topography. The fits to the full 0-3600 km interval are the best in terms of r and σ . Figure 4.11d isolates the values of r and σ for east-central Aphrodite alone from Figures 4.11a-c. Here, too, the only consistently good fits are those over the entire 3600 km length of the profiles.

These results are summarized more compactly in Table 4.4. For the Earth, the majority of the variance in the topography (given by r^2) may be explained by the divergent thermal boundary model. Within 600 km of the rise crest, the fits are excellent, σ is small (300 m), and the mean velocity and rise height match the observations well. Over the maximum length of the profiles, a higher rms residual is observed, and the velocities are overestimated due to increasing contributions from processes unrelated to the divergence and cooling of new lithosphere. For Venus, most of the fits to comparable distances are generally poor, with low r and σ

~ 700 m. Over the maximum length of the Venus profiles (3600 km), the 'averaging out' of the blocky, convex profiles of parts of Aphrodite Terra leads to a higher correlation coefficient, but the small mean velocity (< 20 mm/y) indicates that the \sqrt{x} relation is not valid at these distances, and so estimates of v based on the full solution to divergent thermal boundary layer topography would be even smaller. The fits to only the distant half of the profiles are very poor. For east-central Aphrodite alone, regressions over the full profile length show a reasonable correlation coefficient, modest σ , a rise height close to the predicted value, and typical spreading rates of 30-40 mm/y. However, the goodness of fit rapidly degrades for other distance intervals, which suggests that the agreement may be fortuitous.

Under the plate-divergence model the velocities should also show a systematic variation along the plate boundary due to the constraint of plate rigidity. For a specified angular velocity ω between two plates, the velocity v as function of distance Δ from the Euler pole is

$$v = \omega R \sin \Delta \quad (4.3)$$

where R is the planetary radius. From known values of v and Δ , equation (4.3) may be solved by least squares for ω ; this approach depends on knowledge of individual plate boundaries. Figure 4.12 shows the variation of inferred spreading velocity with geographic location; the latter is specified simply by profile identification number, which increases from west to east for Venus and from north to south for Earth. Figure 4.12a gives the results for 0-600 km regressions for the MAR. The spreading rates are in the range of 10-40 mm/y, in broad agreement

with observations. A rotation rate of $0.32^\circ/\text{m.y.}$ was recovered for the North American - African plate rotation by this method, which compares favorably with the observed value of $0.28^\circ/\text{m.y.}$ [Minster and Jordan, 1978]. Such agreement was not found, however, for the North American - Eurasian or South American - African plate pairs; in fact, the apparent velocities decrease instead of increase as Δ approaches 90° . This exercise illustrates that there is some potential to recover approximate relative angular velocities from topographic data alone, but the calculations are unreliable.

Figure 4.12b shows the variation of v with location for \sqrt{x} regressions over the full length of the Atlantic profiles, averaging 1500 km. The inferred spreading rates are larger, in the range of several tens of millimeters per year, due to the flattening of depth with distance for the mature thermal boundary layer and due to other contributions to seafloor relief. Figure 4.12c compares the apparent velocities for Aphrodite to 1500 km distance; in this figure zero velocity indicates a positive correlation of elevation with distance, for which v is undefined. Profiles with apparent velocities undefined or several hundred millimeters per year appear to separate areas with more or less regular spreading rates; inferred values are ~ 2 mm/y in Ovda Regio, 5-10 mm/y in Thetis Regio, and 10-40 mm/y in east-central Aphrodite. Velocities less than 10 mm/y may not be consistent with the \sqrt{x} model over these distances, and therefore even smaller velocities may be inferred for Ovda Regio, and probably for Thetis Regio as well.

Over the full 3600 km interval in Aphrodite (Figure 4.12d), all apparent spreading rates are less than 60 mm/y and show regular variations with location. Again, the slowest velocities in central Ovda and Thetis Regiones are not consistent with the \sqrt{x} form of thermal boundary layer topography. In east-central

Aphrodite, however, v is consistent with model assumptions and appears to increase systematically eastward. Such a variation might be consistent with a rotation pole for the this region alone located somewhere to the southwest of Aphrodite. The Euler pole for all CSD segments in east-central Aphrodite, corresponding to a time-averaged rotation pole applicable to the entire $e(\sqrt{x})$ fit, lies at $23 \pm 10^\circ\text{N}$, $222 \pm 30^\circ\text{E}$, in disagreement with the prediction based on inferred spreading rates. However, given the inability to recover accurately rotation rates from known terrestrial pole positions given above, this result is not conclusive.

In summary, a divergent thermal boundary-layer component to topography cannot be unequivocally resolved in the spreading direction suggested by *Crumpler and Head* [1988a], and so contributions to relief other than those from a thermal boundary layer must generally be dominant. East-central Aphrodite alone is broadly consistent with spreading at $v = 20\text{-}40$ mm/y when averaged over the full profile, but the topography is much rougher than terrestrial analogs, especially near the rise crest. This conclusion does not exclude the plate divergence model, but only indicates that thermal boundary layer topography is not a discriminating criterion.

TESTS FOR TOPOGRAPHIC BILATERAL SYMMETRY

Crumpler and Head [1988a] have described both a broad, long-wavelength symmetry in the shape of Aphrodite and detailed matches of short-wavelength features on either side of the symmetry axis in a direction parallel to the CSDs. This mapping was based on the qualitative identification (i.e., by eye) of individual topographic elements in the Pioneer Venus altimetry. *Crumpler and Head* also tested quantitatively for bilateral symmetry by taking the cross-correlation between

the two sides of the highland, following removal of a best-fitting \sqrt{x} curve. In this section, we apply a more detailed cross-correlation technique to the question of bilateral symmetry across Aphrodite Terra, and we calculate statistical confidence limits for these correlations.

The cross-correlation r between two signals a and b is

$$r = \frac{\sum_{i=1}^N a_i b_i}{\sqrt{\sum_{i=1}^N a_i^2 \sum_{i=1}^N b_i^2}} \quad (4.4)$$

where N is the number of data. If the signals do not have zero mean, then the cross-correlation will always be nonzero. We emphasize that since r is designed to measure the degree of linear correlation between two variables, it is sensitive largely to phase differences without regard to any difference in mean amplitude. For example, a perfect match ($r = \pm 1$) can be obtained between two identical signals differing by a multiplicative factor. In the simplest useful test of correlation, Pearson's r or the coefficient of linear correlation [e.g., *Press et al.*, 1986] is given by subtracting the individual means of a and b before substituting into (4). For a topographic signal, such a test will be sensitive only to the large-amplitude, long-wavelength components and is appropriate for quantifying the broad bilateral symmetry of an elevated region. *Crumpler and Head* [1988a] calculated this cross-correlation for several profiles across Aphrodite and found values in the range 0.79 to 0.94.

In order to test for bilateral symmetry of smaller elements of topography, the long-wavelength components must be removed. *Crumpler and Head* [1988a]

attempted to do so by subtracting the best-fitting \sqrt{x} curve from each profile; however, such functions lead to residual topography that is correlated with distance (see discussion of thermal boundary layer topography above), so it is not unreasonable that Crumpler and Head still found high correlation coefficients (0.65 to 0.95).

One approach to recovering the small-scale topography alone is through spectral filtering. Unfortunately, the different power spectra of Aphrodite Terra and the MAR preclude any simple comparison of phase coherence as a function of wavelength. In particular, the greater proportion of short wavelengths that must be phase-matched at $x = 0$ to form the concave and sharply peaked profile of the mid-ocean ridge, in contrast to the broad and often convex shape of Aphrodite, results in a distinctly higher cross-correlation for the Earth than for Venus. Such problems may be alleviated by beginning the Fourier transform at some distance from the rise crest, but at the expense of a loss of both spatial and spectral information.

Instead, we confine our approach to the spatial domain, and we remove long-wavelength features by detrending the profile in a series of segments or windows. Each window of length L_w contains $N_w = L_w / \Delta x + 1$ points, where Δx is the grid spacing. The best-fitting linear trend is removed, and the cross-correlation (equation 4.4), denoted by r_w , is computed. These windowing operations then yield the variation of the cross-correlation with distance, which allows the recognition of individual symmetric features. We adopt a minimum window size of 600 km, comparable to the size of the smaller features identified as symmetric across Aphrodite Terra by *Crumpler and Head* [1988a]. An alternate size of 1200 km is also analyzed, in order to sample better some larger features also identified

by these workers.

An overall cross-correlation r_p for the entire profile may be calculated from each point on the detrended profile. In order to make the estimate of r_p more robust, and to ensure that any symmetric features are adequately sampled, the windows are overlapped by half their length. In this manner, most of the profile is doubly sampled, and, in effect, a second profile with detrending filters offset by $L_w/2$ is constructed. By weighting the observations inversely with the number of times they are sampled, the profile cross-correlation is corrected for bias introduced for the first half-window and last half-window of a profile which are only singly sampled and for the endpoints of each window which are sampled by adjacent windows. The origin is not included in the calculation, as its elevation is, by definition, the same for both sides of the profile. Finally, a global cross-correlation r_g can be calculated in the same manner as for r_p , simply by extending the summation over all N_g data pairs in all profiles.

The cross-correlation alone is not a complete measure of whether bilateral symmetry exists. Rather, a t test for r may be formulated which gives the probability that the observed correlation is consistent with a sample drawn from a random distribution. Assuming that a and b are drawn from a joint binormal distribution, the test statistic for Pearson's r is [Press *et al.*, 1986]

$$T = \sqrt{\frac{N-2}{1-r^2}} \quad (4.5)$$

and follows a t distribution with $\nu = N - 2$ degrees of freedom under the null hypothesis, $H_0: r = 0$. The null hypothesis may be rejected at significance level α

in favor of the one-sided alternative hypothesis $H_1: r > 0$ when $T > t_{\alpha, \nu}$. Rejection of this null hypothesis is the minimum quantitative requirement for the recognition of bilateral symmetry of specific features. Conversely, for a specified r , we may solve for the significance level α at which the null hypothesis may be rejected. The significance level represents the probability that the observed correlation is due to chance. A complementary expression for α is given by the confidence level (CL), usually expressed as a percentage: $CL = 100(1-\alpha)$. For each individual window, then, both r_w and the corresponding CL may be calculated. However, the number of degrees of freedom is $\nu_w = N_w - 4$ under linear detrending, as there are two degrees of freedom lost for both a and b .

In principle, it is also possible to calculate confidence levels for both r_p and r_g . However, there is a systematic bias to the estimation procedure for these quantities which invalidates the corresponding null hypotheses. Although the linear detrending scheme is adequate to remove wavelengths much larger than the window size, short wavelengths which define the base or "foot" of an elevated region are incompletely removed by a first-order polynomial, which leads to correlated residuals and an enhanced correlation coefficient.

We have calculated r_g for a series of synthetic profiles in order to assess this effect on overall bilateral symmetry. For the Earth, a divergent-plate model [Parsons and Sclater, 1977] was used to generate a reference profile to a distance of 1500 km; we tested velocities of 10 and 20 mm/y, which approximately span the present spreading half-rates of the MAR. Random noise with 400 m amplitude, comparable to those rms residuals derived for the terrestrial profiles in the previous section, was added, and the global cross-correlation over 35 profiles was taken. This procedure was repeated ten times; the mean values for r_g at $v = 10$ mm/y are

0.91, 0.36, and 0.05 for Pearson's r and for linear detrending within 1200 km and 600 km windows, respectively. At $v = 20$ mm/y, these values of r_g fall to 0.88, 0.14, and 0.02, respectively, because the faster-spreading ridge does not flatten as sharply. The test was repeated for a model Aphrodite where a typical profile was approximated by an inverted parabola 4 km in height with a half width of 1500 km at the base; 38 profiles of length 3600 km were tested. The global cross-correlations for Pearson's r , $L_w = 1200$, and $L_w = 600$ are 0.98, 0.40, and 0.11, respectively; higher values are observed for these profiles because the inverted parabola has the sharpest "foot" of all three models.

We further examined the ability to detect specific bilaterally symmetric features in such synthetic profiles by adding symmetric gaussian features with amplitude 1 km (comparable in relief to those features identified by *Crumpler and Head* [1988a] and to some terrestrial oceanic plateaus) and half-width 250 km. For both terrestrial and venusian model topography, $r_g \sim 0.6-0.7$ at $L_w = 1200$ km and $r_g \sim 0.3-0.4$ at $L_w = 600$ km. These values are not strongly dependent on the shape of the rise because the matched features dominate the cross-correlation.

Our approach to interpreting the global cross-correlations, then, is to compare observations with the values expected from synthetic trials where no symmetry is present but which include biases similar to those present in the real data. The range of mean r_g derived from these random models is given in Table 4.5. We restrict these comparisons to a qualitative level because these models are only approximate; a quantitative test for the discrimination between observed and predicted r_g is precluded since the true underlying distributions of topography are not well-constrained.

Three cross-correlation tests for bilateral symmetry are applied to profile 18 of

the MAR in Figure 4.13. Figure 4.13a shows the two sides of the rise superimposed, with their individual means removed. The cross-correlation calculated from this approach (Pearson's r) is large (0.94) because of the contributions from long-wavelength topography. Figure 4.13b shows the same profile following linear detrending in 1200 km windows; because of the modest length of the profile, only two such overlapping windows are possible. The individual r_w and CL are given in Figure 4.13c. The decay of topography immediately adjacent to the rise crest is adequately removed in the first window, and there is no significant correlation of residual topography. The second window, however, shows a strong signature both from the "foot" of the rise and from the equidistant locations of the Bermuda Rise to the west and the Cape Verde Rise to the east. Since both features are substantially younger than the underlying oceanic lithosphere [*Tucholke and Mountain, 1979; Lancelot et al., 1977*], the agreement is fortuitous. However, an argument can be made that their common flowline indicates a genetic relation to anomalously weak lithosphere at the rise crest, which facilitates the later development of hotspot volcanism [M.K. McNutt, personal communication, 1988]; thus the topography may be related to rise-crest processes. The strong correlation in the second window yields a high cross-correlation for the entire profile, $r_p = 0.73$. Figure 4.13d show the same profile linearly detrended with $L_w = 600$ km, giving $r_p = 0.26$. Long-wavelength contributions are completely removed, and the corresponding values of r_w and CL (Figure 4.13e) indicate that there is no significant bilateral symmetry at this scale.

Profile 30 in the South Atlantic is shown for the same three calculations of the cross-correlation in Figure 4.14. The long-wavelength correlation (Figure 4.14a) is high, $r_p = 0.89$. However, the residual cross-correlations for both the 1200 km and

600 km windows (Figures 4.14b and 4.14c) are negative, -0.43 and -0.42, respectively. In fact, Figure 4.14d shows that topography is negatively correlated for each window at $L_w = 600$ km.

Cross-correlations are given for profile 9 across Aphrodite Terra in Figure 4.15. As expected, Pearson's r is large, 0.84 (Figure 4.15a). At $L_w = 1200$ km (Figures 4.15b and 4.15c), the "foot" effect of the base of Ovda Regio is clearly seen in the high correlation of residual topography at 1200 km distance. The feature at $x = 3000$ km is also strongly correlated and is due to the presence of symmetric ridges to the north and south of Ovda. These features were noted by *Crumpler and Head* [1988a] and constitute a key element in their arguments for symmetry of shorter-wavelength features. Because of intervening negatively correlated topography, however, $r_p = 0.10$. Similar results are obtained for $L_w = 600$ km (Figures 4.15d and 4.15e).

The most strongly symmetric profile in our sample is shown in Figure 4.16. Profile 19 crosses central Thetis Regio and shows a consistent correlation of small-scale features to a distance of 2500 km for $L_w = 1200$ km (Figures 4.16b and 4.16c), giving $r_p = 0.61$. The correlation is significant ($r_p = 0.49$) but less impressive at $L_w = 600$ km; discarding the "foot" effect, individual matches are seen at 600 km and 2100 km. The nearest corresponding profile in the work of *Crumpler and Head* [1988a] shows matched features at 500, 1800, and 3000 km.

A sample profile (number 29) across Diana Chasma is given in Figure 4.17. Cross-correlations for both 1200 and 600 km windows are negative, $r_p = -0.13$ and -0.33, respectively. The nearest profile given by *Crumpler and Head* [1988a] shows three short-wavelength features within $x = 1200$ km. Our best matches are at 1600 and 2700 km (Figure 4.17e), but both are below the 90% confidence level.

Profile cross-correlations are summarized by profile number in Figures 4.18 - 4.20 for both Earth and Venus for the cases of Pearson's r and for linear detrending within 1200 and 600 km windows, respectively. Figure 4.18 shows generally high values of r_p (mean ~ 0.7 for both Earth and Venus), indicating that the center of a broadly symmetric rise has been properly identified. For $L_w = 1200$ km, the mean r_p is 0.28 for Earth and 0.22 for Venus, whereas for $L_w = 600$ km, these statistics fall to 0.18 and 0.13, respectively. The irregular form of Figures 4.18 - 4.20 in itself suggests that there is little continuity of short-wavelength features parallel to the rise axes.

A better statistic of the overall symmetry is not the mean of r_p , but the global cross-correlation r_g , obtained by extending the summation of equation (4.4) over all profiles. These results are given in Table 4.5, along with some test values for synthetic profiles. Comparing the full profiles across the MAR and Aphrodite to these random models, the data cannot be clearly distinguished as having a higher correlation coefficient. We conclude that there is no strong evidence for regional bilateral symmetry on either planet at a scale much smaller than that of the broadly elevated rises. This conclusion is not changed by considering any different distance interval in Table 4.5.

The absence of demonstrable regional bilateral symmetry from these tests conflicts not only with assertions to the contrary for Venus, but for the Earth as well. For the Atlantic ocean basin, *Crumpler and Head* [1988c] have noted several examples of topographic features in the Atlantic inferred to have formed at or near the rise crest and to have been (or to currently being) subsequently split and separated: Iceland, Corner Rise/Great Meteor Seamount, Ceara Rise/Sierra Leone Rise, and Rio Grande Rise/Walvis Ridge. We have examined

corresponding profiles in our data set to check if these features can be individually detected. Iceland itself cannot be so tested because it is presently at the rise crest; what few gridded data exist on the narrow Iceland ridge are negatively correlated (Figure 4.20). The Corner Rise and Great Meteor Seamount appear on profile 16; these small features are well correlated for $L_w = 600$ km, although the Great Meteor Seamount dominates the pair. The correlation for the entire profile is $r_p = 0.30$, which is larger than the mean value for the Atlantic (0.18) and comparable to that predicted for such a feature in synthetic tests (0.35). The Ceara Rise/Sierra Leone Rise pair do not give a good match, because the former feature is rather small and partially superimposed on the South American continental rise. The Rio Grande Rise and Walvis Ridge show a strong correlation at $L_w = 1200$ km, and $r_p = 0.66$; however, this match does not appear for the shorter window.

We also tested five profiles on the Southeast Indian Ridge which cross the Kerguelen Rise and Broken Ridge. The global cross-correlations r_g for these profiles are 0.33 for $L_w = 1200$ km and 0.22 for $L_w = 600$ km, and the mean values for r_p correspond quite closely to r_g . These values are lower than found for similar calculations for the MAR because the fast-spreading Southeast Indian Ridge ($v = 37$ mm/y [Minster and Jordan, 1977]) does not show a prominent "foot" or base which biases correlation estimates. Synthetic profiles with a superimposed random component as described above show r_g equal to 0.07 for $L_w = 1200$ km and 0.02 for $L_w = 600$ km.

Therefore we find that although some individual oceanic plateaus and hotspots are symmetrically situated about the ridge axis, they contribute negligibly to the overall topography. Such a result does not preclude that similar isolated individual elements may exist for Aphrodite as well, but their number must be substantially

smaller than those features indicated by *Crumpler and Head* [1988a].

As a final test for bilateral symmetry of Aphrodite Terra in the direction suggested by *Crumpler and Head* [1988a], we examined whether a preferred direction of symmetry exists for profiles taken through the approximate centers of Ovda and Thetis. Profiles 11 and 21, respectively, pass very nearly through the centers of these plateaus, so a series of profiles at different azimuths was taken through these points. Figure 4.21a shows r_p as a function of azimuth for Ovda for all three cross-correlation tests. The spreading azimuth suggested by *Crumpler and Head* is approximately -20° . The long-wavelength symmetry, given by Pearson's r , is nearly independent of azimuth, except along nearly east-west profiles where the presence of Thetis Regio causes a strong misfit. When long-wavelength components are removed using $L_w = 1200$ km and $L_w = 600$ km, the correlation as a function of azimuth varies randomly. Similar results for Pearson's r are found for Thetis Regio (Figure 4.21b). At both $L_w = 1200$ km and $L_w = 600$ km, there is a slight positive correlation from azimuth -20° to $+40^\circ$ but no preferred direction.

DISCUSSION

We now turn to the implications of these tests for the vertical-tectonics, plate-divergence, and distributed-deformation models for Aphrodite Terra. We also offer predictions that may be tested by Magellan observations.

The analysis of topographic bilateral symmetry has shown that if any such symmetry exists, its contribution to the resolvable topography of the MAR and Aphrodite Terra at wavelengths of several hundred kilometers is modest at best. Since bilateral symmetry cannot be reliably distinguished at present, it cannot be used as

a test for crustal divergence. Even if the regional-scale symmetry analyzed here is in fact negligible, unambiguous identification of individual symmetric features (e.g., hotspot traces) by Magellan would nevertheless support crustal divergence, under either rigid-plate or distributed-deformation models.

Our analysis of the thermal boundary layer topography of Aphrodite has shown that in all cases Venus scores more poorly in goodness of fit and residual topography than does the Earth. East-central Aphrodite alone provides the best fit for Venus, but under the condition that the distance of the fit is restricted to the longest interval. Although a thermal boundary layer component of topography cannot be rejected, unmodelled mechanisms contribute more than half of the variance in most cases. Therefore thermal boundary-layer arguments cannot be used to support a rigid-plate divergence model over the alternative models. Magellan data are unlikely to alter this conclusion, as this result depends only on topographic length scales already resolved by Pioneer Venus.

The burden of proof rests with the CSDs, which we have shown are not consistent with simple two-plate divergence. In a multiple-plate geometry, additional plate boundaries must be identified. The CSDs are the only identified major tectonic features that may be posited as such boundaries, and should be dominated by transform motion. In principle, if such a candidate CSD is identified for, say, a three-plate system, bounds on the non-transform component of motion (or at least its sign) across the boundary may be established by differencing the angular velocity vectors of the two divergent plate pairs. The angular velocity vectors may be constructed from Euler pole fits and topographically-inferred velocities. Unfortunately, uncertainties in both of these parameters preclude such tests. We can, however, make the following qualitative prediction: if a

plate-bounding CSD is a pure transform, then it must lie along a small circle. In fact, the near-constant strike of the CSDs in Mercator projection indicates that they lie more nearly along rhumb lines, and so they must have either compressional or extensional components to their deformation. Therefore, if the plate-divergence hypothesis is correct, then one or more plate-bounding CSDs must exist and would be distinguishable from fracture zones by geological evidence for compression or extension across the CSD. If such evidence is not found, then the plate-divergence model must be rejected in favor of distributed deformation, under which CSD geometry is not so constrained. The vertical-tectonics model faces its strongest obstacle in the mere existence of the CSDs and can survive only if these lineaments cannot be verified.

CONCLUSIONS

We have considered three alternative hypotheses for Aphrodite Terra for the interaction of mantle convective flow with the surface: vertical tectonics, plate divergence, and distributed deformation. We find no convincing evidence of regional bilateral symmetry across Aphrodite Terra at length scales of several hundred kilometers, nor are we able to resolve unambiguously a thermal boundary-layer component to the topography of Aphrodite. Therefore neither of these observations may be used to support rigid-plate divergence. The existence of cross-strike discontinuities (CSDs) in Aphrodite implies large-scale horizontal motion and argues against purely vertical tectonics. The near-constant azimuths of CSDs are not consistent with rigid two-plate divergence and imply unusual apparent polar wander paths in a multiple plate system. If the plate-divergence hypothesis is correct, one or more CSDs must be plate boundaries and should

show non-transform deformation in high-resolution images. If this is not observed, then the CSDs are incompatible with rigid plates, and they must represent the traces of mantle flow upon a thin lithosphere. Accurate mapping and careful study of the CSDs from Magellan images will lead to the resolution of these competing ideas.

REFERENCES

- Banerdt, W.B., Support of long-wavelength loads on Venus and implications for internal structure, *J. Geophys. Res.*, *91*, 403-419, 1986.
- Banerdt, W.B., Global dynamic stress modelling on Venus (abstract), *Lunar and Planetary Science XIX*, 25-26, 1988.
- Bindschadler, D.L., and E.M. Parmentier, Tectonic features due to gravitational relaxation of topography (abstract), *Lunar and Planetary Science XVIII*, 75-76, 1987.
- Buck, W.R., When does small-scale convection begin beneath oceanic lithosphere?, *Nature*, *313*, 775-777, 1985.
- Bullard, E.C., J.E. Everett, and A.G. Smith, Fit of the continents around Atlantic, *Phil. Trans., Roy. Soc. Lond. Ser A*, *258*, 41-75, 1965.
- Campbell, D.B., J.W. Head, J.K. Harmon, and A.A. Hine, Venus: Volcanism and Rift formation in Beta Regio, *Science*, *226*, 167-170, 1984.
- Cande, S.C., J.L. LaBrecque, and W.F. Haxby, Plate kinematics of the South Atlantic: Chron C-34 to present, *J. Geophys. Res.*, in press, 1988.
- Crumpler, L.S., and J.W. Head, Bilateral topographic symmetry patterns across Aphrodite Terra, Venus, *J. Geophys. Res.*, *93*, 301-312, 1988a.
- Crumpler, L.S., and J.W. Head, Divergent plate boundary characteristics in eastern Aphrodite Terra, Venus (abstract), *Lunar and Planetary Science XIX*, 233-234, 1988b.
- Crumpler, L.S., and J.W. Head, Split and separated topography on Earth's seafloor: A comparison to bilateral symmetry in Aphrodite Terra, Venus (abstract), *Lunar and Planetary Science XIX*, 235-236, 1988c.
- Crumpler, L.S., J.W. Head, and J.K. Harmon, Regional linear cross-strike discontinuities in western Aphrodite Terra, Venus, *Geophys. Res. Lett.*, *14*, 607-610,

1987.

- Ford, P.G., Pioneer Venus hypsometry, Center for Space Research, M.I.T., Cambridge, Mass., 12 pp., 1986.
- Forsyth, D.W., The early structural evolution and anisotropy of the oceanic upper mantle, *Geophys. J. Roy. Astron. Soc.*, *43*, 103-162, 1975.
- Head, J.W., and L.S. Crumpler, Evidence for divergent plate-boundary characteristics and crustal spreading on Venus, *Science*, *238*, 1380-1385, 1987.
- Heestand, R.L., and S.T. Crough, The effect of hotspots on the ocean age-depth relation, *J. Geophys. Res.*, *86*, 6107-6114, 1981.
- Herrick, R.R., and B.G. Bills, Analysis of gravity data over Aphrodite Terra, Venus (abstract), *Lunar and Planetary Science XIX*, 481-482, 1988.
- Jarvis, G.T., and W.R. Peltier, Mantle convection as a boundary layer phenomenon, *Geophys. J. Roy. Astron. Soc.*, *68*, 389-427, 1982.
- Kaula, W.M., and R.J. Phillips, Quantitative tests for plate tectonics on Venus, *Geophys. Res. Lett.*, *8*, 1187-1190, 1981.
- Kiefer, W.S., and B.H. Hager, Mantle plumes on Venus (abstract), *Lunar and Planetary Science XVIII*, 489-490, 1987.
- Kiefer, W.S., M.A. Richards, and B.H. Hager, A dynamic model of Venus's gravity field, *Geophys. Res. Lett.*, *13*, 14-17, 1986.
- Klitgord, K.D., and H. Schouten, Plate kinematics of the central Atlantic, in *The Geology of North America, Volume M, The Western North Atlantic Region*, edited by P.R. Vogt and B.E. Tucholke, pp. 351-378, Geological Society of America, Boulder, Colo., 1986.
- Lancelot, Y., E. Seibold, et al., *Initial Reports of the Deep Sea Drilling Project*, *41*, U.S. Government Printing Office, Washington, D.C., 1977.
- LePichon, X., Sea-floor spreading and continental drift, *J. Geophys. Res.*, *73*,

3661-3697, 1968.

Masursky, H., E. Eliason, P.G. Ford, G.E. McGill, G.H. Pettengill, G.G. Schaber, and G. Schubert, Pioneer Venus radar results: Geology from images and altimetry, *J. Geophys. Res.*, **85**, 8232-8260, 1980.

McGill, G.E., S.J. Steenstrup, C. Barton, and P.G. Ford, Continental rifting and the origin of Beta Regio, Venus, *Geophys. Res. Lett.*, **8**, 737-740, 1981.

McGill, G.E., J.L. Warner, M.C. Malin, R.E. Arvidson, E. Eliason, S. Nozette, and R.D. Reasenber, Topography, surface properties, and tectonic evolution, in *Venus*, edited by D.M. Hunten, L. Colin, T.M. Donahue, and V.I. Moroz, pp. 69-130, Univ. of Arizona Press, Tucson, 1983.

McKenzie, D.P., Some remarks on heat flow and gravity anomalies, *J. Geophys. Res.*, **72**, 6261-6273, 1967.

Minster, J.B., and T.H. Jordan, Present-day plate motions, *J. Geophys. Res.*, **83**, 5331-5354, 1978.

Morgan, P., and R.J. Phillips, Hot spot heat transfer: Its application to Venus and implications to Venus and Earth, *J. Geophys. Res.*, **88**, 8305- 8307, 1983.

Parker, R.L., and D.W. Oldenburg, Thermal model of ocean ridges, *Nature Phys. Sci.*, **242**, 137-139, 1973.

Parsons, B., and D. McKenzie, Mantle convection and the thermal structure of plates, *J. Geophys. Res.*, **83**, 4485-4496, 1978.

Parsons, B., and J.G. Sclater, An analysis of the variation of ocean floor bathymetry and heat flow with age, *J. Geophys. Res.*, **82**, 803-827, 1977.

Pettengill, G.H., E. Eliason, P.G. Ford, G.B. Lorient, H. Masursky, and G.E. McGill, Pioneer Venus radar results: Altimetry and surface properties, *J. Geophys. Res.*, **85**, 8261-8270, 1980.

Phillips, R.J., A mechanism for tectonic deformation on Venus, *Geophys. Res. Lett.*,

13, 1141-1144, 1986.

Phillips, R.J., W.L. Sjogren, E.A. Abbot, J.C. Smith, R.N. Wimberly, and C.A. Wagner, The gravity field of Venus: A preliminary analysis, *Science*, 205, 93-96, 1979.

Phillips, R.J., W.M. Kaula, G.E. McGill, and M.C. Malin, Tectonics and evolution of Venus, *Science*, 212, 879-887, 1981.

Phillips, R.J., and M.C. Malin, The interior of Venus and tectonic implications, in *Venus*, edited by D.M. Hunten, L. Colin, T.M. Donahue, and V.I. Moroz, pp. 159-214, Univ. of Arizona Press, Tucson, 1983.

Press, W.H., B.P. Flannery, S.A. Teukolsky, and W.T. Vetterling, *Numerical Recipes*, Cambridge Univ. Press, Cambridge, 818 pp., 1986.

Robinson, E.M., B. Parsons, and S.F. Daly, The effect of a shallow low viscosity zone on the apparent compensation of mid-plate swells, *Earth Planet Sci. Lett.*, 82, 335, 1987.

Schaber, G.G., Venus: Limited extension and volcanism along zones of lithospheric weakness, *Geophys. Res. Lett.*, 9, 499-502, 1982.

Schubert, G., C. Froidevaux, and D.A. Yuen, Oceanic lithosphere and asthenosphere: thermal and mechanical structure, *J. Geophys. Res.*, 81, 3525-3540, 1976.

Stofan, E.R., J.W. Head, D.B. Campbell, S.H. Zisk, A.F. Bogomolov, O.N. Rzhiga, A.T. Basilevsky, and N. Armand, Nature and sequence of volcanic and tectonic activity in Beta Regio, Venus (abstract), *Lunar and Planetary Science XVIII*, 952-953, 1987.

Tucholke, B.E., and G.S. Mountain, Seismic stratigraphy, lithostratigraphy, and paleosedimentation patterns in the North American Basin, in *Deep Drilling Results in the Atlantic Ocean: Continental Margins and Paleoenvironment*,

Maurice Ewing Series, vol. 3, edited by M. Talwani, W. Hay, and B.F. Ryan, pp. 58-86, Amer. Geophys. Union, Washington, D.C., 1979.

Turcotte, D.L., and E.R. Oxburgh, Finite amplitude convective cells and continental drift, *J. Fluid Mech.*, 28, 29-42, 1967.

U.S. Naval Oceanographic Office, *Digital Bathymetric Database 5 (DBDB5)*, National Geophysical Data Center, Boulder, Colo., 1985.

Vine, F., Spreading of the ocean floor: New evidence, *Science*, 154, 1405-1415, 1966.

TABLE 4.1. Cross-strike discontinuity segments separating offset linear centers of bilateral topographic symmetry in Aphrodite Terra

Latitude, ^a °N	Longitude, ^a °E	Azimuth, deg	Uncertainty, ^b deg
-2.5	73.0	-22	14
-5.0	77.2	-19	7
-8.5	81.5	-23	9
-5.0	94.0	-19	7
-5.5	98.7	-19	10
-7.5	107.5	-22	14
-8.5	129.2	-26	13
-7.0	137.2	-20	12
-9.5	148.2	-26	21
-12.5	156.5	-30	30
-12.5	163.5	-38	28

From L.S. Crumpler (personal communication, 1987).

^aLatitude and longitude correspond to the position on the CSD midway between the offset centers of bilateral topographic symmetry.

^bCalculated from the variation in azimuth assuming that the uncertainty in locating individual features is $\pm 1^\circ$ for Ovda and Thetis Regiones and $\pm 3^\circ$ for east-central Aphrodite.

TABLE 4.2. Locations of topographic profiles across Aphrodite Terra

Number	Latitude, °N	Longitude, °E	Azimuth, deg	Number	Latitude, °N	Longitude, °E	Azimuth, deg
1	-4.4	62.5	-21	20	-9.4	125.0	-21
2	-3.7	64.3	-21	21	-8.8	126.8	-21
3	-2.9	66.1	-21	22	-8.6	131.5	-21
4	-2.2	67.9	-21	23	-7.9	133.2	-21
5	-1.5	69.6	-21	24	-7.2	135.0	-21
6	-7.5	83.8	-21	25	-7.5	140.0	-21
7	-6.7	85.5	-21	26	-6.8	141.8	-21
8	-6.0	87.3	-21	27	-6.0	143.5	-21
9	-5.2	89.1	-21	28	-16.2	153.8	-28
10	-4.5	90.9	-21	29	-15.2	155.5	-28
11	-5.0	96.2	-21	30	-12.0	159.5	-30
12	-6.2	101.8	-21	31	-16.2	173.7	-30
13	-5.5	103.6	-21	32	-15.1	175.3	-30
14	-9.4	110.2	-21	33	-14.1	176.9	-30
15	-12.8	116.2	-21	34	-13.1	178.5	-30
16	-12.1	117.9	-21	35	-14.5	183.9	-30
17	-11.4	119.7	-21	36	-13.5	185.5	-30
18	-10.8	121.5	-21	37	-12.5	187.0	-30
19	-10.1	123.3	-21	38	-11.5	188.5	-30

Profiles follow great-circle paths from the specified starting point at the indicated azimuth to a distance of 3600 km. Profiles 4, 9, 11, 13, 21, 24, 25, and 29 correspond approximately to profiles A, G, I, J, K, L, M, and N, respectively, given by *Crumpler and Head* [1988a].

TABLE 4.3. Locations of bathymetric profiles across the Mid-Atlantic Ridge

Number	Latitude, °N	Longitude, °E	Length, km	Number	Latitude, °N	Longitude, °E	Length, km
1	64.0	340.0	400	19	21.3	314.9	2000
2	62.0	334.0	400	20	19.2	314.2	2000
3	60.0	330.0	500	21	17.0	313.8	2000
4	58.1	327.3	500	22	13.6	315.4	1400
5	56.1	325.3	900	23	5.2	327.6	1800
6	53.7	324.7	900	24	2.2	329.6	1500
7	50.3	331.0	1000	25	-3.8	347.8	1700
8	48.4	332.3	1100	26	-5.9	348.8	1700
9	46.5	332.6	900	27	-8.4	346.8	1800
10	44.6	331.8	1200	28	-10.4	346.9	1800
11	42.5	330.8	1300	29	-13.2	345.8	1400
12	40.5	330.8	1500	30	-15.3	346.3	1600
13	36.3	326.5	2100	31	-17.3	346.5	1500
14	34.3	323.1	2000	32	-18.8	347.1	1500
15	32.6	320.3	2000	33	-20.7	348.4	1500
16	30.8	318.6	2000	34	-24.2	346.9	1500
17	28.5	316.6	2000	35	-27.0	346.5	2100
18	25.8	315.3	2000				

Profiles follow spreading flowlines (i.e., parallel to fracture zone traces) until truncated by a continental rise. Anomalous features include Iceland (profile 1), the Corner Rise and Great Meteor Seamount (profile 16), the Ceara and Sierra Leone Rises (profile 23), and the Rio Grande and Walvis Ridges (profile 35).

TABLE 4.4. Summary of least-squares tests of thermal boundary layer topography for Earth and Venus, $e = e_0 + \delta (x/v)^{1/2}$

Distance Interval, km	Fraction with $r < 0$	Mean r	σ , m	mean e_0 , km	mean v , mm/y	median v , mm/y
<i>Earth, all profiles</i>						
0 - 600	1.0	-0.84	320	4.4	18	16
max. length	1.0	-0.80	460	4.1	58	24
<i>Venus, all profiles</i>						
0 - 600	0.29	+0.08	660	1.8	39	0
0-1500	0.89	-0.47	720	2.8	57	11
0-3600	1.0	-0.72	680	2.6	19	16
1500-3600	0.76	-0.19	540	0.8	100	60
<i>Venus, East-Central Aphrodite only</i>						
0-600	0.28	+0.08	770	0.6	120	0
0-1500	0.72	-0.35	590	1.2	20	16
0-3600	1.0	-0.66	480	1.3	36	34
1500-3600	0.55	-0.23	310	0.7	40	3

TABLE 4.5. Global Cross-Correlation Coefficients for Bilateral Topographic Symmetry

Window Size, km	Atlantic	Aphrodite	Random Models
<i>Distance Interval: full profile</i>			
full profile	0.70	0.74	0.88-0.98
1200	0.27	0.17	0.14-0.40
600	0.07	0.08	0.02-0.12
<i>Distance Interval: 0-600 km</i>			
600	0.12	-0.06	
<i>Distance Interval: 0-1200 km</i>			
1200	0.35	0.20	
600	0.12	0.08	
<i>Distance Interval: 1200-3600 km</i>			
1200	-	0.14	
600	-	0.08	

Cumulative cross-correlation over all profiles at specified distance interval, taken within windows of specified length. Individual windows have best-fitting line removed, except where window is taken to be the full profile, wherein only the mean is subtracted. Random models are bilaterally symmetric rises with a superimposed random component (see text).

FIGURE CAPTIONS

- Figure 4.1. Topography of Aphrodite Terra, simplified from Pioneer Venus altimetric data [Pettengill *et al.*, 1980; Ford; 1986]. Mercator projection, 1 km contour interval.
- Figure 4.2. System of cross-strike discontinuities, or CSDs, and linear centers of bilateral topographic symmetry (heavy lines) in Aphrodite Terra mapped by Crumpler *et al.* [1987] and Crumpler and Head [1988a]. CSDs appear discontinuous because only the most clearly defined segments are included (L.S. Crumpler, personal communication, 1987). Topographic contours are from Figure 4.1.
- Figure 4.3. Schematic illustrations of the three models for Aphrodite Terra tested in this paper: (a) vertical tectonics, (b) plate divergence, (c) distributed deformation.
- Figure 4.4. Best-fitting pole of rotation (Euler pole) to the azimuths of portions of the CSDs lying between offset linear centers of bilateral topographic symmetry (Table 4.1). The pole is at $20 \pm 3^\circ\text{N}$, $204 \pm 17^\circ\text{E}$ (cross); level curves for one and two standard deviations are also shown. Several small circles about the Euler pole (curved lines) show the trajectories that CSDs would follow if Aphrodite Terra were a two-plate system with a rotation pole fixed with respect to the plate boundary. Mercator projection.

Figure 4.5. System of CSDs and topographic symmetry centers in Mercator projection about the best-fitting Euler pole. For a fixed pole separating two diverging rigid plates, CSDs should follow lines of latitude in this projection.

Figure 4.6. Traces of topographic profiles across Aphrodite Terra analyzed in this paper. Each profile follows a great circle approximately perpendicular to the linear center of bilateral topographic symmetry. Profile spacing is approximately 200 km, and centers are taken no closer than about 150 km to the nearest mapped CSD. Profiles cross distant CSD segments in only a few cases.

Figure 4.7. Traces of bathymetric profiles across the Mid-Atlantic Ridge (MAR), for comparison with Aphrodite Terra. Traces follow spreading flowlines [*Klitgord and Schouten, 1986; Cande et al., 1988*] in most cases, except for short profiles on the Reykjanes Ridge and near the equator, which are taken along small circles about the best-fitting two-plate rotation pole [*Minster and Jordan, 1978*]. Profile centers are selected in a similar fashion to those for Aphrodite Terra, spaced approximately 200 km apart and no closer than about 150 km to large-offset ($> 1^\circ$) transform faults. Profiles are truncated where they intersect continental rises or oceanic plateaus with continental basement.

Figure 4.8. Topographic profiles of Aphrodite Terra constructed from individual Pioneer Venus measurements. Figure is divided into Ovda Regio (60-110° E), Thetis Regio (110-150° E), and east-central Aphrodite (150-190° E). Within each region, the longitude of the profile center increases upward on the figure. Profiles are offset by 3 km in elevation for clarity.

Figure 4.9. Bathymetric profiles across the Mid-Atlantic Ridge, constructed from DBD5 digital bathymetry degraded to Pioneer Venus resolution (see text). Figure is divided by plate pair (North American - Eurasian, North American - African, South American - African) for convenience. For each plate pair, profiles are arranged from north to south going down the figure, and are offset by 3 km in depth for clarity.

Figure 4.10. Least-squares fits of elevation e versus the square root of distance x from topographic profiles across Aphrodite Terra and the Mid-Atlantic Ridge. Statistical parameters and apparent rates of divergence are given in the text for each fit.

(a) MAR profile 18 (north of the Kane Fracture Zone); fits to 600 and 2000 km distances.

(b) MAR profile 30 (north of the St. Helena Fracture Zone); fits to 600 and 1600 km distances.

(c) Aphrodite Terra profile 9 (Ovda Regio); fits to 600, 1500, 3600 km distances and to the interval 1500-3600 km.

(d) Aphrodite Terra profile 29 (east-central region); fits to 600, 1500, 3600 km distances and to the interval 1500-3600 km.

Figure 4.11. Summary of rms error σ versus linear correlation coefficient r for \sqrt{x} regressions for all profiles on Earth (circles) and Venus (triangles).

(a) Regressions to 600 km distance.

(b) Regressions to 1500 km distance for Venus and full profile length (averaging 1500 km) for Earth.

(c) Regressions for Venus only to 3600 km distance (triangles) and for the distance interval 1500-3600 km (squares).

(d) Regressions for east-central Aphrodite alone to distances of 600 km (squares), 1500 km (circles), 3600 km (triangles), and for the interval 1500-3600 km (crosses).

Figure 4.12. Variation of apparent half spreading rate v with geographic location, given by profile number.

(a) MAR, 600 km fits. The boundary between the Eurasian and African plates occurs between profiles 12 and 13, and that between the North American and South American plates is between profiles 21 and 22.

(b) MAR, full length of individual profiles (mean 1500 km).

(c) Aphrodite, 1500 km fits. Zero velocity indicates a positive correlation of elevation with distance; for such profiles a measureable cooling boundary layer component may be rejected.

(d) Aphrodite, 3600 km profiles.

Figure 4.13. Tests of bilateral symmetry for MAR profile 18.

- (a) West (solid) and east (dashed) sides of profile 18, with means subtracted.
- (b) Same profile with windowed detrending operations applied to remove long-wavelength components of topography. Window length in this example is 1200 km, and the best-fitting line has been removed. Overlapping windows offset by 2 km in depth for clarity.
- (c) Correlation coefficient (solid line) as a function of distance for the windowed, detrended profiles in (b). Dashed lines show confidence levels at which the null hypothesis for each window may be rejected.
- (d) Atlantic profile 18 linearly detrended within 600-km windows. There are now five individual, overlapping window segments within the profile.
- (e) Correlation coefficient as a function of distance for (d).

Figure 4.14. Tests of bilateral symmetry for MAR profile 30.

- (a) Full profile to 1600 km, with means subtracted from each side.
- (b) Profile after linear detrending in 1200 km windows; since the profile length is 1600 km, only a single window is used.
- (c) Four overlapping 600-km windows for the same profile.
- (d) Correlation coefficients and confidence levels for (c).

Figure 4.15. Tests of bilateral symmetry for Aphrodite Terra profile 9, Ovda Regio.

- (a) Full profile (3600 km), with means subtracted.
- (b) Profile linearly detrended in 1200-km windows.
- (c) Correlation coefficients and confidence levels for (b).

- (d) Profile linearly detrended within 600-km windows
- (e) Correlation coefficients and confidence levels for individual windows for (d).

Figure 4.16. Tests of bilateral symmetry for Aprodite Terra profile 19 (Thetis Regio), the profile observed to be the most highly symmetric at short wavelengths.

- (a) Full profile (3600 km), with means subtracted.
- (b) Profile linearly detrended in 1200-km windows.
- (c) Correlation coefficients and confidence levels for (b).
- (d) Profile linearly detrended within 600-km windows
- (e) Correlation coefficients and confidence levels for individual windows for (d).

Figure 4.17. Tests of bilateral symmetry for Aphrodite profile 29 (East-Central Region, across Dali Chasma).

- (a) Full profile (3600 km), with means subtracted.
- (b) Profile linearly detrended in 1200-km windows.
- (c) Correlation coefficients and confidence levels for (b)
- (d) Profile linearly detrended within 600-km windows.
- (e) Correlation coefficients and confidence levels for individual windows for (d).

Figure 4.18. Summary of profile correlation coefficients, given by profile number, for simple cross-correlations of full profiles. Strong correlation is evident in all cases for this method because of the broad central

elevated region. (a) Earth, (b) Venus

Figure 4.19. Summary of profile correlation coefficients under linear detrending within 1200-km windows. On both planets, systematic contributions to cross-correlations arise from correlated residuals after linearly detrending across the base of elevated region. (a) Earth, (b) Venus.

Figure 4.20. Summary of profile correlation coefficients under linear detrending within 600-km windows. There is no consistent evidence for symmetric features at this scale on either planet. (a) Earth, (b) Venus.

Figure 4.21. Profile correlation coefficients as a function of azimuth from the approximate centers of (a) Ovda Regio and (b) Thetis Regio. Solid line, mean topography subtracted; long dash, linear detrending within 1200-km windows; short dash, linear detrending within 600 km windows.

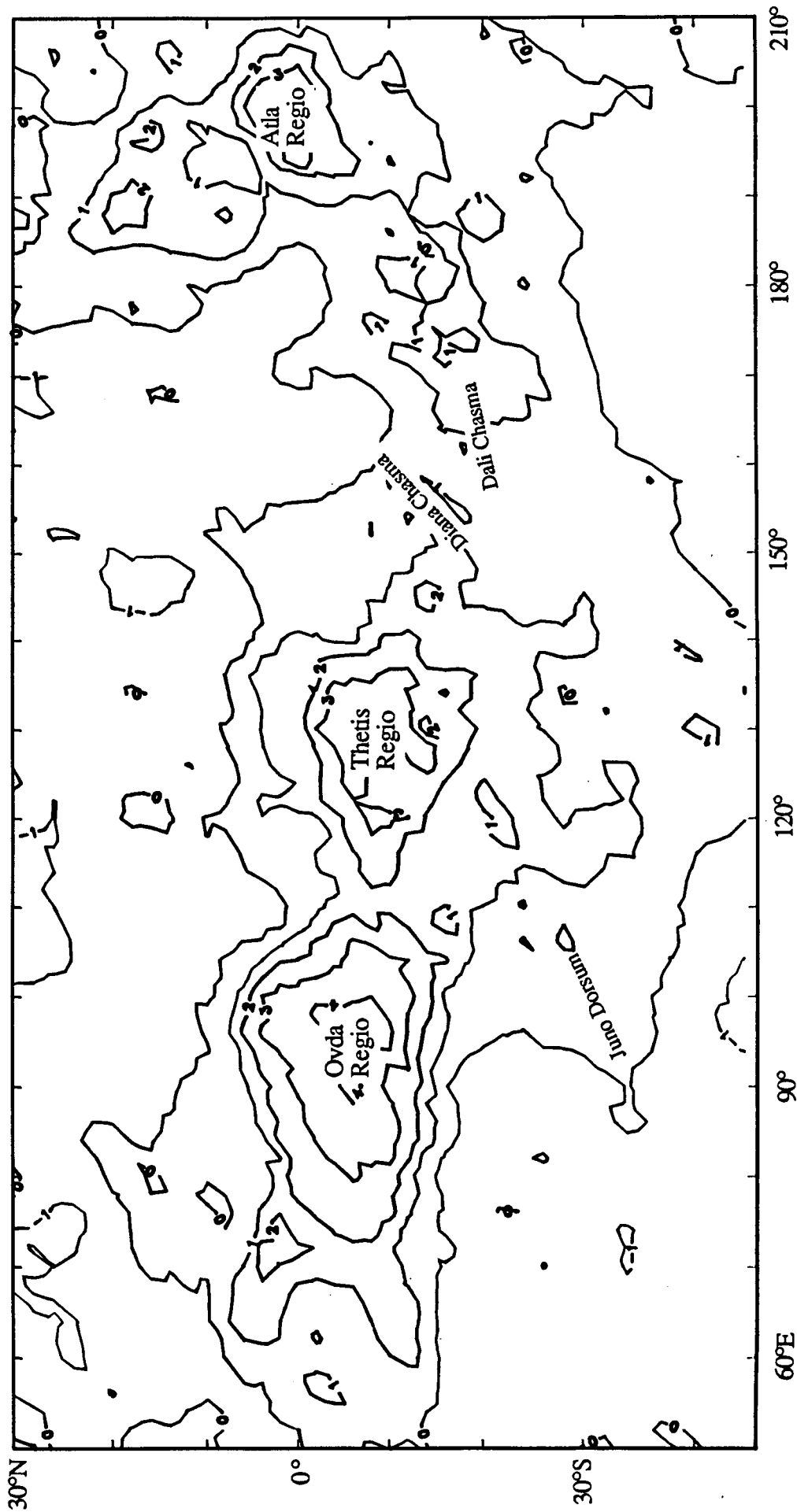


Figure 4.1

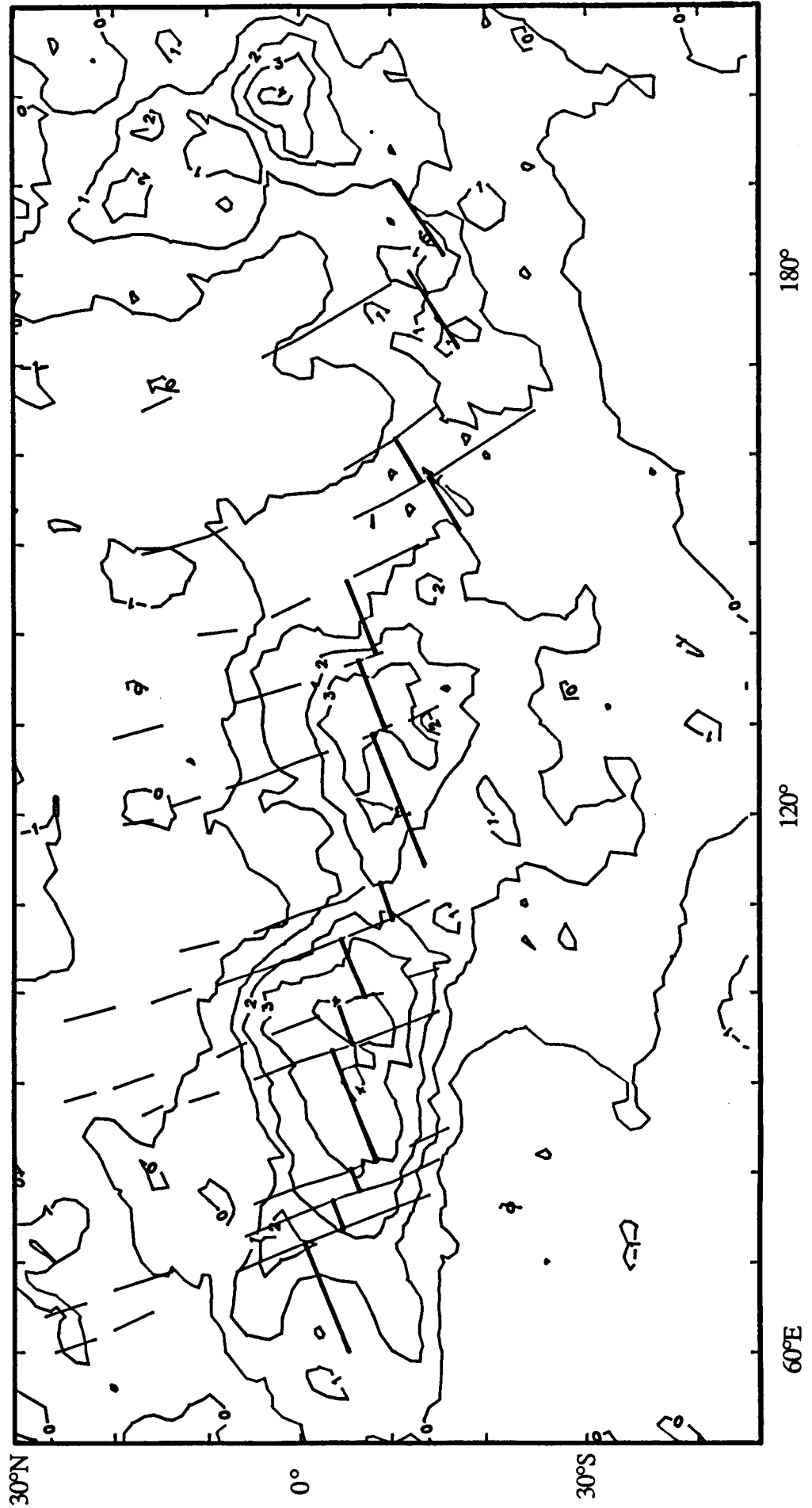


Figure 4.2

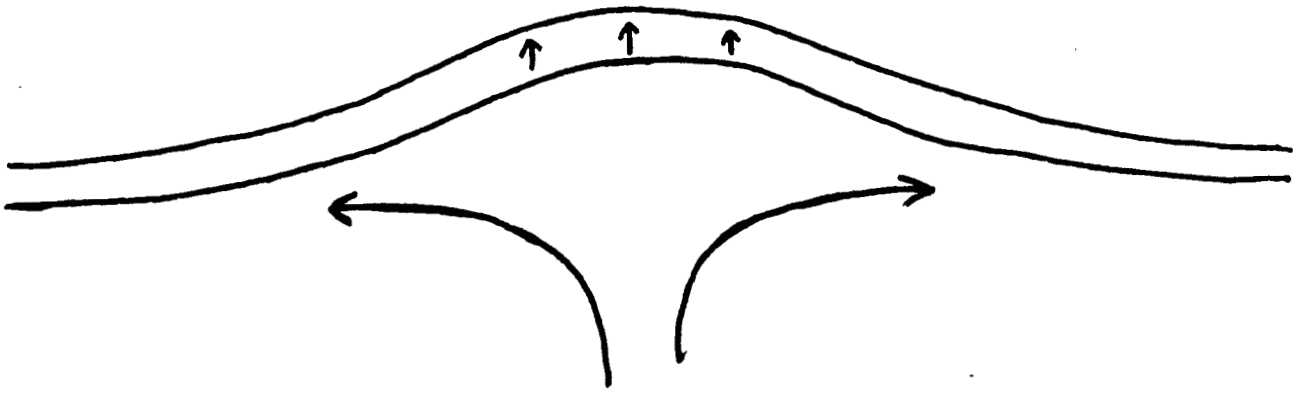
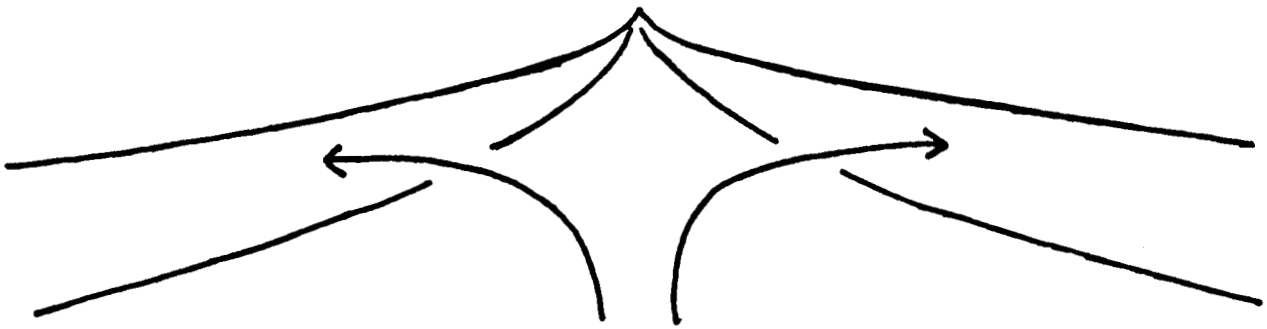


PLATE DIVERGENCE



DISTRIBUTED DEFORMATION

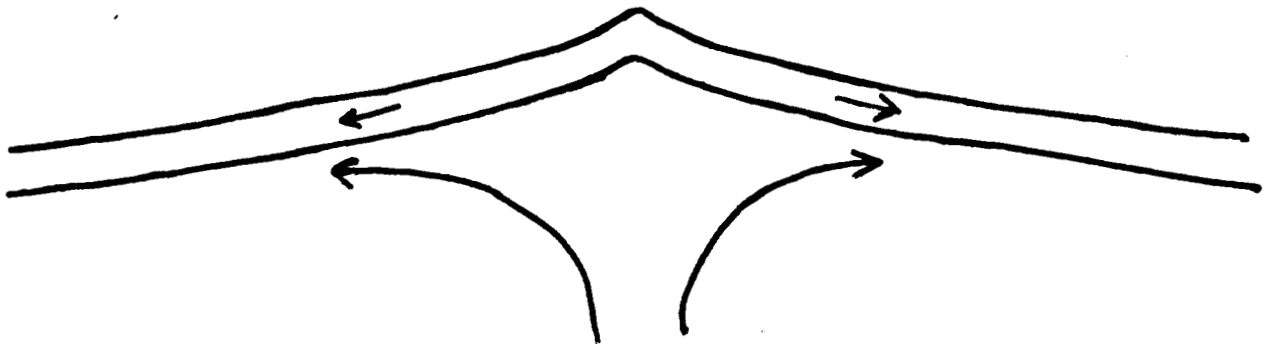


Figure 4.3

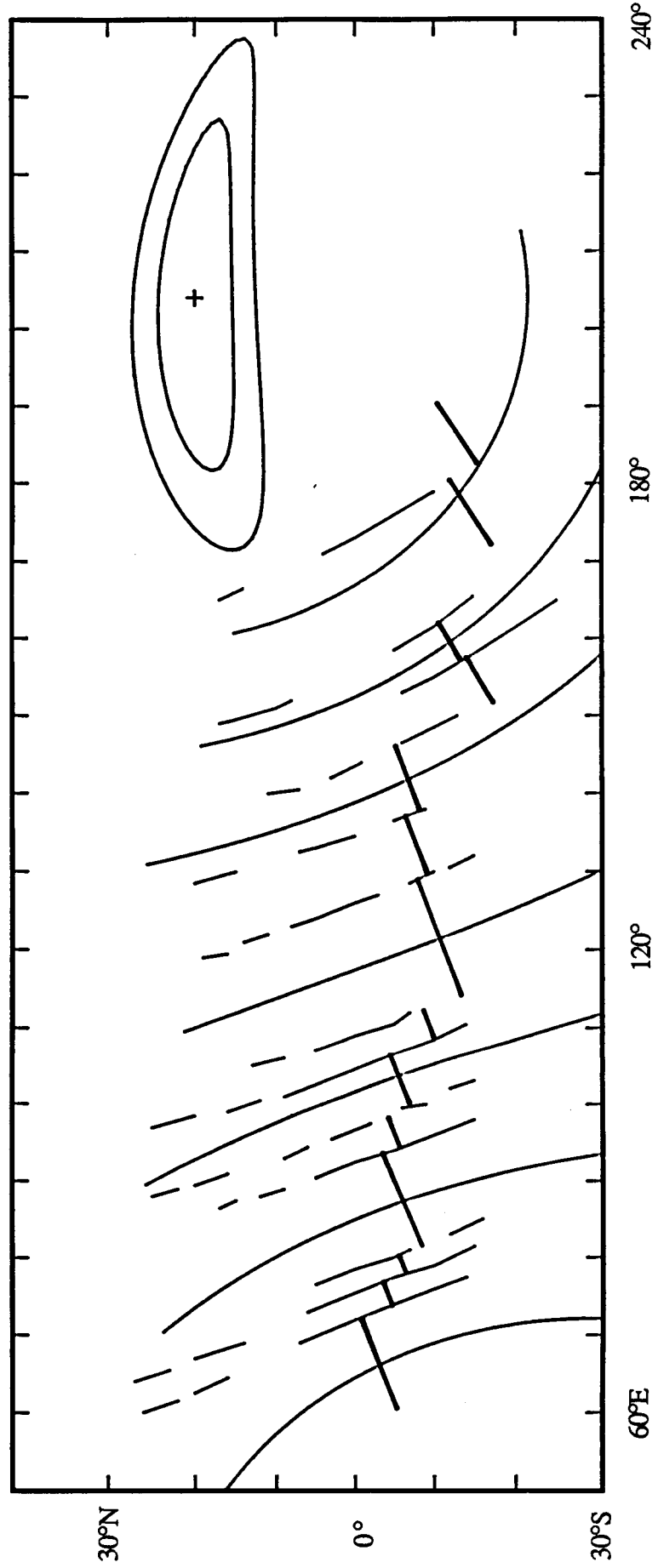


Figure 4.4

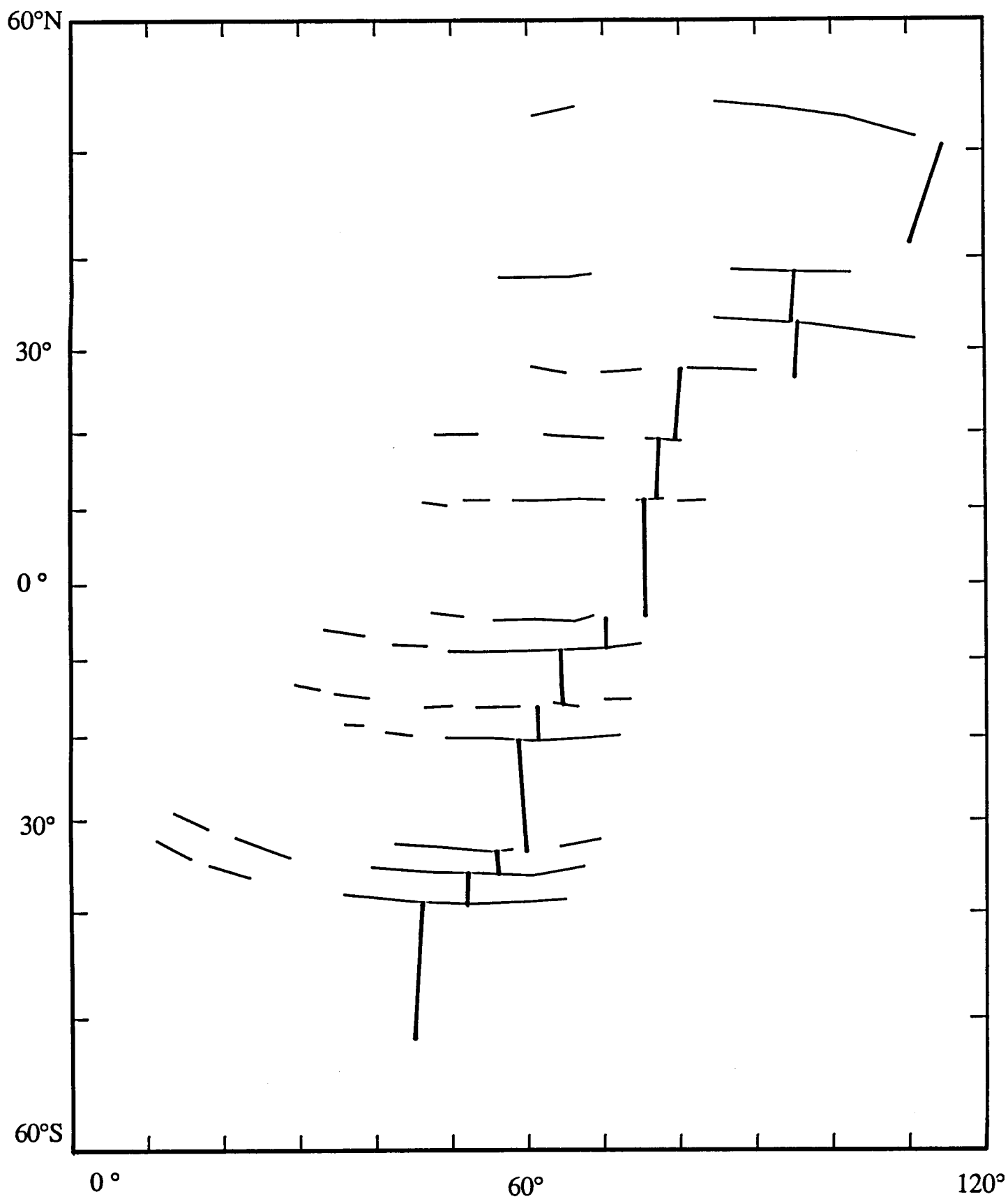


Figure 4.5

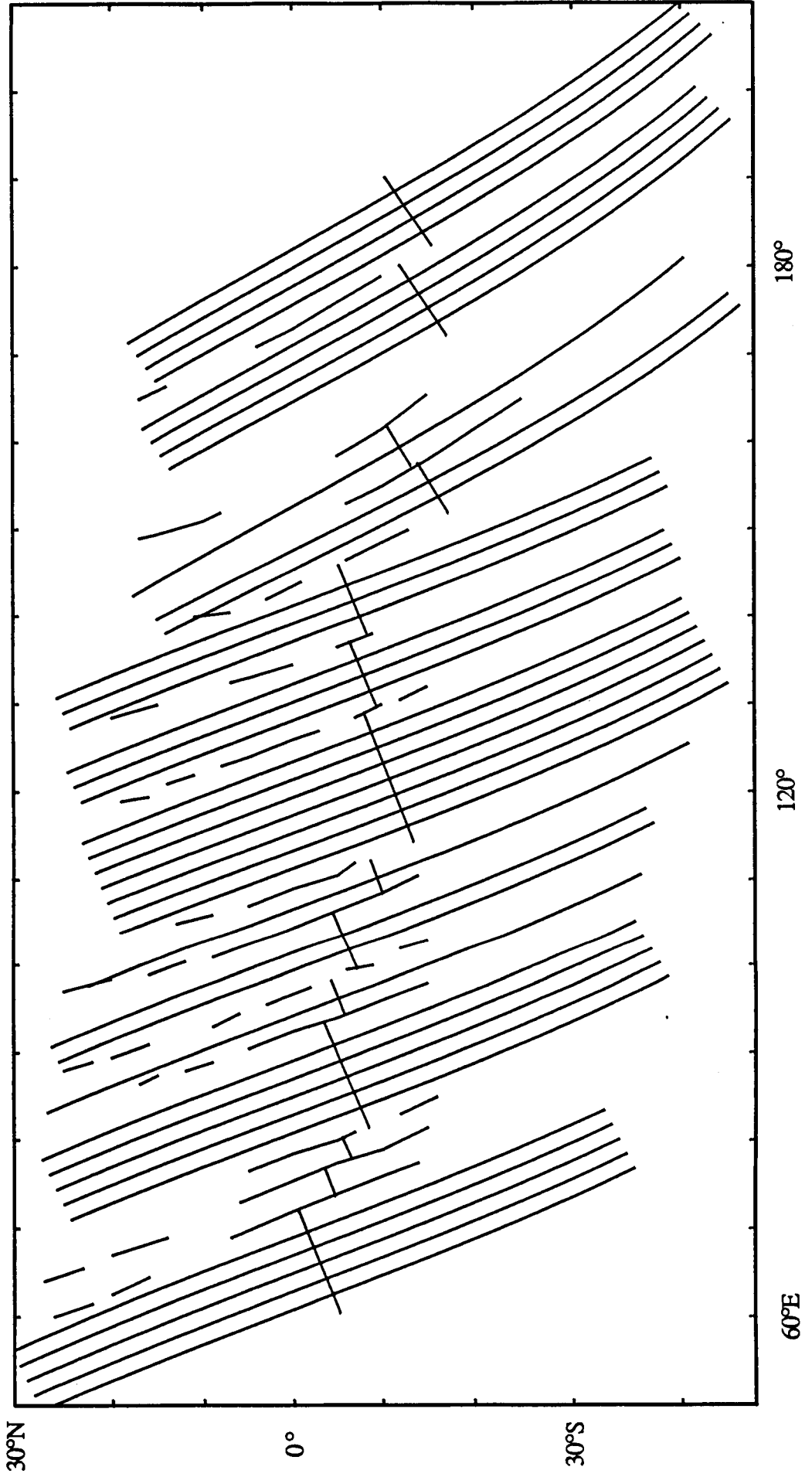


Figure 4.6

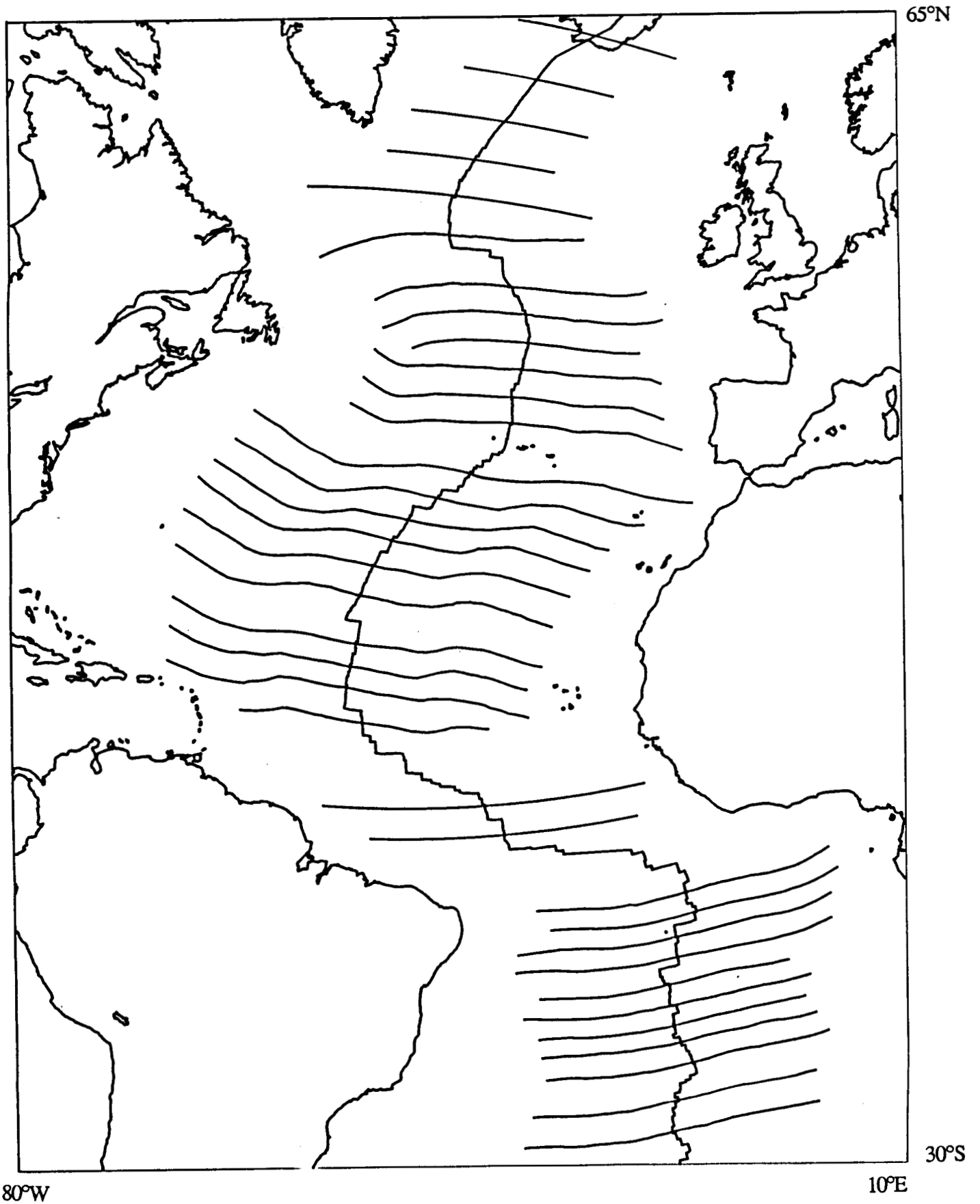


Figure 4.7

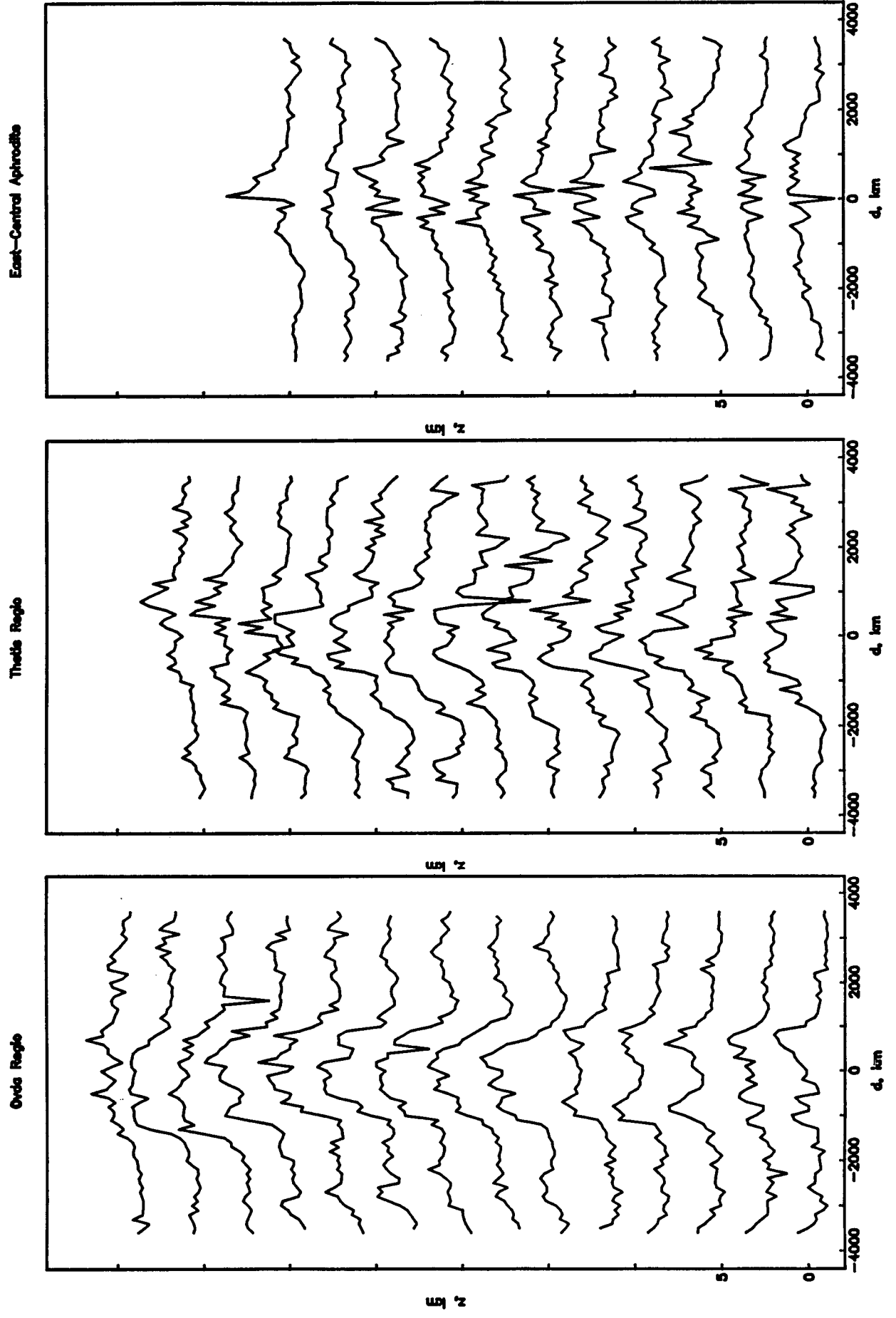


Figure 4.8

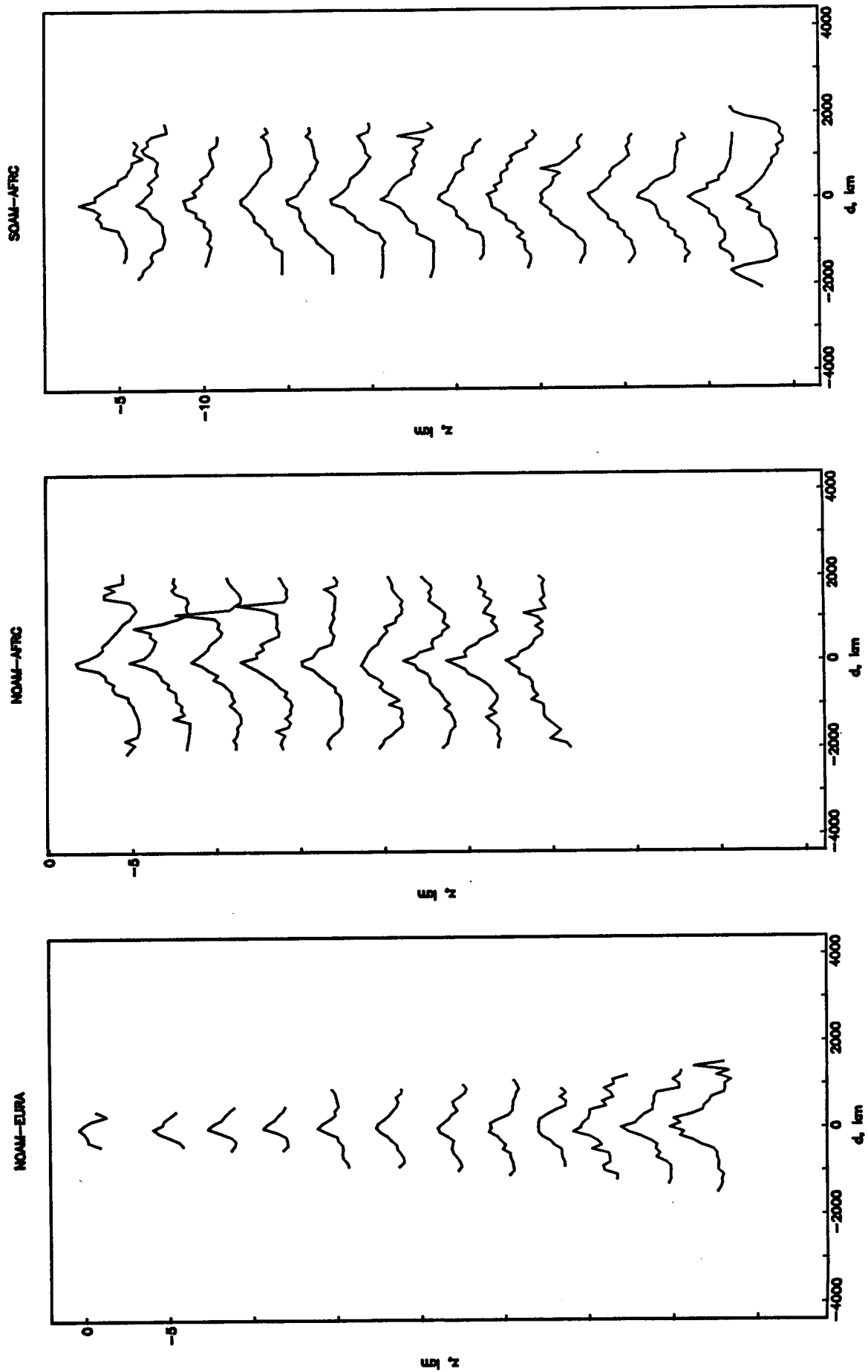


Figure 4.9

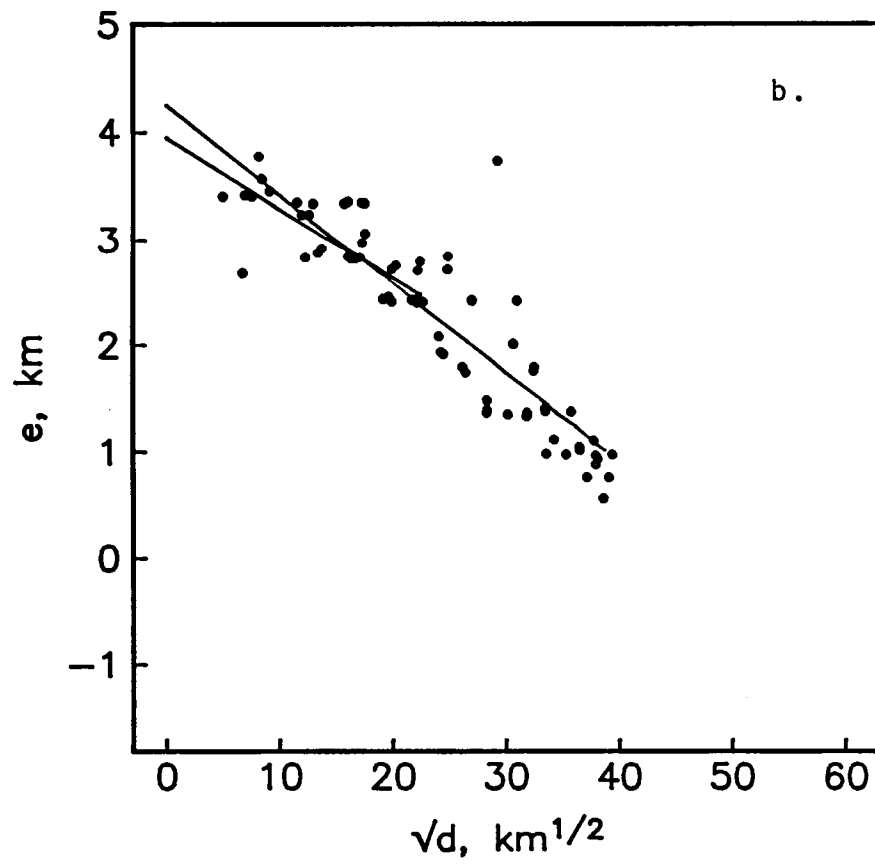
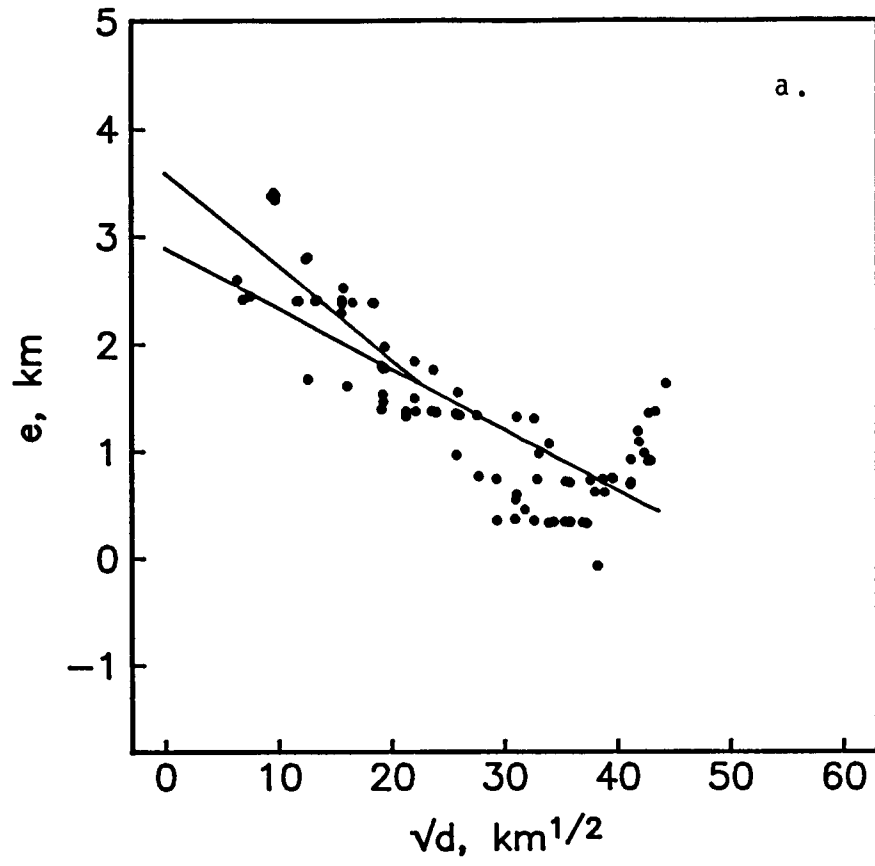


Fig. 4.10ab

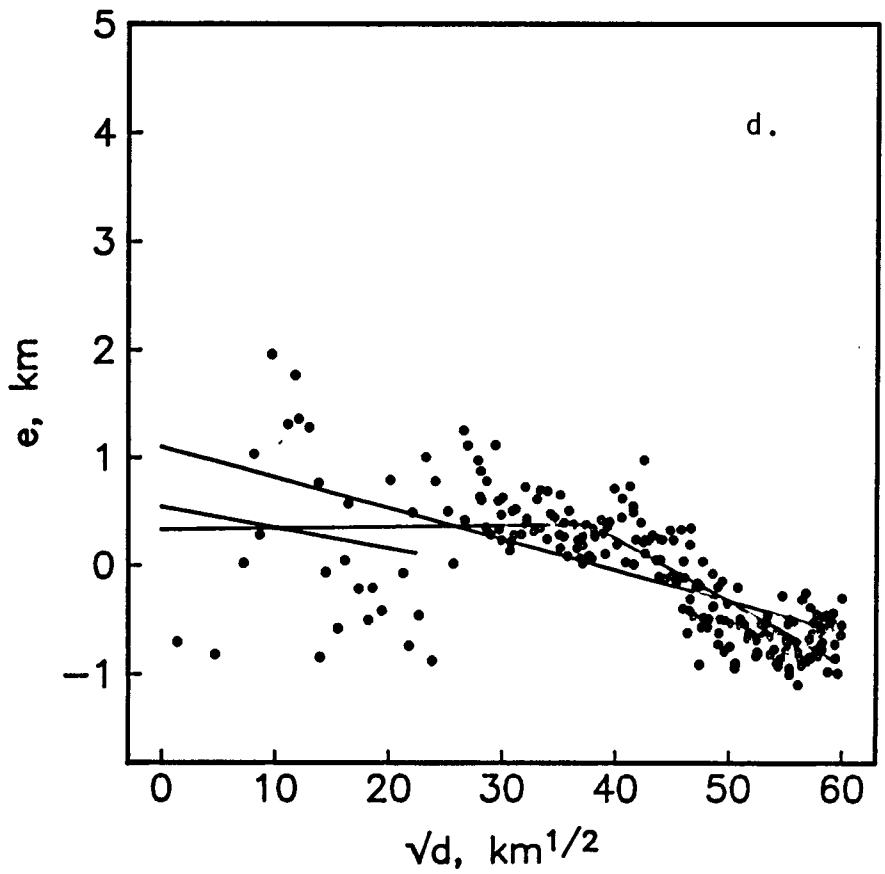
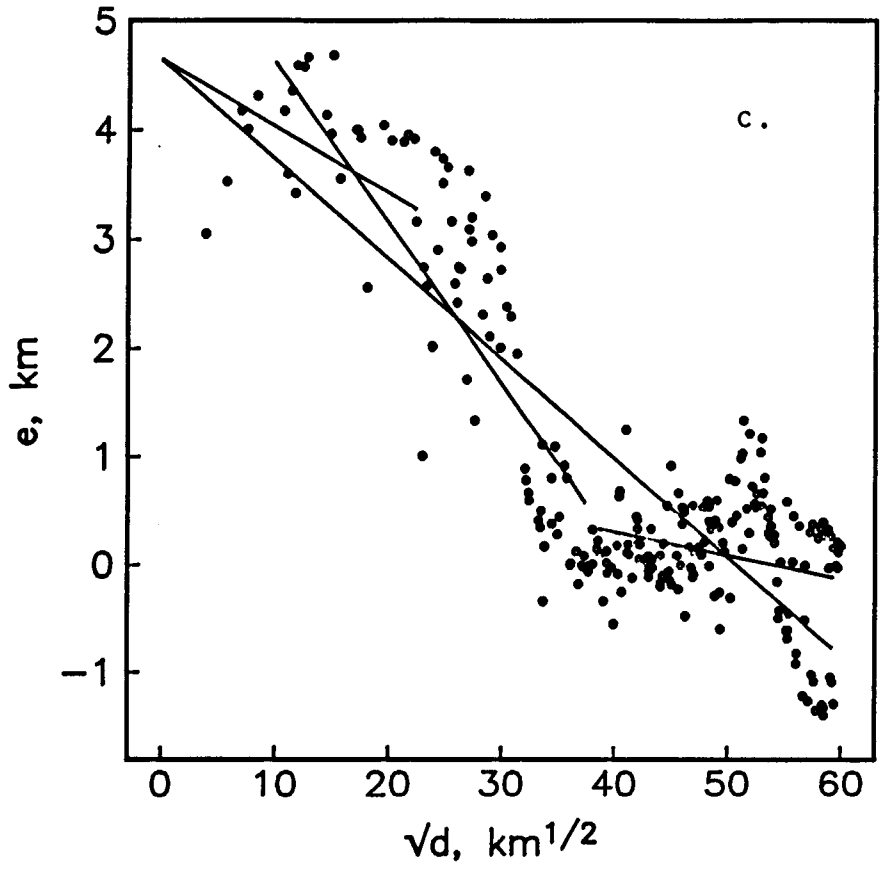


Fig. 4.10cd

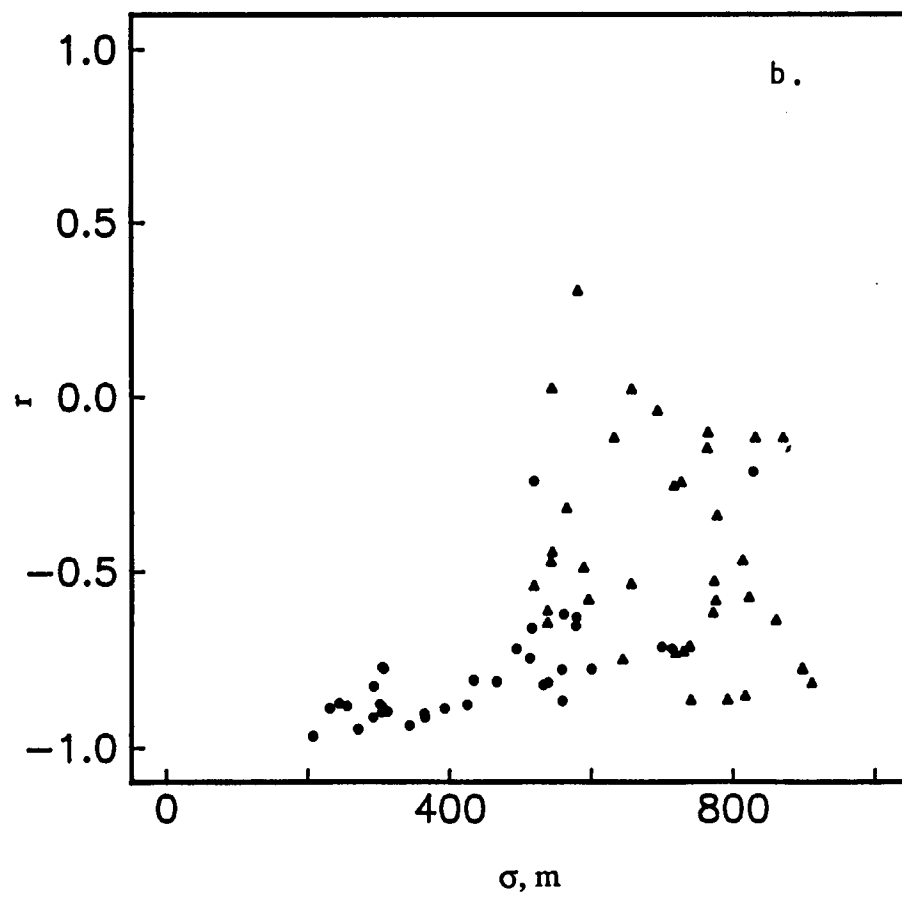
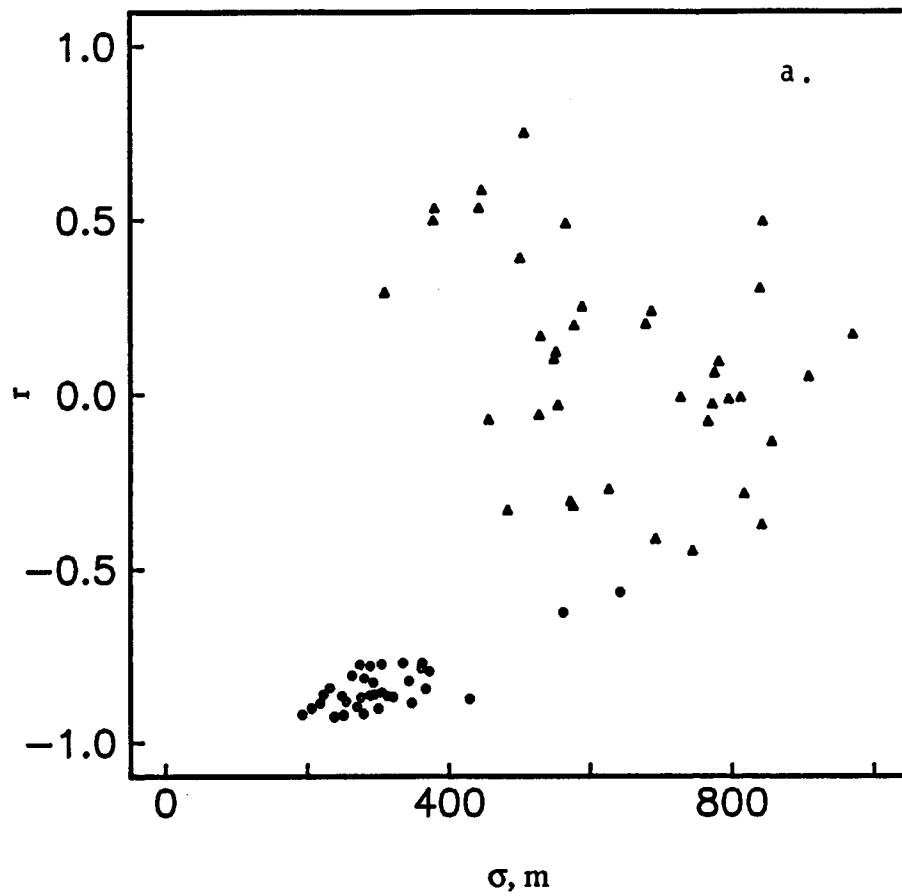


Fig. 4.11ab

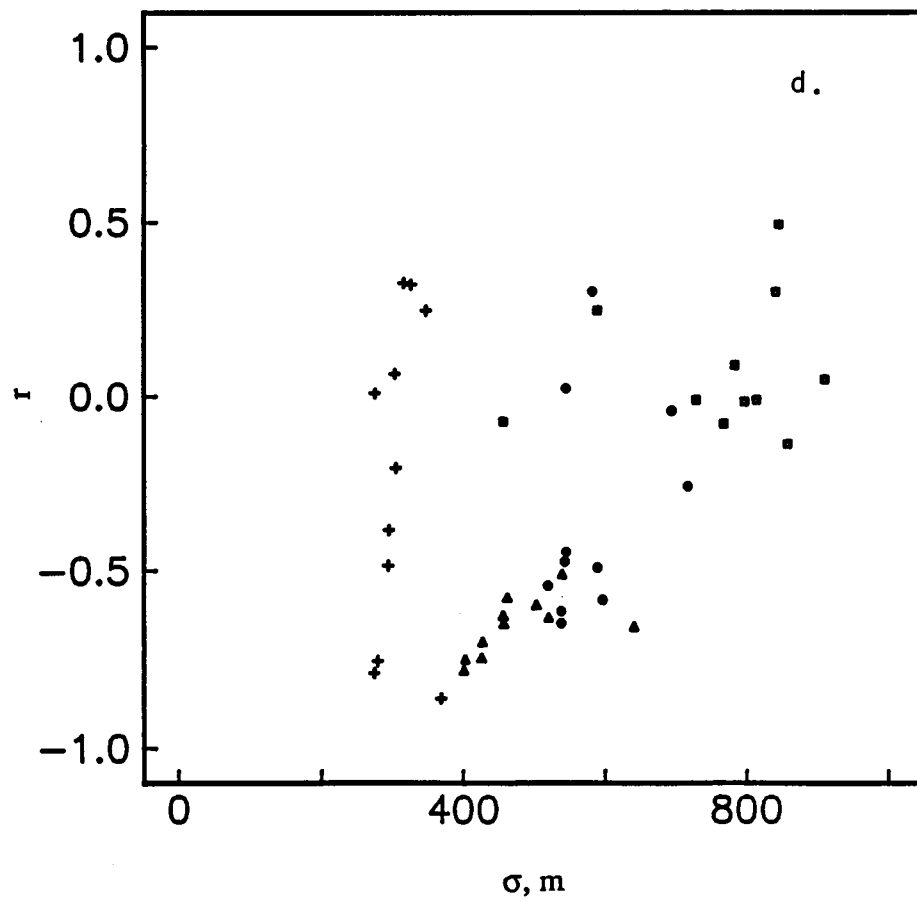
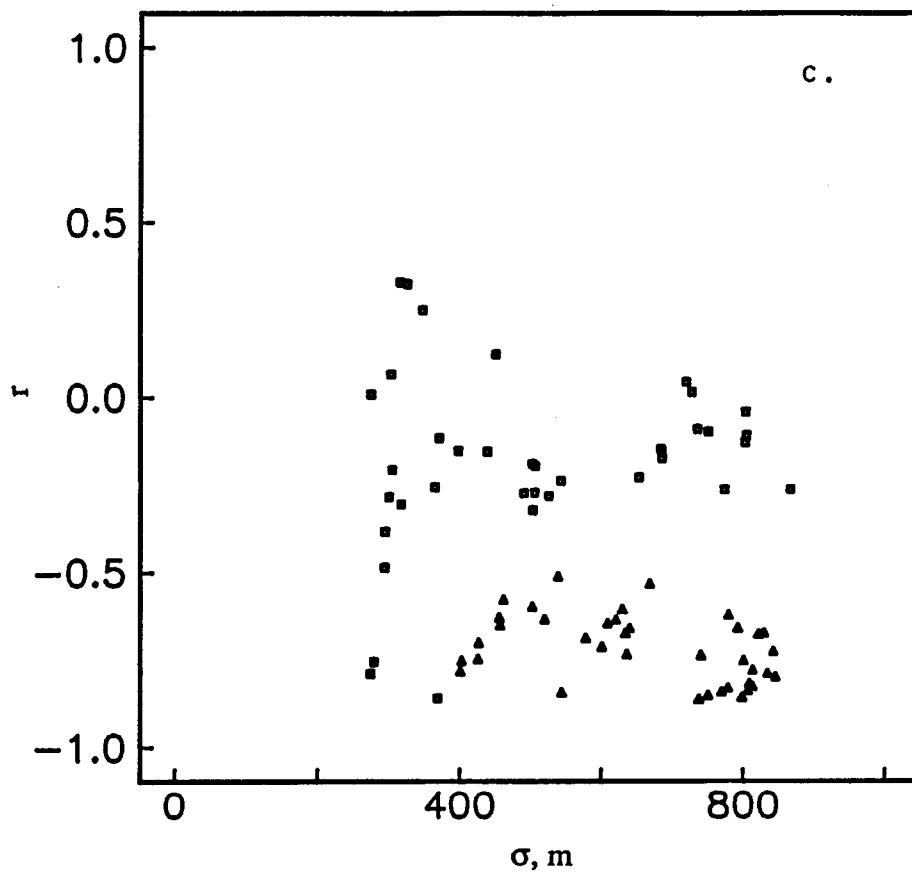


Fig. 4.11cd

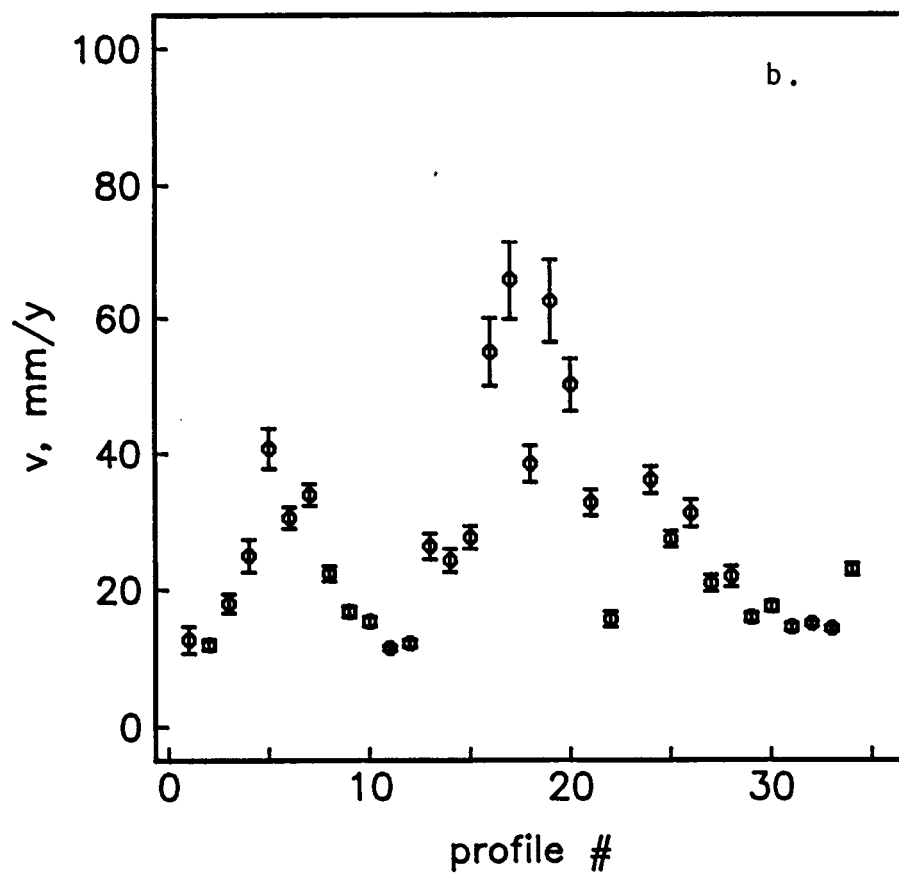
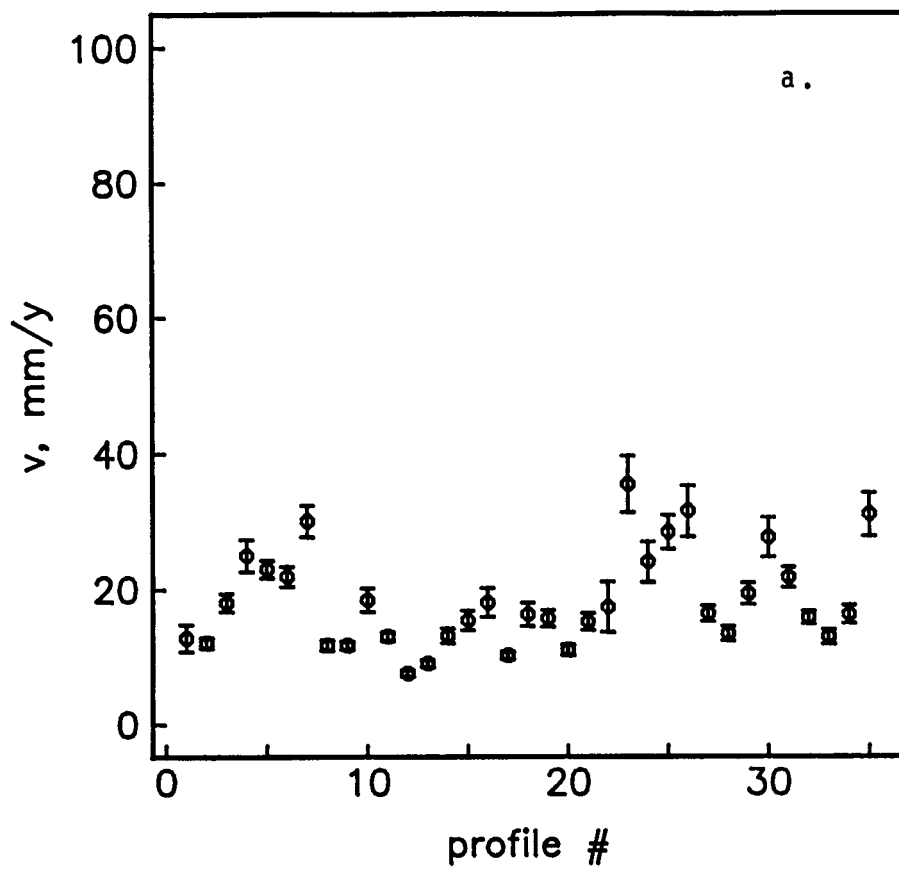


Fig. 4.12ab

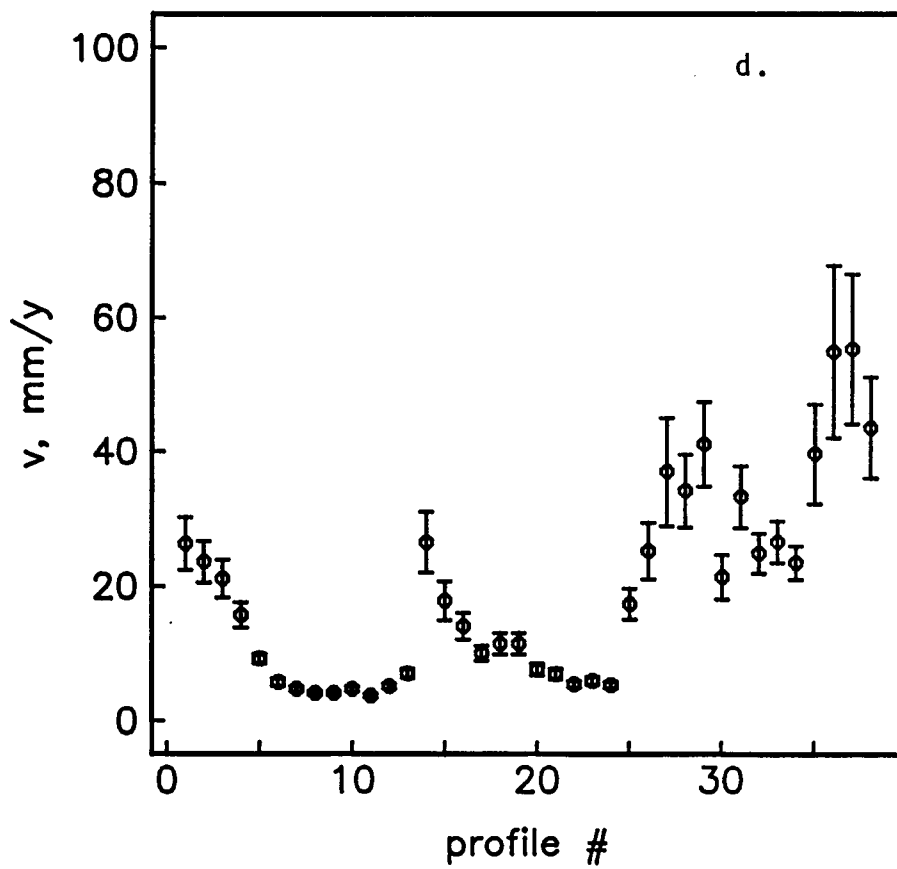
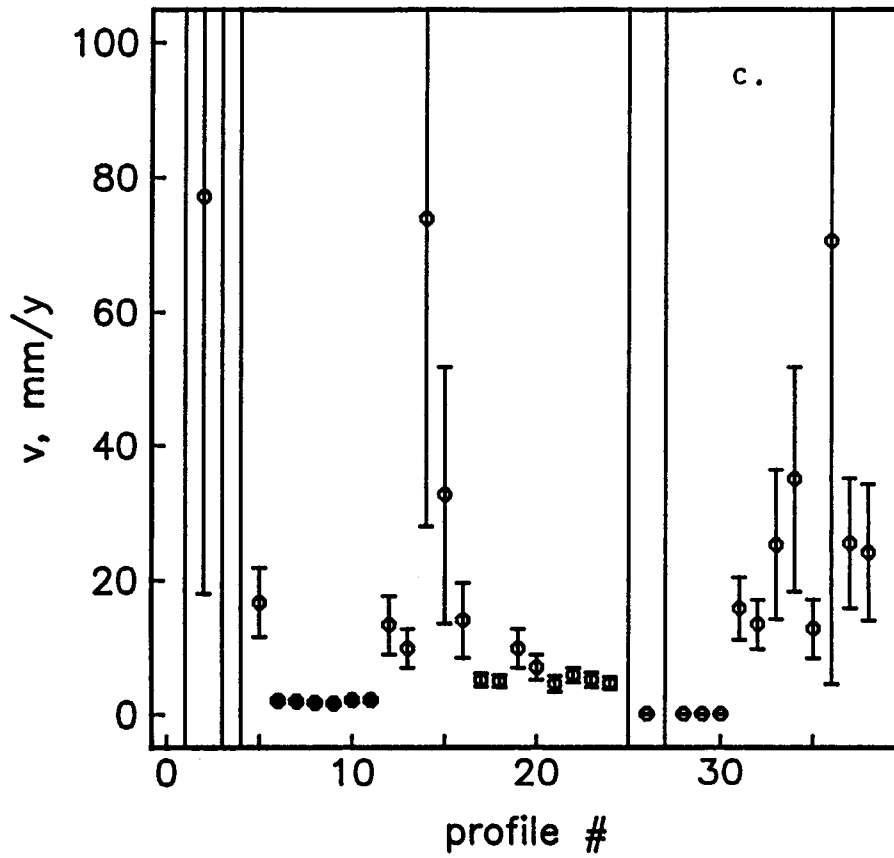


Fig. 4.12cd

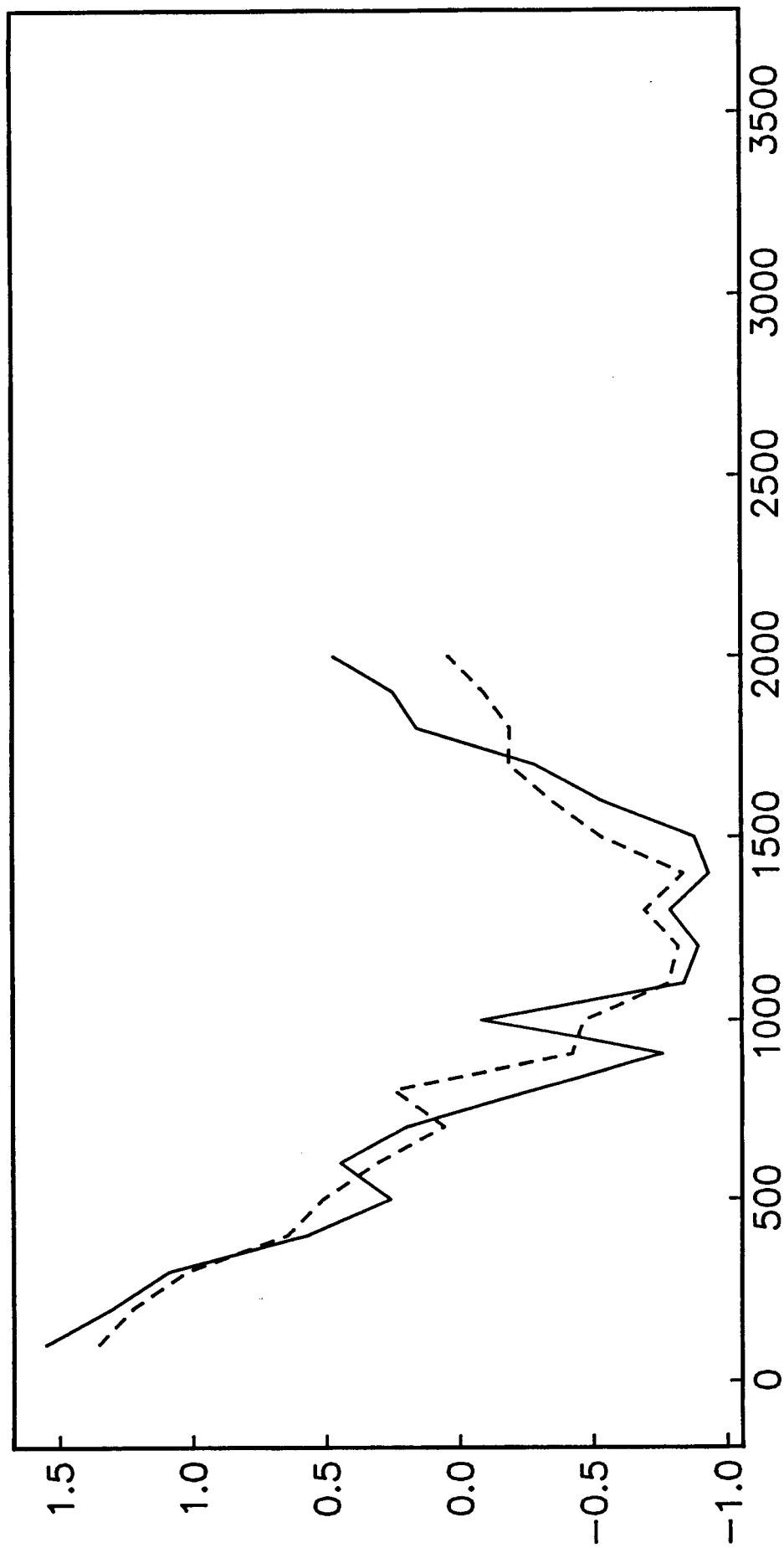


Fig. 4.13a

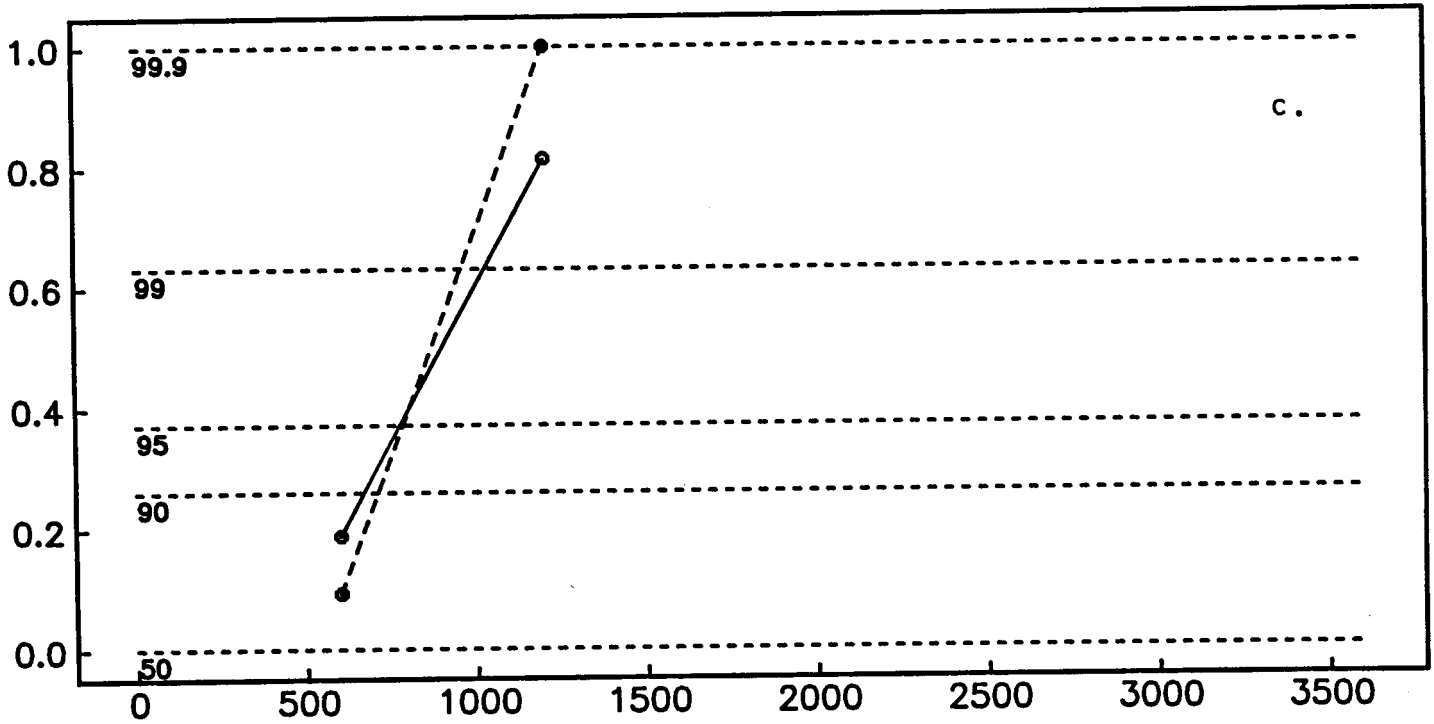
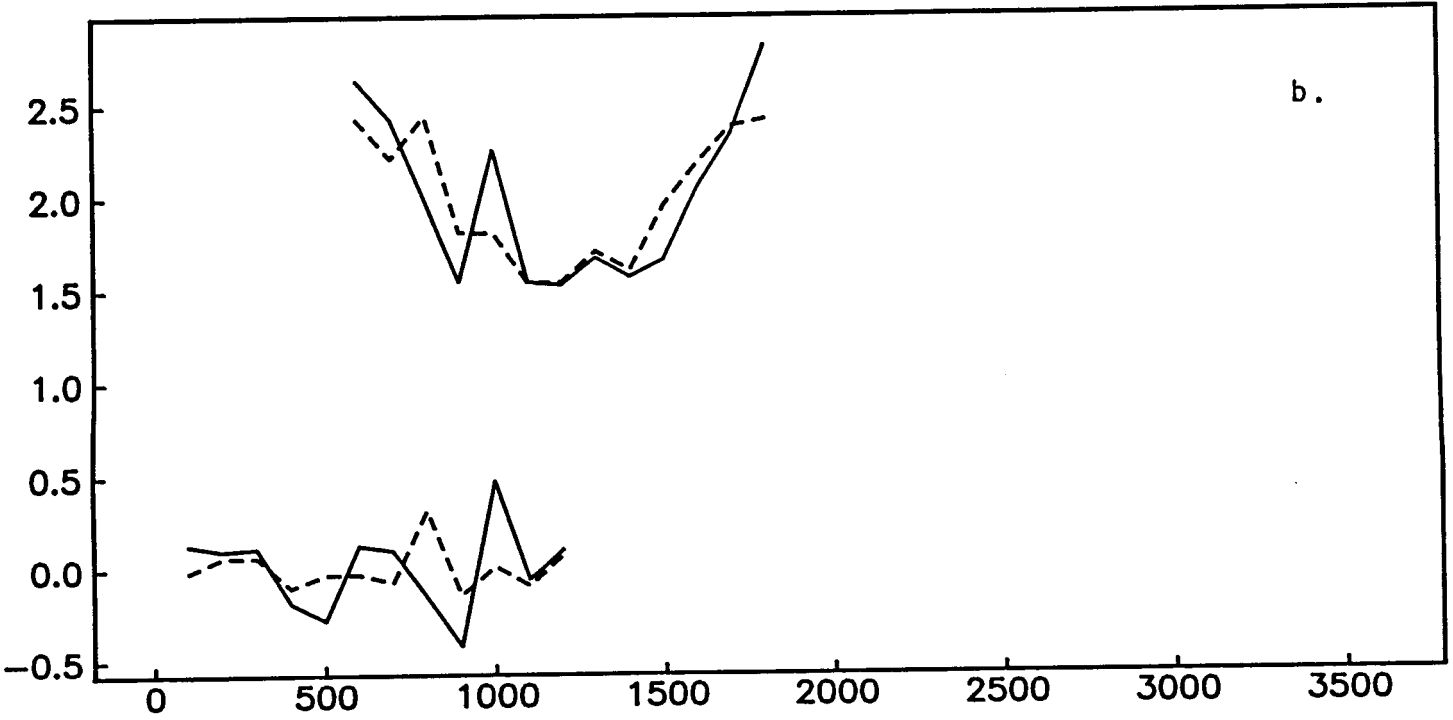


Fig. 4.13bc

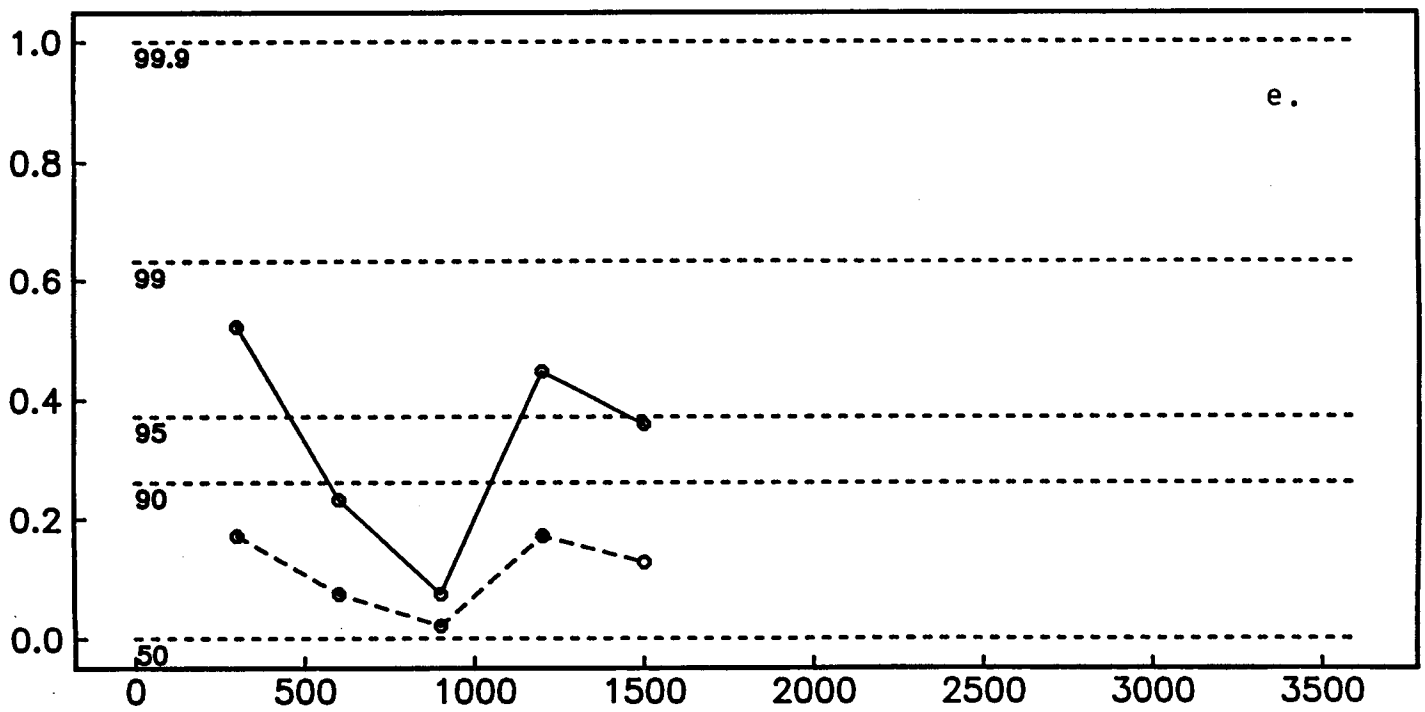
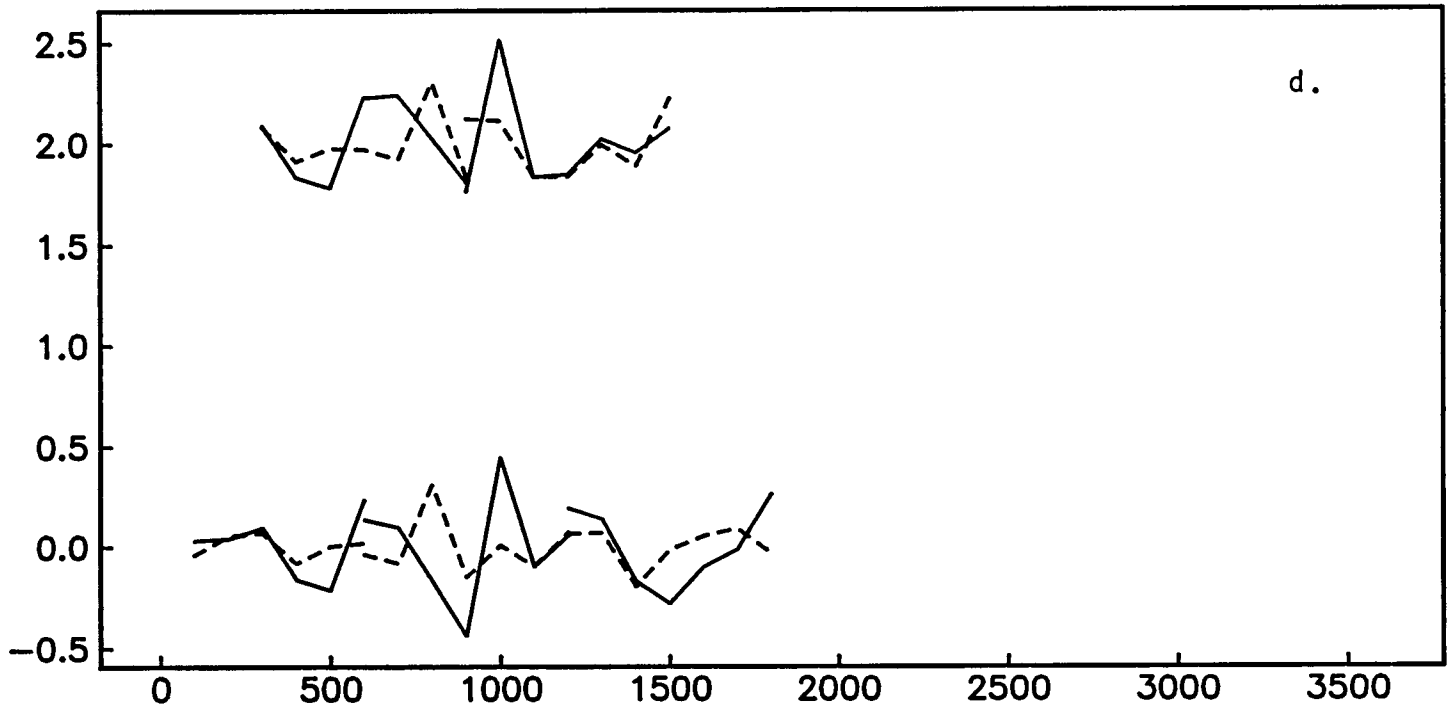


Fig. 4.13de

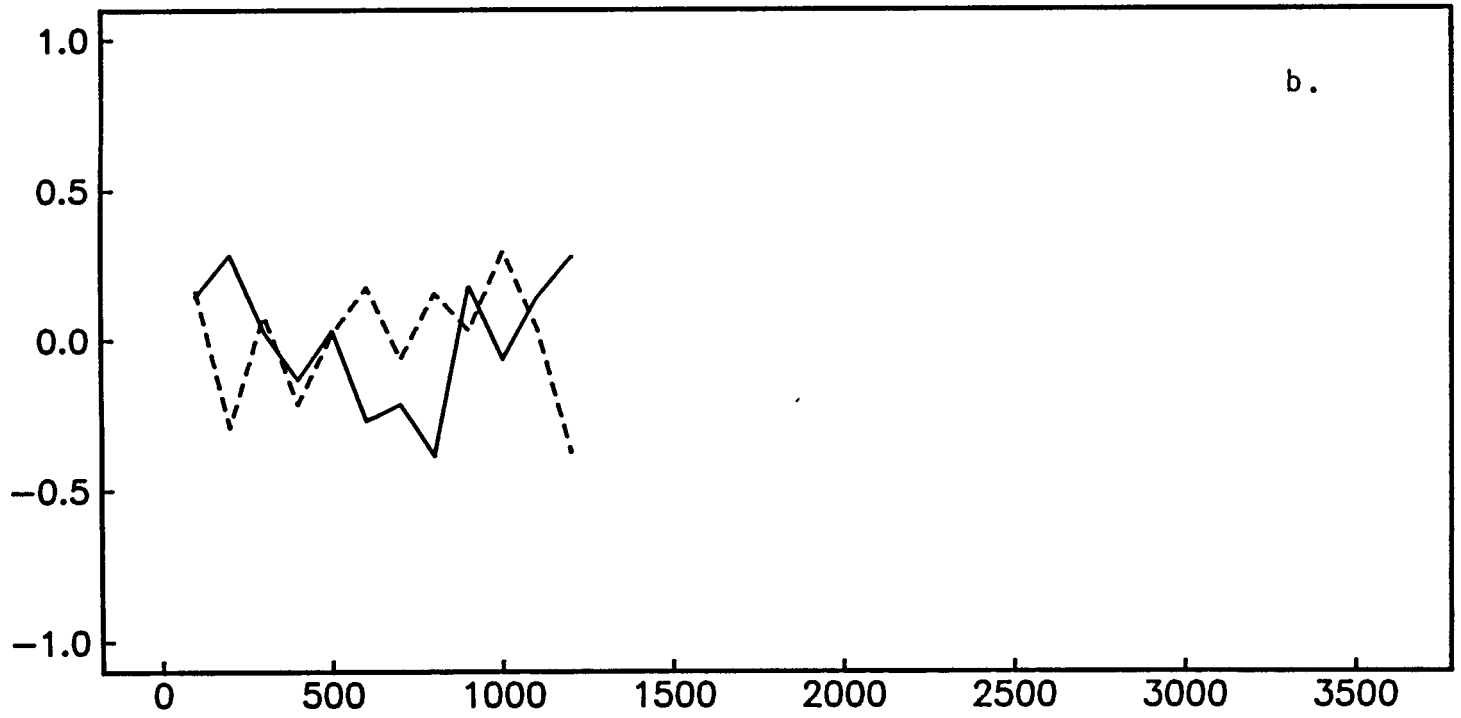
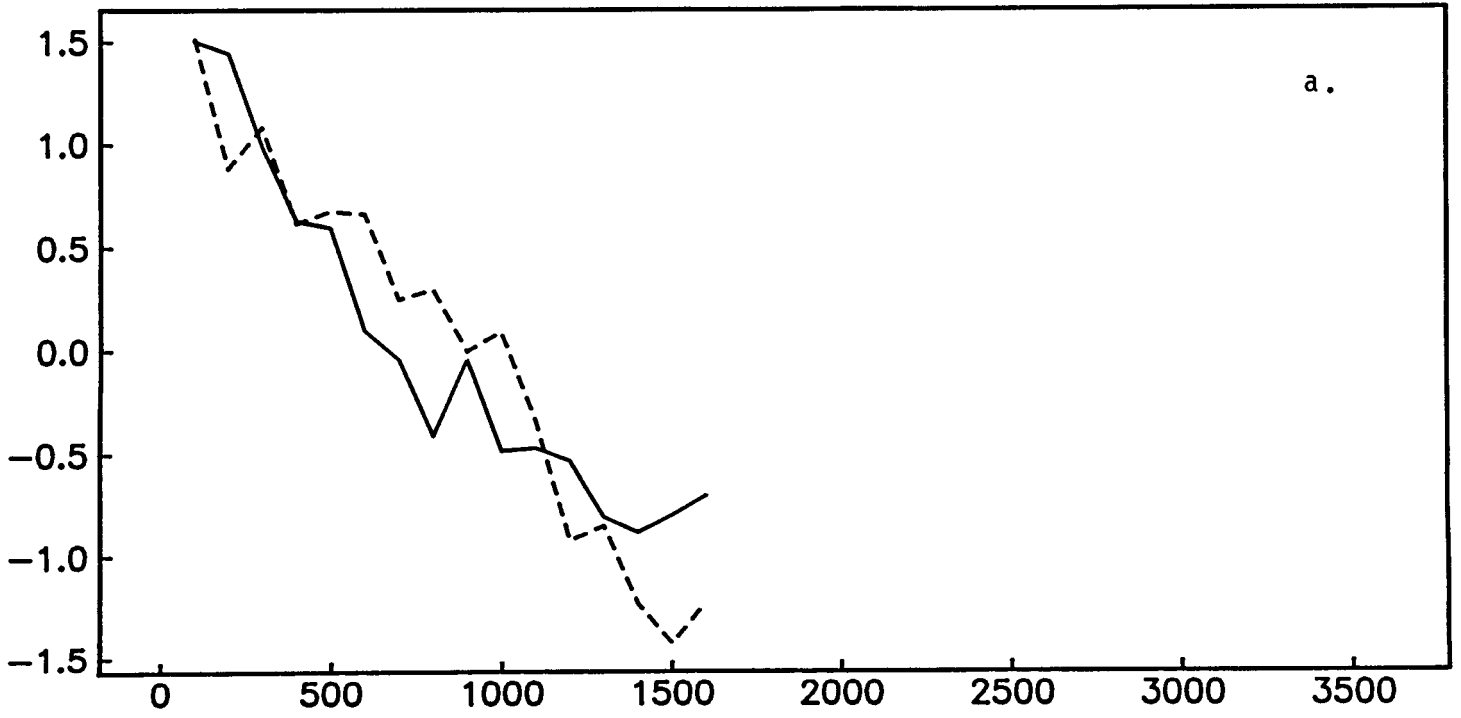
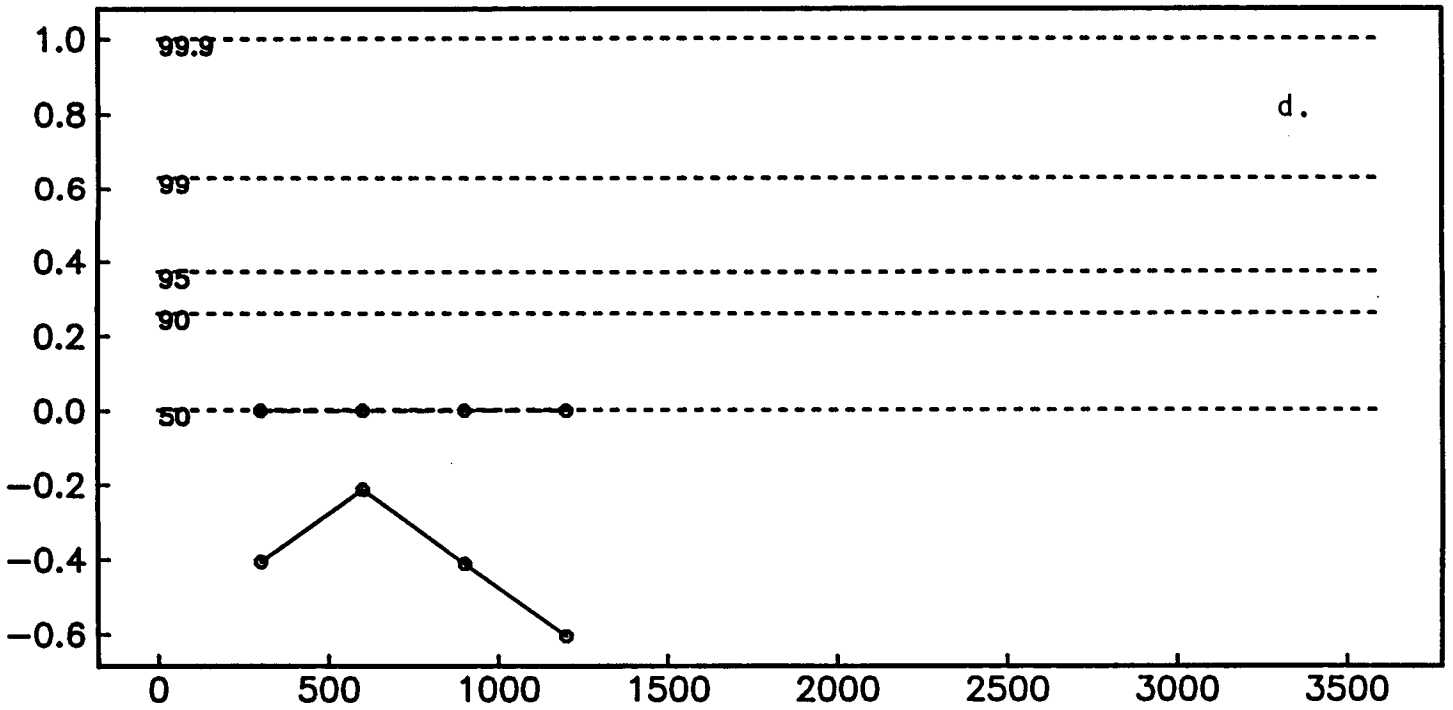
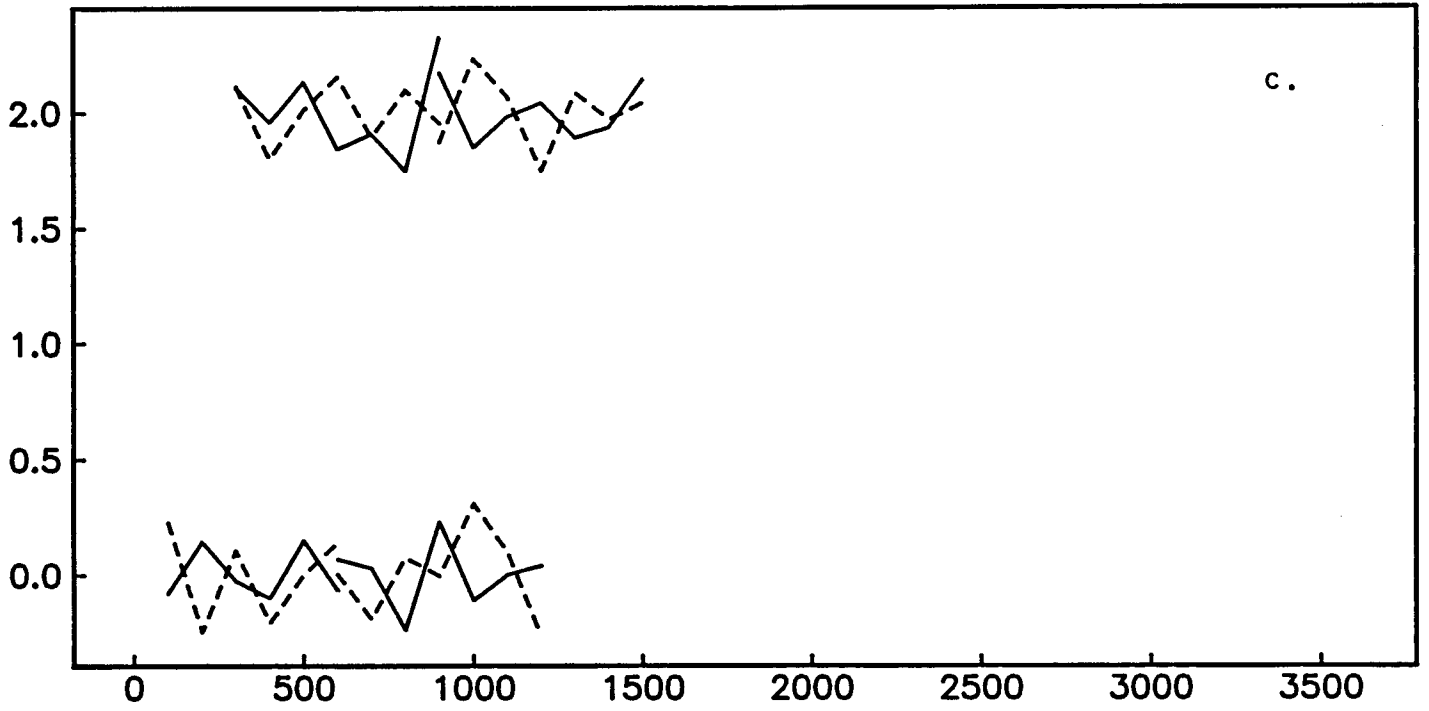


Fig. 4.14ab



C-3

Fig. 4.14cd

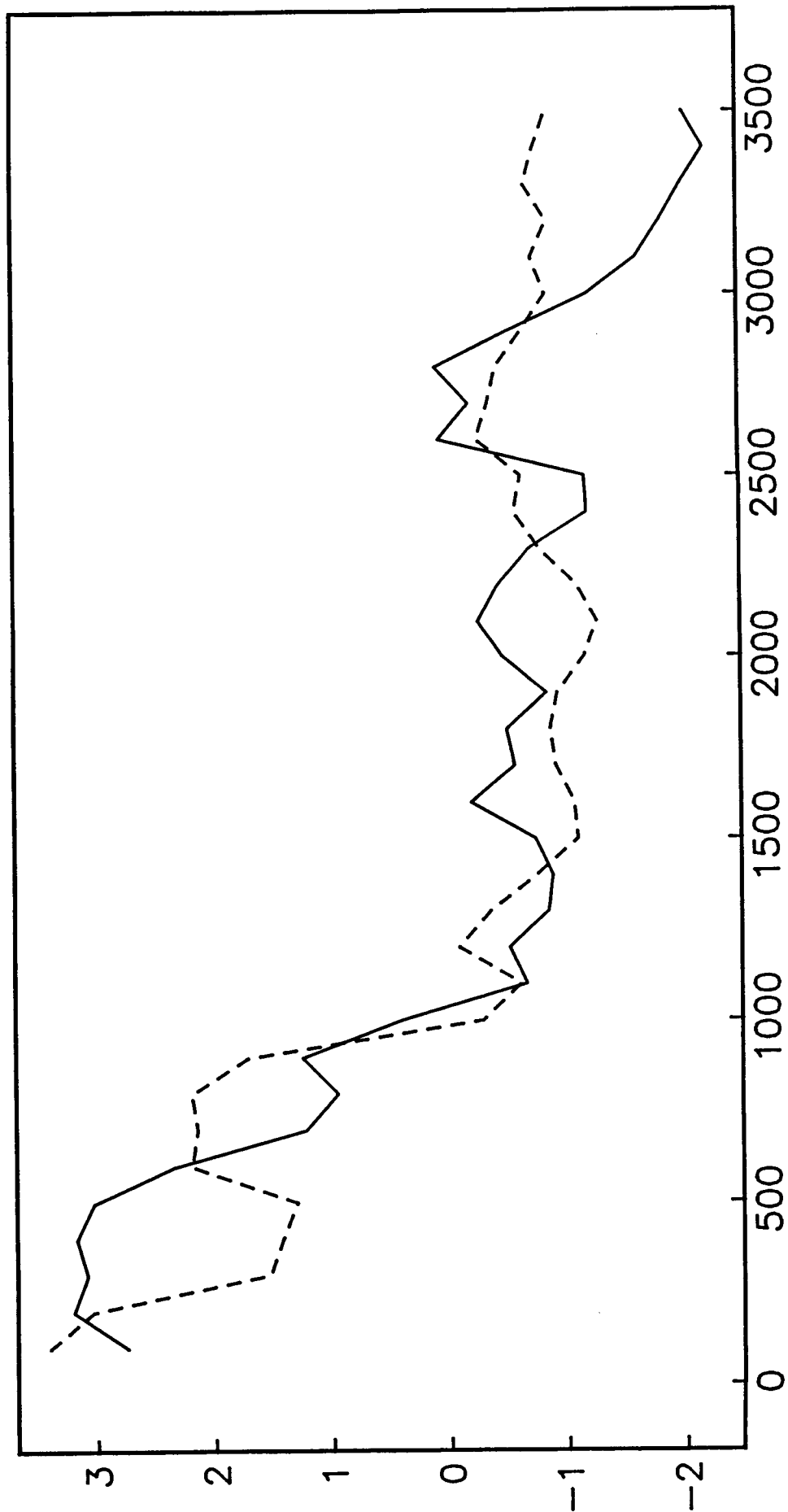


Fig. 15a.

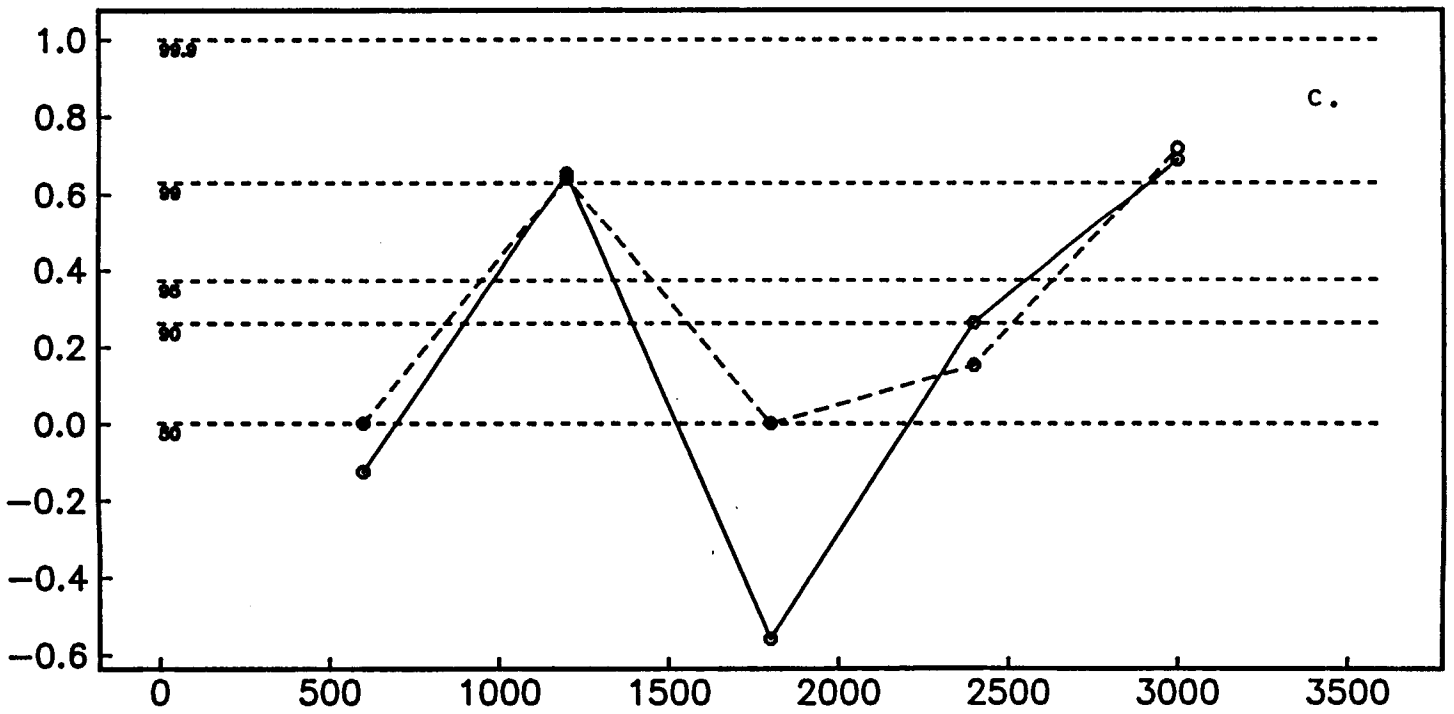
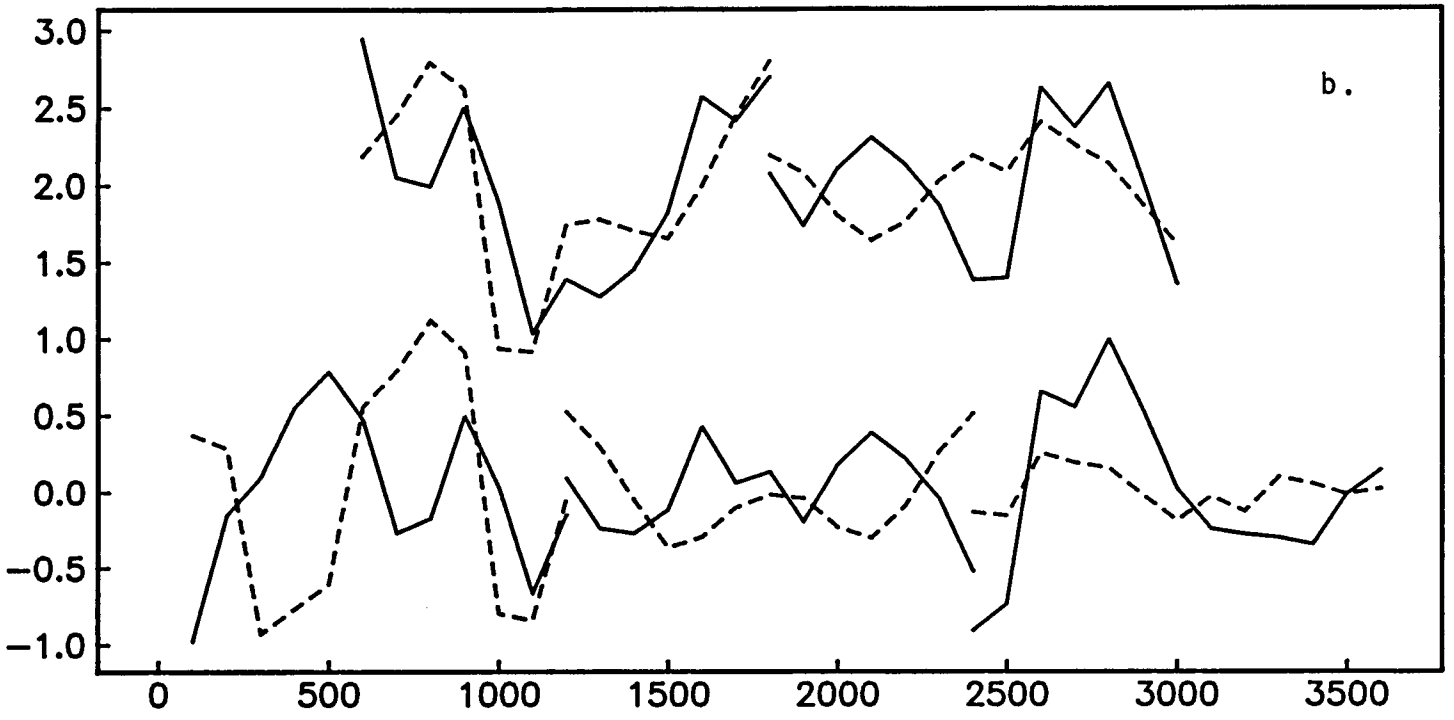


Fig. 4.15bc

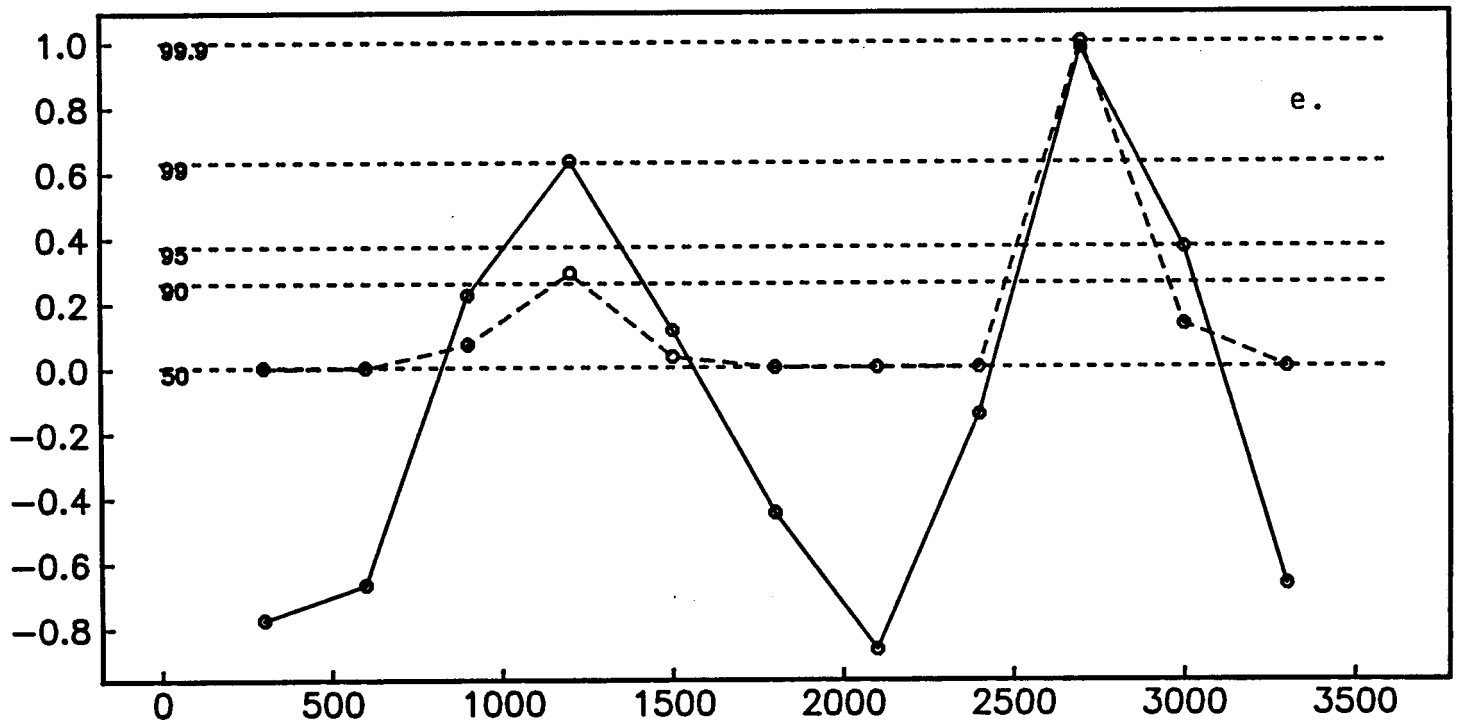
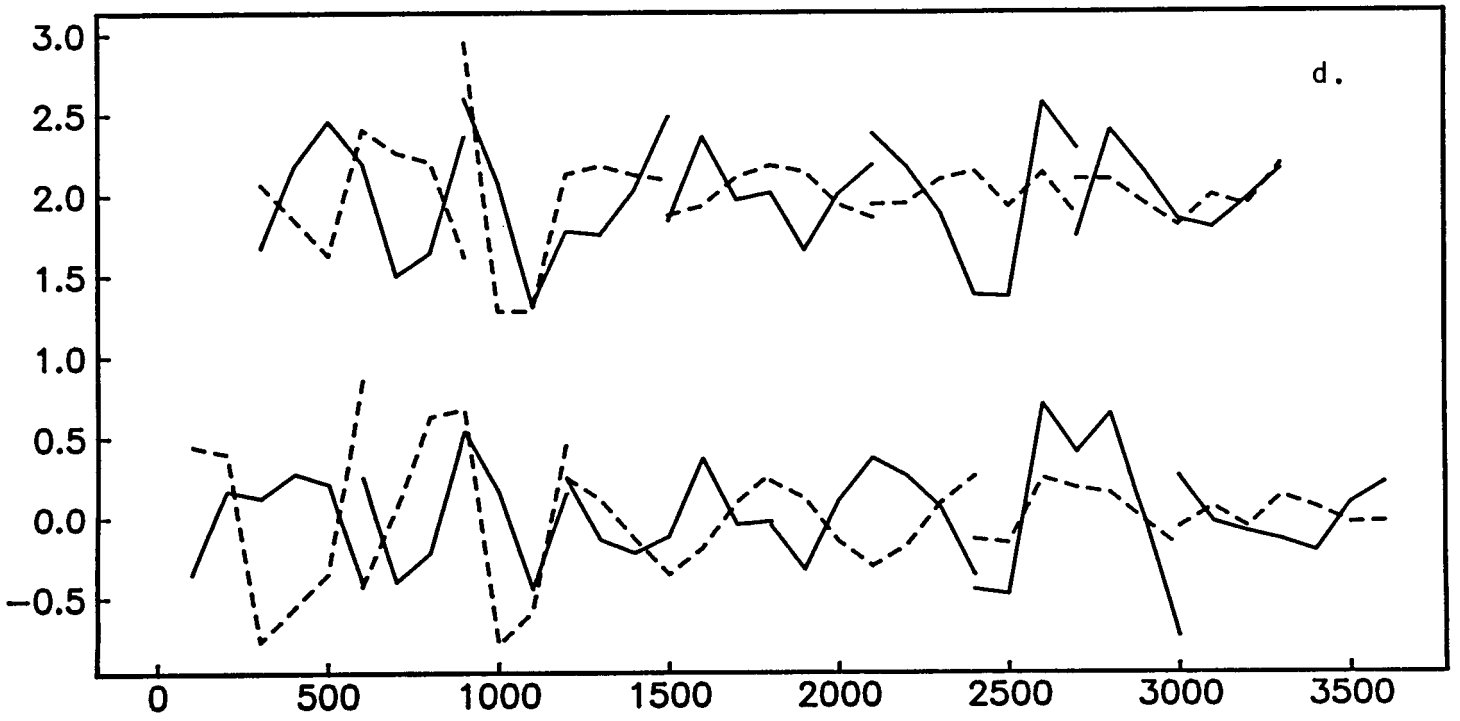


Fig. 4.15de

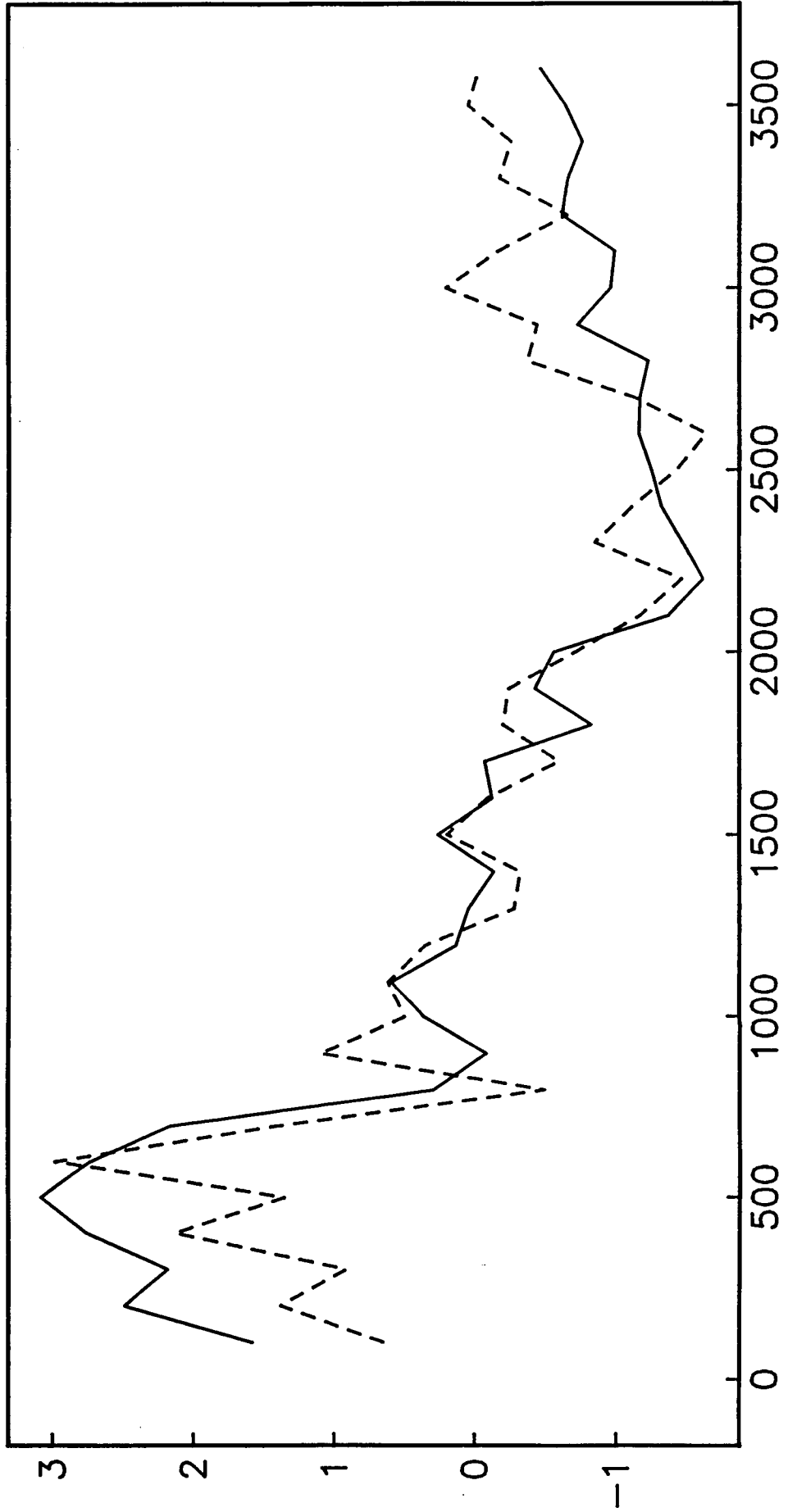


Fig. 4.16a

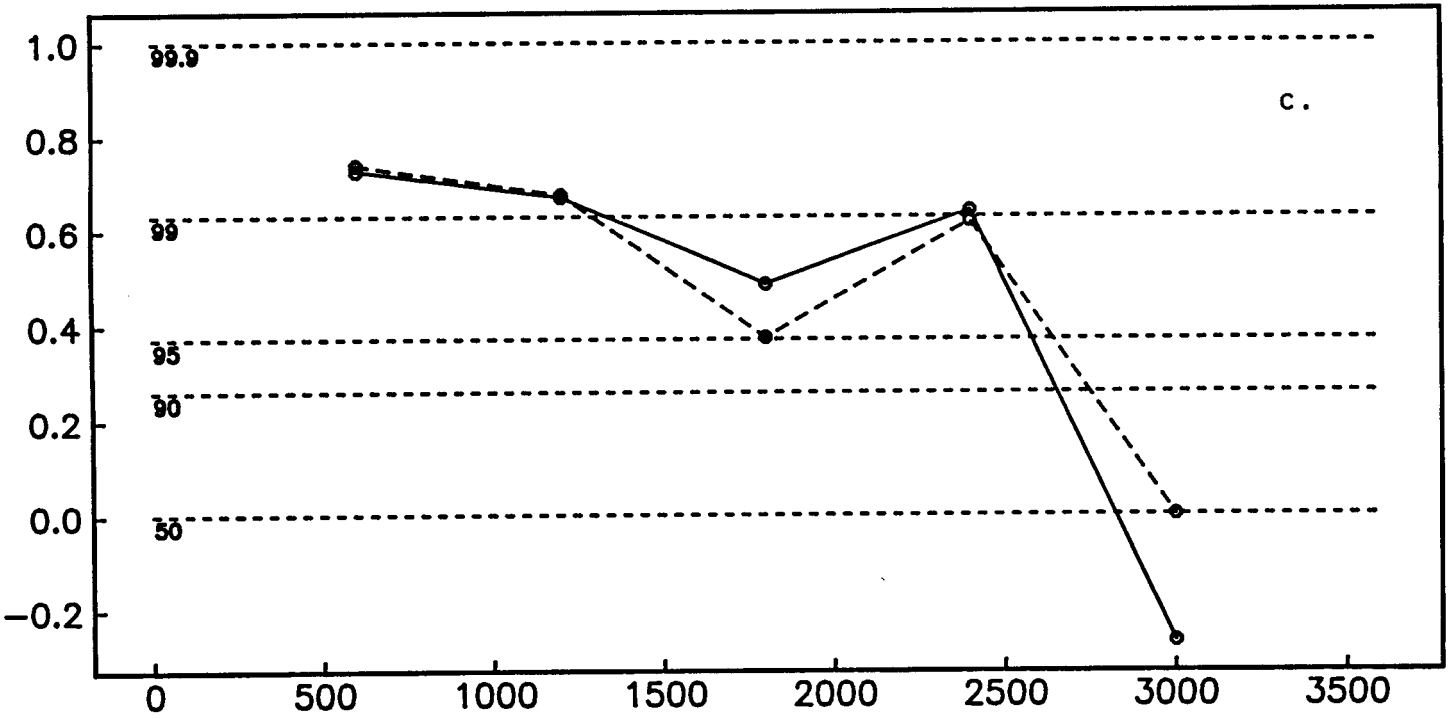
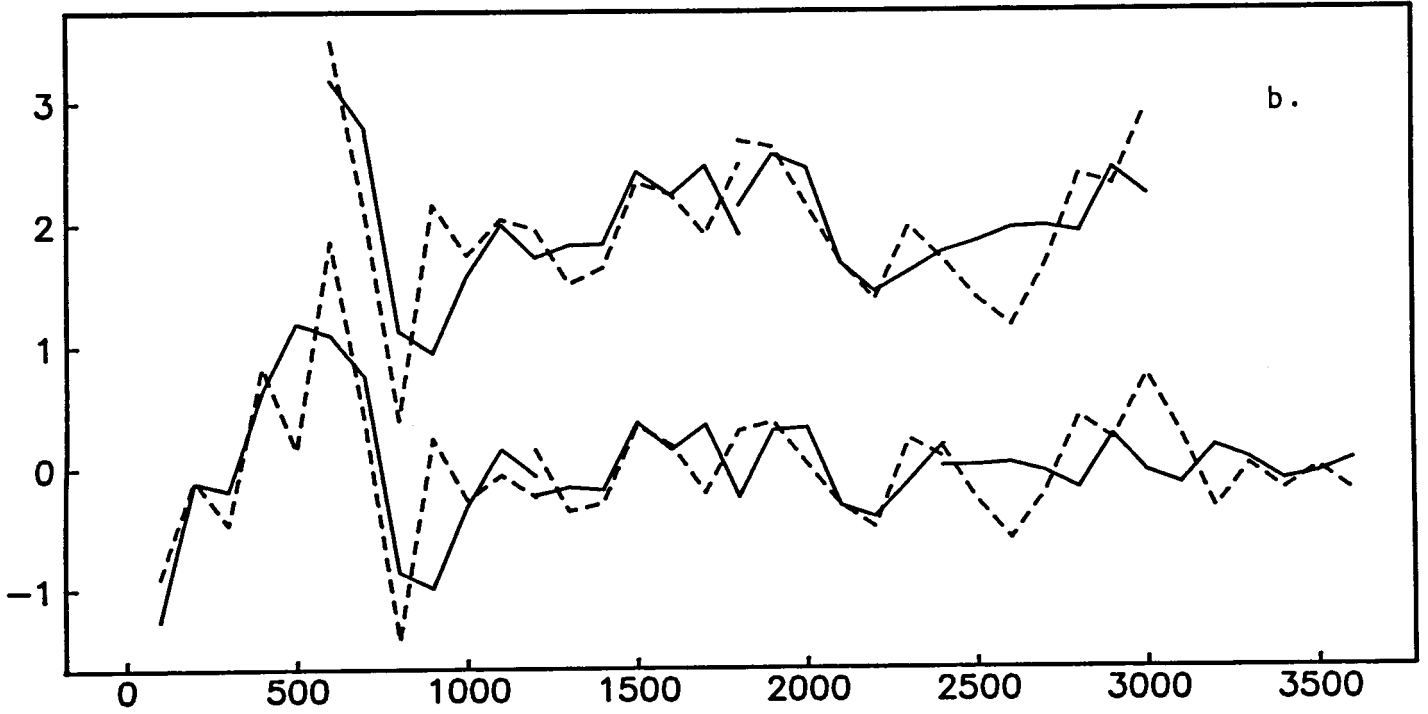


Fig. 4.16bc

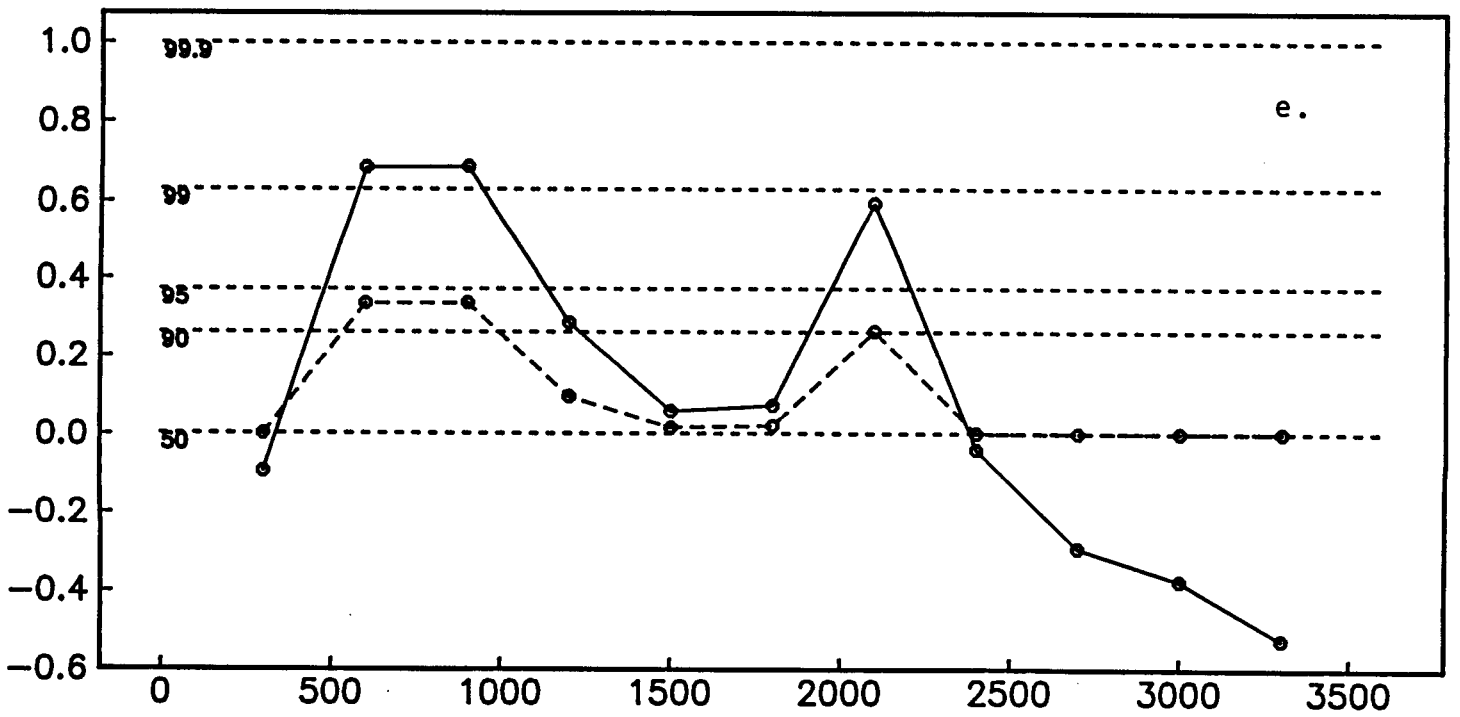
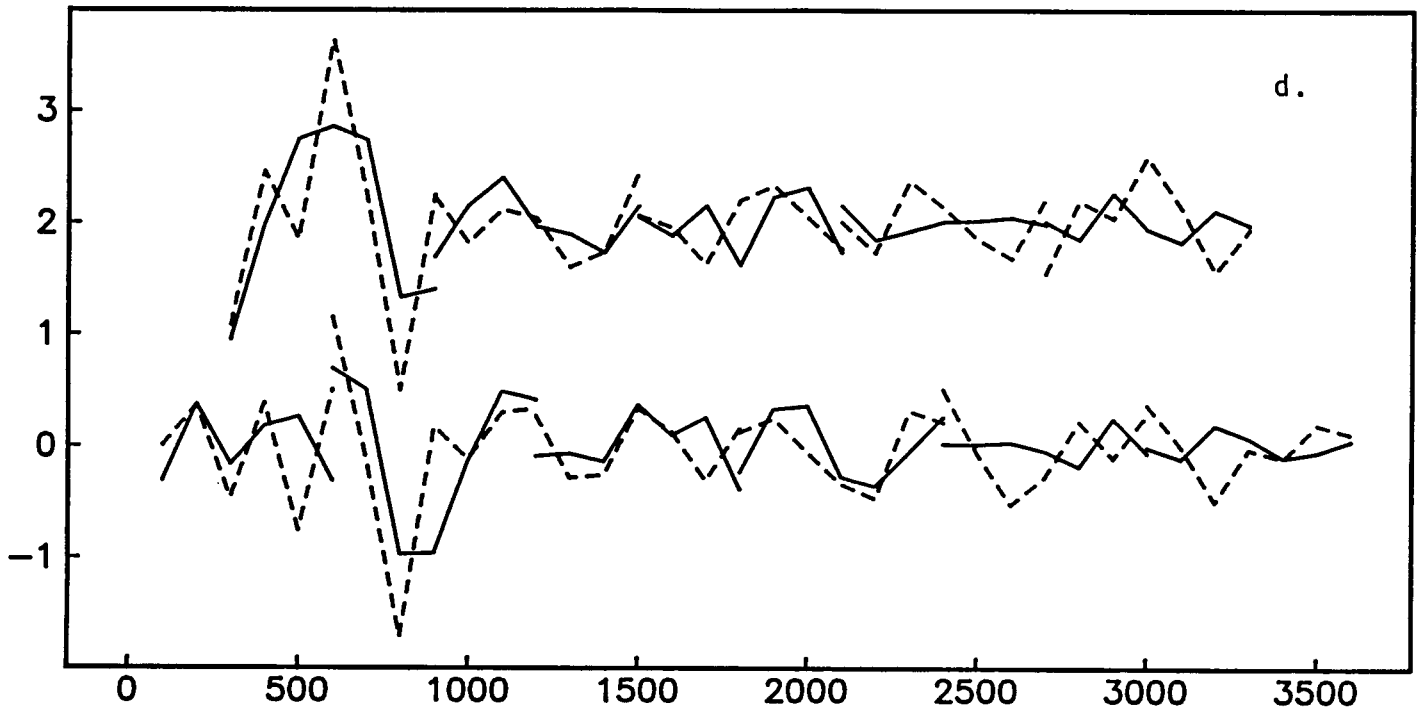


Fig. 4.16de

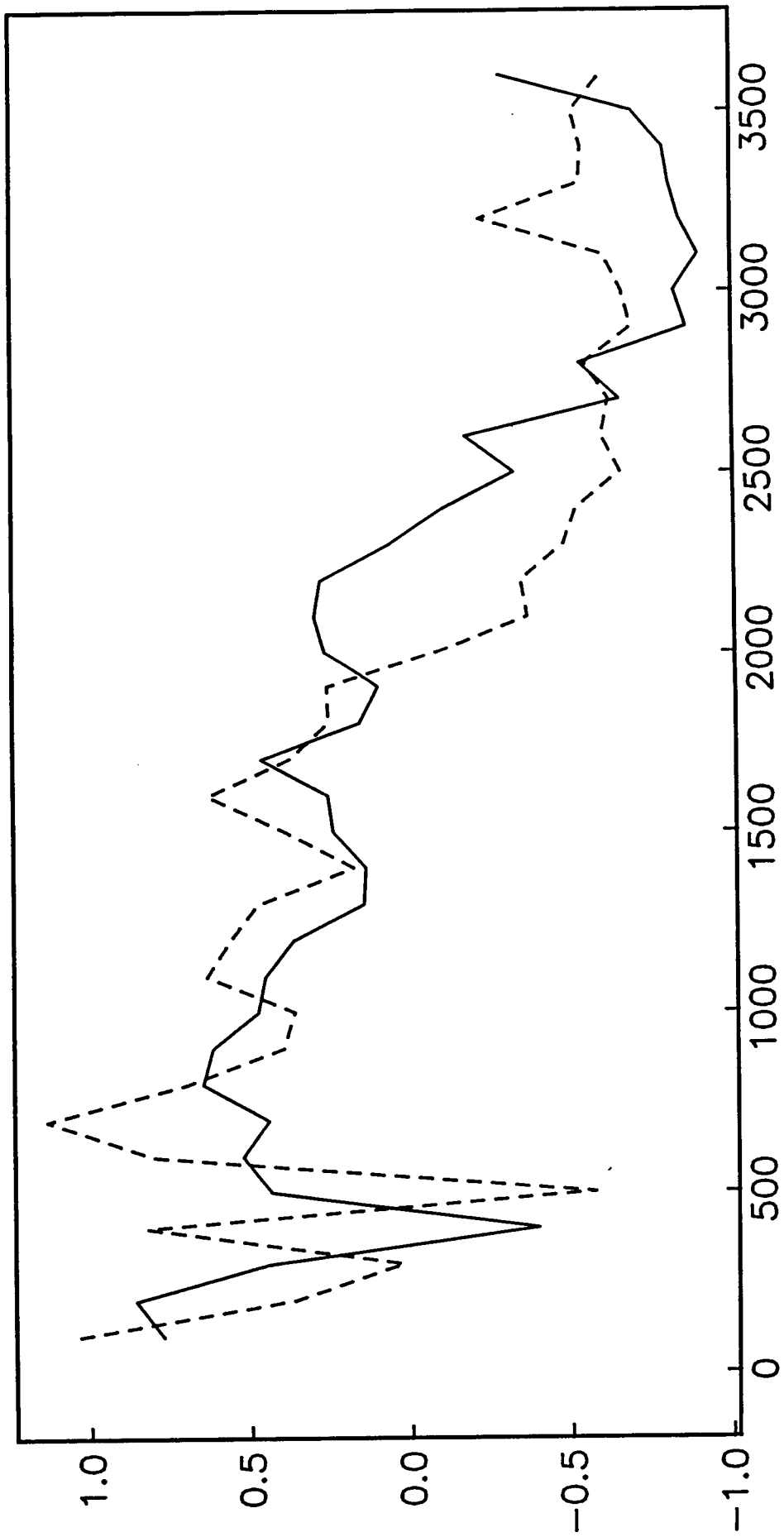


Fig. 4.17a

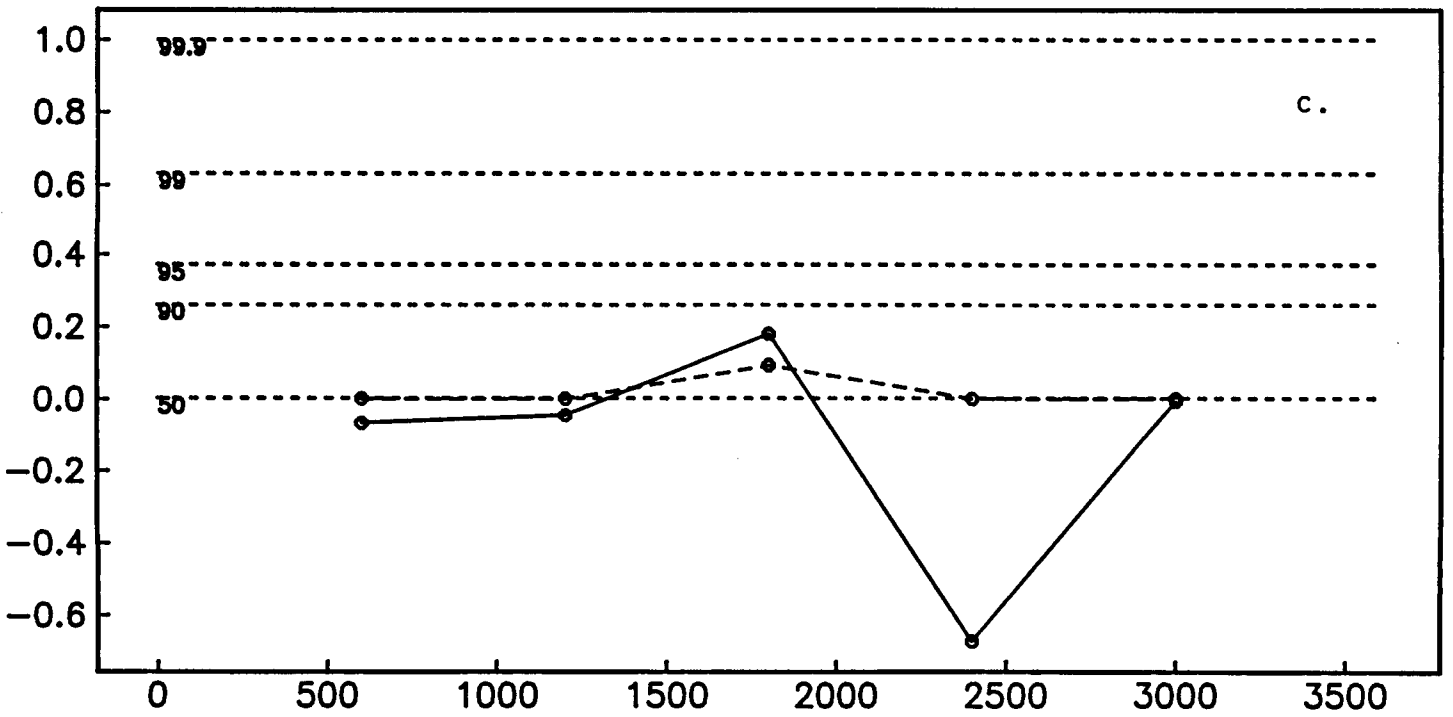
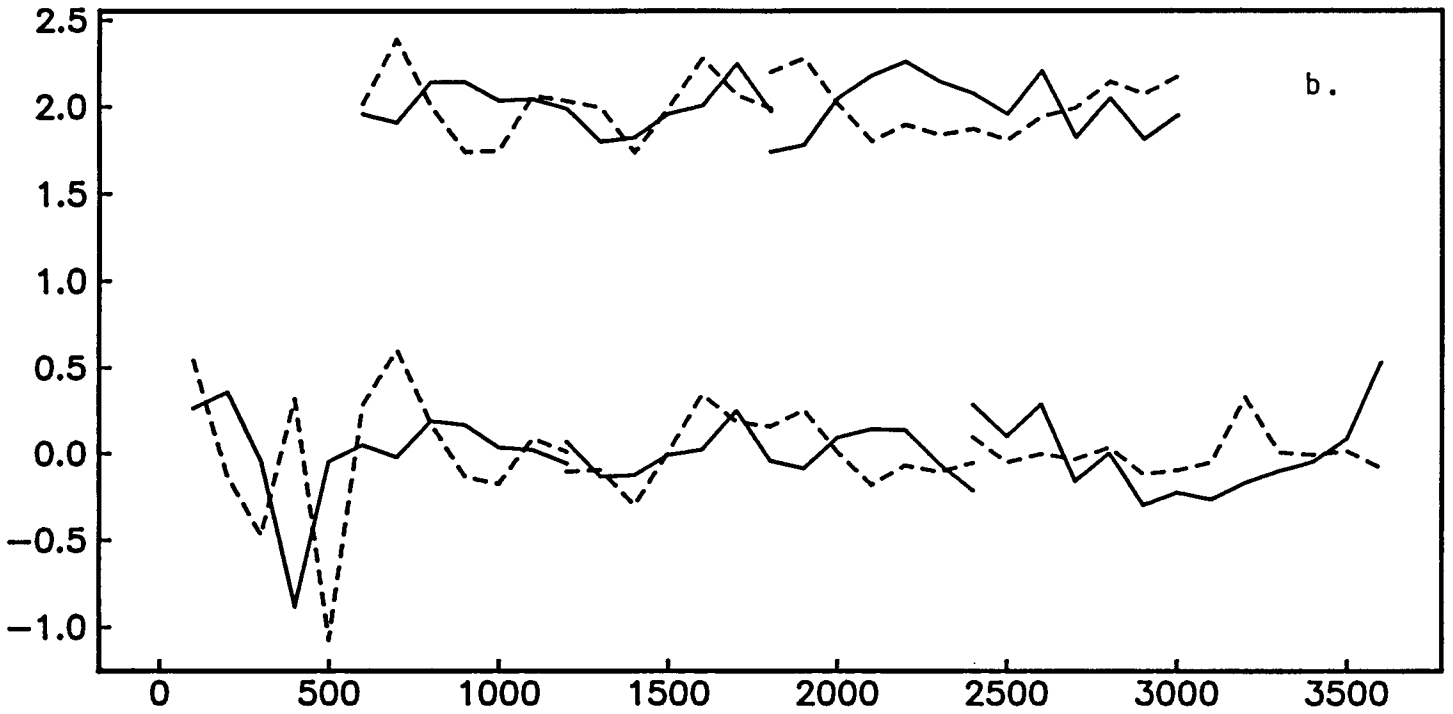


Fig. 4.17bc

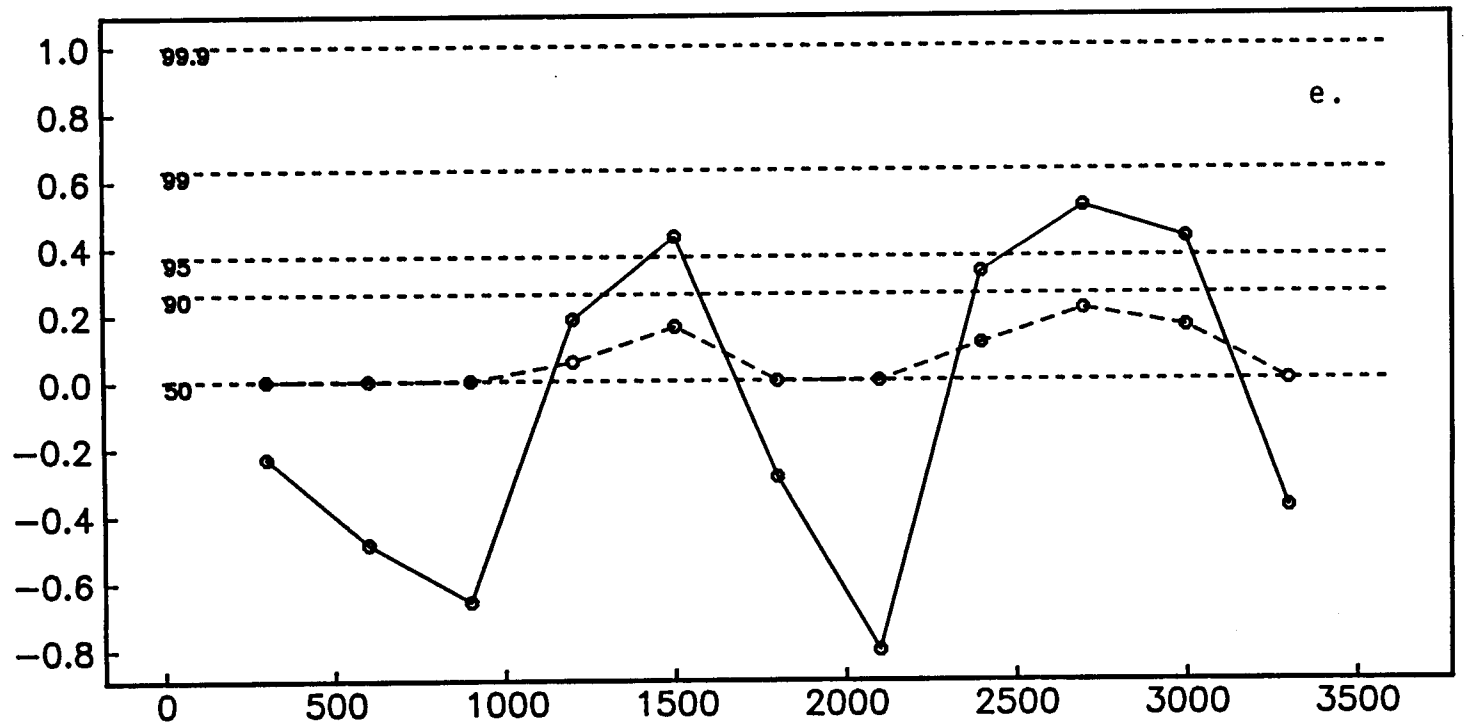
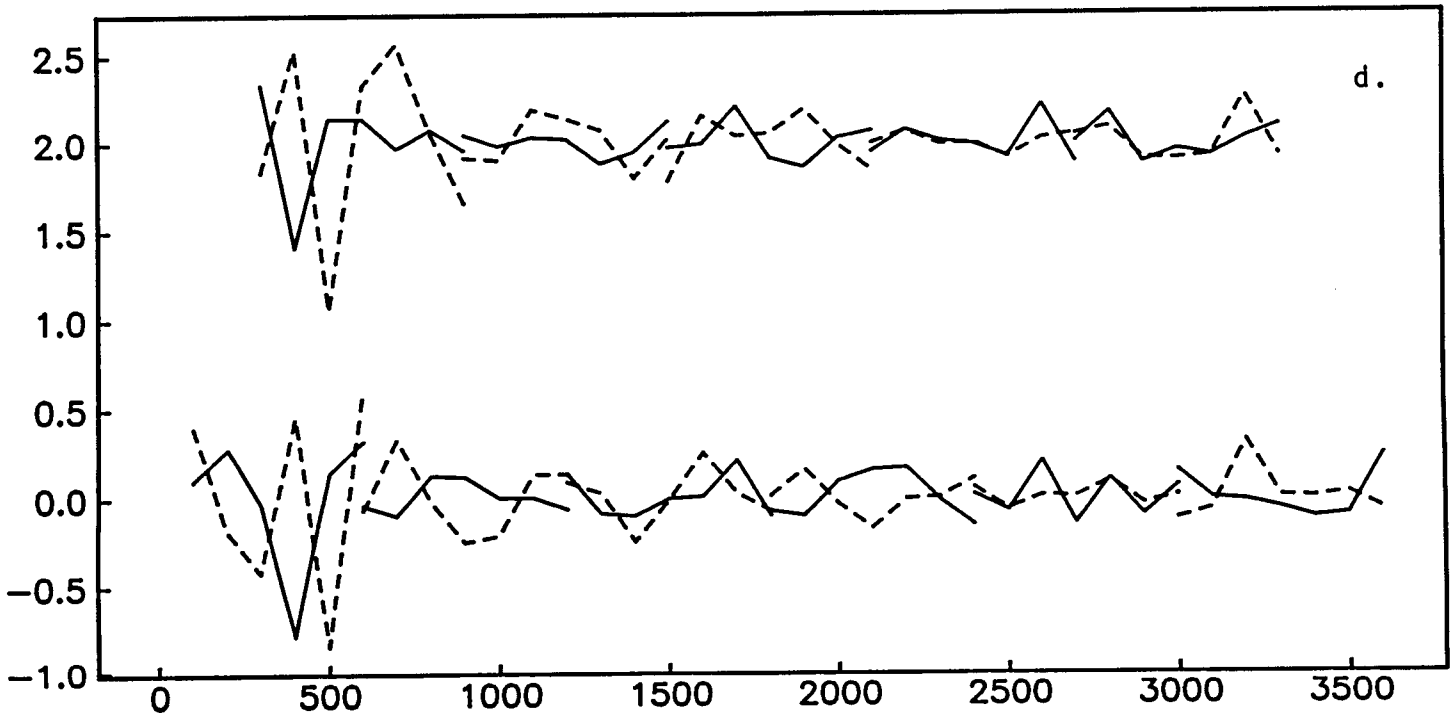


Fig. 4.17de

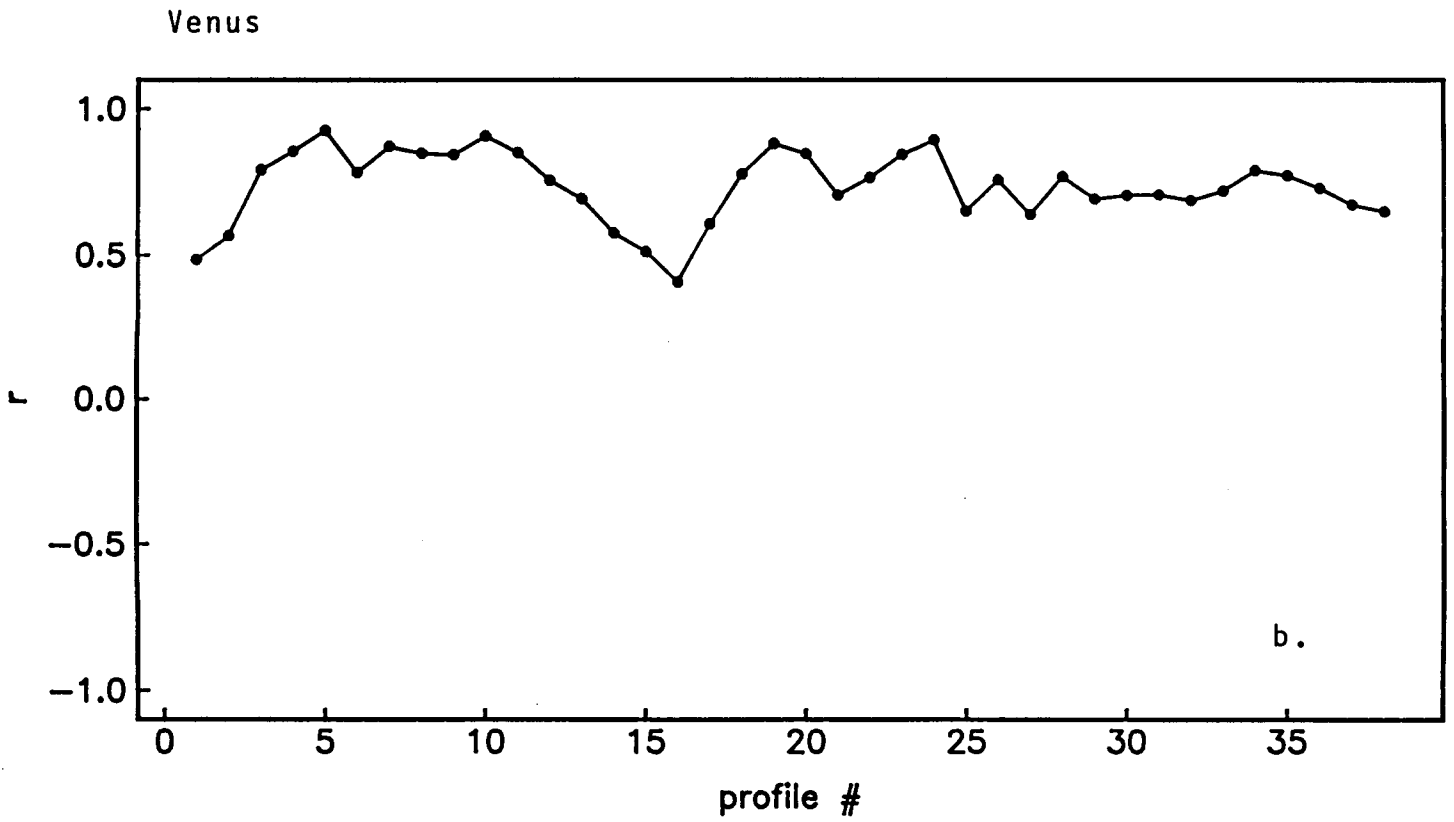
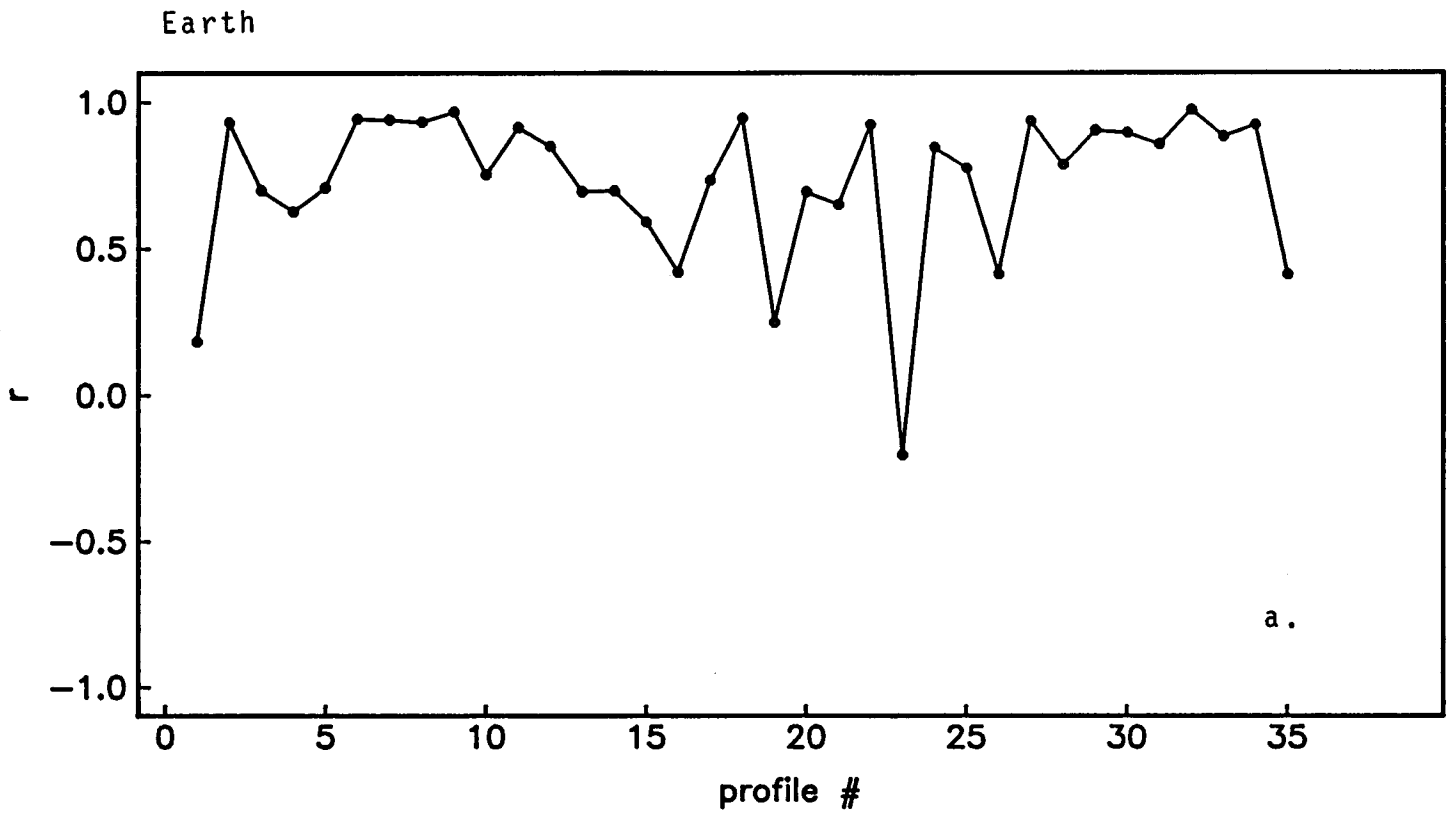


Figure 4.18

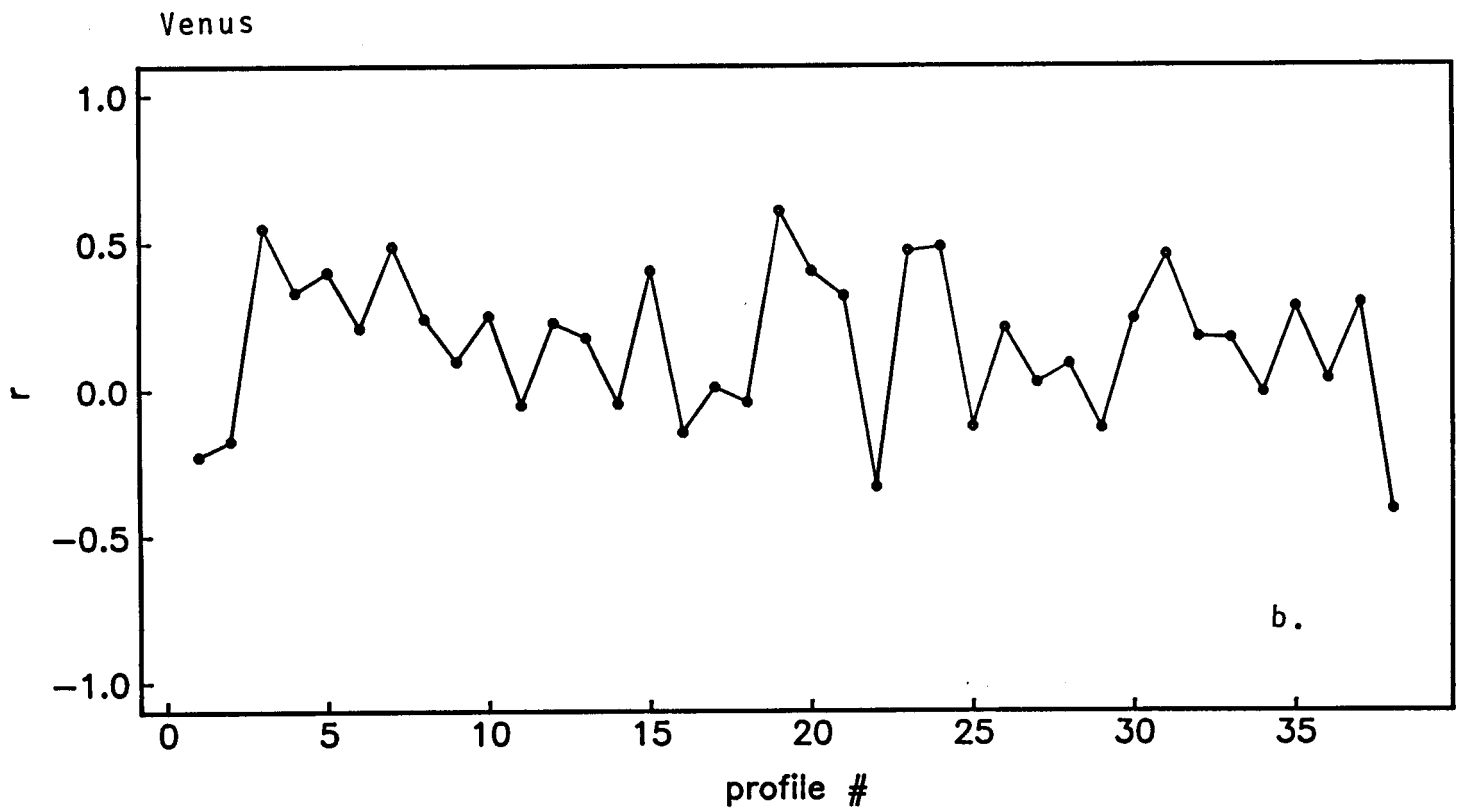
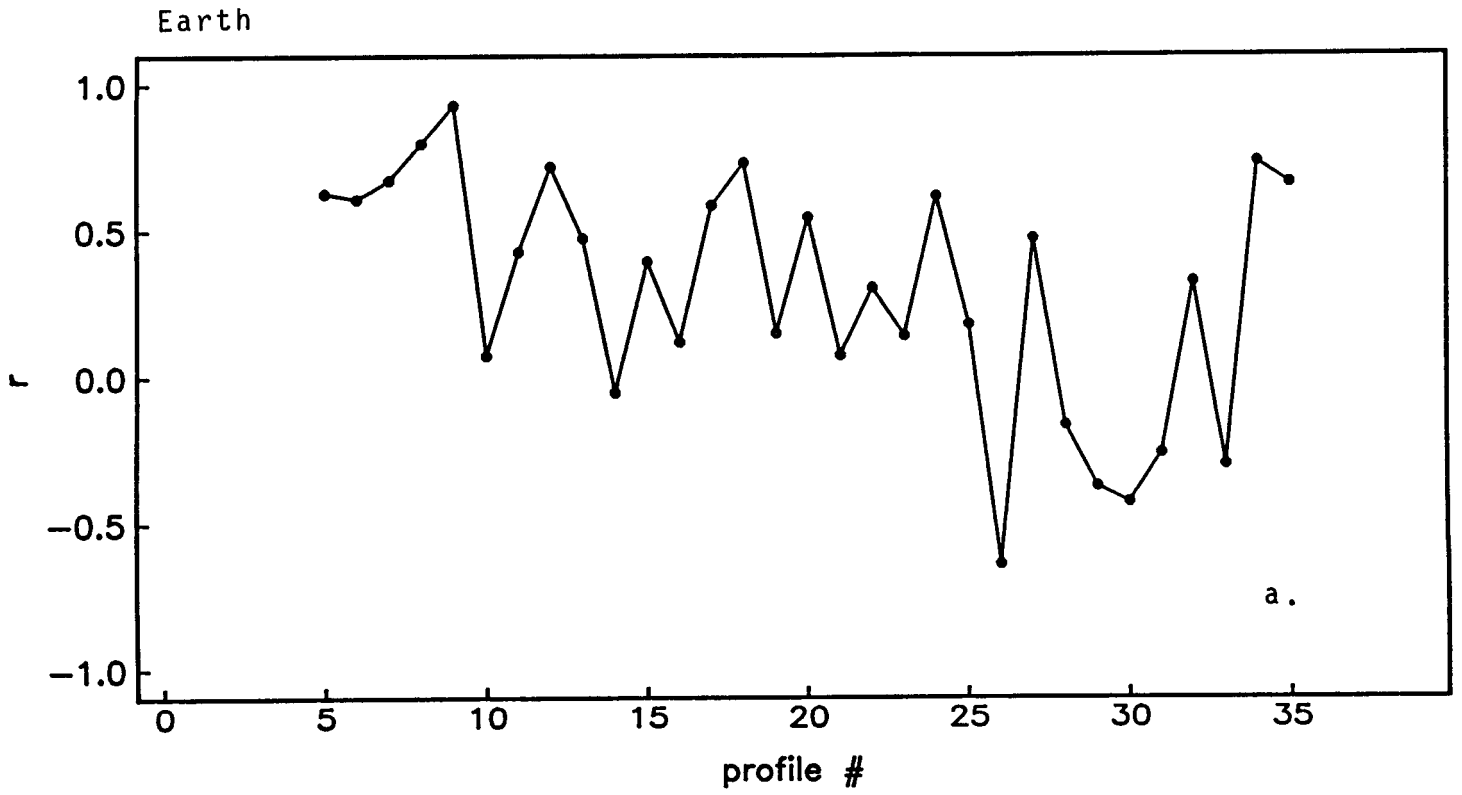


Figure 4.19

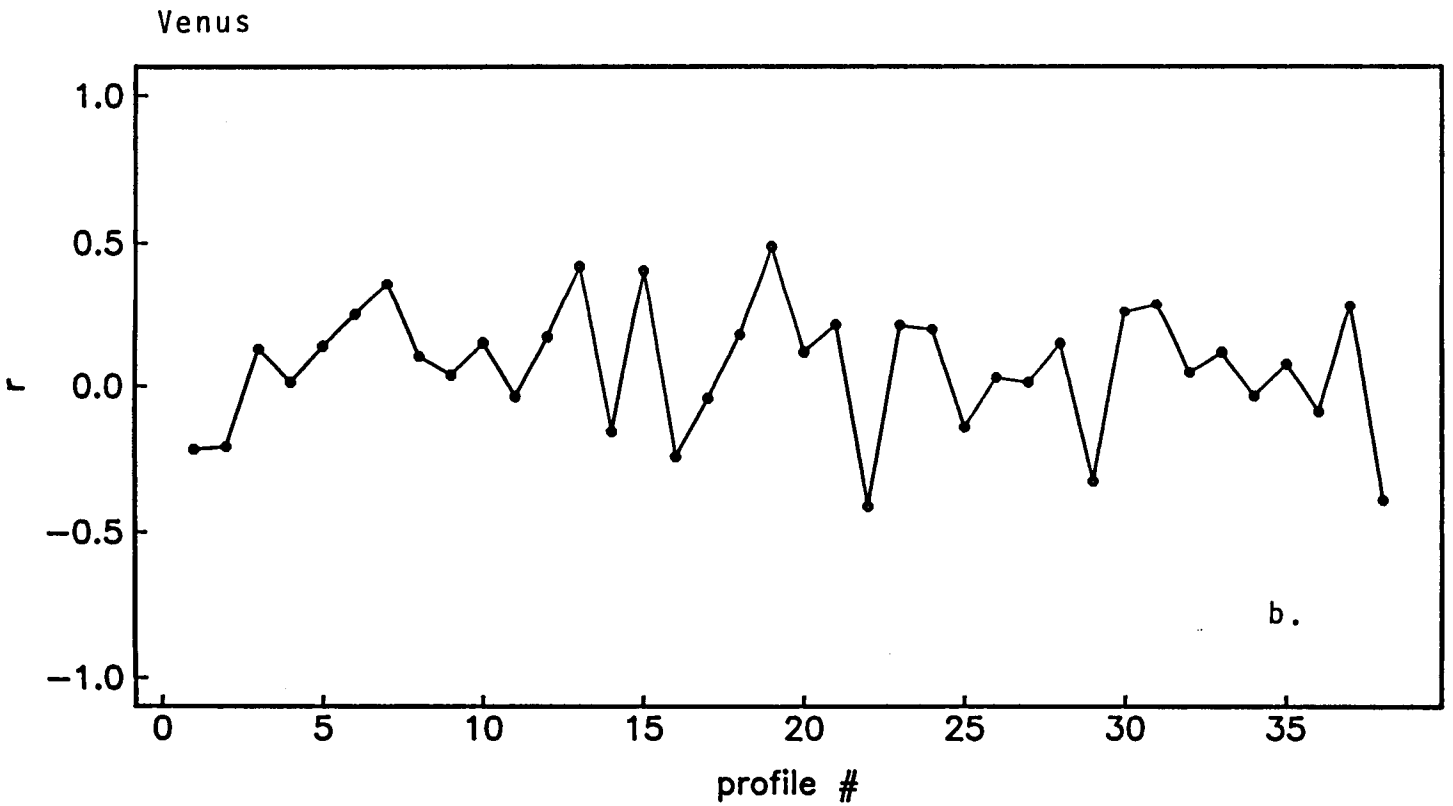
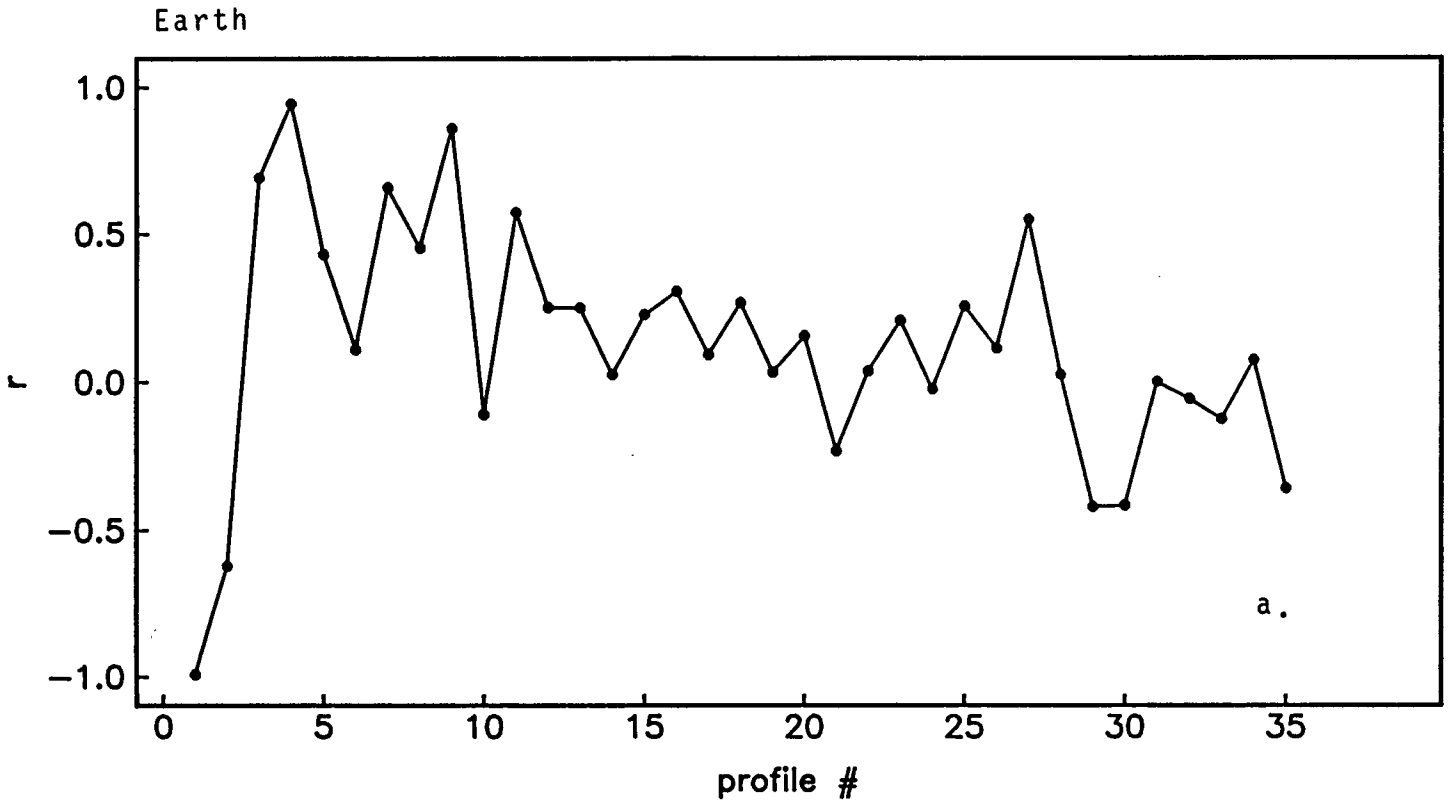
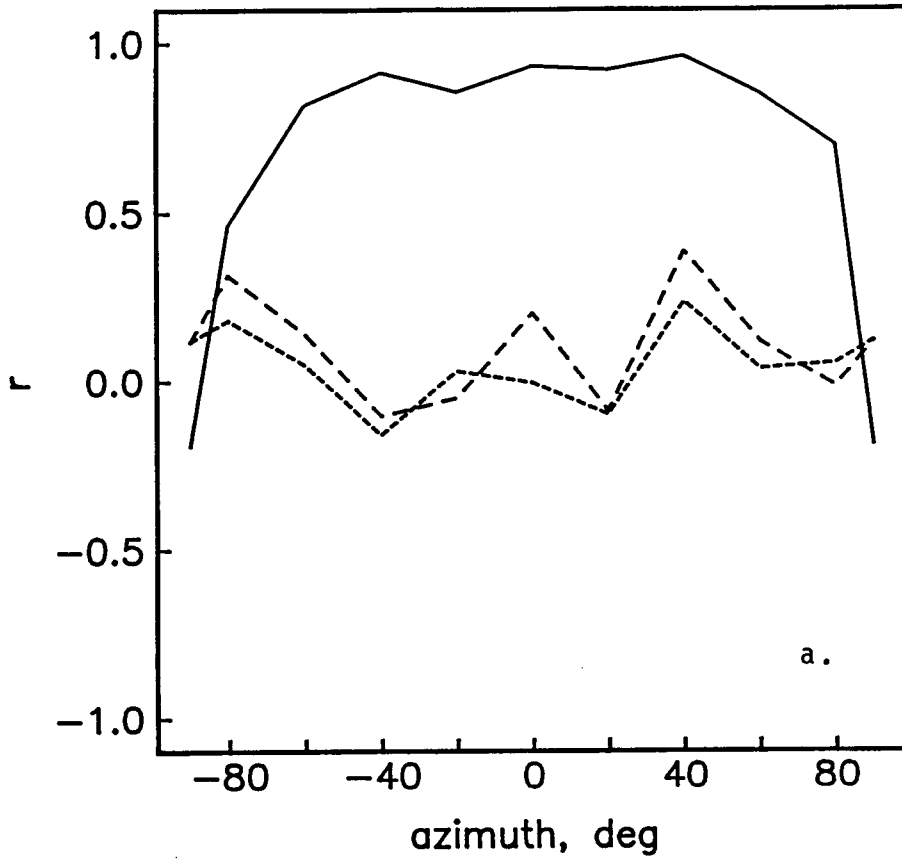


Figure 4.20



Thetis

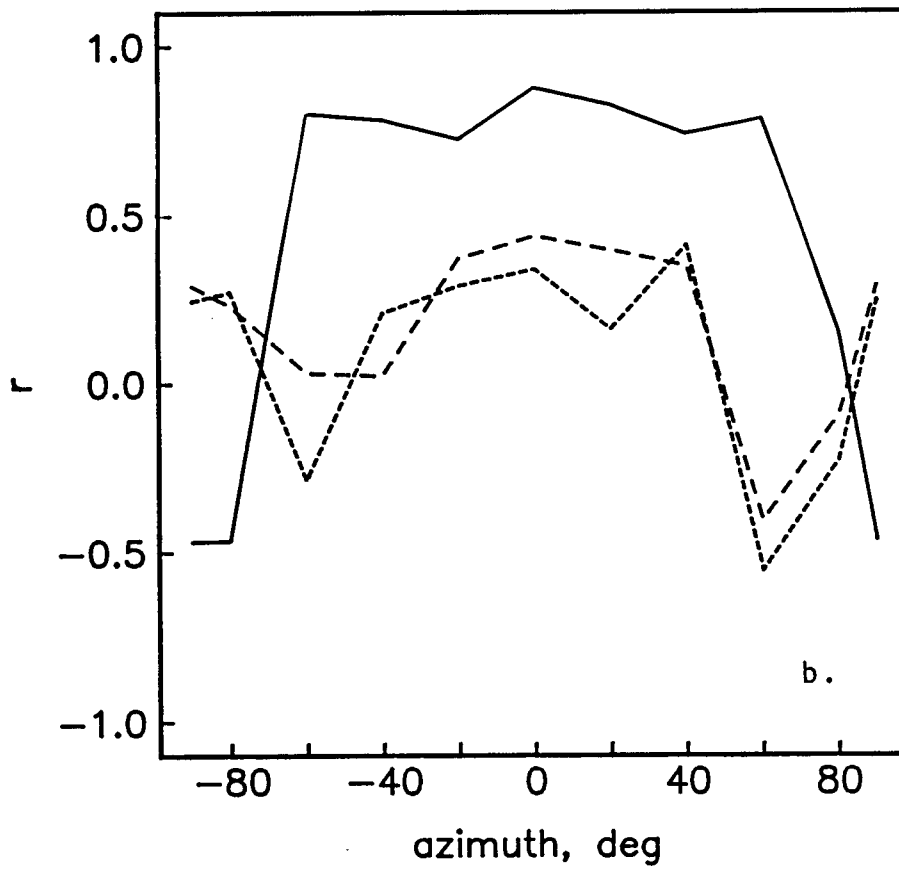


Figure 4.21

CHAPTER 5:

**PENECONTEMPORANEOUS METAMORPHISM, FRAGMENTATION, AND
REASSEMBLY OF ORDINARY CHONDRITE PARENT BODIES**

INTRODUCTION

Studies of the thermal evolution of ordinary chondrites are founded on observations of two basic parameters: (1) the distribution of peak metamorphic temperatures for the various petrologic types, as inferred from mineralogy, and (2) cooling rates as measured by metallographic, fission track, or radiogenic gas retention methods. The correlation between these parameters is not clear, mainly due to disagreement between the various cooling rate methods. Simple models for internally (i.e., radioactively) heated chondrite parent bodies should produce an inverse correlation, that is, slow cooling in the deep interior for higher petrologic types, and more rapid cooling near the periphery for lower petrologic types. However, *Scott and Rajan* [1981] noted that there appears to be no correlation between the metallographic data and petrologic type, so they devised a "metamorphosed-planetesimal" model to resolve this discrepancy, in which heating occurs in small objects that are subsequently randomly accreted into larger parent bodies. In this paper, I review the thermal and accretional requirements of the metamorphosed planetesimal model and suggest an alternative, consistent with the metallographic cooling rate constraints, in which ordinary chondrite parent bodies are collisionally fragmented and then rapidly reassembled before metamorphic heat has been dissipated.

THERMAL HISTORY OF ORDINARY CHONDRITES

Ordinary chondrites have been heated to temperatures varying from ~400°C for type 3 to ~950°C for extreme type 6 [*Dodd*, 1981]. The classification of ordinary chondrites by chemical group (H, L, LL) is not of direct importance here except to constrain the different groups to separate parent bodies or accretion zones with

little mixing between them. The volume abundances of the various petrologic types [Wasson, 1974], although different for each group, show that the more intensely metamorphosed type 5 and 6 materials are the most common. Reproduction of petrologic type distribution, and hence distribution of maximum metamorphic temperatures, is the first constraint that thermal models of chondrite parent bodies must satisfy.

Cooling rates provide a second constraint on thermal models. Cooling rates in ordinary chondrites have been measured directly by metallographic and fission-track methods and have been inferred indirectly from isotopic ages. The metallographic method [Wood, 1967], using Ni-diffusion in metal phases, yields cooling rates of 1-10°C/m.y. as the material cooled through ~500°C (Ni-diffusion becomes sluggish at lower temperatures). An important result of these measurements, pointed out by *Scott and Rajan* [1981], is that there appears to be no correlation between cooling rate and petrologic type in the 27 measurements summarized by *Wood* [1979]. Although simple models, such as the "onion-shell" model discussed below, should produce some correlation, it is not clear that the metallographic measurements should always reflect this for lower petrologic types. That is, such measurements of cooling rates near 500°C for type 3 chondrites may reflect initial slow cooling just beyond the peak temperature of these meteorites, while similar measurements of type 4-6 chondrites represent relatively rapid cooling well below peak temperatures of these materials. Hence the issue of correlation between metallographic cooling rate and petrologic type may not be meaningful if the cooling rate measurements reflect different parts of the metamorphic history of, say, type 6 and type 3 chondrites. However, in spite of the fact that I will exclude type 3 chondrites from this analysis, the lack of correlation of petrologic type with metallographic cooling rate among types 4-6 still persists.

Furthermore, other cooling rate data are in disagreement with the metallographic method. *Pellas and Storzer* [1979] obtained H chondrite cooling rates from ^{244}Pu fission tracks that are inversely correlated with petrologic type (~3-7°C/m.y. for type 6, 7-17°C/m.y. for type 5, and >10-44°C/m.y. for type 4). Similar measurements on L chondrites [*Pellas*, 1982] are more perplexing. Some have cooling rates inversely correlated with petrologic type, as in the H chondrites, except slower than corresponding metallographic rates. Others have extremely rapid cooling rates ("almost instantaneous" within the resolution of the method) for L5-6 material and slower rates for L4-5 samples, thus showing a direct correlation between cooling rate and petrologic type, the reverse of the H case.

Turner et al. [1978], using ^{40}Ar - ^{39}Ar methods, deduced that ordinary chondrites must have passed through the argon closure temperature interval (360-100°C) between 50 and 100 m.y. after formation. *Wood* [1979] has noted that metallographic cooling rates are slower than Ar retention ages by a factor of about six not only for ordinary chondrites, but also for irons, pallasites, and mesosiderites. *Willis and Goldstein* [1981] have revised the original ordinary chondrite metallographic cooling rates upward by a factor of two.

In summary, the variations in measured cooling rates and correlation with petrologic type between different methods preclude a simple unified picture. Diverse techniques yield direct correlations (some L group fission track), inverse correlation (fission track for H and some L group), or no correlation (metallographic). For the rest of this discussion, I will assume that any error in the metallographic method is a constant factor for type 4-6 chondrites and therefore that the lack of correlation between metallographic cooling rate and petrologic type is significant.

ONION-SHELL MODEL

Conventional ("onion-shell") thermal models of ordinary chondrite parent bodies [e.g., *Herndon and Herndon, 1977; Minster and Allegre, 1979; Miyamoto et al., 1981*] envision rocky asteroids of ~100-km radius that are accreted cold in $\sim 10^5$ yr and are subsequently heated by decay of ^{26}Al (half-life 7.2×10^5 yr). Other heat sources have been proposed, such as other short-lived radionuclides, superheavy elements, electrical induction, and solar, tidal, and impact heating. *Sonett and Reynolds [1979]* have reviewed the problem of primordial heat sources. Since the discovery of relict ^{26}Mg in Allende refractory inclusions by *Lee et al. [1976]*, ^{26}Al has been the favorite such heat source. Evidence for ^{26}Al has been strengthened recently by the detection of relict ^{26}Mg in an anorthite-bearing chondrule in the Semarkona chondrite [*Hutcheon et al., 1988*]. For consistency with previous models, ^{26}Al is the assumed heat source for the rest of this discussion. The principal conclusions of this work are not affected by the specific choice of heating mechanism, as long as the time scales are similar (e.g., solar electromagnetic heating).

The onion-shell model requires rapid accretion of bodies several hundred kilometers in diameter prior to significant ^{26}Al decay (neglecting the formation interval of ^{26}Al relative to the formation of the solar system). This time scale ($\sim 10^5$ yr) is consistent with numerical simulations of the collisional and gravitational interactions of early solar system bodies of *Greenberg et al. [1978]*. On the other hand, the theory of gas-free accumulation [*Safronov, 1979; Wetherill, 1980*] predicts accretion time scales of $\geq 10^7$ yr for such bodies in the vicinity of the asteroid belt. This latter time scale is a necessary condition for the metamorphosed-planetesimal model, discussed below. Since the problem of accretion remains moot, assumptions of accretion time scale in the context of chondrite thermal models must be viewed as *ad hoc*.

The onion-shell models produce type 6 material in their cores, surrounded by successive zones of types 5, 4, and finally type 3 material near the surface (Figure 5.1). The observed distribution of petrologic types among H chondrites can be produced using a parent body with a radius of 85 km, thermal diffusivity κ of $5 \times 10^{-3} \text{ cm}^2 \text{ s}^{-1}$, and initial $^{26}\text{Al}/^{27}\text{Al}$ ratio of 5×10^{-6} [Miyamoto *et al.*, 1981]. Cooling rates are in agreement with fission track measurements by Pellas and Storzer [1979] and are inversely correlated with petrologic type. An inverse correlation is expected for such a model, as regions near the core cool slowly and material nearer to the periphery cools more rapidly.

In the context of metallographic cooling rates, however, the onion-shell model fails distressingly, as these data indicate no correlation with petrologic type. Hence some two-stage process apparently is required to fit the metallographic data, first metamorphosing the ordinary chondrites, and then transporting them to random cooling locations prior to slow cooling through 500°C . Two such models will be described and compared.

METAMORPHOSED-PLANETESIMAL MODEL

A "metamorphosed-planetesimal" model has been proposed by Scott and Rajan [1981] and Taylor *et al.* [1982]. They suggest that if accretion of 100-km-radius bodies takes $\geq 10^7$ yr and if ^{26}Al decay is the dominant heat source, then maximum temperatures are reached (i.e., petrologic types are established) in small planetesimals with $r \leq 10$ km. Cooling rates in these bodies are controlled by their burial depth as they are subsequently randomly accreted into larger $r \sim 100$ km parent bodies; therefore cooling rates appear uncorrelated with petrologic types (Figure 5.2).

This model rests on several assumptions that must be explored more

thoroughly. Consider the first stage of the process, the heating of $r \leq 10$ km planetesimals. In order to heat these objects sufficiently, they must initially have either a greater proportion of radionuclides or a much poorer thermal diffusivity than $r \sim 100$ km bodies, or both. *Wood* [1979] describes such a model, wherein particulate matter ($\kappa = 10^{-5} \text{ cm}^2\text{s}^{-1}$, $^{26}\text{Al}/^{27}\text{Al} = 6 \times 10^{-5}$) accretes at exponentially decreasing rates. Upon reaching a critical temperature, the "dust" grains irreversibly sinter to rocky, chondritic material ($\kappa = 5 \times 10^{-3} \text{ cm}^2\text{s}^{-1}$). Wood's model produces melting temperatures on bodies that grow to 10-20 km radius.

Yomogida and Matsui [1984] have developed an improved sintering model, but their results differ from Wood's largely because they do not consider accretion and use only long-lived radionuclides. An interesting feature of their model is that peak temperatures are nearly uniform in the interior, more so than even the onion-shell model, which produces such large proportions of petrologic types 5 and 6. In the sintering model, large gradients exist only at the unsintered, powdery surface layer. This implies that planetesimals of different sizes are each composed of nearly a single petrologic type, in agreement with the assumptions of the metamorphosed-planetesimal model.

Hence a major difference between the metamorphosed-planetesimal and the onion-shell parent body is the consolidation state of the object in which metamorphism occurs. The onion-shell model is based on the assumption that solid bodies exist before significant endogenic heating begins (10^5 - 10^6 yr). Carbonaceous chondrites, for example, have not been heated above $\sim 300^\circ\text{C}$, yet many are highly compacted [*Cain and McSween*, 1984]. Since the physical properties of primitive solar system material remain unknown, neither model can be excluded. Material properties are also important in collisional studies as discussed below.

The second step in the metamorphosed-planetesimal model is the accretion of $r < 10$ km bodies into $r \sim 100$ km objects on a timescale $\geq 10^7$ yr. An implicit assumption here is that the planetesimals accrete fairly intact (i.e., like a bunch of grapes) in order to retain sufficient heat so that cooling rates at 500°C can only be achieved under one of the following circumstances: (1) fragments are rapidly covered by other impacting debris, (2) fragments are emplaced by impact at a depth of ~ 4 km under regolith or ~ 40 km under rock, or (3) planetesimals are shattered but not dispersed by impact, in a manner analogous to a snowball striking a wall (R. Greenberg, personal communication, 1984). The required long accretion times of 100 km bodies implies that fragments will not be covered by debris from other incoming planetesimals quickly enough to prevent rapid cooling. On the other hand, the maximum depth of emplacement can be estimated by considering the impact of a 10-km radius planetesimal at 100 m/s (the escape velocity of a 3 g/cm^3 , 77-km radius body). A crater diameter of ~ 13 km is predicted in a crystalline target [Dence *et al.*, 1977]. A typical diameter: depth ratio of 5 for craters of this size [Gault *et al.*, 1975] gives a crater depth of 2.6 km. Earlier accreting planetesimals will form smaller and shallower craters because of lower impact velocities. Thus even though this calculation is strictly valid only for hypervelocity impacts onto surfaces of planet-size objects, it is apparent that isolated fragments of a shattered metamorphosed planetesimal can cool slowly only if they are completely buried at maximum excavation depths. Since it seems unlikely that much material was emplaced this way, I conclude that the metamorphosed-planetesimal model is valid only if the $r \leq 10$ km bodies can accrete more or less intact into $r \sim 100$ km chondrite parent bodies or if the fragmentation of accreting planetesimals is strongly nondispersive. Models of the collisional evolution of objects in the solar system can illuminate this problem. I have tested

the metamorphosed-planetesimal accretion scheme against such a model and have used it to search for other mechanisms to explain apparently uncorrelated metamorphic grades and metallographic cooling rates in ordinary chondrites.

COLLISION DYNAMICS

A significant result of the work of *Greenberg et al.* [1978] applicable to the present problem was the development of a comprehensive collision model. Impact velocity is given by $v_i^2 = v_0^2 + v_e^2$, where v_0 is the encounter velocity, and v_e is the mutual escape velocity of the two bodies. Outcomes of collisions are divided into four categories: (1) rebound intact, (2) cratering of both bodies and rebound, (3) smaller body shattered, larger cratered, and (4) both bodies shattered. The result for a particular collision depends on the impacting bodies' resistance to both simple cratering and catastrophic disruption. These results are accompanied by the accretion of none, part, or all of the impacting material, depending on the partitioning of kinetic energy between the two impactors and their ejecta. Data for materials ranging from loosely bound regolith to basalt were included.

The collision algorithm of *Greenberg et al.* [1978] may be used to investigate the effects of accretion mechanics on metamorphic models of ordinary chondrites, employing parameters given by these workers for solid rock and for an intermediate material between rock and regolith (perhaps corresponding to coherent dirt clods). These parameters were chosen as representative endmembers for material properties of early solar system planetesimals or meteorite parent bodies. *Greenberg et al.* [1978] give full details of the method.

Two characteristic encounter velocities were studied. *Safronov* [1972] analytically calculated that equilibrium encounter velocities are comparable to the escape velocities of the largest bodies in the population. Accordingly, the upper

velocity used was 100 m/s (velocities of several hundred m/s may be applicable but do not affect the conclusions). On the other hand, *Greenberg et al.* [1978] found that encounter velocities are comparable to the escape velocities of the original bodies in the population, i.e., a few m/s. Hence a lower velocity of 5 m/s was adopted.

The lower velocity collision results are shown in Figure 5.3. The most important feature to note is that, except for a small field of nearly equal-sized rocky planetoids, collisions involving a body ≥ 50 km in diameter cannot result in accretion intact or with relatively minor cratering. In terms of the metamorphosed-planetesimal model, this means that impacting $r \leq 10$ km planetesimals will be shattered when the parent body has grown to only 20-30-km radius. Heat losses for dispersed fragments will be rapid compared with the required long accretion timescale, so the metamorphosed-planetesimal model breaks down in this case, unless the fragments remain closely aggregated.

At higher encounter velocities (Figure 5.4), there are no fields at all that allow "intact" accretion. All outcomes result in the shattering of one or both bodies, and objects ≤ 50 km do not have sufficient gravitational binding energy to reaccrete; instead the fragments escape. Increased encounter velocities result in progressively more disruption. Therefore the metamorphosed-planetesimal model is probably most applicable to strong, rocky bodies at low encounter velocities, so that accretion proceeds without shattering. Since high impact strength is needed in this case, metamorphosed-planetesimals must be more or less completely sintered to rock before they are accreted. Even then, $r \sim 100$ km objects must be accreted in a stepwise fashion, first assembling several $r \leq 10$ km planetesimals and then accreting several of these intermediate aggregates (so as to pass from field I to field II in Figure 5.3b). These constraints may be relaxed if nondispersive

shattering of impacting planetesimals occurs.

FRAGMENTATION-AND-REASSEMBLY MODEL

Is there an alternative accretion scheme to explain uncorrelated petrologic types and cooling rates? Figures 5.3 and 5.4 show sizable areas (field IV) where the kinetic energy delivered per unit volume is sufficient to catastrophically fragment both bodies, but the remains will reaccumulate into a gravitationally bound "rubble pile" [Davis *et al.*, 1979]. At the relatively low encounter velocities described here, this result occurs for comparable size bodies (larger: smaller diameter ratio ≤ 5), with the larger object's diameter ≥ 100 km. Hartmann [1979a,b] has investigated collisions of comparable size bodies for a variety of initial conditions. He concludes that impacts between comparable size bodies may account for several peculiar asteroid observations by producing unfractured or partially brecciated contact binaries, totally brecciated spheroids, or coorbiting groups. For example, Trojan asteroid 624 Hektor may be a highly fractured contact binary.

A series of collisions between comparable-size objects could rescue the metamorphosed-planetesimal model, as described at the end of the previous section. Such collisions could also account for the inferred ordinary chondrite thermal histories in the following manner.

First, rapid accretion causes peak temperatures due to ^{26}Al heating to occur in objects of ~ 100 km radius, as in the onion-shell model. The relative proportions of the various petrologic types are established at this stage (Figure 5.5a).

Second, maximum metamorphic temperatures are maintained for several tens of million years in bodies of this size. Collision with another object on this time scale completely fragments both bodies (Figure 5.5b). Collisions capable of

shattering a hypothetical onion-shell parent body are comparatively rare in the present solar system. Using the collision model of *Greenberg et al.* [1978] and the impactor fluxes given in *Greenberg and Chapman* [1983], and assuming a mean encounter velocity of 5 km/s, I calculate that such collisions should occur approximately on a time scale varying from 10^8 to 10^{10} yr, depending on target material properties. In contrast, the earliest planetesimal evolution may have been characterized by extremely common, mutually fragmenting encounters. A characteristic fragmentation encounter time for $r \sim 100$ km objects of only 10^2 to 10^4 yr is predicted from the numerically simulated planetesimal distributions produced at $\sim 2 \times 10^4$ yr by the *Greenberg et al.* [1978] model. Hence a fragmentation timescale of $\sim 10^7$ - 10^8 yr, as required by the characteristic cooling time of the onion-shell model, is not inconsistent with plausible planetesimal size and speed distributions intermediate between the earliest and the present-day populations.

Third, the fragments reassemble into a megaregolith rubble pile while they are still hot (Fig. 5c). Factors affecting reassembly time are complex (such as size and speed distribution of fragments and partitioning of translational versus rotational energy), but an approximate estimate can be made assuming that gravitationally bound fragments reaccrete promptly and do not form coorbiting swarms. Under this assumption, a characteristic reaccretion time is given by the ballistic flight time of ejecta. In the *Greenberg et al.* [1978] model, the velocity of fragments is computed such that all have the same speed and their kinetic energy is 50% of the impact energy, an upper limit for their experiments with basalt. For two 3 g/cm^3 , 100-km radius asteroids with an encounter velocity of 100 m/s, the characteristic fragment velocity is 135 m/s ($0.83V_0$), and the ballistic flight time is about 3.5 hr. Therefore fragments greater than a few meters in diameter could retain sufficient heat so that cooling rates at 500°C are controlled by burial depth in the reaccreted

parent body. For example, a 10-m diameter fragment would require around 45 days to cool from 800°C to 500°C at its center.

The likelihood of a significant fraction of the shattered chondrite parent body occurring in such sizeable fragments can be estimated from a mass distribution model. *Greenberg et al.* [1978] used a conventional power-law mass distribution of the form $N = Cm^{-b}$ where N is the number of fragments with mass $> m$, and C and b are constants. *Hartmann* [1969] found that b varies from about 0.67 when fragmentation energy is minimal to near unity in high-energy collisions or where extensive regrinding takes place. For a fragmented 100-km radius parent object, and for values of b up to ~ 0.8 , over 99% of the mass is found in fragments > 10 m in diameter. Thus even for more energetic collisions (although they might preclude reassembly) or encounters in which secondary collisions cause further comminution, much of the mass is distributed in fragments capable of retaining metamorphic heat for many days, perhaps months. If these fragments are reaccreted before much of this time has elapsed, then cooling rates will appear uncorrelated with petrologic type, assuming that the fragments are thoroughly mixed by the collision.

DISCUSSION

The fragmentation-and-reassembly model of chondrite parent bodies requires two of the same assumptions as does the metamorphosed-planetesimal model. First, accretion must preserve overall homogeneity among H, L, and LL chondrites; that is, there is little interaction between these objects (or groups of objects). Second, the accreting objects must have comparable thermal states, i.e., heated to ordinary chondrite metamorphic temperatures ~ 400 - 950°C . If not, rapid heat losses to cold fragments would cause cooling rates much larger than the usual tens

of degrees per million years or so (however, recall that some L chondrites have very fast cooling rates).

Other workers have suggested that meteorite parent bodies may have been collisionally fragmented and then gravitationally reassembled one or more times over solar system history [Hartmann, 1979b; Taylor *et al.*, 1982]. Greenberg and Chapman 1983] calculated that asteroids in the diameter range 30-300 km have undergone this process several to many times (the number of such events decreases with larger objects). However, none consider the possibility of such collisions occurring early, while parent bodies were still at metamorphic temperatures.

Rubin *et al.* [1983] found that some fragmental breccia (predominantly L and LL) had incorporated melt rock clasts prior to metamorphism, while others (mostly H) had acquired melt rock clasts after metamorphism. Scott and Rajan [1981] studied metallographic cooling rates in xenolithic clasts in four ordinary chondrite breccias. Cooling rates in clasts from two of the meteorites varied widely, whereas clasts in the other two had coherent cooling rates. The former case was interpreted as compaction of host and clasts after cooling through 500°C, and the latter as incorporation of clasts before or during metamorphism. Scott and Rajan [1981] and Taylor *et al.* [1982] invoke fragmentation and reassembly to explain association of breccia clasts with a wide range of cooling rates (the resulting wide range of burial depths could probably not be sampled without shattering the parent body.) However, they propose metamorphosed-planetesimals to account for the lack of correlation between petrologic type and cooling rate and for penecontemporaneous compaction and metamorphism of clasts in other meteorites. Repeated fragmentation and reassembly of the ordinary chondrite parent bodies is a single mechanism that can explain both uncorrelated cooling rates and petrologic types

and incorporation of melt-rock and xenolithic clasts before, during, or after metamorphism.

CONCLUSIONS

The metamorphosed-planetesimal model has been proposed previously to explain the apparent lack of correlation between petrologic type and metallographic cooling rate by suggesting that if accretion of $r \sim 100$ km bodies takes $\geq 10^7$ yr, then peak temperatures due to ^{26}Al heating are reached in objects of $r \leq 10$ km. Cooling rates at 500°C are then fixed by burial depth of these planetesimals in the growing parent body. The model requires that initial materials have much lower thermal diffusivities and/or greater proportions of radionuclides than assumed for conventional onion-shell parent bodies. In addition, the metamorphosed-planetesimal model demands relatively intact accretion or nondispersive fragmentation of $r < 10$ km bodies so that cooling rates are controlled by burial depth. If these requirements are not met, fragments will cool rapidly near the surface instead of slowly at depth.

Alternatively, onion-shell parent bodies could be completely fragmented and then gravitationally reassembled by low-velocity collision of comparable-size objects. If such collisions occurred during the few tens of m.y. of peak metamorphic temperatures, then cooling rates at 500°C would be determined by burial depth in the reaccreted parent body, because reassembly times may be quite short.

All models described here are chiefly dependent on the thermal properties and radionuclide proportions of primitive solar system material, the style and timescale of accretion, and the "true" nature of the relationship between cooling rate and petrologic type. No model can be eliminated until the answers to these questions are better resolved.

REFERENCES

- Cain, P. M., and H. Y. McSween, Jr., Interpretation of structural fabric in the Leoville carbonaceous chondrite (abstract), *Lunar and Planetary Science XV*, 116-117, 1984.
- Davis, D. R., C. R. Chapman, R. Greenberg, S. J. Weidenschilling, and A. W. Harris, Collisional evolution of asteroids: Populations, rotations, and velocities, in *Asteroids*, edited by T. Gehrels, pp. 528-557, University of Arizona, Tucson, 1979.
- Dence, M.R., R. A. F. Grieve, and P. B. Robertson, Terrestrial impact structures: Principal characteristics and energy considerations, in *Impact and Explosion Cratering*, edited by D. J. Roddy, R. O. Pepin, and R. B. Merrill, pp. 247-275, Pergamon, New York, 1977.
- Dodd, R. T. Jr., *Meteorites: A Petrologic-Chemical Synthesis*, Cambridge Univ. Press, 386 pp., 1981.
- Gault, D. D., J. E. Guest, J. B. Murray, D. Dzurizin, and M. C. Malin, Some comparisons of impact craters on Mercury and the Moon, *J. Geophys. Res.*, *80*, 2444-2460, 1975.
- Greenberg, R., and C. R. Chapman, Meteorites and asteroids: Parent bodies and delivered samples, *Icarus*, *45*, 455-481, 1983.
- Greenberg, R., J. F. Wacker, W. K. Hartmann, and C. R. Chapman, Planetesimals to planets: Numerical simulation of collisional evolution, *Icarus*, *35*, 1-26, 1978.
- Hartmann, W. K., Terrestrial, lunar, and interplanetary rock fragmentation, *Icarus*, *10*, 201-213, 1969.
- Hartmann, W. K., A special class of planetary collisions: Theory and evidence, *Proc. Lunar Planet. Sci. Conf. 10th*, 1897-1916, 1979a.
- Hartmann, W. K., Diverse puzzling asteroids and a possible unified explanation, in *Asteroids*, edited by T. Gehrels, 466-479, University of Arizona, Tucson, 1979b.
- Herndon, J. M., and M. A. Herndon, Aluminum-26 as a planetoid heat source in the early solar system, *Meteoritics*, *12*, 459-465, 1977.

- Housen, K. R., L. L. Wilkening, C. R. Chapman, and R. J. Greenberg, Regolith development and evolution on asteroids and the moon, in *Asteroids*, edited by T. Gehrels, 601-627, University of Arizona, Tuscon, 1979.
- Hutcheon, I.D., R. Hutchison, and G.J. Wasserburg, Evidence of the in-situ decay of ^{26}Al in a Semarkona chondrule (abstract), *Lunar and Planetary Science XIX*, 523-524, 1988.
- Lee, T., D. A. Papanastassiou, and G. J. Wasserburg, Correction, Demonstration of excess ^{26}Mg in Allende and evidence for ^{26}Al , *Geophys. Res. Lett.*, **3**, 109-112, 1976.
- Minster, J. F., and C. Allégre, ^{87}Rb - ^{87}Sr chronology of H chondrites: Constraints and speculations on the early evolution of their parent body, *Earth Planet. Sci. Lett.*, **42**, 333-347, 1979.
- Miyamoto, M., N. Fujii, and H. Takeda, Ordinary chondrite parent body: An internal heating model, *Proc. Lunar Planet. Sci. Conf. 12B*, 1145-1152, 1981.
- Pellas, P., Early thermal histories of L chondrites (abstract), *Lunar and Planetary Science XII*, 825-827, 1982.
- Pellas, P., and D. Storzer, Differences in the early cooling histories of the chondritic asteroids (abstract), *Meteoritics*, **14**, 513-515, 1979.
- Rubin, A. E., A. Rehfeldt, E. Peterson, K. Keil, and E. Jarosewich, Fragmental breccias and the collisional evolution of ordinary chondrite parent bodies, *Meteoritics*, **18**, 179-196, 1983.
- Safronov, V. S., Evolution of the protoplanetary cloud and formation of earth and the planets, *NASA-TT-F-677*, 211 pp., 1972.
- Scott, E. R. D., and R. S. Rajan, Metallic minerals, thermal histories, and parent bodies of some xenolithic, ordinary chondrites, *Geochim. Cosmochim. Acta*, **45**, 53-67, 1981.
- Sonett, C. P., and R. T. Reynolds, Primordial heating of asteroidal parent bodies, in

- Asteroids*, edited by T. Gehrels, pp. 822-848, University of Arizona, Tuscon, 1979.
- Taylor, G. J., E. R. D. Scott, A. E. Rubin, P. Maggiore, and K. Keil, Structure and fragmentation of the parent asteroids of ordinary chondrites (abstract), *Lunar and Planetary Science XIII*, 799-800, 1982.
- Taylor, G.J., P. Maggiore, E.R.D. Scott, A.E. Rubin, and K. Keil, Original structures, and fragmentation and reassembly histories of asteroids: Evidence from meteorites, *Icarus*, 69, 1-13, 1987.
- Turner, G., M. C. Enright, and P. H. Cadogan, The early history of chondrite parent bodies inferred from ^{40}Ar - ^{39}Ar ages, *Proc. Lunar Planet. Sci. Conf. 9th*, 989- 1025, 1978.
- Wasson, J. T., *Meteorites: Classification and Properties*, Springer-Verlag, New York, 360 pp., 1974.
- Wetherill, G. W., Accumulation of the terrestrial planets, in *Protostars and Planets*, edited by T. Gehrels, pp. 565-578, University of Arizona, Tuscon, 1978.
- Willis, J., and J. I. Goldstein, A revision of metallographic cooling rate curves for chondrites, *Proc. Lunar Planet. Sci. 12B*, 1135-1143, 1981.
- Wood, J. A., Chondrites: Their metallic minerals, thermal histories, and parent bodies, *Icarus*, 6, 1-49, 1967.
- Wood, J. A., Review of the metallographic cooling rates of meteorites and a new model for the planetesimals in which they formed, in *Asteroids*, edited by T. Gehrels, pp. 849-891, University of Arizona, Tuscon, 1979.
- Yomogida, K., and T. Matsui, Multiple parent bodies of ordinary chondrites, *Earth Planet. Sci. Lett.*, 68, 34-42, 1984.

FIGURE CAPTIONS

- Figure 5.1: Sample "onion-shell" rocky parent body for H chondrites showing successive zones of petrologic types 3-6, after *Miyamoto et al.* [1981]. Peak temperatures are fairly uniform in the deep interior and drop smoothly near periphery. Cooling rates at 500°C are predicted to be inversely correlated with petrologic type.
- Figure 5.2: "Metamorphosed-planetesimal" model, after *Scott and Rajan* [1981]. Chondrite metamorphism occurs in small, loosely consolidated planetesimals, which then accrete into larger parent bodies. Cooling rates at 500°C are controlled by burial depth and appear uncorrelated with petrologic type.
- Figure 5.3: Results of low velocity two-body collisions using model of *Greenberg et al.* [1978]: I-bodies accrete intact; II-bodies crater each other and accrete; III-smaller body shattered, larger cratered, fragments accrete; IV both bodies shattered, fragments accrete; V-as result III, fragments escape; VI-as result IV, fragments escape. Brackets on ordinate and abscissa give approximate sizes of metamorphosed-planetesimals and parent bodies into which they accrete, respectively. Metamorphosed-planetesimal is valid under outcome I or II; applicability under result III is doubtful (see text). Result IV shows fragmentation and reassembly, providing an alternative model.

Figure 5.4: As Figure 5.3, but with higher encounter velocity. Smaller bodies have insufficient gravitational binding energy to prevent disruption following collision, and escape fields dominate as velocities approach 1 km/s.

Figure 5.5: Fragmentation and reassembly model. Chondrite metamorphism occurs in 100-200-km diameter bodies that are fragmented by collision with a comparable-size object and then gravitationally reassembled within a few hours-days. Cooling rates for fragments greater than a few meters in diameter are controlled by burial depth in the reaccreted parent asteroid.

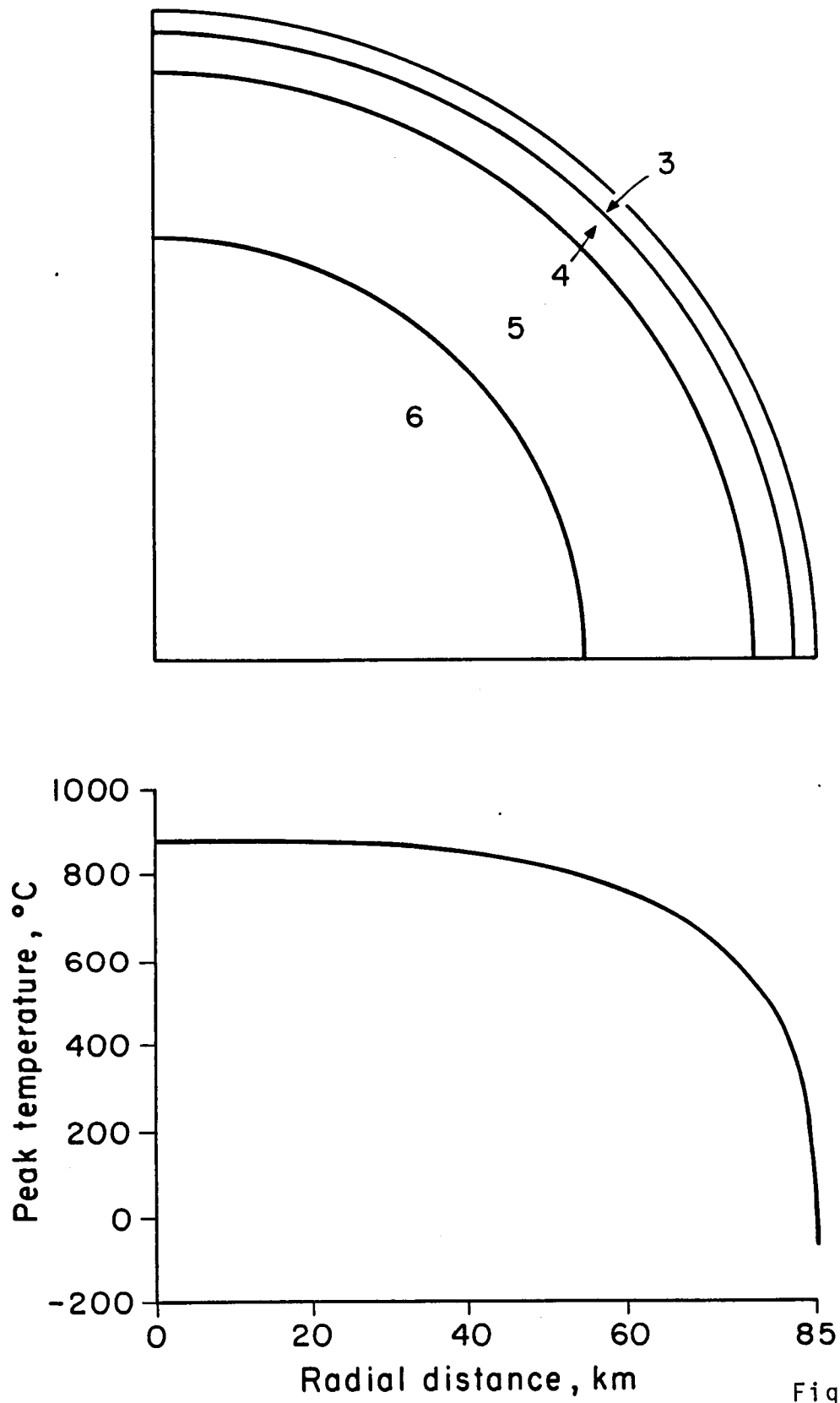


Figure 5.1

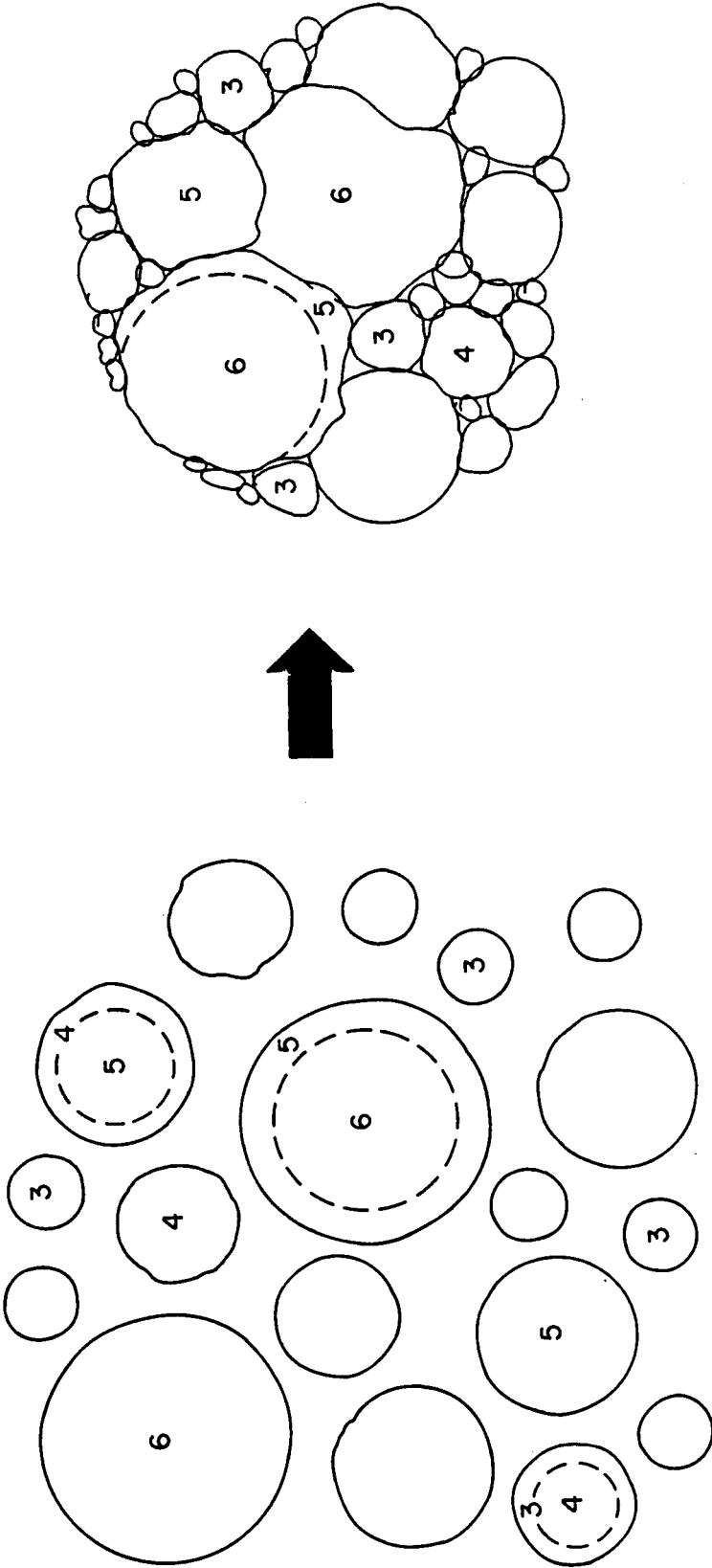


Figure 5.2

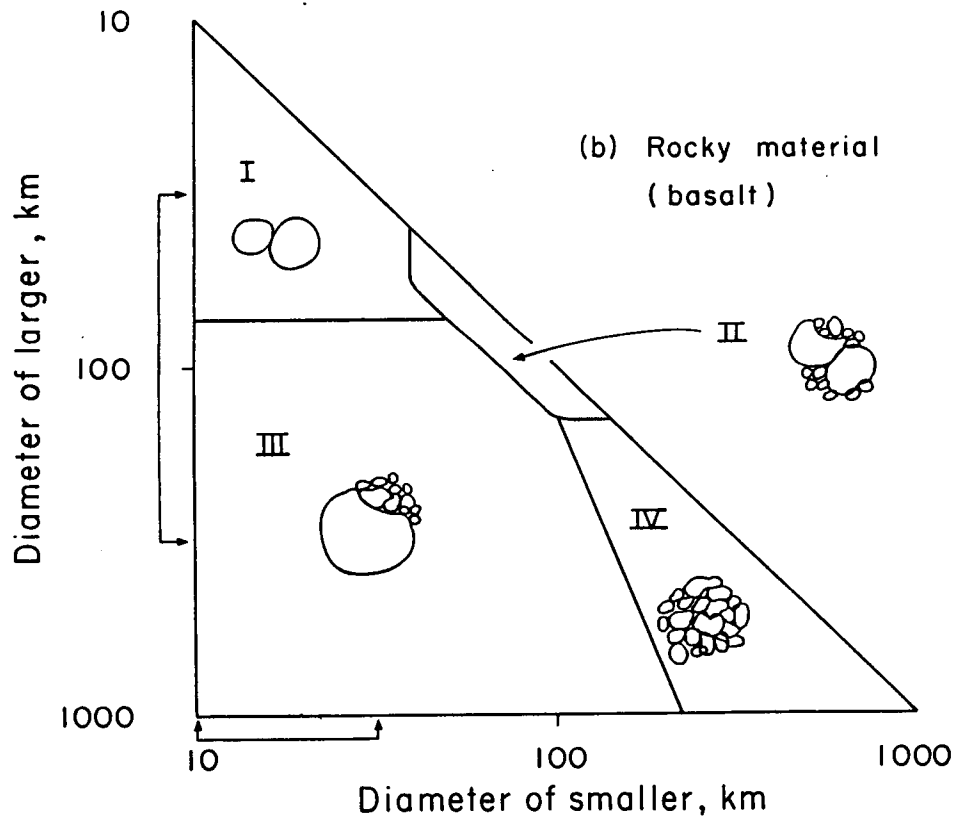
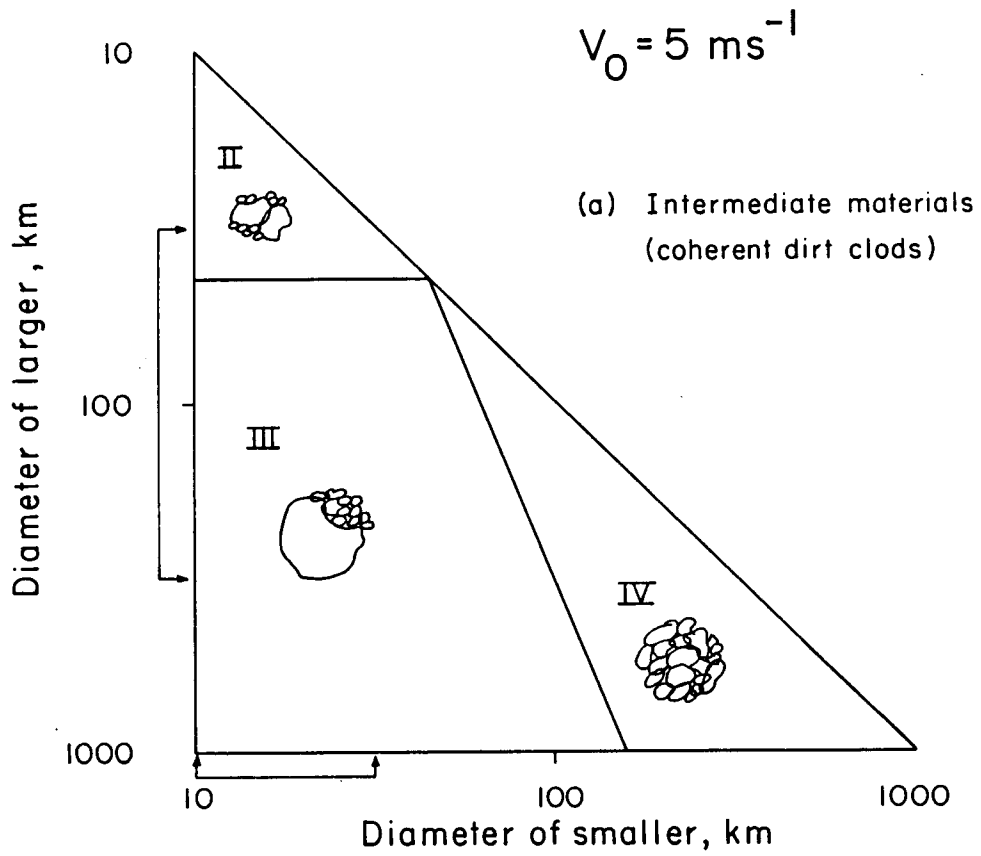


Figure 5.3

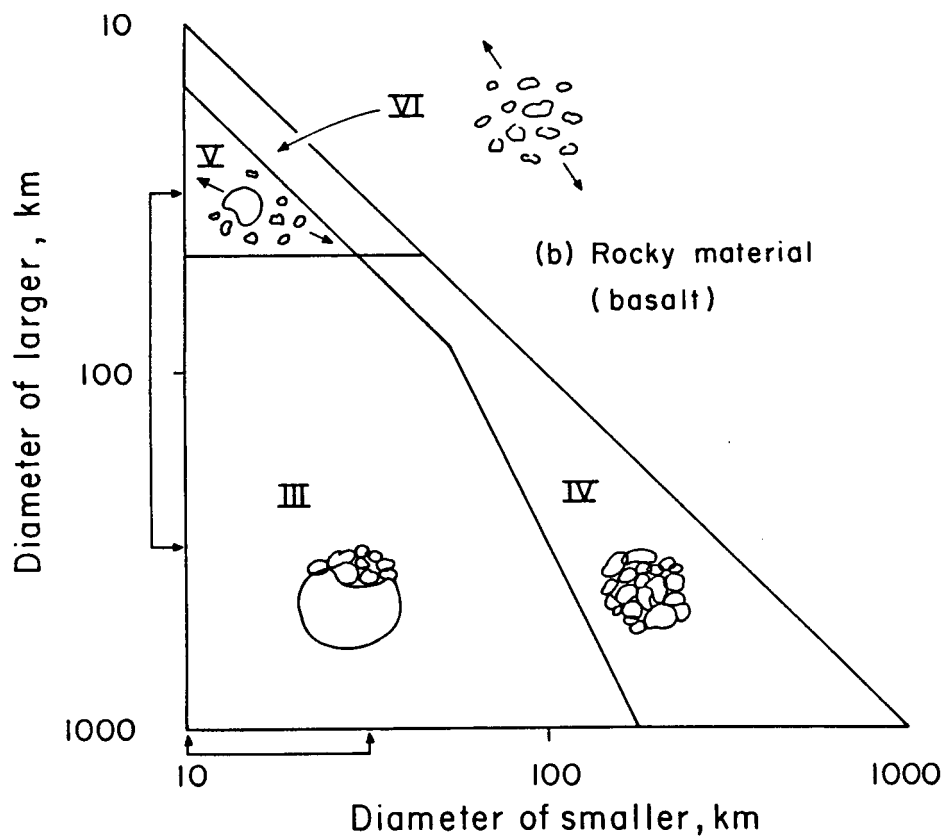
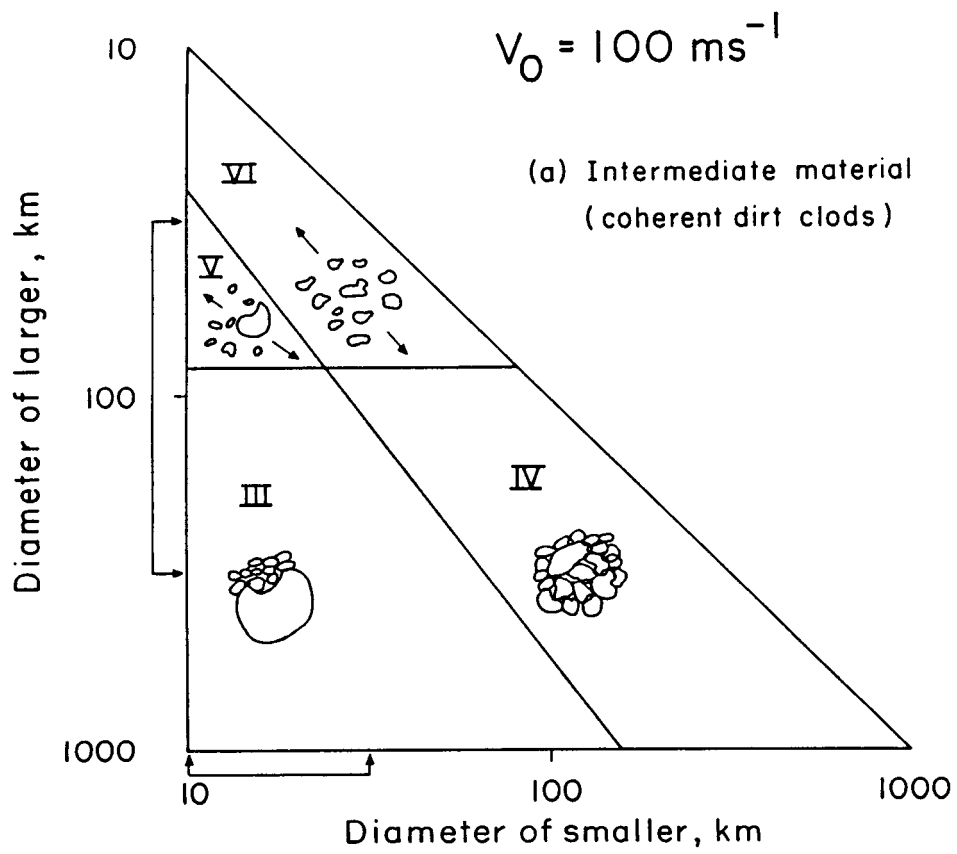


Figure 5.4

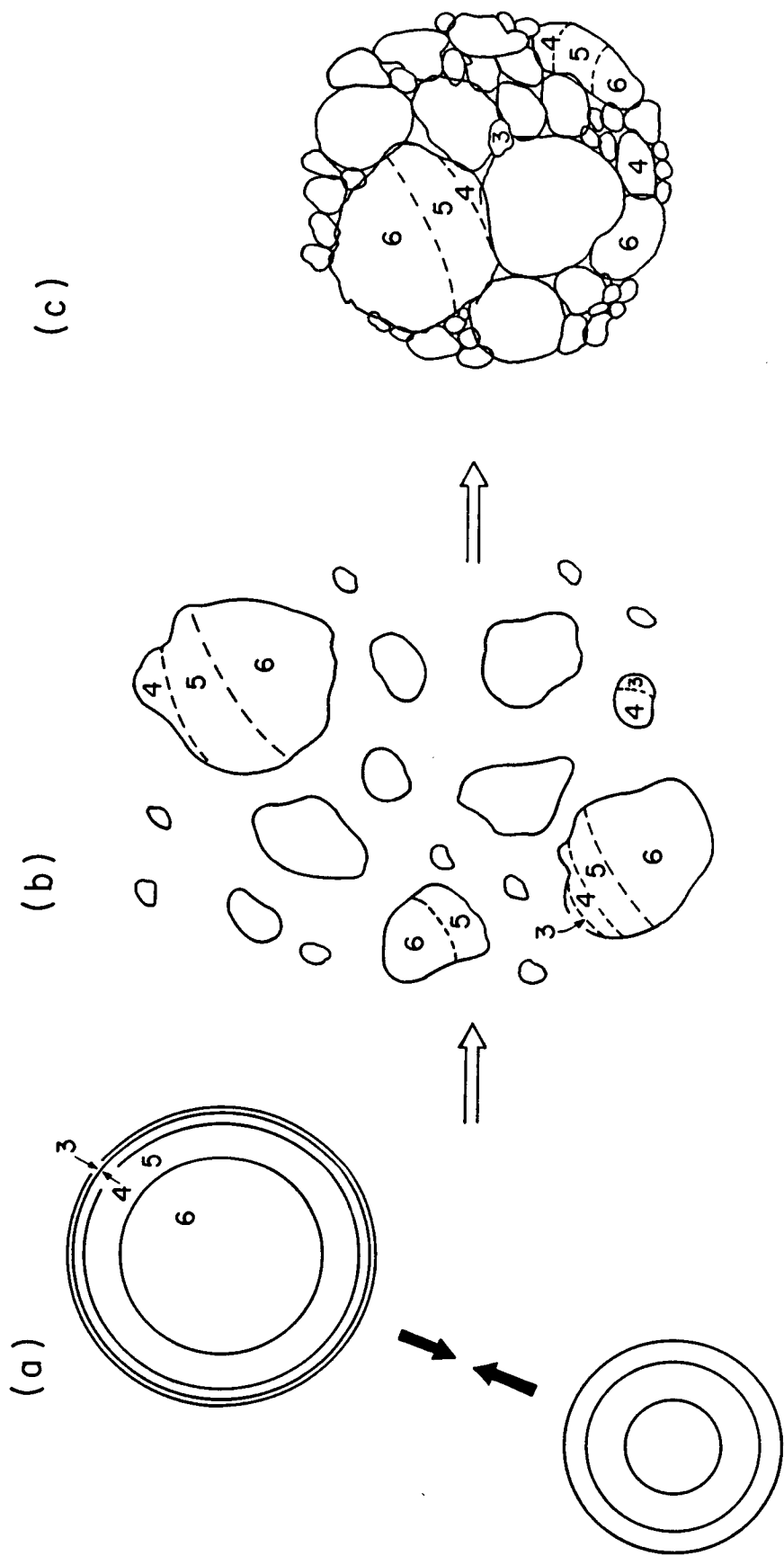


Figure 5.5

CHAPTER 6:

**WATER AND THE THERMAL EVOLUTION
OF CARBONACEOUS CHONDRITE PARENT BODIES**

INTRODUCTION

Carbonaceous chondrites, though among the most chemically primitive materials in the solar system, have been nonetheless modified within their parent bodies. Aqueous alteration, in particular, has played an important role in the petrogenesis of CM and CI chondrites [*Kerridge and Bunch, 1979; McSween, 1979*]. In the first attempt to understand the link between thermal evolution and aqueous alteration, *DuFresne and Anders [1962]* proposed a qualitative model for a carbonaceous chondrite parent body in which internal heating released water from pre-existing hydrous minerals until a liquid zone extended to just below the surface. Aqueous alteration was thought to have occurred there over a period of a few thousand years, with the retention of free H₂O on the parent object limited by subsolar sublimation of ice. More recent research on carbonaceous chondrites has not addressed the thermal driving mechanism for alteration, but has focused on the complex mineralogy of altered matrix and vein materials [*Richardson, 1978; Bunch and Chang, 1980; Barber, 1981; McKinnon and Zolensky, 1984; Tomeoka and Buseck, 1985, 1988; McSween, 1987*]. Oxygen isotope systematics [*Clayton and Mayeda, 1984*] have nevertheless provided constraints on temperature and water volume present during the alteration process.

In this paper, we develop the first quantitative models for the thermal evolution of carbonaceous chondrite parent objects in which the thermodynamic and transport properties of water are shown to exert a strong influence. In contrast to the approach taken by *DuFresne and Anders [1962]*, we assume that these parent bodies were initially mixtures of ice and anhydrous rock. We argue that there are two likely alternatives for the parent body aqueous alteration environment and subsequent sample delivery. In the first model, the interior of a carbonaceous chondrite parent object is nearly homogeneously altered, and samples are derived following subsequent catastrophic break-up. In the second model, carbonaceous

chondrites are derived solely from regoliths, without sampling the deep interiors. For interior alteration, bounds on parent body size, composition, and heat source magnitude are given consistent with constraints on peak temperature and homogeneity. We present representative calculations showing the thermal effects of aqueous alteration reactions. Several mechanisms for introducing water into near-surface regions are illustrated for the regolith-alteration hypothesis, and we address the issue of long-term retention of ice on parent bodies. Finally, we discuss the remaining discrepancies between theory and observation, and we suggest revised models for the aqueous alteration environment of carbonaceous chondrites.

ALTERATION IN CARBONACEOUS CHONDRITE PARENT BODIES

Two important processes that affected early carbonaceous chondrite history were brecciation and aqueous alteration. Most, and possibly all, CM and CI chondrites are breccias. As such textures have been interpreted as indicating that these meteorites have been exposed and reworked in a surficial regolith, it is then important to ask if aqueous alteration, too, occurred in a regolith environment [*Kerridge and Bunch, 1979; Bunch and Chang, 1980*]. Although many carbonaceous chondrites are gas-rich [*Goswami et al., 1984*], the "planetary" abundance pattern of noble gases does not support solar irradiation within a regolith.

Petrographic observations of carbonaceous chondrites [*Richardson, 1978; Kerridge and Bunch, 1979; Tomeoka and Buseck, 1988*] indicate that phyllosilicate formation and filling of fractures by mineralizing fluids occurred in several stages, consistent with the idea that mineralization and impact brecciation were contemporaneous. However, earlier alteration in asteroidal interiors cannot be ruled out, as some observations of compositional variations suggest that aqueous alteration of matrix materials may have largely preceded mechanical reworking.

McSween and Richardson [1977] found that matrix compositions in CI chondrites are fairly constant within individual breccia clasts but vary between different clasts; similarly, host and clasts in CM chondrites also have distinct compositions [*McSween*, 1987]. Moreover, *Richardson* [1978] was able to describe the compositions of vein mineralizing solutions by local leaching of pre-existing matrix phyllosilicates, which suggests that filling of fractures postdated primary alteration.

From the isotopic evolution of Sr in CI carbonate, *Macdougall et al.* [1984] inferred that vein formation occurred very early, within 100 m.y. of the 4.55 b.y. formation time of unaltered chondrites. Fission-track compaction ages, representing the times at which altered phyllosilicate and isolated olivine grains came into final contact, range from 4.4 to 4.2 b.y. for CM chondrites [*Macdougall and Kothari*, 1976]; individual ages are accurate only to within 100 m.y. or so due to uncertainty in the initial $^{244}\text{Pu}/^{238}\text{U}$ ratio. Taken together, these measurements provide an approximate upper limit of a few hundred million years for the duration of brecciation and alteration.

Both brecciation and aqueous alteration of carbonaceous chondrites, then, must have occurred very early, either during or shortly after accretion, although the relative timing of these processes remains uncertain. Two broad classes of hypotheses that can account for aqueous alteration differ in the location of, and thus the heat sources and physical mechanisms involved in, the hydration of matrix minerals. In the first class, alteration may have occurred within planetesimal interiors, and brecciation produced during accretion into parent bodies, or alteration may have taken place within the interiors of the final parent bodies, with samples later excavated by catastrophic break-up. *Scott and Rajan* [1981] and *Grimm* [1985] have suggested similar models for ordinary chondrite metamorphic history. In a competing class of hypotheses, brecciation and alteration may have taken place contemporaneously within a regolith. Because these processes

occurred early in the history of the parent body, such a regolith could probably not be defined in the usual sense of a soil layer gradually excavated from underlying bedrock, but instead might include material above some depth to which the most recently accreted material was incompletely consolidated. These two classes of hypotheses may be termed *interior alteration* and *regolith alteration*, respectively.

The extent of alteration within a particular environment warrants further consideration. Carbonaceous chondrite parent bodies may have experienced pervasive aqueous alteration under either interior alteration or regolith alteration, with the result that these zones were largely petrologically homogeneous, or alteration could have been limited, such that these regions contained significant amounts of unaltered materials. Two lines of evidence that bear on this problem are asteroid collision mechanics and carbonaceous chondrite chemistry and texture.

Studies of asteroidal collisional histories [*Davis et al.*, 1979; *Housen et al.*, 1979] suggest that catastrophic impacts, which result in complete fragmentation of a body, may have occurred repeatedly for most asteroids over solar system history, although the largest objects (diameters from 300 to 1000 km) probably experienced few, if any, such events [*Greenberg and Chapman*, 1983]. Most sizable asteroids gravitationally reaccrete following catastrophic collisions, but some mass fraction is lost. Although surficial rocks may be accelerated to greater velocities and preferentially escape during catastrophic collisions, it is likely that some samples from the asteroidal interior would also be ejected, especially over several episodes of fragmentation and reassembly. Moreover, the object may eventually be disrupted and dispersed. From these considerations, we may reasonably infer that if a parent body has been totally shattered one or more times, then samples exist which show chemical and mineralogical features typical of conditions within the object's interior, if not representative of the entire range of

conditions. Strong heterogeneity in the extent of alteration in an interior-alteration scenario, then, seems unlikely on the grounds that it is unreasonable that only altered carbonaceous chondrites would be delivered from a shattered parent body without any samples of other kinds of interior mineralogy. A homogeneously altered parent body offers the most straightforward way to sample a parent body interior and obtain only altered materials.

A regolith site for aqueous alteration may be excavated by either catastrophic or noncatastrophic collisions. Catastrophic events again raise the preceding question regarding sampling, leading to the identical conclusion that a homogeneous object is the most plausible condition. Alternatively, carbonaceous chondrites may be "chipped off" by noncatastrophic events that sample shallow depths of the parent object only (i.e., normal impact cratering). If the parent object experienced only these kinds of events over the age of the solar system, the implied strength against fragmentation probably is consistent only with a large asteroid. The regolith-alteration scenario, therefore, may be restricted to large objects, although the composition of the parent body's interior is unconstrained.

The near one-to-one correspondence between petrologic type and chemical group among carbonaceous chondrites (i.e., the absence of unaltered and altered chondrites of the same group) argues further that processes which altered texture and mineralogy were pervasive, supporting either a homogeneous object or homogeneous regolith. In addition, although individual CM and CI chondrites are largely brecciated, they almost invariably contain only altered materials. The only exceptions are a few C3 clasts in Murchison [*Olsen et al.*, 1988], a minor component that appears to have been a late addition from elsewhere after the bulk of Murchison was altered.

The principal alternative models for the aqueous alteration environment under consideration here, then, are that of homogeneous alteration of an object's interior,

either in parent bodies or accreting planetesimals, or regolith alteration on a large object where the conditions at depth are unknown (Figure 6.1). Of course, the comparatively small number of samples, and the presumably smaller number of parent body impact events responsible for their excavation, make these hypotheses only the most likely out of a range of possibilities.

CONSTRAINTS ON THERMAL MODELS

Thermal models of ordinary chondrite parent bodies [e.g., *Miyamoto et al.*, 1981] may be constrained to match peak temperatures inferred from the distribution of petrologic types among a particular chemical group, as well as cooling rates inferred from metallographic or isotopic closure methods. Among carbonaceous chondrites, differences in petrologic type may indicate variations in the extent of aqueous alteration rather than variations in temperature [*McSween*, 1979]. Peak temperature constraints are available for the carbonaceous chondrites, however, on a group basis. Moreover, hydrous:anhydrous mineral ratios and isotopically-determined water:rock ratios provide additional constraints on prior history. Metallographic cooling rates, in contrast, are not a meaningful guide to parent body size or thermal history type for chondrites of petrologic type 3 or lower, because the low peak temperatures experienced by these meteorites lie within or below the metallographic closure interval [*Miyamoto et al.*, 1981; *Grimm*, 1985].

Peak Temperatures

The peak temperatures experienced by CM and CI chondrites, while in contact with water, have been estimated by *Clayton and Mayeda* [1984]. The strong oxygen isotope fractionation between calcite and hydrous matrix phases restricts the temperature during aqueous alteration to 25°C or less for CM chondrites. Under the assumption that CI chondrites had an anhydrous precursor

similar to that observed in CMs, *Clayton and Mayeda* [1984] derived a limiting alteration temperature of 150°C for CI meteorites. These are the only available temperature estimates for the alteration process, although the higher temperatures inferred for CI chondrites may be inconsistent with the observation that CI phyllosilicates are more poorly crystallized than those in CM chondrites [*Tomeoka and Buseck*, 1988].

These bounds are applicable only for the period during which rock was in contact with water; if water was later expelled or exhausted by chemical reactions, subsequent temperatures would have been free to rise. *Rietmeijer and Mackinnon* [1985] inferred that temperatures of approximately 190°C for CI and 260°C for CM chondrites were necessary to produce the observed ordering in poorly graphitized carbon. However, these estimates are accurate only to within 100°C, and temperatures may also be systematically shifted to lower values by catalytic activity or long heating times. An alternative peak temperature constraint is imposed by dehydration of matrix phyllosilicates. Textures characteristic of partial dehydration of serpentine-type phyllosilicates have been observed recently in two CM chondrites [*Akai*, 1988]. Although the search for similar textures in other carbonaceous chondrites is incomplete, it is clear that these meteorites did not experience temperatures significantly in excess of the dehydration interval, or else there would be no water-rich matrix. *Akai* [1988] experimentally reproduced the patchy, disordered and defect structures observed in two Antarctic CM chondrites by heating samples of Murchison to 500°C for one hour. Such textures were not observed at 400°C. The short duration of these experiments, however, makes extrapolation to geological time scales uncertain. Instead, we adopt a value of 350°C as the value for the long-term dehydration temperature, based on measurements by *Johannes* [1968] of the equilibrium phase boundary for the reaction transforming serpentine and brucite to forsterite and water. We discuss this

reaction further in a later section. A temperature of 350°C may then be taken as the limiting value for CI and CM chondrites following expulsion or exhaustion of H₂O. For anhydrous CO chondrites, textural, mineralogical, and chemical studies limit the peak temperature to 450°C [McSween, 1977].

Timing and Extent of Aqueous Alteration

The strontium isotopic composition of vein carbonate in CI chondrites [Macdougall *et al.*, 1984] and compaction ages for CM chondrites [Macdougall and Kothari, 1976] limit the alteration period to within a few hundred million years of accretion. Since we will argue below that the alteration reaction itself was rapid, this constraint applies principally to the duration of heat sources and the availability of water. It is assumed here that the entire matrices of CI and CM chondrites are composed of altered materials; the required volume fractions v_h and v_a of hydrous and anhydrous minerals are then in the ratios $v_h/v_a \sim 1.0$ and ~ 0.5 , respectively [Dodd, 1981]. CO chondrites are taken to be completely unaltered, so $v_h = 0$.

Water:Rock Ratio

In addition to peak alteration temperatures, Clayton and Mayeda [1984] also estimated water:rock oxygen mass ratios for aqueously altered carbonaceous chondrites. These ratios may be expressed as water volume fractions of 0.8 and ~ 0.5 for CI and CM chondrites, respectively. Such estimates correspond to the total volume of water flushed through a volume of rock over time, because no reasonable pore volume can hold 80% water. Therefore H₂O transport is indicated the CI water:rock ratios. Because not all of the water that moves throughout the asteroidal interior will exchange oxygen isotopes with the rock, we may assume that these water volumes are lower limits.

FORMULATION OF THERMAL HISTORY MODELS

Even within the restricted framework of the homogeneous interior alteration or regolith alteration models, uncertainty in the initial conditions generally prohibits a unique solution for all model parameters consistent with observational constraints. A series of interior-alteration models is examined below to test for acceptable combinations of size, water volume fraction, and heat source abundance that satisfy peak temperature and homogeneity constraints. We consider only qualitatively the constraints of water:rock ratios. We complete the interior-alteration investigations with some simple tests of aqueous alteration chemical reactions on parent body thermal history. For regolith-alteration models, our approach is of necessity more exploratory. By explicit models, we seek to test the viability of possible mechanisms for introducing water into such an environment under representative conditions.

In our basic model, carbonaceous chondrite parent bodies are taken to be initially cold mixtures of ice and anhydrous silicates heated by ^{26}Al and chondritic complements of long-lived radionuclides. When ice is melted, water may react with the rock to produce hydrous silicates. The effects of latent heat are included for both H_2O and silicates. Dehydration is assumed to occur at 350°C . Under sufficiently large temperature gradients, hydrothermal circulation may develop, redistributing heat so the interior reaches an isothermal state. Gas diffusion occurs as temperatures rise and increasing amounts of H_2O are vaporized. At high pressures, the overlying rock will fracture, and H_2O will be vented into the regolith or to space. Although we have attempted to identify several important processes that contribute to the thermal history of carbonaceous chondrite parent bodies, in practice not all elements of this model are evaluated simultaneously.

While the mathematical details of the thermal history models are given in Appendix 6.A, supporting arguments for this model are presented in this section.

We discuss separately those processes occurring before the period of aqueous alteration and those taking place during alteration. Among the former processes are nebular condensation, accretion, and lithification of carbonaceous chondrite parent bodies. Among the issues important for the alteration stage are the heat sources responsible for volatile mobilization and mild metamorphism, the permeability of parent bodies undergoing hydrothermal circulation and gas transport, and the rate of aqueous alteration.

Nebula Condensation

The equilibrium condensation sequence [Grossman, 1972; Lewis, 1972; Goettel and Barshay, 1978] has provided a basis for understanding the radial compositional structure of the solar system. For potential aqueous alteration of carbonaceous chondrites, two crucial events were the formation of major H₂O-bearing phases such as serpentine and talc at $T < 400$ K and the condensation of water ice at $T < 200$ K [Lewis, 1972]. The radial distances at which these phases appear may be estimated from models of the pressure and temperature structure of the solar nebula [Cameron and Pine, 1973; Wood and Morfill, 1988]. Lewis's model shows the formation of talc in the region of the asteroid belt, while ice did not condense until nearly the distance of Saturn. By this model, hydrated silicates provided the original source of water in the region from Mars to Jupiter, including the putative asteroidal sources of meteorites. This assumption was implicit in the *DuFresne and Anders* [1962] model for carbonaceous chondrite parent bodies.

Chemical and isotopic evidence in carbonaceous chondrites for the nebular equilibration of dust and gas has been critically reviewed by *Bunch and Chang* [1980], who suggested instead that direct condensation of ice and its accretion into parent bodies was possible. Recently, *Prinn and Fegley* [1988] have questioned

whether the equilibrium condensation assumption itself is valid, i.e., was chemical equilibrium reached within 10^5 - 10^6 y, the lifetime of the solar nebula? By simple thermokinetic arguments, Prinn and Fegley showed that formation of hydrous minerals under nebular conditions would require time scales $> 10^{15}$ y for solid-solid reactions and 10^9 - 10^{10} y for gas-solid reactions. Even the more rapid case is 10^4 times longer than the lifetime of the solar nebula, providing a powerful argument that formation of primary hydrous minerals from the solar nebula at $T < 300$ K is kinetically inhibited. On the basis of revised condensation and nebula models, Prinn and Fegley favored direct condensation of ice at the distance of the present-day outer asteroid belt. Considering the equilibration and thermokinetic arguments together, we assume that H_2O was incorporated into primary parent objects as ice instead of as an earlier generation of hydrous minerals.

The initial proportion of ice and its degree of mixing with rock depends on the relative timing of ice condensation and parent body accretion. We consider a homogeneous accretion scenario, so that ice and rock are intimately mixed throughout the parent body. *Dodd* [1981] described carbonaceous chondrite matrix materials as "chemically unfractionated and the result of essentially complete condensation of nebular gas". It is not known, however, if this quenching extended to temperatures low enough for H_2O condensation, so that ice and rock would accrete together. Voids interpreted to have formed during evaporation of volatiles have been observed in the Orgeuil CI chondrite [*Tomeoka and Buseck*, 1988], but unambiguous textural evidence for the presence of ice-rock mixtures has not been found. An upper limit to the H_2O volume fraction of ~ 0.8 is given by cosmic abundances [*Anders and Ebihara*, 1982]; such high proportions of ice are appropriate for a cometary origin of carbonaceous chondrites at solar distances much further than the asteroids. At present, however, we limit the volume fraction of ice to 0.4 based on mechanical considerations (see below).

Accretion

We assume that accretion is rapid compared with interior heating, so that the initial temperature profile is uniform and equal to the surface value in equilibrium with insolation (impact heating during accretion is negligible). Because plausible heat sources have durations of $10^6 - 10^7$ y (see below), accretion times must be shorter than these values if this assumption is to be valid. Numerical simulations of planetesimal accretion at 2.7 A.U. [Greenberg *et al.*, 1978] show that objects several hundred kilometers in diameter may form within $\sim 10^5$ y. Recent revisions to this algorithm [Patterson and Spaute, 1988] have resulted in a sharp upward revision of accretion times for the smallest objects, but the integrated time to accretion of large asteroids is relatively unaffected. On the other hand, analytical approaches [Safronov, 1979; Wetherill, 1980] predict $\sim 10^7$ y accumulation times for large asteroids. As an upper limit, asteroid accretion times are constrained by the growth time of Jupiter. By gravitational perturbations due to Jupiter itself, or by the scattering of Jupiter-zone planetesimals into the asteroid belt, encounter velocities between asteroids were increased such that further accretion was halted in favor of fragmentation and dispersal [Safronov, 1972, 1979]. Numerical studies by Davis *et al.* [1979] suggest that interactions with earth-sized Jupiter-scattered planetesimals raise typical asteroid encounter velocities to 5 km/s within 10^6 - 10^7 y. These calculations are based on the presumed pre-existence of such planetesimals, which may themselves take $\sim 10^8$ y to accrete [Wetherill, 1980]; however, a runaway growth could occur here as well [Patterson and Spaute, 1988]. Since the time scale for accretion cannot be adequately resolved from the time scale for internal heating, the assumption of short accretion times must be viewed as *ad hoc*. Isotopic techniques cannot be considered to date accretion times reliably, in light of possible late disturbance by aqueous alteration.

Following accretion, temperatures and compositional changes are assumed to

be the result only of the internal evolution of the parent object. There is some evidence among ordinary chondrites, however, to suggest that internal evolution was contemporaneous with further accretion [Scott and Rajan, 1981] or with collisional disruption and gravitational reassembly of the parent object [Grimm, 1985]. We address contemporaneous alteration and accretion by finding the lower limit in size for objects that can satisfy the appropriate peak temperature constraints.

Parent Body Compaction

It is assumed that carbonaceous chondrites are fully lithified throughout the history represented by these calculations, although the mechanisms that could lead to consolidation and lithification in meteorites, such as overburden [Cain *et al.*, 1985], impact [Sugiura and Strangway, 1983; Sneyd *et al.*, 1988], thermal recrystallization [Yomogida and Matsui, 1983, 1984], or pressure solution, are poorly understood. Most chondrites are coherent breccias in which clasts are also well lithified; the properties of these samples suggests that their parent bodies were well indurated. It is not known, however, if this induration was achieved before aqueous alteration. This assumption is critical, because if carbonaceous chondrites were still unconsolidated when H₂O was mobilized, differentiation of water and silicates may have occurred.

An upper limit to the rate of upward expulsion of water from a rock skeleton may be specified if the silicates are completely deformable, so that pressures in the solid and fluid are the same. The separation velocity u is then given by Darcy's law, driven by a pressure proportional to the density difference $\Delta\rho$ between the two phases: $u = K \Delta\rho g / \eta$, where K is the permeability, g is the gravitational acceleration, and η is the viscosity of water. The Darcy segregation time $t_D \sim R/u$ is the characteristic time to move water over a length scale R . Taking g to be the

average gravitational acceleration by volume within a uniform sphere of radius R and density ρ , $g = \pi \rho G R$, where G is the gravitational constant. With $\rho = 3 \text{ Mg/m}^3$ and $\eta = 10^{-3} \text{ Pa-s}$, we find $t_D \sim 10^{-13} / K$, expressed in millions of years. If this quantity is small compared with the characteristic thermal diffusion time for a sphere, $t \sim 0.1 R^2/\kappa$, where κ is the thermal diffusivity, then water-silicate separation may occur. Since $\kappa \sim 10^{-6} \text{ m}^2\text{s}^{-1}$, the thermal diffusion and Darcy segregation times are comparable for $KR^2 \sim 10^{-4}$. At $K = 10^{-13} \text{ m}^2$, then, upward expulsion of H_2O may begin at $R \sim 30 \text{ km}$, with significant effects probably restricted to $R > 100 \text{ km}$. However, the permeability is poorly constrained (see below) and could vary by two orders of magnitude in either direction. A more realistic treatment of the problem of fluid expulsion from an elastic, deformable skeleton follows from soil consolidation theory [e.g., *Lambe and Whitman, 1969*] but at the expense of introducing additional unknown parameters. We find no reason to reject hypotheses that H_2O expulsion by silicate compaction is either fast or slow. Our assumption that it is slow is largely for convenience in the present model, although we have considered the effect of complete water-rock differentiation on carbonaceous chondrite thermal history in a preliminary report [*Grimm and McSween, 1988*]; suggestions for future models with large water volumes are given in the Discussion below. The maximum water volume fraction in the fully-lithified case is then limited by the amount that will fit into the pores of a connected rock skeleton, approximately 40% by volume.

Heat Source

The heat source for primordial metamorphism and melting of meteorite parent bodies is still unresolved [*Sonett and Reynolds, 1979*]. However, two leading candidates have emerged: solar electromagnetic induction and the decay of the short-lived radionuclide ^{26}Al .

Electromagnetic heating of asteroids by the interaction of the early solar wind and solar magnetic field was first studied in detail by *Sonett et al.* [1970]. A scenario constructed by *Herbert and Sonett* [1979] for anhydrous objects shows marginal silicate melting on Vesta but none on Ceres; this is principally caused by the inverse square falloff of spherically symmetric plasma flow and associated induction heating. The thermal histories inferred from the observed spectrophotometric structure of the asteroid belt with solar distance [*Gradie and Tedesco*, 1982; *Bell*, 1986] may be a strong constraint on heating models. However, there are a number of unknown model parameters associated with the physical state of the early sun, and an asteroid's response is sensitive to its electrical conductivity. Therefore, the extent of electromagnetic heating and uniqueness of model scenarios are difficult to evaluate quantitatively.

Aluminum-26 is the most favored of the potential short-lived radionuclides because of its expected high abundance, high decay energy, and reasonably long half-life [*Sonett and Reynolds*, 1979]. Since the discovery of its decay product (excess ^{26}Mg) in Allende by *Lee et al.* [1976], numerous thermal models for meteorite parent bodies have been constructed using ^{26}Al as a heat source (see *Basaltic Volcanism Study Project* [1981] for a review).

Because the ^{26}Mg excess was detected by *Lee et al.* [1976] only in a refractory inclusion in Allende, the inferred initial abundance of ^{26}Al (initial $^{26}\text{Al}/^{27}\text{Al} = 6 \times 10^{-5}$) may not be representative of the amount of ^{26}Al incorporated into parent bodies. In addition, it was immediately recognized by these workers that such levels of ^{26}Al would melt all but the smallest objects. Radiogenic ^{26}Mg had not been detected outside of refractory inclusions until *Hutcheon et al.* [1988] reported a ^{26}Mg excess in an anorthite-bearing chondrule in an ordinary chondrite, from which they inferred an initial $^{26}\text{Al}/^{27}\text{Al}$ of $(8 \pm 2) \times 10^{-6}$. The discovery of radiogenic ^{26}Mg outside of CAIs suggests that ^{26}Al was incorporated into parent bodies.

Although this new figure for initial $^{26}\text{Al}/^{27}\text{Al}$ may represent an upper limit, the value reported by *Hutcheon et al.* [1988] is not very different from that deduced from thermal models of ordinary chondrites. Under the assumption that the current collections of ordinary chondrites are representative samples of the H and L chondrite parent bodies, *Miyamoto et al.* [1981] found that an initial $^{26}\text{Al}/^{27}\text{Al}$ of 5×10^{-6} for both objects would have been sufficient to explain the observed distribution of petrologic types and their inferred peak temperatures.

We believe that these modeling and experimental efforts support the case for ^{26}Al as an important primordial heat source for chondrite parent bodies. The present model, then, is formulated in terms of radionuclide heat sources; however, the principal conclusions on the thermal evolution of carbonaceous chondrite parent bodies are not markedly affected by choice of heat source, because both ^{26}Al and electromagnetic induction operate on time scales of $\sim 10^6$ y and the internal temperature profiles produced by both sources are broadly similar [*Basaltic Volcanism Study Project*, 1981].

Since the heating requirements for aqueous alteration of carbonaceous chondrites are modest, mechanisms that have been ruled out for the heating of meteorite parent bodies -- in particular, impacts -- could apply here. *Lange et al.* [1985] have experimentally demonstrated that shock dehydration of serpentine occurs over the pressure interval 25-59 GPa. Such release of H_2O could be responsible for later secondary alteration and veining, but is not relevant to the melting of primordial ice required for primary alteration. Shock melting of ice occurs over the interval 8-10 GPa; the corresponding minimum impact velocities, appropriate for a rock projectile and an ice target, are ~ 3 km/s [*Chapman and McKinnon*, 1986]. During the accretion period, encounter velocities are comparable to the escape velocity of the largest object in the population [*Safronov*, 1972], which indicates that impact velocities between asteroids during accretion were only

several hundred meters per second at most. Impact melting of ice is therefore not likely during accretion. Encounter velocities among asteroids were gradually raised to the present value of ~ 5 km/s, however, by gravitational interactions with Jupiter or its scattered planetesimals. As described previously, consideration of the both the time scale for such planetesimal growth [Wetherill, 1980; Patterson and Spaute, 1988] and the time scale required to pump up asteroid velocities [Davis et al., 1979] only weakly constrains the time scale on which impact melting of ice can become effective to $10^6 - 10^8$ y. Since accretion times are probably $10^5 - 10^7$ y, it appears that impact melting can effectively melt ice in postaccretional regoliths. Carbonaceous chondrites show only weak evidence of shock, which suggests that they were not subjected to hypervelocity impact. Unfortunately, the correlation of shock facies [Dodd and Jarosewich, 1979; Sneyd et al., 1988] and shock pressure [Sears et al., 1984] established for ordinary chondrites cannot be used to estimate shock pressures for carbonaceous chondrites, because significant strain could be accommodated by ductile matrix or ice. The shock levels experienced by carbonaceous chondrites and the contribution of impact release of water to aqueous alteration is therefore an open question. Nevertheless, carbonaceous chondrites still require some additional heat source to explain mild static metamorphism of the CO group [McSween, 1977].

H₂O Transport

When heating of the parent asteroid reaches several hundred kelvins, large internal redistributions of H₂O may occur due to evaporation of water in the deep interior, diffusion through the porous interior, and recondensation in a (comparatively) near-surface shell. In addition, under sufficient heating, pore water itself may become gravitationally unstable and undergo hydrothermal circulation. Both of these processes are sensitive to the permeability, a quantity which is not

reliably known.

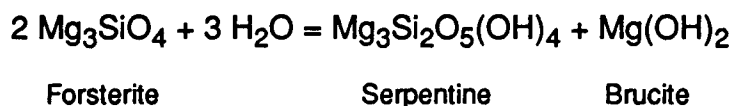
Sugiura et al. [1984] measured the permeability of Allende (CV3) to be $\approx 10^{-15}$ m², a rather low value characteristic of terrestrial silt or clay [*Lambe and Whitman*, 1969] but consistent with the fine texture of the matrix. In the field, however, and presumably in asteroids, permeability is sensitive to the presence of fractures, which may greatly accelerate rates of fluid transport. *Bunch and Chang* [1980] described CM chondrites as having textures similar to terrestrial hydrothermally altered tuffs and mafic rocks. A possible terrestrial analog to such rocks is the Waiora formation, a 600-800 m thick unit of pumice breccias and vitric tuffs in New Zealand's Wairakei hydrothermal region. *Mercer et al.* [1975] adopted $K = 10^{-13}$ m² (at observed porosity 0.2) for the bulk permeability of this unit, which includes the contribution from fractures. The volcanic rocks of the Waiora formation have larger grain (pore) sizes than the Allende matrix, so the bulk permeability of the Waiora formation probably will exceed that of Allende's parent body, unless the size and density of fractures between these two brecciated units varies substantially. The value 10^{-13} m² may be taken as a reasonable upper limit for the permeability of lithified asteroids. In the case of unlithified material, as discussed above, however, the permeability may have been as high as 10^{-11} m², an approximate upper limit for terrestrial sediments [*Lambe and Whitman*, 1969]. In addition, if the highly porous, silt-to-fine-sand texture of the lunar regolith [*Costes and Mitchell*, 1970] is any guide to asteroids, the near-surface permeability should lie in the range 10^{-11} - 10^{-12} m².

If fluid or gas pressures exceed the sum of the rock's tensile strength and the lithostatic pressure, fracturing will occur and H₂O will be vented. Compressive strengths of equilibrated ordinary chondrites measured by *Buddhue* [1942] range from 62 bar to 3.7 kbar. From a typical ratio of compressive to tensile strength of 10 and typical tensile strengths of both sedimentary and crystalline rocks [*Jaeger and*

Cook, 1976], 100 bar (10^7 Pa) is taken as representative of the tensile strength of asteroidal interiors. Such a value implies that resistance to gas or fluid fracturing is dominated by the tensile strength (and therefore is approximately constant) for objects less than about 200 km in diameter; lithostatic pressure becomes increasingly important at larger sizes.

Rate of Aqueous Alteration

Aqueous alteration has profoundly affected the textures of carbonaceous chondrites, from millimeter-scale fractures to micron-scale matrix phyllosilicate grains. *DuFresne and Anders* [1962] suggested that water was available for $> 10^3$ y, on the basis of the regularity of dolomite crystals in CI chondrites. The actual aqueous alteration reactions in carbonaceous chondrites were complex, leading to hydrous minerals such as serpentines, septechlorites, and montmorillonites. In order to assess quantitatively the time scale for aqueous alteration, the reaction



is taken to be representative of carbonaceous chondrite aqueous alteration. Both hydration and dehydration rates for this reaction were studied by *Wegner and Ernst* [1983], who give the time for 99% hydration of olivine as a function of fluid pressure, temperature, and grain size. Even at the low fluid pressures relevant to this problem, hydration of mm-size grains at 0°C will be complete in $\sim 10^4$ y. For the micron-size grains of carbonaceous chondrite matrices, hydration should take only about a year at 25°C (an upper limit to the alteration temperature inferred from isotopic studies, discussed above). *Olsen et al.* [1988] also concluded that the duration of carbonaceous chondrite aqueous alteration was short, $\sim 10^2$ y.

Because aqueous alteration is fast compared with the thermal evolution time scales of asteroids, we may consider such reactions to be instantaneous in the context of thermal models. Although characterized by a different time constant, dehydration rates are also rapid [Wegner and Ernst, 1983], due to increased thermal activation.

In these models we assume that the fluid phase is pure H₂O. On CM and CI parent bodies, mineralizing fluids had more complex chemistries, as evidenced by the fact that Ca-Mg-Fe carbonates and sulfates precipitated sequentially [Richardson, 1978]. Any kinetic effects of lowered activity of H₂O is ignored in these calculations.

RESULTS FOR INTERIOR-ALTERATION MODELS

Common parameters for both interior-alteration and regolith-alteration models are orbital semimajor axis 3 A.U., albedo 0.05, and emissivity 0.8 (estimated values for C-type asteroids). In order to obtain upper limits to hydrothermal convection, a reference permeability of 10^{-13} m² at saturated 20% pore volume is used.

Effect of H₂O on Peak Temperature and Limits on ²⁶Al Abundance

The following series of calculations demonstrates the primary effects of water on thermal evolution. The pore volume is taken to be saturated with H₂O; because this simplification easily leads to hydraulic fracturing at modest temperatures, venting of water is not included. Aqueous alteration and degassing are also neglected for purposes of these illustrations. The remaining variables are parent object diameter, water volume fraction, and initial ²⁶Al/²⁷Al ratio. In terms of these quantities, the problem may be formulated to find upper and lower limits to the radionuclide abundance at specified size and rock:ice ratio. The lower limit is that amount of ²⁶Al required just to melt water in the deep interior. Obviously, melting of

a small volume fraction of the object will not expose much of its rock mass to water or lead to a homogeneously altered interior, but such a level of ^{26}Al may be regarded as a lower bound. The upper limit to ^{26}Al is constrained by the peak temperature for each group described above. In order to estimate this bound conservatively for the homogeneous model, the volume-averaged peak temperature is used; core temperatures may be somewhat higher.

The thermal history for an object 100 km in diameter and 30% ice by volume, which is brought just past the H_2O melting point by an initial $^{26}\text{Al}/^{27}\text{Al}$ ratio of 1.6×10^{-6} , is shown in Figure 6.2. Following a rapid (< 1 m.y.) rise in temperature to the melting point, the interior remains so for several million years while the latent heat of fusion of ice is absorbed. Under this minimum-melting scenario, only a negligible volume in the asteroid's center rises a few degrees above freezing and is altered.

The thermal history of a similar object is given in Figure 6.3, but with an initial $^{26}\text{Al}/^{27}\text{Al}$ ratio of 2.0×10^{-6} . Following H_2O melting, the central temperature rises to 310 K in about 5 m.y. Water is gravitationally stable and no circulation occurs. The volume-averaged peak temperature of all rocks exposed to liquid water is 298 K (25°C); these temperatures match the upper limit for CM chondrites. However, less than half of the volume has melted -- the outer 11 km stay frozen. This result illustrates a problem with constraining CM chondrites to small parent bodies: the bulk of the object must remain frozen in order to accommodate the narrow range of allowable temperatures, and the homogeneous alteration assumption is then violated. We return to this point below.

Figure 6.4a shows a similar calculation applicable to CI chondrites. An initial $^{26}\text{Al}/^{27}\text{Al}$ ratio of 4.3×10^{-6} results in melting of ice throughout 70% of the object's volume, and the mean peak temperature is 423 K (150°C). Hydrothermal convection has been suppressed in this calculation. Figure 6.4b shows a

complementary model, also matching the CI peak temperature (initial $^{26}\text{Al}/^{27}\text{Al} = 6.0 \times 10^{-6}$), in which hydrothermal convection is allowed. Circulation of H_2O has a strong effect on the thermal evolution, homogenizing temperatures within the interior with the result that the object almost uniformly reaches the required peak temperature. Enhanced heat transfer allows melting of ice closer to the surface while suppressing strong temperature increases in the deep interior. Since the adopted approximation for convection yields an overestimate of the heat transfer (Appendix 6.A), Figures 6.4a and 6.4b bound the range of thermal histories in an homogeneous CI parent body undergoing hydrothermal convection.

The calculations above have been repeated for a range of rock:ice compositions and object sizes. Results are summarized in Figure 6.5. At a specified parent body diameter D , the lowermost curve gives the lower bound on ^{26}Al concentration, i.e., the level required just to melt ice. The next higher curve gives the maximum initial $^{26}\text{Al}/^{27}\text{Al}$ which produces volume-averaged temperatures equal to the inferred CM peak temperatures, and the next corresponds to CI. Hydrothermal circulation does not develop in CM models, but it does for CI, and has been suppressed in this third curve as for the calculations in Figure 6.4a. The uppermost, dashed curve gives the upper bound to ^{26}Al abundance, given generous assumptions on the efficiency of hydrothermal convection in CI objects. From Figure 6.5, it can be seen that more ^{26}Al is needed, of course, to attain the same peak temperatures at a higher initial ice volume fraction. The radionuclide abundance must also be larger at smaller diameters to compensate for the increased heat loss. At $D = 1000$ km, peak temperatures for all cases can be achieved by the decay of long-lived radionuclides alone, with the exception that a limited amount of ^{26}Al may be required in such a large CI parent body if hydrothermal convection is particularly efficient. The interval between minimum- melting and CM peak temperatures is smallest at $D = 100$ km because

such objects are large enough to be insulating on the ^{26}Al decay time scale, but not on the decay time scale of K, Th, and U.

A calculation for anhydrous CO chondrites has also been carried out for each parent body diameter in Figure 6.5. Since the observed porosity of carbonaceous chondrites is $\sim 25\%$ [Yomogida and Matsui, 1983], the initial void volume fraction is taken to be 0.25 to illustrate the difference in thermal evolution between dry and H_2O -saturated cases. The similarity of maximum radionuclide abundances between CI and CO chondrites suggests that water may play an important role in controlling their different thermal evolution; that is, water in CI chondrites may have acted as a thermal buffer to prevent the metamorphism experienced by CO chondrites. Moreover, the required initial $^{26}\text{Al}/^{27}\text{Al}$ ratios (several parts per million) are within the observational upper limit established for ordinary chondrites by *Hutcheon et al.* [1988] (8×10^{-6}), and reasonable agreement with the value inferred by *Miyamoto et al.* [1981] (5×10^{-6}) from thermal modeling of ordinary chondrite parent bodies can be found near $D=100$ km. These arguments are more difficult to apply to CM chondrites, however, as their low inferred peak temperatures limit the initial $^{26}\text{Al}/^{27}\text{Al}$ ratios to a factor of 2-3 below CI parent bodies for the same diameter. If CM parent objects are smaller, more ^{26}Al can be accommodated, but at the expense of a smaller altered fraction of the interior.

These models explicitly satisfy peak temperature constraints only. It is possible also to consider, but only qualitatively, the water:rock ratio derived from oxygen isotope data. Because hydrothermal circulation does not develop in homogeneous CM objects, the bulk water content must be at least 50% by volume, a value beyond those considered here. This is a lower bound, because exchange of water between liquid and silicates during aqueous alteration has been neglected in these calculations. Because of the greater range in temperature for CI chondrites, hydrothermal circulation is more likely, and hence it is possible that the

time-integrated water:rock ratio for some samples could be large.

Finally, the presumption of interior homogeneity must be tested. We assume that at least 50% of interior rocks must be exposed to liquid water, in order that delivered samples of altered carbonaceous chondrites are representative of the later-disrupted parent body. CM models satisfy this constraint at $D = 300$ km but do not at $D = 100$ km. For CI models without hydrothermal circulation, $D = 100$ km may be accepted, but $D = 30$ km is marginal. At large diameters, melting extends closer to the surface for water-convecting interiors than nonconvecting ones. However, there is not much difference for smaller sizes, and so CI models with hydrothermal circulation at $D = 30$ km still produce $\sim 50\%$ altered rocks. Therefore, in addition to the restrictions on initial ^{26}Al specified by Figure 6.5, homogeneous interior-alteration models may be constrained to parent bodies a few hundred kilometers in diameter and larger for CM chondrites and several tens of kilometers in diameter and larger for CI objects.

We described earlier a scenario in which interior alteration occurred in planetesimals, before incorporation into parent bodies. Such a model may be excluded for CM chondrites because of the large object diameters required for homogeneous alteration, although accretion of smaller CI planetesimals plausible.

Thermal Effect of Aqueous Alteration

In the preceding models, we neglected H_2O chemical exchange in order to demonstrate the thermophysical effects of the presence of the liquid phase alone. Three calculations are given here in the context of interior-alteration models to illustrate the potential effects of chemical reactions. Since little gas diffusion occurs below 273 K, degassing is again neglected, but finite strength against gas fracture is included. Figure 6.6a shows temperature profiles in a minimum-melting scenario for a 100-km-diameter object heated at an initial $^{26}\text{Al}/^{27}\text{Al}$ ratio of 1.2×10^{-6} . The

object's porosity is 20% and is saturated with H₂O. Melting of ice occurs over about a 3 m.y. interval. Since aqueous alteration is rapid, hydrous minerals are effectively formed instantaneously. The final hydrous:anhydrous mineral ratio is ~ 1 (comparable to that observed in CM chondrites), and essentially all of the water at depth is exhausted by the reactions (Figure 6.6b). The temperature in the deep interior increases markedly (~ 150 K) due to the substantial heat of reaction released, but the peak temperatures are well below those at which dehydration or thermal recrystallization would occur. Because of the speed of the reaction, the peak temperature during alteration is taken to be ~ 0°C, although in reality heat release from progressive alteration might cause substantial temperature excursions while liquid water is still available. As a minimum-melting scenario, this CM model also suffers from a paucity of rocks exposed to water. However, because the oxygen isotope temperature constraints do not apply if water is rapidly removed by aqueous alteration, higher heat source concentrations would push outward the radius of the melting zone.

As core temperatures reach 623 K (350°C), dehydration occurs. Figures 6.7a and 7b show temperature profiles at several times and the final composition profile at 10 m.y., respectively, for a similar object with an initial ²⁶Al/²⁷Al ratio of 5x10⁻⁶. Melting of ice, aqueous alteration, and initiation of dehydration all take place within 1 m.y. The model parent body history becomes rather violent when dehydration reactions occur, because the pore volume is suddenly filled with near-critical H₂O. Since the pressure in the deep interior is several kilobars, immediate H₂O venting of the interior ensues, guaranteeing that that rehydration cannot occur when temperatures again fall below 350°C. In the end, anhydrous minerals again dominate half of the volume, and the altered zone is restricted to depths between 1 and 11 km. As discussed above, there is no evidence for widespread dehydration among CM chondrites. Furthermore, oxygen isotope systematics preclude

rehydration at a temperature as high as 350°C, even if H₂O were not vented from the parent body interior.

A similar calculation ($D = 100$ km, initial $^{26}\text{Al}/^{27}\text{Al} = 5 \times 10^{-6}$) for CI chondrites is shown in Figure 6.8. The highest water volume fraction allowed (0.4) is needed to achieve near-complete alteration of the anhydrous rock. The heat of reaction released is sufficient to send the temperature to the dehydration point, but not through it. In this example, the dehydration reaction is a barrier to further temperature excursions.

RESULTS FOR REGOLITH-ALTERATION MODELS

The release of liquid water occurs readily in interior-alteration models because of the insulating effects of overlying rock. In a cold surface regolith, however, supplying liquid is more difficult. We have conducted several thermal history calculations for internally-heated parent bodies to illustrate the mechanisms by which liquid water may reach near-surface regions. The possible extent of impact melting within a regolith is briefly discussed.

To what depth does regolith alteration extend? *Housen et al.* [1979] numerically modelled regolith formation on asteroids and concluded that typical regolith thicknesses are a few kilometers or less. However, such regoliths develop over the age of the solar system (or until the object is disrupted), a condition that does not apply to the early regolith in which carbonaceous chondrites may have been altered. An upper limit to the thickness of such an accretional regolith may be estimated by considering the depth of the crater resulting from the largest possible impact that does not disrupt the asteroid. This depth is derivable in principle from energy and momentum considerations [*Greenberg et al.*, 1978; *Chapman and McKinnon*, 1986]. A simpler approach is just to use the largest crater depth observed for small bodies (e.g., Herschel on Mimas), which suggests that impact

turnover could extend to a depth of several kilometers. We therefore accept as equally likely any internal heating model which supplies water to within such a distance of the surface. Even if liquid water reaches only the base of the regolith, impact stirring may allow access to upper levels.

Internal Heating

Water may be introduced into the regolith by internal heating in three ways: by direct melting of local ice, which may lead to H₂O circulation and replenishment from below, by venting of liquid or vapor along fractures caused by failure under high pore pressure, or by vapor diffusion through existing pores and cracks. Following the arguments given earlier that regolith-derived carbonaceous chondrites require a large parent body, several models at $D = 300$ km are given which illustrate these mechanisms. Representative values in all cases for the initial ²⁶Al/²⁷Al ratio, porosity, and water volume fraction are taken as 5×10^{-6} , 0.25, and 0.1, respectively.

Figure 6.9a shows the thermal evolution of such an object in which hydrothermal circulation is suppressed. Melting of ice occurs deeper than about 3 km. However, gas pressures lead to venting of H₂O after about 1 m.y., which rapidly results in 70% water loss from the object (Figure 6.9b). This water is removed from the calculation but is equivalent to a saturated surface layer 17 km thick. Therefore fractures initiating at depth can supply large quantities of steam to the regolith; condensation there would provide a low-temperature environment for aqueous alteration. Condensation must occur at least for the late veining, as Cl textures imply that volatiles responsible for fracture-filling must have been in the fluid phase, rather than as gases [S.M. Richardson, quoted in *Kerridge and Bunch, 1979*].

Figure 6.10 illustrates a calculation identical to that of Figure 6.9, but with

hydrothermal convection. Beginning after 0.4 m.y., vigorous circulation and rapid heat losses hold down internal temperatures such that gas pressures achieve only minor venting. Melting of ice, however, extends even closer to the surface (1km) than in the previous example, well within our suggested accretional regolith.

Lastly, an example of gas diffusion is given in Figure 6.11. This transport mechanism has been unimportant in models given heretofore because of sub-boiling liquid-saturated states, homogenization of H₂O distribution by hydrothermal convection, or exhaustion of water by chemical reactions. In the case shown, hydrothermal convection is suppressed so that the H₂O distribution is not homogenized. Under diffusion alone, water vapor is depleted from the deep interior and deposited in the outer 10 km, perhaps within the depth of impact gardening, in the short span of 1 m.y. Therefore, under different initial conditions, direct melting and circulation, venting, and vapor diffusion all appear to be capable of satisfying the requirements of regolith alteration powered by internal heating.

Impact Heating

As discussed above, impacts are insufficient to shock melt ice during accretion but become more effective when asteroid encounter velocities increase via gravitational interactions with Jupiter or its scattered planetesimals. *Safronov* [1978] and *Kaula* [1979] have studied impact heating of the Earth and Moon during accretion. A similar accretional-heating model for aqueous alteration of carbonaceous chondrites is conceptually simple, but the heat source has five free parameters (number of impactors as a function of diameter, velocity, and time; length scale for heat deposition and fraction of impact heat buried) as opposed to the single free parameter (initial ²⁶Al/²⁷Al ratio) required for radionuclide heating. Here we can at least test whether the impact-heating hypothesis may be rejected on the grounds that heat losses will be too rapid to allow aqueous alteration. The

characteristic cooling time t at a depth z is given by $t \sim z^2/\kappa$, where κ is the thermal diffusivity. Given $t \leq 10^4$ y for aqueous alteration (see above) and $\kappa \leq 10^{-6}$ m²s⁻¹ (a typical value for solid rock) for regolith, then $z \leq 1$ km. At shallower depths, smaller values of t or κ are required to accomplish alteration, but there are no restrictions at greater depths. Using simple models for the distribution of impact heat with depth [Kaula, 1979; Bratt *et al.*, 1985], we find that that typical post-accretional impacts can easily melt ice to a depth of several kilometers. The actual cooling time will be affected by other contributions to heat flow, such as heat losses from regolith stirring and release of the heat of the alteration reaction, but these simple calculations indicate that post-accretional impact heating may allow aqueous alteration at depths of a few kilometers within carbonaceous chondrite parent objects.

RETENTION OF H₂O IN CHONDRITE PARENT BODIES

Since we have expanded upon suggestions that ice may have been the original form of H₂O incorporated into parent bodies [Bunch and Chang, 1980; Prinn and Fegley, 1988], it is worthwhile to consider the long-term fate of H₂O in possible asteroidal sources. If aqueous alteration, degassing, or venting are not sufficient to deplete such objects of H₂O during primordial heating, then volatile loss occurs gradually over solar system history, and some fraction of the initial H₂O within meteorite parent bodies may still be present.

Appendix 6.B presents a simplified treatment of the near-surface degassing problem, and gives a relation (equation 6.B7) for the present depth of H₂O loss as a function of permeability and orbital semimajor axis. It should be recognized that this permeability is the *effective* value, including any potential effects of free molecular flow, as discussed in Appendix 6.A. Solving equation (6.A17) for pore sizes of 1mm and 1 μm, the transition temperatures to Knudsen flow are found to

be 250 K and 385 K, respectively. Since the latter value is significantly above the ~ 160 K surface temperature at 3 A.U., free molecular flow can greatly enhance near-surface degassing. The depth of H_2O loss is plotted as a function of permeability for a pore size of 1 mm in Figure 6.12a, and for a pore size of 1 μm in Figure 6.12b. Because the pore size used is the smallest likely value, Figure 6.12b gives conservative upper limits to the depth of H_2O loss.

At 3 A.U., degassing is extremely slow even under the most conservative assumptions, so any primordial ice should still be retained. These results contrast sharply with predictions by *DuFresne and Anders* [1962] that sublimation should limit the lifetime of ice on meteorite parent bodies to only a few million years. However, disturbances to the ^{87}Rb - ^{87}Sr system [*Mittlefehldt and Wetherill*, 1979] in some carbonaceous chondrites suggest that these meteorites were leached of Rb as late as 1 b.y. after their formation. The smooth ^{39}Ar - ^{40}Ar release pattern in Murchison [*Dominik and Jessberger*, 1979] indicates that gas was gradually lost from this CM meteorite at low temperatures. Although primordial heat sources cannot operate on these time scales, these isotopic studies support the idea that volatiles were not rapidly depleted.

Collisional evolution is an additional process that may result in more rapid H_2O loss. Collisions will cause H_2O loss both by an increase in surface area due to comminution and by shock vaporization. The loss due to comminution is probably small, for two reasons. First, the observed size distributions in both asteroids [*Veeder*, 1986] and laboratory fragmentation experiments [*Hartmann*, 1969] indicate that mass is concentrated in larger objects, so that a typical volume is well shielded. Second, most large asteroids probably reaccrete within a few orbital periods of fragmentation, and perhaps within times as short as a few days [*Grimm*, 1985]. Such short exposure times will further minimize the surface area available for H_2O loss. It is more difficult to evaluate the contribution of shock vaporization.

Using impedance-match calculations tabulated by *Kieffer and Simonds* [1980], typical present-day asteroidal collisions should result in stress levels of a few tens of GPa over a length scale comparable to the size of the smaller asteroid (projectile). Since impact vaporization of ice occurs at pressures less than 20 GPa [*Chapman and McKinnon*, 1986], it is apparent that the projectile can be completely devolatilized, as can two comparable-size bodies.

These considerations imply that large, primitive asteroids, e.g., Ceres, are particularly attractive candidates for primordial ice retention because they have undergone fragmentation and reassembly at most a few times, if ever [*Davis et al.*, 1979; *Greenberg and Chapman*, 1983]. Using Figure 6.12b as a guide, we suggest that such objects should still have ice presently accessible within tens of meters of the surface if their regoliths are poorly developed. Ice should nonetheless be retained below a well-stirred regolith, perhaps at a depth of 1 km [*Housen et al.*, 1979]. Slow loss of vapor from the interior might leave thin films of frost on the surface, as inferred from spectrophotometric observations of Ceres [*Lebofsky et al.*, 1981].

Of course, this hypothesis would best be tested by *in situ* sampling or a close flyby of candidate asteroids. Nevertheless, there are two potential experiments that may provide some constraints. Upper limits to the density of H₂O in the asteroid belt may be derivable from ultraviolet spectrometer measurements by the Voyager spacecraft and could provide a boundary condition on a combined model of H₂O production and loss there. Furthermore, high-resolution imaging of Earth-crossing asteroids might directly resolve volatile loss and yield estimates of the H₂O degassing rates of these objects near 1 A.U.

DISCUSSION

The interior-alteration models given here illustrate the potentially important role of H₂O in the divergent thermal histories of CI versus thermally metamorphosed CO and ordinary chondrites. Radiogenic heating can be buffered by the latent heat of fusion and large heat capacity of water, and by enhanced heat loss under hydrothermal convection. Therefore low-temperature aqueous alteration can occur instead of thermal recrystallization at the same heat source abundance. Hydrothermal convection may also be important in homogenizing interior temperatures and attaining locally high water:rock ratios inferred for CI chondrites from oxygen isotope studies.

The CM group is difficult to reconcile with the homogeneous interior-alteration hypothesis, however. At the same ²⁶Al levels inferred for other chondrites, the CM parent body must be small enough to lose heat rapidly in order to maintain low temperatures imposed by oxygen isotope data; in this case strong temperature gradients preclude a homogeneously altered interior. Because convection does not develop in the model CM objects, even under the generous assumptions used, there can be no local water:rock enhancement, and so the interior-alteration model might plausibly be rejected for this meteorite group.

The present treatment of aqueous alteration is undoubtedly oversimplified. Since complete reaction occurs immediately, but only after total melting of ice, water is never free to circulate. Consequently, there is no opportunity to satisfy constraints on water:rock ratios. In reality, melting and alteration might be contemporaneous. Heterogeneity in alteration reactions and significant convection velocities could allow water to circulate without reacting (cf. terrestrial hydrothermal zones).

If alteration occurred in regoliths, some additional inconsistencies may be qualitatively understood. Water can be introduced in great quantities from below

by venting or vapor diffusion, but probably at irregular intervals, and removal of reaction heat is more easily accomplished from a near-surface location. Alteration by local melting of ice still fails to satisfy observed water:rock ratios, unless hydrothermal circulation extends into the regolith. Some fluid-transport mechanism is required to supplement the original *DuFresne and Anders* [1962] model. Aqueous alteration by impact heating faces a similar problem, in that there is no H₂O enhancement over the bulk composition of the regolith and the projectile population, unless impactors become progressively more ice-rich with time, or else the parent body accreted sufficiently far from the sun that near-cosmic proportions of ice were condensed.

All of the scenarios considered here assume that carbonaceous chondrite parent bodies accreted at asteroidal distances with ice proportions of a few tens of percent. Alternatively, the original parent objects could have resembled comets, and later evolved into asteroid-like bodies [*Wasson and Wetherill*, 1979]. Aqueous alteration and oxygen-isotope exchange could occur during water-silicate differentiation [*Grimm and McSween*, 1988], although an improved model might consider sinking of silicate grains through mobilized or partially melted ice. The mechanism for induration of cometary residues into lithified carbonaceous chondrites remains an open question, however.

In spite of the relative detail of the preliminary models developed here, further improvements are necessary to satisfy the observational constraints provided by carbonaceous chondrites. Explicit calculation of oxygen-isotope exchange is needed to assess the total water volume present and the magnitude of variations in oxygen isotope abundance within the parent body. Better information on the rate-limiting processes for aqueous alteration is required -- although alteration can occur rapidly, it may not always do so in nature. These efforts would lead to time-dependent modelling of aqueous alteration. On a more fundamental level,

criteria are needed to distinguish the formation location (inner or outer solar system), alteration environment (regolith or interior), and lithification mechanism of carbonaceous chondrites. Accretion processes and heat sources are also incompletely resolved.

CONCLUSIONS

The following conclusions can be drawn from this study:

(1) Mixtures of anhydrous silicates and ice are suitable starting compositions for carbonaceous chondrite parent bodies that have experienced aqueous alteration.

(2) Aqueous alteration may have occurred within either asteroidal interiors or surficial regoliths. Chemical, textural, and mechanical arguments support a petrologically homogeneous interior for the interior-alteration model and a large parent body for the regolith-alteration model.

(3) The fusion heat of ice, the high heat capacity of water, and the ability of circulating water to enhance rates of heat loss may all significantly contribute to thermal buffering of primordial heat sources for carbonaceous chondrite parent bodies.

(4) The short duration of both plausible primordial heat sources and relevant chemical reactions easily allows aqueous alteration to occur within time constraints imposed by isotope systematics. In fact, exothermic hydration reactions probably require that water was gradually introduced into reaction sites to maintain low temperatures. Because the reverse reaction is endothermic, it is a thermal barrier, which may explain why little dehydration is observed in carbonaceous chondrites.

(5) For the interior-alteration model, bounds on initial $^{26}\text{Al}/^{27}\text{Al}$ ratios for CI chondrites are found comparable to those inferred or observed for both CO and ordinary chondrites. Model CI objects must be greater than several tens of

kilometers in diameter to satisfy the interior homogeneity condition. CM chondrites require lower $^{26}\text{Al}/^{27}\text{Al}$ ratios, and model objects of this group do not develop the hydrothermal circulation that is probably necessary to satisfy water:rock ratios implied by oxygen isotope data.

(6) Regolith alteration may be driven by impacts or by internally-generated heat sources. In internally-heated models, temperatures at depth may reach higher levels than allowed for interior-alteration models. Large quantities of water may be supplied to the regolith from below by hydrothermal circulation, vapor diffusion, or venting. Impacts can provide sufficient heat after parent bodies have accreted but may not be able to deliver the required water volumes.

(7) Retention of primordial ice in carbonaceous chondrite parent bodies is probably not limited by sublimation rates or by collisional comminution, but by shock vaporization.

(8) The present models cannot quantitatively account for all observational constraints imposed by different carbonaceous chondrite groups.

Appendix 6.A:

Mathematical Formulation of the Carbonaceous Chondrite Thermal Model

The mathematical and numerical details are given here of the model used to calculate the internal evolution of carbonaceous chondrite parent objects. The principal assumptions adopted to arrive at this model are described in the text; only supporting details are given below. A summary of nomenclature is given at the end of this appendix, and all units are MKS unless noted otherwise.

Heat Flow

The spherically symmetric heat-conduction equation with internal heating

$$\frac{\partial T}{\partial t} = \frac{1}{r^2} \frac{\partial}{\partial r} \left(r^2 \kappa \frac{\partial T}{\partial r} \right) + \frac{Q}{\rho c_p} \quad (6.A1)$$

is solved by an implicit finite-difference method. The quantities in equation (6.A1) are temperature T , radius r , thermal diffusivity κ , density ρ , specific heat c_p , and heat production per unit mass Q . The thermal conductivity is given by $k = \rho c_p \kappa$. The parameters that control thermal diffusion (k , ρ , and c_p) are taken as simple weighted sums of the contributions of rock, gas, and ice or water. The natural weights for k and ρ are relative volume, whereas the relative mass contributions govern c_p :

$$k = \frac{\sum_j k_j v_j}{\sum_j v_j} \quad \rho = \frac{\sum_j \rho_j v_j}{\sum_j v_j} \quad c_p = \frac{\sum_j c_{p_j} m_j}{\sum_j m_j} \quad (6.A2)$$

where v_j and m_j are the volume and mass fractions, respectively, of the j^{th} component. From equations (6.A2) follows

$$\kappa = \frac{\sum_j k_j v_j}{\sum_j \rho_j c_{p_j} v_j} \quad (6.A3)$$

for the effective thermal diffusivity. More precise formulations of effective thermal conductivity in two-phase media exist, such as the Maxwell formula [*Carslaw and Jaeger, 1947*], but the differences between (6.A2) and these formulations are minor for the present purpose. Temperature-dependent formulae for the thermodynamic and transport properties of rock and H₂O are given in a later section in this appendix.

The heat production Q is the sum of the heat production of individual radioactive elements, weighted by their time-dependent mean abundances in carbonaceous chondrites:

$$Q = m_r \sum_j A_{o_j} Q_{o_j} e^{-\lambda_j t} \quad (6.A4)$$

where A_{o_j} is the initial abundance, Q_{o_j} is the initial heat production per unit mass, and λ_j is the decay constant of the j^{th} radionuclide, and t is time. Since H₂O is also present, an overall weighting factor m_r , the mass fraction of rock, is required. The abundance of ²⁶Al, the primary heat-producing element in the model, is computed from the product of the assumed initial ²⁶Al/²⁷Al ratio and the observed mean Al content of CM chondrites. The relevant elemental abundances are given in Table 6.A1.

The surface temperature is specified by solving the energy-balance equation

$$\frac{S_0}{4d^2}(1 - A) = \epsilon \sigma T^4 + k \left. \frac{\partial T}{\partial r} \right|_{r=R} \quad (6.A5)$$

where S_0 is the solar constant, d is the orbital semimajor axis, A is the albedo, ϵ is the emissivity, σ is the Stefan-Boltzmann constant, and R is the object's radius. The loss of vapor is assumed to occur slowly, and its latent heat is neglected in (6.A5). This assumption follows from consideration of the characteristic time scale for surface degassing (Appendix 6.B) and has been verified by numerical experiments.

Ice - Water Phase Transition

Melting of ice is assumed to occur at a temperature of 273 K, independent of pressure. Since lithostatic pressures exceed a kilobar only for the largest asteroids, the error in this approximation is generally less than 10 K. During the phase transition, thermal energy is absorbed as the latent heat of fusion:

$$\Delta T = \frac{M_i L_f}{M c_p} \quad (6.A6)$$

where ΔT is the temperature rise suppressed during melting, L_f is the latent heat of fusion of ice, and M and M_i are the total mass and mass of ice, respectively. Upon freezing, ΔT is the suppressed decrease in temperature. Temperature changes in regions of the phase transition are tracked using the algorithm of *Reynolds et al.* [1966], which uses a partial melt state and associated partial release and absorption of fusion heat to avoid numerical instabilities associated with finite time steps.

Hydrothermal Convection

Closed circulation of heated water may occur within the asteroid under favorable conditions and provide significant heat transfer. A simple parameterized convection scheme is adopted, similar to calculations of the thermal histories of the Earth [Sharpe and Peltier, 1978], the Moon and the terrestrial planets [Cassen *et al.*, 1979; Schubert *et al.*, 1979; Turcotte *et al.*, 1979], and the Galilean satellites [Thurber *et al.*, 1980].

Buoyant instability in a porous layer of thickness r_w heated from below, with permeability K and average thermal conductivity k , occurs when the Rayleigh number

$$Ra = \frac{\rho_w^2 g \alpha_w c_{p_w} K \Delta T r_w}{\eta_w k} \quad (6.A7)$$

exceeds the critical value $Ra_{cr} = 4\pi^2 \cong 39$ [e.g., Turcotte and Schubert, 1982]; where ρ_w is the reference density of water, g is the gravitational acceleration, α_w is the thermal expansion coefficient of water, ΔT is the temperature drop across the layer, and η_w is the viscosity of water. The efficiency of convection is measured by the Nusselt number Nu , which is ratio of the total heat transported out of the convecting layer to the heat transported by conduction alone, $Nu = q/q_c$. The relation between Ra and Nu has been numerically investigated for two-dimensional hydrothermal convection by Straus [1974]. These results are approximately described by the empirical formulae

$$\begin{aligned} Nu &= Ra'^{1.3} & Ra' < 2 \\ Nu &= 1.6 Ra'^{0.6} & Ra' > 2 \end{aligned} \quad (6.A8)$$

where $Ra' = Ra / Ra_{cr}$. When the layer is heated from within instead of from below, the reciprocal of the nondimensional temperature difference across the layer measures steady-state convective efficiency [Turcotte *et al.*, 1979]; however, Nu may be used for the transient problem when the heat production per time step is small [Cassen *et al.*, 1979].

In the parameterized convection approach, an equivalent conductive solution is sought that has the same heat transfer as the convective system; this may be accomplished by solving (6.A1) with an effective thermal diffusivity $Nu \kappa$ [Sharpe and Peltier, 1978]. The 'actual' temperatures are not those of the equivalent conductive solution, however, but must follow an adiabat within the convecting region. Since the slope of the H₂O adiabat is small at the low gravitational accelerations relevant to this problem, the circulating region is approximately isothermal; its temperature is calculated by matching the total thermal energy from the equivalent conductive solution [Cassen *et al.*, 1979]. A boundary layer of thickness $\sim r_w / Nu$ exists at the top of the convecting layer and is neglected in computing 'actual' temperature profiles; this approximation is valid for $Nu \gg 1$.

Since convection is not limited to upper layers in the object, the effects of spherical geometry will strongly influence the growth of density perturbations and the resulting flow. An analysis of the stability of an internally heated porous sphere has not been found in the literature. However, comparison of the conditions of the onset of convection [Chandrasekhar, 1961] for an internally heated fluid sphere and for a fluid layer heated from below (with mean gravitational acceleration of the sphere) shows that, for the same temperature drop, convection in the sphere requires Ra' approximately twice as large as for the layer. The initiation of instability in the sphere is inhibited by the smaller buoyancy forces resulting from decreased relative volume and lower gravity in the deep interior. Furthermore, Turcotte *et al.* [1979] showed that steady-state heat transfer is more efficient for the

layer than for the sphere at the same value of Ra' . Use of (6.A7) - (6.A8), therefore, must also yield an overestimate of the convective efficiency of the porous sphere. The error is conservative, however, because an upper limit on the efficiency of heat transfer must be used to constrain upper bounds on the size and heat production of carbonaceous chondrite parent objects. The layer approximation satisfies this constraint and renders the problem easily tractable.

A further limitation to the parameterized convection approach is that the stability analysis which leads to the derivation of Ra requires that all properties are constant, with the exception of a linear temperature-dependent variation of density (Boussinesq approximation). Such an approximation is not always satisfied in hydrothermal systems with temperature variations of several hundred degrees; density variations are of order unity, and viscosity variations may span an order of magnitude. Terrestrial hydrothermal convection in a medium of variable thermodynamic properties was studied by *Straus and Schubert* [1977], who found that Ra_{cr} may be much smaller than the Boussinesq value (~ 39). These results may be applied to asteroidal interiors by noting from (6.A7) that the thickness of a layer for which instability occurs scales inversely with gravity. Employing the scaled layer thickness and full temperature interval over which H_2O is liquid, we find from the work of Straus and Schubert that Ra_{cr} may be significantly reduced for objects with diameters greater than 300 km. By using volume-averaged properties in (6.A7), some of these effects may be suppressed; nevertheless, this nonlinearity remains a potential source of error since it does not lead to upper limits to heat production.

Hydrothermal convection will be limited by the degree of H_2O saturation of the pore volume. If water does not completely fill the pores, the medium may be treated as one of reduced effective permeability. The effective porosity in the unsaturated state is just the water volume fraction v_w , and, using the Kozeny-Carman relation

[e.g., *Lambe and Whitman*, 1969], the effective permeability may be expressed as

$$K = K_0 \frac{e/(1+e)}{e_0/(1+e_0)} \quad (6.A9)$$

where e is the void ratio ($e = \phi / (1-\phi)$, where ϕ is the porosity) and the zero subscript denotes the saturated state. Since the variation in K_0 between different rock types spans several orders of magnitude, the onset of convection (and the rate of H_2O vapor loss, discussed below) is very sensitive to the permeability. Arguments for the choices of this parameter are discussed in the text.

The key assumption in evaluating effective permeability in unsaturated states is that water remains continuously interconnected within the pores. In soil mechanics, the maximum capillary head defines the height over which water remains in contact following draining of a soil [*Lambe and Whitman*, 1969]. Since capillary head is inversely proportional to both gravity and pore dimension [*Batchelor*, 1967], very large capillary zones, in the range 1 - 1000 km for pore dimensions of 1 μm to 1 mm, may exist in carbonaceous chondrite parent objects ($g \sim 10^{-2} \text{ m s}^{-2}$). Even if water were not continuously interconnected, it is conservative to assume so, for reasons given previously, in order to provide favorable conditions for convective heat transfer.

Gas Diffusion

The principal assumption of the vapor transport model is that the interior is in a state of quasi-static equilibrium. Under these conditions, the gas pressure always adjusts rapidly to the local temperature and H_2O volume, which change in response to diffusion of gas and thermal energy.

From the Clausius-Clapeyron relation, the vapor pressure has the approximate

form

$$P_{\text{vap}} = P_0 e^{-T_0/T} \quad (6.A10)$$

where P_0 and T_0 have dimensions of pressure and temperature, respectively. By fitting data given in *Keyes* [1928] and *Washburn* [1928], we adopt $P_0 = 3.58 \times 10^{12}$ Pa, $T_0 = 6140$ K for the vapor pressure over ice, and $P_0 = 4.70 \times 10^{10}$ Pa, $T_0 = 4960$ K for the vapor pressure over water.

The equation of state used for H_2O vapor or gas is

$$\begin{aligned} PV &= nRT && (T < 500 \text{ K}) \\ \left(P + \frac{n^2 a}{V^2}\right)(V - nb) &= nRT && (T > 500 \text{ K}) \end{aligned} \quad (A11)$$

where P is the ambient vapor or gas pressure, V is volume, n is the number of moles of H_2O , R is the universal gas constant, and a and b are the van der Waals coefficients. From (6.A11) the gas density $\rho_g = nM/V$ may be found (M is the molar mass); vapor-condensate mass balance then yields the mass of gas M_g in a specified volume of the asteroidal interior:

$$M_g = \rho_g V_g = \frac{\rho_c V \phi - M_0}{\frac{\rho_c}{\rho_g} - 1} \quad (6.A12)$$

where V_g is the volume of gas, ρ_c is the density of condensate (ice or water), V is the total volume, ϕ is the porosity, and M_0 is the total mass of H_2O .

The diffusion of H_2O through the interior must satisfy the equation of continuity

$$\frac{1}{r} \frac{\partial}{\partial r} (r^2 \rho u) = - \frac{\partial \rho}{\partial t} \quad (6.A13)$$

and Darcy's law

$$u = - \frac{K}{\eta} \frac{\partial P}{\partial r} \quad (6.A14)$$

where u is the vertical velocity, η is the viscosity, K is the permeability, and gravitational forces, which are small, have been neglected. Equations (6.A13) and (6.A14) may be combined into the nonlinear equation

$$\frac{\partial \rho}{\partial t} = \frac{1}{r} \frac{\partial}{\partial r} \left(r^2 \frac{K \rho}{\eta} \frac{\partial P}{\partial r} \right) \quad (6.A15)$$

which is solved by an explicit finite-difference method. The gas mass transferred in a given time step is $\Delta M_g = \Delta \rho_g V_g$. An advective temperature change

$$\Delta T = - \frac{\Delta M_g L_v}{M c_{pg}} \quad (6.A16)$$

is caused by the net evaporation or condensation of vapor at a particular location, where L_v is the latent heat of vaporization. Equation (6.A16) holds only when condensate is present and the small change associated with the product of the gas's heat capacity c_{pg} and the temperature difference between adjacent grid locations is neglected.

In this treatment of the gas diffusion problem, H₂O gas and condensate are considered immiscible fluids. The permeability is calculated from (6.A9), using v_g for the effective porosity and $1-v_r$ for the reference porosity. At low temperatures, however, the efficiency of diffusion may be greatly enhanced by free molecular (Knudsen) flow, which occurs when the mean free path of a gas molecule is significantly larger than the characteristic pore dimension:

$$\frac{RT}{4\sqrt{2}\pi N_A P_{\text{vap}} b^2} \gg d \quad (6.A17)$$

where N_A is Avogadro's number, b is the radius of the H₂O molecule, and d is the pore size. Equation (6.A17) may be solved as an equality for the approximate transition temperature to Knudsen flow under equilibrium conditions. Following *Sugiura et al.* [1984], free molecular flow may be parameterized as an increase in the effective permeability inversely proportional to the vapor pressure at temperatures below the transition temperature. In practice, Knudsen flow is of little importance during the active thermal history of the asteroid but becomes relevant to the treatment of secular degassing (Appendix 6.B).

Venting of H₂O

Gas diffusion obeying (6.A14) will generally be smooth, unless pressures become so large that failure occurs. In this case H₂O may move rapidly to upper levels in the asteroid where it may recondense in available pores or escape directly into space. Failure occurs when the pore pressure exceeds the sum of the lithostatic pressure and the tensile strength of the rock [*Jaeger and Cook, 1976*]:

$$P > P_{\text{lith}} + \tau \quad (6.A18)$$

The lithostatic pressure is given by

$$P_{\text{lith}} = \frac{4}{3} \pi G \int_0^R \rho_r^2 r \, dr \quad (6.A19)$$

When gas fracturing occurs, H₂O has a direct path to the surface and might be free to boil away completely in an isothermal environment. However, advective heat losses will limit the rate of venting. In practice, (6.A16) is solved for the vented gas mass due to a temperature increase in a given time step, and the temperature is then reset to its original value, so that heating at a given location is balanced by venting of gas. As long as condensate is available, the temperature is constant and the pressure is maintained at the failure strength. The vented H₂O may be expressed as the thickness of a saturated surface layer of equal volume as a convenient measure of the depth to which significant liquid water may be available in the regolith.

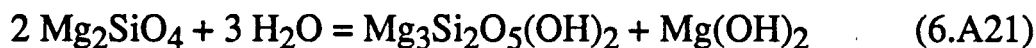
An additional failure mode, hydraulic fracturing, is possible when thermal expansion would lead to a volume of water in excess of the available pore volume. In this case, the pressure is given by

$$P = B \left(\frac{V_w - \phi V}{\phi V} \right) \quad (6.A20)$$

where B is the bulk modulus of water, ϕV is the total pore volume, and V_w is the volume to which water would expand. If (6.A18) is satisfied, the difference between these volumes is lost by hydraulic fracturing.

Hydration and Dehydration Reactions

The formation of serpentine and brucite from forsterite and water is taken to represent the reactions characterizing aqueous alteration of carbonaceous chondrites:



The water:rock volume ratio of the reactants, which is denoted β , is 0.63, and the volume ratio of the products to the reacting forsterite, which is denoted γ , is 1.56. Assuming that net volume changes between the silicate phases are accommodated entirely by the pore volume, i.e., there is no net expansion of the asteroid, the volume balance for (6.A21) is:

$$\Delta v_a + \Delta v_h + \Delta v_w + \Delta v_v = 0 \quad \Delta v_w / \Delta v_a = \beta \quad \Delta v_h / \Delta v_a = -\gamma \quad (6.A22)$$

where Δv is the change in volume fraction and the subscripts a, h, w, and v imply anhydrous minerals (forsterite), hydrous minerals (serpentine and brucite), water, and voids, respectively. Note that $\phi = v_w + v_v$. For the hydration (retrograde) reaction, two cases may be distinguished. If $v_w/\beta < v_a$, then incomplete alteration of anhydrous minerals will occur, and all water will be exhausted. If $v_w/\beta > v_a$, then complete alteration of all anhydrous minerals occurs, and some excess water remains. Using only the subscripts, the changes in volume fraction for incomplete hydration are

$$\Delta w = -w \quad \Delta a = -w/\beta \quad \Delta h = \gamma w/\beta \quad \Delta v = -w(1+\beta-\gamma)/\beta \quad (6.A23)$$

and the fractional volume changes for complete hydration are

$$\Delta a = -a \quad \Delta w = -\beta a \quad \Delta h = \gamma a \quad \Delta v = -a(\gamma - \beta - 1) \quad (6.A24)$$

From the standard heats of formation tabulated by *Robie and Waldbaum* [1968], the heat of reaction released at 25°C is $H = 233$ kJ/kg. The increase in temperature is

$$\Delta T = \frac{\Delta M_h H}{M c_p} \quad (6.A25)$$

where ΔM_h is the mass of hydrous minerals formed by the reaction. Since the reaction time is small compared with the thermal diffusion time (see text), formation of hydrous minerals and release of reaction heat are assumed to occur instantaneously upon complete melting of ice.

The equilibrium phase boundary for this reaction has been determined by *Johannes* [1968] to lie at ~360°C at a fluid pressure of 1 kbar. Fluid pressures in asteroids will usually lie below this value, even if they approach lithostatic pressure. Therefore, 350°C is taken to be the temperature of the dehydration (prograde) reaction. All hydrous minerals are assumed to dehydrate instantaneously, resulting in the fractional volume changes

$$\Delta h = -h \quad \Delta a = h/\gamma \quad \Delta w = \beta h/\gamma \quad \Delta v = h(\gamma - \beta - 1)/\gamma \quad (6.A26)$$

The changes in the enthalpies of forsterite and brucite at 600 K are negligible, and the enthalpy of water changes by only 14%. The high-temperature enthalpy of serpentine was not given by *Robie and Waldbaum* [1968], but changes in other phyllosilicate minerals are also negligible. The heat of the dehydration reaction at 350°C, then, is assumed to be -233 kJ/kg. When the temperature falls below 350°C, rehydration of the silicates occurs. In practice, temperature changes are

evaluated by the same algorithm used for melting and freezing of ice, by using a partial reaction state to avoid numerical instabilities.

Temperature-dependent material properties

The low-temperature thermal diffusivity of rock is taken to be that measured by *Yomogida and Matsui* [1983] for Leoville (CV3):

$$\kappa_r = 3.02 \times 10^{-7} + 2.78 \times 10^{-4} / T$$

Since the mineralogies of unaltered and altered rock are considered to be roughly those of olivine and serpentine, the density of rock ρ_r is taken to be either 3.3 Mg/m³ or 2.5 Mg/m³, respectively. Specific heat measurements of carbonaceous chondrites are lacking, so c_{pr} is taken to be 700 J/kg-K, a typical value for ordinary chondrites [*Alexeyeva*, 1958; *Yomogida and Matsui*, 1983].

Since 400 K was the highest temperature at which measurements on Leoville were performed by *Yomogida and Matsui* [1983], k_r is dominated by lattice phonon conductivity. At higher temperatures, radiation becomes important. On the basis of thermal measurements of olivine and pyroxene, *Schatz and Simmons* [1972] include a radiative conductivity term that is directly proportional to temperature above 500 K. Assuming that the total thermal conductivity between 500 K and 1000 K of the minerals measured by *Schatz and Simmons* [1972] and Leoville differ by a multiplicative constant, the total (lattice + radiative) conductivity k_r' is

$$k_r' = k_r + 2.1 \times 10^{-3} (T - 500 \text{ K})$$

at temperatures greater than 500 K.

The thermal conductivity and heat capacity of hexagonal ice are given by

Hobbs [1974]:

$$k_i = 0.465 + 488 / T$$

$$c_{pi} = 7.67 T$$

and, for simplicity, the density of ice is taken to be $\rho_i = 1.0 \text{ Mg/m}^3$. Since amorphous ice is unstable at $T > 135 \text{ K}$ [Klinger, 1980], its different thermal properties need not be considered at temperatures typical of asteroidal surfaces.

A fourth-order polynomial was constructed for the density of water, by fitting measurements summarized by Keyes [1928]:

$$\rho_w = -221 + 13.1 T - 5.07 \times 10^{-2} T^2 + 8.49 \times 10^{-5} T^3 - 5.48 \times 10^{-8} T^4$$

Gaseous H_2O is taken to behave ideally below 500 K and as a van der Waals gas at higher temperatures; the density ρ_g may be calculated from the relevant equation of state. Details are given above in the section on gas diffusion.

The thermal conductivity of H_2O liquid and gas are given by Touloukian *et al.* [1970]:

$$k_w = -0.581 + 6.34 \times 10^{-3} T - 7.93 \times 10^{-6} T^2 \quad T < 410 \text{ K}$$

$$k_w = -0.142 + 4.12 \times 10^{-3} T - 5.01 \times 10^{-6} T^2 \quad T > 410 \text{ K}$$

$$k_g = -1.43 \times 10^{-2} + 1.02 \times 10^{-4} T$$

The specific heat of water is given by Touloukian and Makita [1970], and the specific heat of gaseous H_2O was taken from Zemansky and Dittman [1981]:

$$c_{pw} = 4200 \quad T < 410 \text{ K}$$

$$c_{pw} = -4.67 \times 10^4 + 333 T - 0.731 T^2 + 5.40 \times 10^{-4} T^3 \quad T > 410 \text{ K}$$

$$c_{pg} = 1680 + 0.552 T$$

where the small variation in the specific heat of water below 400 K and higher-order terms in the specific heat of H₂O gas have been neglected.

The viscosity of H₂O liquid and gas is given by *Touloukian et al.* [1975]:

$$\eta_w = 2.414 \times 10^{-5} 10^{247.8/(T-140)}$$

$$\eta_g = 8.04 \times 10^{-6} + 4.07 \times 10^{-8} T$$

Nomenclature

a	first Van der Waals coefficient, 0.546 m ⁶ mol ⁻²
a	(subscript) anhydrous rock
A	radioactive element abundance, wt. fraction
A	albedo
b	second Van der Waals coefficient, 3.05 × 10 ⁻⁵ m ³ mol ⁻¹
b	radius of water molecule, ~ 5 × 10 ⁻¹¹ m
B	bulk modulus of water, 2 × 10 ⁹ Pa
c	(subscript) H ₂ O condensate (water or ice)
c _p	specific capacity at constant pressure, J kg ⁻¹ K ⁻¹
d	orbital semimajor axis, m
d	grain or pore diameter, m
D	object diameter, m
e	void ratio
g	gravitational acceleration, m s ⁻²
g	(subscript) gas
G	gravitational constant, 6.67 × 10 ⁻¹¹ Nm ² kg ⁻²
h	(subscript) hydrated rock

H	heat of reaction for $2 \text{Fo} + 3 \text{H}_2\text{O} = \text{serp} + \text{bru}$, $2.33 \times 10^5 \text{ J kg}^{-1}$
i	(subscript) ice
j	summation index for bulk rock- H_2O composition or radionuclides
k	thermal conductivity, W/m-K
K	permeability, m^2
K_0	reference permeability, m^2
L_f	latent heat of fusion of H_2O , $3.34 \times 10^5 \text{ J kg}^{-1}$
L_v	latent heat of vaporization of H_2O , $2.26 \times 10^6 \text{ J kg}^{-1}$
m	mass fraction
M	mass, kg
M	molar mass of H_2O , $18 \times 10^{-3} \text{ kg mol}^{-1}$
n	moles
N_A	Avogadro's number, $6.02 \times 10^{23} \text{ molecules mol}^{-1}$
Nu	Nusselt number
P	pressure, Pa
P_0	pressure parameter for vapor pressure equation
Q	radionuclide heat generation, W kg^{-1}
r	radius, m
r	(subscript) rock
r_w	radius of liquid water, i.e., width of potential convecting layer
R	object radius, m
R	universal gas constant, $8.314 \text{ J mol}^{-1} \text{ K}^{-1}$
Ra	Rayleigh number
Ra'	Rayleigh number, expressed as multiple of critical value
S_0	solar constant, 1360 W m^{-2}
t	time, s
T	temperature, K
T_0	temperature parameter for vapor pressure equation
u	velocity, m/s
v	volume fraction
v	(subscript) void
V	volume, m^3
α	volumetric coefficient of thermal expansion, K^{-1}
β	water/rock volume fraction for hydration
γ	volume expansion factor of hydrous minerals
ϵ	emissivity

η	viscosity, Pa-s
κ	thermal diffusivity, $\text{m}^2 \text{s}^{-1}$
λ	radionuclide decay constant
ρ	density, kg/m^3
σ	Stefan-Boltzmann constant, $5.67 \times 10^{-8} \text{ W m}^{-2} \text{ K}^{-4}$
τ	tensile strength, Pa
ϕ	porosity

Appendix 6.B:

Degassing and Secular Retention of H₂O

The model derived in Appendix 6.A may be used to calculate the diffusion of H₂O throughout an asteroidal interior and the eventual loss of volatiles to space. In this appendix, a simple dimensional analysis of the degassing from the asteroidal surface is given, and a relation is derived for the depth to which free H₂O should be largely depleted as a function of orbital semimajor axis and regolith permeability.

Consider the one-dimensional diffusion of a constant-viscosity gas at low temperature in a medium of fixed permeability. Gas transport must satisfy the equation of state, the continuity equation, and Darcy's law:

$$PV = nRT \quad \frac{\partial(\rho u)}{\partial z} = -\frac{\partial \rho}{\partial t} \quad u = -\frac{K}{\eta} \frac{\partial P}{\partial z} \quad (6.B1)$$

where all symbols follow the definitions given in Appendix 6.A. Equations (6.B1) may be combined into the single equation

$$\frac{\partial P}{\partial t} = \frac{K}{\eta} \left[P \frac{\partial^2 P}{\partial z^2} + \left(\frac{\partial P}{\partial z} \right)^2 \right] \quad (6.B2)$$

Dimensional analysis of (6.B2) gives, to order of magnitude,

$$\frac{\Delta P}{\Delta t} = \frac{K}{\eta} \frac{\Delta P^2}{\Delta z^2} \quad (6.B3)$$

from which follows the time scale t_0 for degassing

$$t_0 = \frac{\eta \Delta z^2}{K \Delta P} \quad (6.B4)$$

Equation (6.B4) applies to a region without gas sources. However, if the interior is in a state of vapor-condensate equilibrium, a special, self-limiting source exists: the vapor pressure P_{vap} is maintained as long as condensate is available. Under equilibrium conditions, the amount of vapor, expressed in moles, is just $n_{\text{vap}} = v_v P_{\text{vap}} V / RT$, where v_v is the volume fraction of voids ($\sim 1 - v_r - v_i$). Since asteroidal interiors are nearly isothermal over most of solar system history, the vapor pressure may be evaluated at the surface temperature, and the pressure drop from the surface through the degassed zone to the region of vapor-condensate equilibrium is $\Delta P = P_{\text{vap}}$. From (6.B4), then, an amount of $\text{H}_2\text{O} \sim n_{\text{vap}}$ is lost on a time scale t_0 . However, the total amount of H_2O present is $n_{\text{tot}} = v_i \rho_i V / M$, where M is the molar mass. Therefore the number of characteristic degassing time scales that can be endured before ice is exhausted is

$$N = n_{\text{tot}} / n_{\text{vap}} = v_i \rho_i R T / v_v M P_{\text{vap}} \quad (6.B5)$$

Dropping the comparable quantities v_i and v_v , the *total* degassing time scale, $t = N t_0$, is

$$t = \frac{\rho_i \eta R T \Delta z^2}{K M P_{\text{vap}}^2} \quad (6.B6)$$

which may be rearranged to give the depth scale Δz of degassing over time scale t :

$$\Delta z = P_{\text{vap}}(T) \sqrt{\frac{K M t}{\rho_i \eta R T}} \quad (6.B7)$$

Substituting (6.A10) for the vapor pressure and (6.A5) for the surface temperature, Δz may be found as a function of permeability and orbital semimajor axis. Figure 6.B1 compares the approximate result (6.B7) with a numerical calculation performed using the analysis given in Appendix 6.A, with $K = 10^{-7} \text{ m}^2$, $\eta = 10^{-5} \text{ Pa-s}$, and at a distance of 1 A.U. Reasonable agreement is found for the depth of the devolitized zone as a function of time. In contrast, the time scales for similar degassing depths given by (6.B4) or by the rate of free sublimation [e.g., *Zemansky and Dittman, 1981*] are only a month or less.

REFERENCES

- Akai, J., Incompletely transformed serpentine-type phyllosilicates in the matrix of Antarctic meteorites, *Geochim. Cosmochim. Acta*, *52*, 1593-1599, 1988.
- Alexeyeva, K.N., Physical properties of stony meteorites and their interpretation in the light of hypotheses regarding the origin of the meteorites (in Russian), *Meteoritika*, *17*, 67-77, 1958.
- Anders, E., and M. Ebihara, Solar-system abundances of the elements, *Geochim. Cosmochim. Acta*, *44*, 1543-1577, 1982.
- Barber, D.J., Matrix phyllosilicates and associated minerals in C2M carbonaceous chondrites, *Geochim. Cosmochim. Acta*, *45*, 945-970, 1981.
- Basaltic Volcanism Study Project, *Basaltic Volcanism on the Terrestrial Planets*, 1286 pp., Pergamon, New York, 1981.
- Batchelor, G.K., *An Introduction to Fluid Dynamics*, 615 pp., Cambridge University Press, 1967.
- Bell, J.P., Mineralogical evolution of meteorite parent bodies (abstract), *Lunar and Planetary Science XVII*, Lunar and Planetary Institute, Houston, 985-986, 1986.
- Bratt, S.R., S.C. Solomon, and J.W. Head, The evolution of impact basins: Cooling, subsidence, and thermal stress, *J. Geophys. Res.*, *90*, 12415-12433, 1985.
- Buddhue, J.D., The compressive strength of meteorites, *Contrib. Soc. Res. Meteorites*, *3*, 39-40, 1942.
- Bunch, T.E., and S. Chang, Carbonaceous chondrites - II. Carbonaceous chondrite phyllosilicates and light element geochemistry as indicators of parent body processes and surface conditions, *Geochim. Cosmochim. Acta*, *44*, 1543-1577, 1980.
- Cain, P.M., H.Y. McSween, Jr., and N.B. Woodward, Structural deformation of the Leoville chondrite, *Earth Planet. Sci. Lett.*, *77*, 165-175, 1986.
- Cameron, A.G.W., and M.R. Pine, Numerical models of the primitive solar nebula,

- Icarus*, 18, 377-406, 1973.
- Carslaw, H.S., and J.C. Jaeger, *Conduction of Heat in Solids*, 386 pp., Oxford Univ. Press, London, 1947.
- Cassen, P., R.T. Reynolds, F. Graziani, A. Summers, J. McNellis, and L. Blalock, Convection and lunar thermal history, *Phys. Earth. Planet. Inter.*, 19, 183-196, 1979.
- Chandrasekhar, S., *Hydrodynamic and Hydromagnetic Stability*, 654 pp., Oxford University Press, London, 1961.
- Chapman, C.R., and W.B. McKinnon, Cratering of planetary satellites, in *Satellites*, edited by J.A. Burns and M.S. Matthews, Univ. of Arizona Press, Tuscon, 492-580, 1986.
- Clayton, R.M., and T.K. Mayeda, The oxygen isotope record in Murchison and other carbonaceous chondrites, *Earth Planet. Sci. Lett.*, 67, 151-161, 1984.
- Costes, N.C., and J.K. Mitchell, Apollo 11 soil mechanics investigation, *Proc. Apollo 11 Lunar Sci. Conf., Geochim. Cosmochim. Acta., Suppl.*, 2025-2044, 1970.
- Davis, D.R., C.R. Chapman, R. Greenberg, S. Weidenschilling, and A.W. Harris, Collisional evolution of asteroids: Populations, rotations, and velocities, in *Asteroids*, edited by T. Gehrels, Univ. of Arizona Press, Tuscon, 528-557, 1979.
- Dodd, R.T., *Meteorites: A Petrologic-Chemical Synthesis*, 368 pp., Cambridge University Press, 1981.
- Dodd, R.T., and E. Jarosewich, Incipient melting in and shock classification of L-group chondrites, *Earth Planet. Sci. Lett.*, 44, 335-340, 1979.
- Dominik, B., and E.K. Jessberger, ^{40}Ar - ^{39}Ar dating of Murchison, Allende, and Leoville whole rock samples (abstract), in *Lunar and Planetary Science X*, Lunar and Planetary Institute, Houston, 306-308, 1979.
- DuFresne, E.R., and E. Anders, On the chemical evolution of the carbonaceous chondrites, *Geochim. Cosmochim. Acta*, 26, 1085-1114, 1962.

- Goettel, K.A., and S.S. Barshay, The chemical equilibrium model for condensation in the solar nebula: Assumptions, implications, and limitations, in *The Origin of the Solar System*, edited by S.F. Dermott, J. Wiley and Sons, New York, 611-627, 1978.
- Goswami, J.N., D. Lal, and L.L. Wilkening, Gas-rich meteorites: Probes for particle environment and dynamical processes in the inner solar system, *Space Sci. Rev.*, **37**, 111-159, 1984.
- Gradie, J., and E. Tedesco, Compositional structure of the asteroid belt, *Nature*, **216**, 1405-1407, 1982.
- Greenberg, R., and C.R. Chapman, Asteroids and meteorites: Parent bodies and delivered samples, *Icarus*, **55**, 455-481, 1983.
- Greenberg, R., J.F. Wacker, W.K. Hartmann, and C.R. Chapman, Planetesimals to planets: Numerical simulation of collisional evolution, *Icarus*, **35**, 1-26, 1978.
- Grimm, R.E., Penecontemporaneous metamorphism, fragmentation, and reassembly of ordinary chondrite parent bodies, *J. Geophys. Res.*, **90**, 2022-2028, 1985.
- Grimm, R.E., and H.Y. McSween, Jr., Water and the thermal history of the CM carbonaceous chondrite parent body (abstract), in *Lunar and Planetary Science XIX*, Lunar and Planetary Institute, Houston, 427-428, 1988.
- Grossman, L., Condensation in the primitive solar nebula, *Geochim. Cosmochim. Acta*, **36**, 597-619, 1972.
- Hartmann, W.K., Terrestrial, lunar, and interplanetary rock fragmentation, *Icarus*, **31**, 168-174, 1969.
- Herbert, F., and C.P. Sonett, Electromagnetic heating of minor planets in the early solar system, *Icarus*, **48**, 484-496, 1979.
- Hobbs, P.V., *Ice Physics*, 837 pp., Clarendon Press, Oxford, 1974.
- Housen, K.R., L.L. Wilkening, C.R. Chapman, and R.J. Greenberg, Asteroidal

- regoliths, *Icarus*, 39, 317-351, 1979.
- Hutcheon, I.D., R. Hutchison, and G.J. Wasserburg, Evidence of the in-situ decay of ^{26}Al in a Semarkona chondrule (abstract), in *Lunar and Planetary Science XIX*, Lunar and Planetary Institute, Houston, 523-524, 1988.
- Jaeger, J.C., and N.G.W. Cook, *Fundamentals of Rock Mechanics*, 585 pp., Chapman and Hall, London, 1976.
- Johannes, W., Experimental investigation of the reaction forsterite + H_2O = serpentine + brucite, *Contrib. Mineral. Petrol.*, 19, 309-315, 1968.
- Kaula, W.M., Thermal evolution of the Earth and Moon growing by planetesimal impacts, *J. Geophys. Res.*, 84, 999-1008, 1979.
- Kerridge, J.F., and T.E. Bunch, Aqueous activity on asteroids: Evidence from carbonaceous chondrites, in *Asteroids*, edited by T. Gehrels, Univ. of Arizona Press, Tucson, 745-764, 1979.
- Keyes, F.G., Vapor pressures and orthobaric volumes for H_2O , NH_3 , CO_2 , and SO_2 above one atmosphere, in *International Critical Tables*, vol. 3, edited by E.W. Washburn, McGraw-Hill, New York, 233-236, 1928.
- Kieffer, S.W., and C.H. Simonds, The role of volatiles and lithology in the impact cratering process, *Rev. Geophys. Space Phys.*, 18, 143-181, 1980.
- Klinger, J., Influence of a phase transition of ice on the heat and mass balance of comets, *Science*, 209, 271-272, 1980.
- Lambe, T.W., and R.V. Whitman, *Soil Mechanics*, 553 pp., J. Wiley and Sons, New York, 1969.
- Lange, M.A., P. Lambert, and T.J. Ahrens, Shock effects on hydrous minerals and implications for carbonaceous chondrites, *Geochim. Cosmochim. Acta*, 49, 1715-1726, 1985.
- Lebofsky, L.A., M.A. Feierberg, A.T. Tokunaga, H.P. Larson, and J.R. Johnson, The 1.7 to 4.2-mm spectrum of asteroid 1 Ceres: Evidence for structural water in

- clay minerals, *Icarus*, 48, 453-459, 1981.
- Lee, T., D.A. Papanastassiou, and G.J. Wasserburg, Correction: Demonstration of excess ^{26}Mg in Allende and evidence for ^{26}Al , *Geophys. Res. Lett.*, 3, 109-112, 1976.
- Lewis, J.S., Low-temperature condensation from the solar nebula, *Icarus*, 16, 241-252, 1972.
- Macdougall, J.D., and B.K. Kothari, Formation chronology for C2 chondrites, *Earth Planet. Sci. Lett.*, 33, 36-44, 1976.
- Macdougall, J.D., G.W. Lugmair, and J.F. Kerridge, Early solar system aqueous activity: Sr isotope evidence from the Orgueil CI meteorite, *Nature*, 307, 249-251, 1984.
- Mason, B., *Handbook of Elemental Abundances in Meteorites*, 555 pp., Gordon and Breach, New York, 1971.
- McKinnon, I.D.R., and M. Zolensky, Proposed structures for poorly characterized phases in C2M carbonaceous chondrite meteorites, *Nature*, 309, 240-242, 1984.
- McSween, H.Y., Jr., Carbonaceous chondrites of the Ornans type: A metamorphic sequence, *Geochim. Cosmochim. Acta*, 41, 477-491, 1977.
- McSween, H.Y., Jr., Are carbonaceous chondrites primitive or processed? A review, *Rev. Geophys. Space Phys.*, 17, 1059-1078, 1979.
- McSween, H.Y., Jr., Aqueous alteration in carbonaceous chondrites: Mass balance constraints on matrix mineralogy, *Geochim. Cosmochim. Acta*, 51, 2469-2477, 1987.
- McSween, H.Y., Jr., and S. M. Richardson, The composition of carbonaceous chondrite matrix, *Geochim. Cosmochim. Acta*, 41, 1145-1161, 1977.
- Mercer, J.W., G.F. Pinder, and I.G. Donaldson, A Galerkin-finite element analysis of the hydrothermal system at Wairakei, New Zealand, *J. Geophys. Res.*, 80,

- 2608-2621, 1975.
- Mittlefehldt, D.W., and G.W. Wetherill, Rb-Sr studies of CI and CM chondrites, *Geochim. Cosmochim. Acta*, **43**, 201-206, 1979.
- Miyamoto, M., N. Fujii, and H. Takeda, Ordinary chondrite parent body: An internal heating model, *Proc. Lunar Planet. Sci. Conf.*, **12B**, 1145-1152, 1981.
- Olsen, E.J., A.M. Davis, I.D. Hutcheon, R.N. Clayton, T.K. Mayeda, and L. Grossman, Murchison xenoliths, *Geochim. Cosmochim. Acta*, **52**, 1615-1626, 1988.
- Patterson, C., and D. Spaute, Self-termination of runaway growth in the asteroid belt (abstract), papers presented at *Asteroids II*, 1988.
- Prinn, R. G., and B. Fegley, Jr., Solar nebula chemistry: Origin of planetary, satellite, and cometary volatiles, in *Origin and Evolution of Planetary and Satellite Atmospheres*, edited by S. Atreya, J. Pollack, and M. Matthews, Univ. of Arizona Press, Tuscon, in press, 1988.
- Reynolds, R.T., P.E. Fricker, and A.L. Summers, Effects of melting upon thermal models of the Earth, *J. Geophys. Res.*, **71**, 573-582, 1966.
- Richardson, S.M., Vein formation in the C1 carbonaceous chondrites, *Meteoritics*, **13**, 141-159, 1978.
- Rietmeijer, F.J.M., and I.R.D. Mackinnon, Poorly graphitized carbon as a new cosmo-thermometer for primitive extraterrestrial materials, *Nature*, **315**, 733-736, 1985.
- Robie, R.A., and D.R. Waldbaum, Thermodynamic properties of minerals and related substances at 298.15 °K and one atmosphere (1.013 bars) pressure and at high temperatures, *U.S. Geol. Survey Bull.*, **1259**, 1968.
- Safronov, V.S., Evolution of the protoplanetary cloud and formation of the earth and the planets, (Moscow: Nauka Press), trans. from the Russian, *NASA Tech. Trans.*, **F-677**, 211 pp., 1972.

- Safronov, V.S., The heating of the earth during its formation, *Icarus*, 33, 1-12, 1978.
- Safronov, V.S., On the origin of asteroids, in *Asteroids*, edited by T. Gehrels, Univ. of Arizona Press, Tuscon, 975-991, 1979.
- Schatz, J.F., and G. Simmons, Thermal conductivity of Earth materials at high temperatures, *J. Geophys. Res.*, 77, 6966-6983, 1972.
- Schubert, G., P. Cassen, and R.E. Young, Subsolidus convective cooling histories of terrestrial planets, *Icarus*, 38, 192-211, 1979.
- Scott, E.R.D., and R.S. Rajan, Metallic minerals, thermal histories, and parent bodies of some xenolithic, ordinary chondrites, *Geochim. Cosmochim. Acta*, 45, 53-67, 1981.
- Sears, D.W., J.R. Ashworth, C.P. Broadbent, and A.W.R. Bevan, Studies of an artificially shock-loaded H group chondrite, *Geochim. Cosmochim. Acta*, 48, 343-360, 1984.
- Sharpe, H.N., and W.R. Peltier, Parameterized convection and the Earth's thermal history, *Geophys. Res. Lett.*, 5, 737-740, 1978.
- Sneyd, D.S., H.Y. McSween, Jr., N. Sugiura, D.W. Strangway, and G.L. Nord, Jr., Origin of petrofabric and magnetic anisotropy in ordinary chondrites, *Meteoritics*, submitted, 1988.
- Sonett, C.P., D.S. Colburn, K. Schwartz, and K. Keil, The melting of asteroidal-sized bodies by unipolar dynamo induction from a primordial T-Tauri sun, *Astrophys. Space Sci.*, 7, 446-488, 1970.
- Sonett, C.P., and R.T. Reynolds, Primordial heating of asteroidal parent bodies, in *Asteroids*, edited by T. Gehrels, Univ. of Arizona Press, Tuscon, 822-848, 1979.
- Straus, J.M., Large amplitude convection in porous media, *J. Fluid Mech.*, 64, 51-63, 1974.

- Straus, J.M., and G. Schubert, Thermal convection of water in a porous medium: Effects of temperature- and pressure-dependent thermodynamic and transport properties, *J. Geophys. Res.*, *82*, 325-333, 1977.
- Sugiura, N., and D.W. Strangway, Magnetic anisotropy and porosity of chondrites, *Geophys. Res. Lett.*, *10*, 83-86, 1983.
- Sugiura, N., N.S. Brar, D.W. Strangway, and T. Matsui, Degassing of meteorite parent bodies, *Proc. Lunar Planet. Sci. Conf. 14th, J. Geophys. Res.*, *89*, Suppl., B641-B644, 1984.
- Thurber, C.H., A.T. Hsui, and M.N. Toksoz, Thermal evolution of Ganymede and Callisto: Effects of solid-state convection and constraints from Voyager imagery, *Proc. Lunar. Planet. Sci. Conf. 11th, 1957-1977*, 1980.
- Tomeoka, K., and P.R. Buseck, Indicators of aqueous alteration in CM carbonaceous chondrites: Microtextures of a layered mineral containing Fe, S, O, and Ni, *Geochim. Cosmochim. Acta*, *49*, 2149-2163, 1985.
- Tomeoka, K., and P.R. Buseck, Matrix mineralogy of the Orgueil CI carbonaceous chondrite, *Geochim. Cosmochim. Acta*, *52*, 1627-1640, 1988.
- Touloukian, Y.S., P.E. Liley, and S.C. Saxena, *Thermophysical Properties of Matter*, vol. 3, 577 pp., IFI/Plenum, New York, 1970.
- Touloukian, Y.S., and T. Makita, *Thermophysical Properties of Matter*, vol. 6, 338 pp., IFI/Plenum, New York, 1970.
- Touloukian, Y.S., S.C. Saxena, and P. Hestermans, *Thermophysical Properties of Matter*, vol. 11, 649 pp., IFI/Plenum, New York, 1975.
- Turcotte, D.L., F.A. Cooke, and R.J. Willemann, Parameterized convection within the moon and terrestrial planets, *Proc. Lunar. Sci. Conf. 10th*, 2375-2392, 1979.
- Turcotte, D.L., and G. Schubert, *Geodynamics*, 450 pp., J. Wiley and Sons, New York, 1982.
- Veeder, G.J., The IRAS asteroid data, in *IRAS Asteroid and Comet Survey, Preprint*

- Version No. 1*, edited by D.L. Matson, 2:1-2:54, Internal Document D-3698, Jet Propulsion Laboratory, Pasadena, 1986.
- Washburn, E.W., Vapor pressure of ice and water < 100° C, in *International Critical Tables*, vol. 3 , edited by E.W. Washburn, McGraw-Hill, New York, 210-212, 1928.
- Wasson, J.T., and G.W. Wetherill, Dynamical, chemical, and isotopic evidence regarding the formation locations of asteroids and meteorites, in *Asteroids*, edited by T. Gehrels, Univ. of Arizona Press, Tuscon, pp. 926-974, 1979.
- Wegner, W.W., and W.G. Ernst, Experimentally determined hydration and dehydration reaction rates in the system MgO-SiO₂-H₂O, *Am. J. Sci.*, 238-A, 151-180, 1983.
- Wetherill, G.W., Formation of the terrestrial planets, *Ann. Rev. Astron. Astrophys.*, 18, 77-113, 1980.
- Wood, J.A., and G.E. Morfill, A review of solar nebula models, in *Meteorites and the Early Solar System*, edited by J.F. Kerridge and M.S. Matthews, Univ. of Arizona Press, Tuscon, in press, 1988.
- Yomogida, K., and T. Matsui, Physical properties of ordinary chondrites, *J. Geophys. Res.*, 88, 9513-9533, 1983.
- Yomogida, K., and T. Matsui, Multiple parent bodies of ordinary chondrites, *Earth Planet. Sci. Lett.*, 68, 34-42, 1984.
- Zemansky, M.W., and R.H. Dittman, *Heat and Thermodynamics*, 543 pp., McGraw-Hill, New York, 1981.

Table 6.A1. Assumed abundances of heat-producing elements

Nuclide	Initial Abundance ^a (mass fraction)	Decay Constant (y ⁻¹)	Initial Heat Production (W/kg)
²⁶ Al	(²⁶ Al/ ²⁷ Al) specified	9.63x10 ⁻⁷	4.21x10 ⁻³ (²⁶ Al/ ²⁷ Al) ^b
²³⁸ U	2.64x10 ⁻⁸	1.55x10 ⁻¹⁰	2.48x10 ⁻¹²
²³⁵ U	8.60x10 ⁻⁹	7.91x10 ⁻⁹	4.98x10 ⁻¹²
²³² Th	5.21x10 ⁻⁸	4.99x10 ⁻¹¹	1.36x10 ⁻¹²
⁴⁰ K	6.60x10 ⁻⁷	5.48x10 ⁻¹⁰	19.9x10 ⁻¹²

^a Observed C2 abundances [Mason, 1971] extrapolated to t = 4.60 b.y. before present.

^b Using observed ²⁷Al abundance of 1.17 wt% in CM chondrites [Dodd, 1981].

FIGURE CAPTIONS

Figure 6.1. Schematic illustration of the alternative models tested in this paper for aqueous alteration of carbonaceous chondrites. (a) Alteration occurs uniformly throughout the parent body interior. Hydrothermal circulation may develop at sufficiently large thermal gradients. (b) Alteration occurs within a regolith. Under internal heating, water may be supplied to the regolith by *in situ* melting and hydrothermal circulation, by venting through fractures that accompany tensile failure of the parent body interior at high fluid or gas pressures, or by simple vapor diffusion through pre-existing pores and cracks. Impacts can also contribute to melting of ice within the regolith.

Figure 6.2. Profiles of temperature versus radius within a parent body 100 km in diameter with 30% ice by volume and an initial $^{26}\text{Al}/^{27}\text{Al}$ ratio of 1.6×10^{-6} . The deep interior is brought just past H_2O melting in 10 m.y. This scenario gives the minimum heating required to produce interior aqueous alteration in at the specified size and composition.

Figure 6.3. Thermal evolution of an object similar to that in Figure 6.2, but with initial $^{26}\text{Al}/^{27}\text{Al} = 2.0 \times 10^{-6}$. The average peak temperature of all rocks exposed to liquid water is 25°C , matching the peak temperature of CM chondrites inferred from oxygen isotope studies [Clayton and Mayeda, 1984]. However, the altered rock fraction is not representative of the interior.

Figure 6.4. Thermal evolution of an object similar to that in Figure 6.2, but matching the CI peak temperature of 150°C and illustrating potential effects of hydrothermal circulation. (a) Initial $^{26}\text{Al}/^{27}\text{Al} = 4.3 \times 10^{-6}$; convection suppressed. Altered fraction is representative of the interior. (b) Initial $^{26}\text{Al}/^{27}\text{Al} = 6.0 \times 10^{-6}$, with vigorous convection allowed so that excess heat is removed. The approximation for convective heat transfer yields an overestimate of the Nusselt number, so the indicated heat production is an upper limit at this size and composition.

Figure 6.5. Summary of allowed initial $^{26}\text{Al}/^{27}\text{Al}$ ratio as a function of parent body size, ice:rock composition, and carbonaceous chondrite group produced. In each panel, the lower curve gives the minimum $^{26}\text{Al}/^{27}\text{Al}$ required just to melt interior ice. The next two curves give initial $^{26}\text{Al}/^{27}\text{Al}$ required to match peak temperatures of CM and CI chondrites, respectively. The uppermost (dashed) curve gives an upper bound to ^{26}Al abundance in CI objects under efficient hydrothermal circulation; gravitational instability of water does not occur for CM models. Long-lived radionuclides alone are sufficient to heat $D = 1000$ object to CI temperatures. Open square gives maximum initial $^{26}\text{Al}/^{27}\text{Al}$ for anhydrous CO chondrites. Comparable $^{26}\text{Al}/^{27}\text{Al}$ ratios inferred for CI and CO chondrite parent bodies and also for ordinary chondrite parent objects [Miyamoto *et al.*, 1981; Hutcheon *et al.*, 1988] suggest that water may have played an important role in their different thermal histories.

Figure 6.6. Evolution of a CM object ($D = 100$ km, ice fraction = 0.2, initial $^{26}\text{Al}/^{27}\text{Al} = 1.2 \times 10^{-6}$) explicitly including thermal and compositional changes associated with aqueous alteration. (a) Temperature profiles. Following complete absorption of the latent heat of fusion of H_2O , temperatures increase sharply due to release of chemical heat of reaction. Oxygen isotopic constraints apply only during aqueous alteration, so peak temperature is limited instead by inferences from carbonaceous chondrite textures. (b) Compositional profile following alteration, showing volume fractions of H_2O (solid line), anhydrous minerals (long dash), and hydrous minerals (short dash). Hydrous: anhydrous mineral ratio matches CM proportions, but altered zone is confined to the deep interior in this example.

Figure 6.7. Evolution of an object similar to that in Figure 6.6, but with initial $^{26}\text{Al}/^{27}\text{Al} = 5 \times 10^{-6}$. (a) Temperature profiles, showing rapid rise through hydration at 273 K to dehydration temperature (623K) and maintenance of near-constant value during absorption of the latent heat of reaction. High pore pressures due to release of superheated water lead to failure of the surrounding rock and venting of H_2O . (b) Final compositional profile. Venting of H_2O following dehydration of deep interior leaves only anhydrous minerals there. Altered zone is restricted to 1-11 km depth.

Figure 6.8. Object with the same size and initial $^{26}\text{Al}/^{27}\text{Al}$ ratio as Figure 6.7, but initial H_2O is doubled (volume fraction = 0.4). Such an H_2O fraction is needed to achieve the nearly complete alteration of anhydrous minerals observed in CI chondrites. Heating is insufficient to drive

dehydration reaction, so dehydration temperature can act as a barrier to further temperature excursions. The final state (not shown) consists nearly uniformly of altered minerals, although in reality partial dehydration textures would be evident.

Figure 6.9. Aqueous alteration within the regolith of a large ($D=300$ km) parent body with initial $^{26}\text{Al}/^{27}\text{Al} = 5 \times 10^{-6}$, but the pore volume of 25% is taken to be undersaturated with only 10% H_2O . Hydrothermal circulation and chemical reactions are not included. (a) Temperature profiles. If only regolith is sampled, the high internal temperatures are irrelevant. (b) Final H_2O distribution. Large internal gas pressures cause failure of the surrounding rock, leading to venting of 70% of the object's H_2O . If part of this vented H_2O condenses in the regolith, a favorable environment for aqueous alteration would be provided.

Figure 6.10. Regolith-alteration calculation following that in Figure 6.9, but allowing hydrothermal circulation. Vigorous convection holds down temperatures in the interior so that only minor venting of H_2O occurs. Melting also extends to within 1 km of the surface, closer than in Figure 6.9. Regolithic water is continuously recharged by hydrothermal circulation.

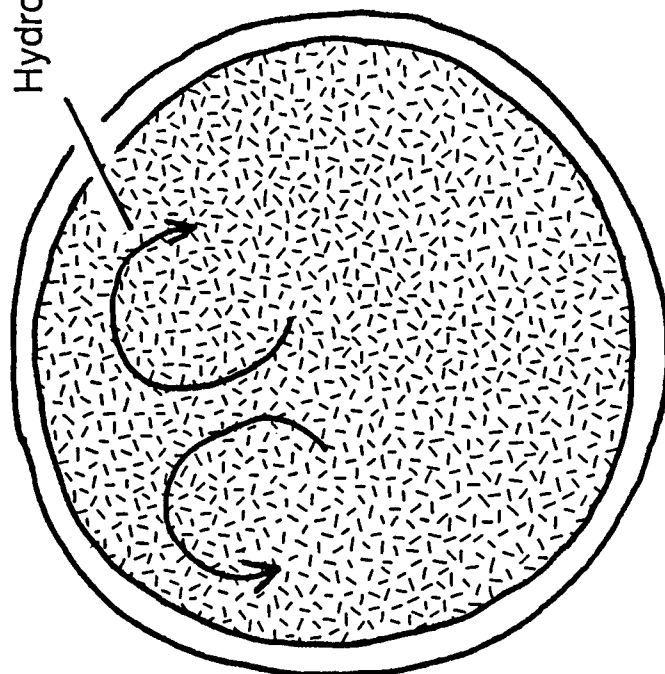
Figure 6.11. Regolith-alteration model following that in Figure 6.9, but including H_2O vapor diffusion. (a) Temperature profiles. (b) H_2O distribution. Hydrothermal convection must be suppressed or else water distribution is homogenized. Upper 10 km has steady supply of vapor

over time scales of ~ 1 m.y., providing an additional mechanism for introduction of water into the regolith.

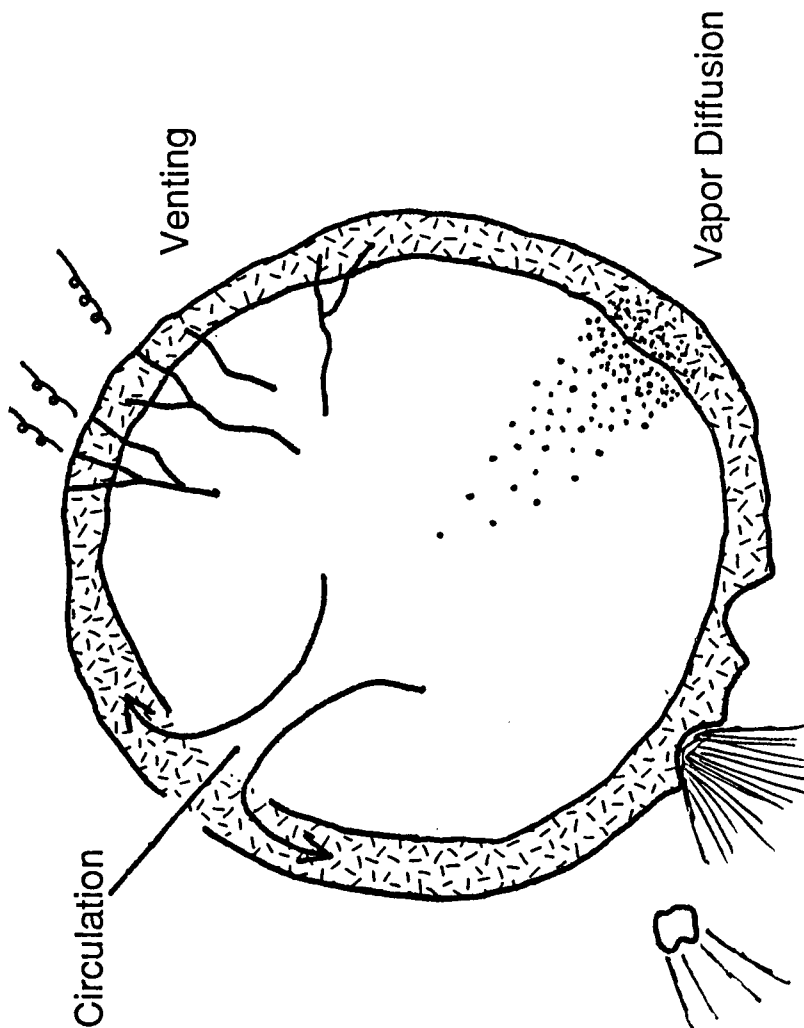
Figure 6.12. Depth of H_2O loss over the age of the solar system as a function of reference permeability, for different values of solar distance. Effective permeability may be enhanced by low-temperature molecular flow and depends on pore size. (a) Pore diameter 1 mm, appropriate to the sizes of chondrules and clasts in carbonaceous chondrites. (b) Pore diameter 1 μm , appropriate to the size of carbonaceous chondrite matrix particles. Easier transition to molecular flow occurs for smaller pores, allowing greater H_2O loss. Degassing at asteroidal distances is nevertheless limited to depths of tens of meters.

Figure 6.B1. Example of one-dimensional vapor diffusion at 1 A.U. solar distance, for a regolith with 10% H_2O volume, 25% porosity, and permeability 10^{-7} m^2 . Numerical calculation (solid) compares well with simple approximation (dash) from dimensional analysis for the depth of nearly complete H_2O loss.

Interior Alteration



Regolith Alteration



Impacts

Figure 6.1

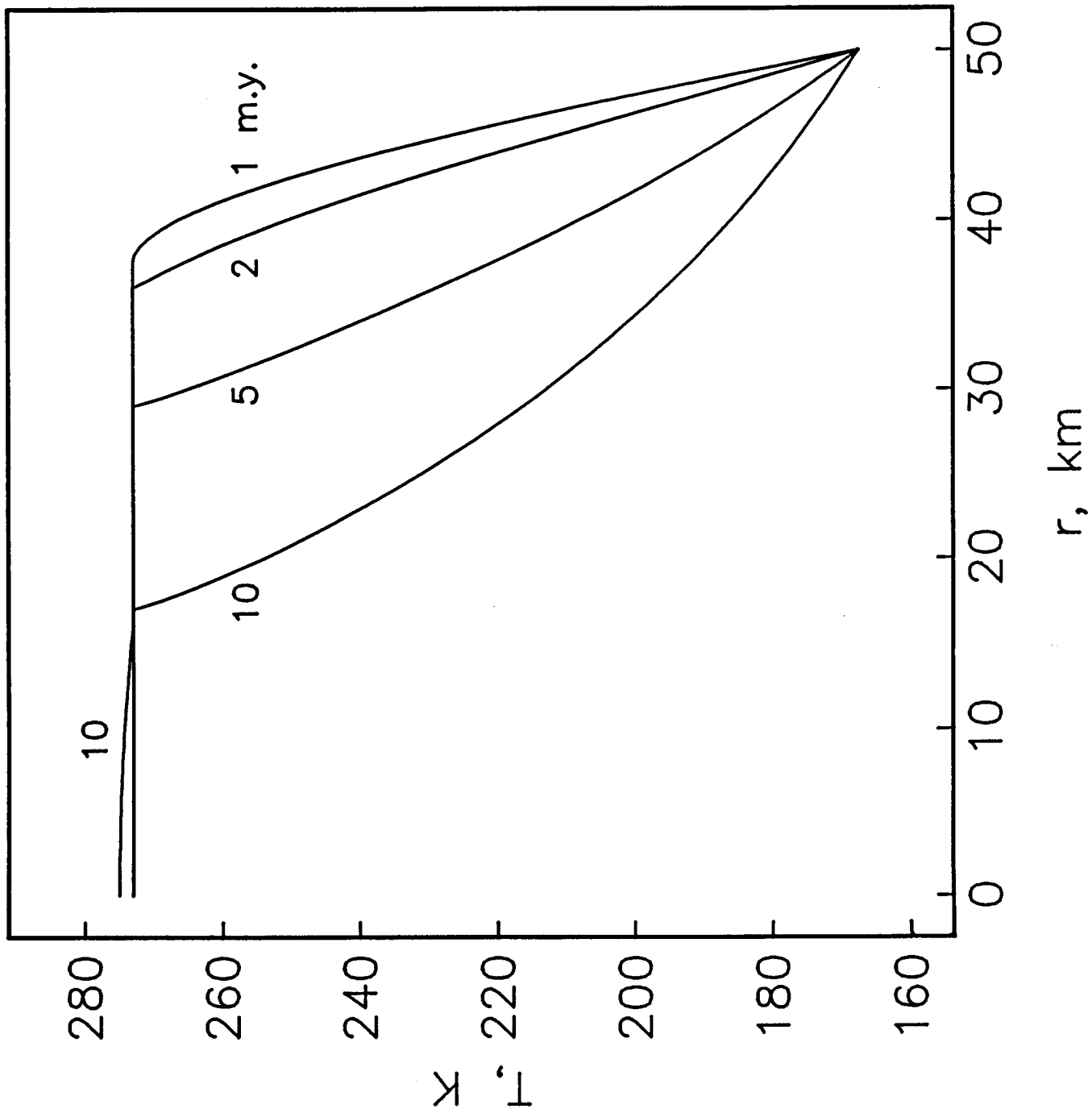


Figure 6.2

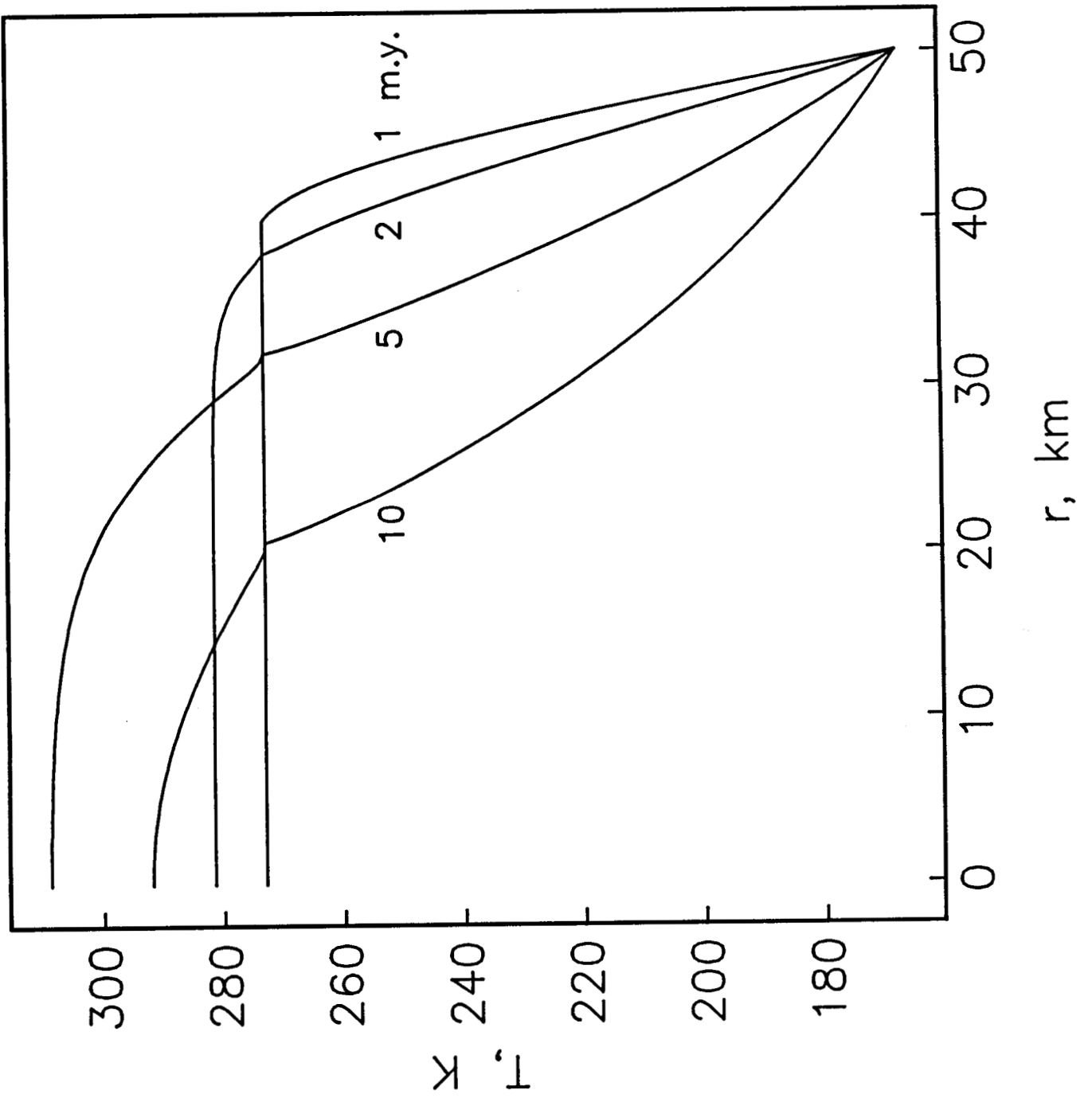


Figure 6.3

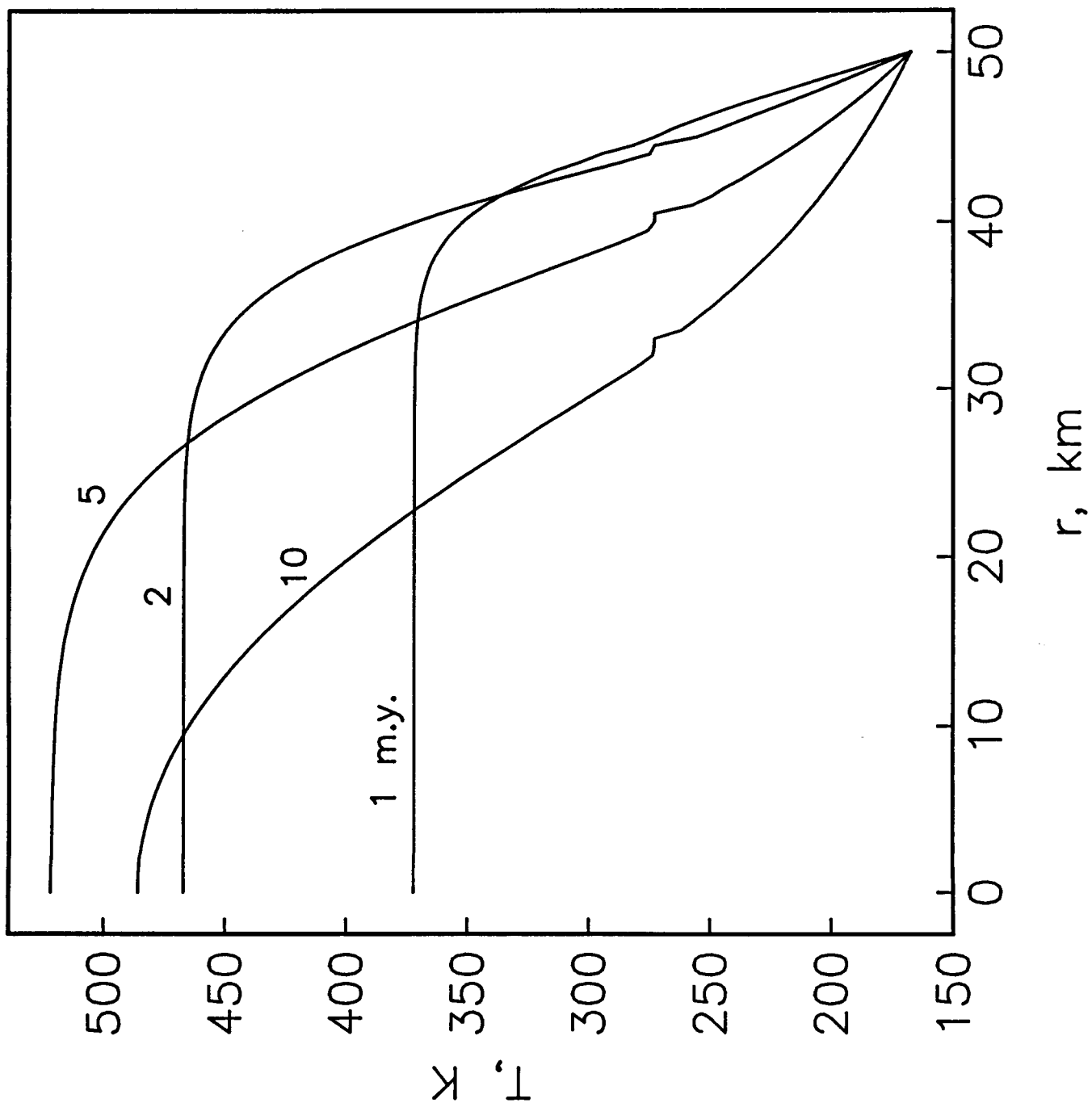


Figure 6.4a

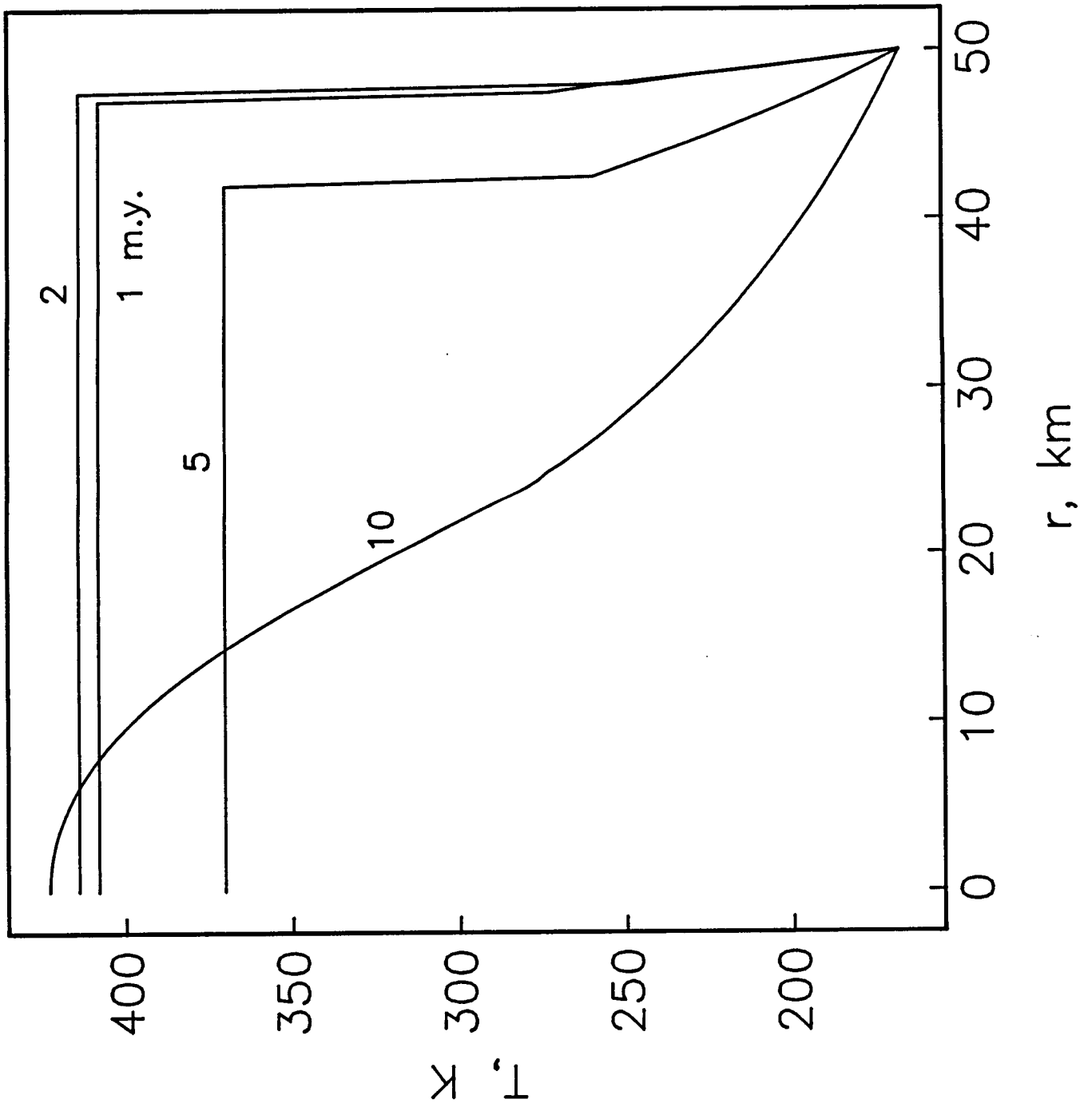


Figure 6.4b

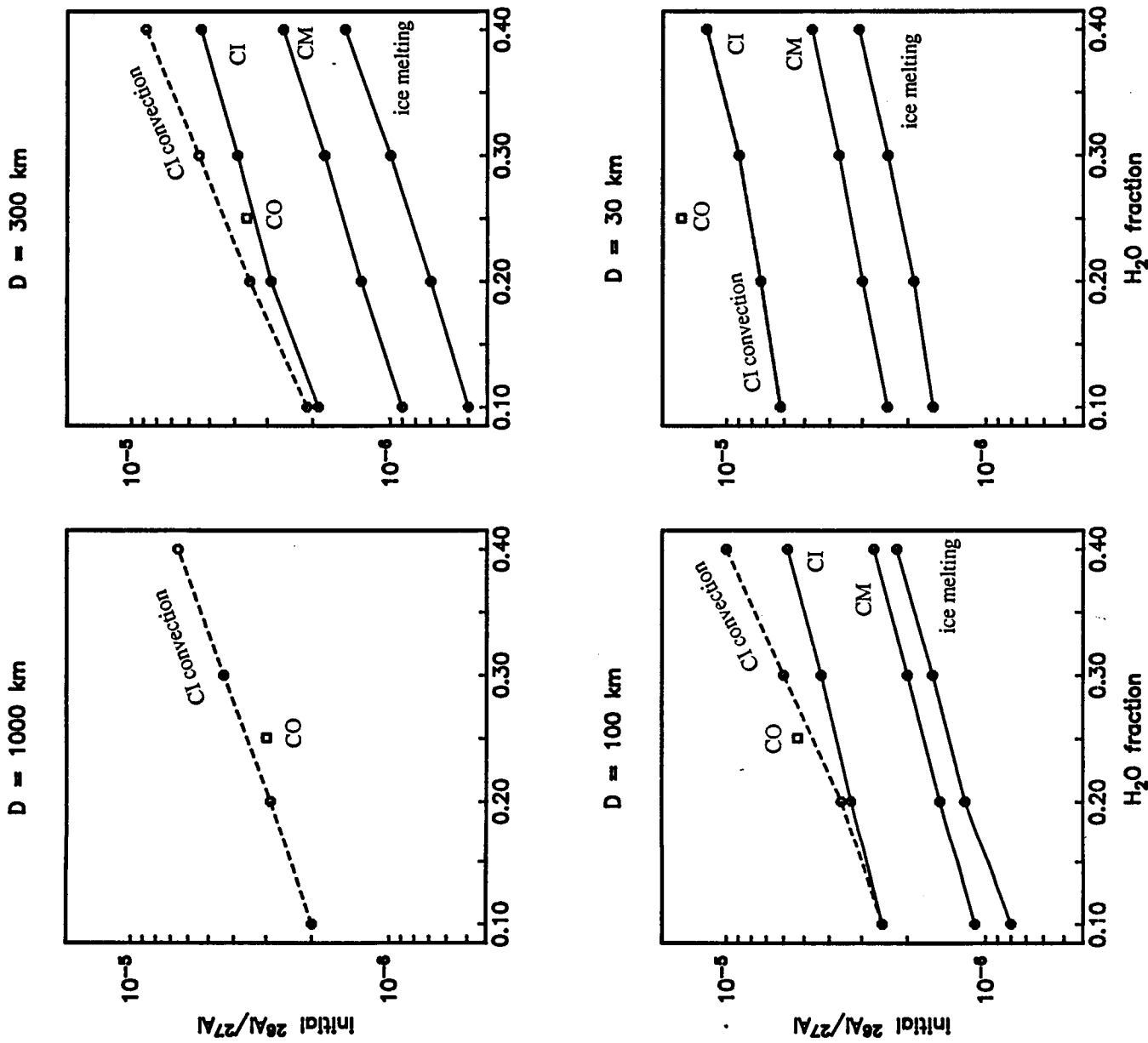


Figure 6.5

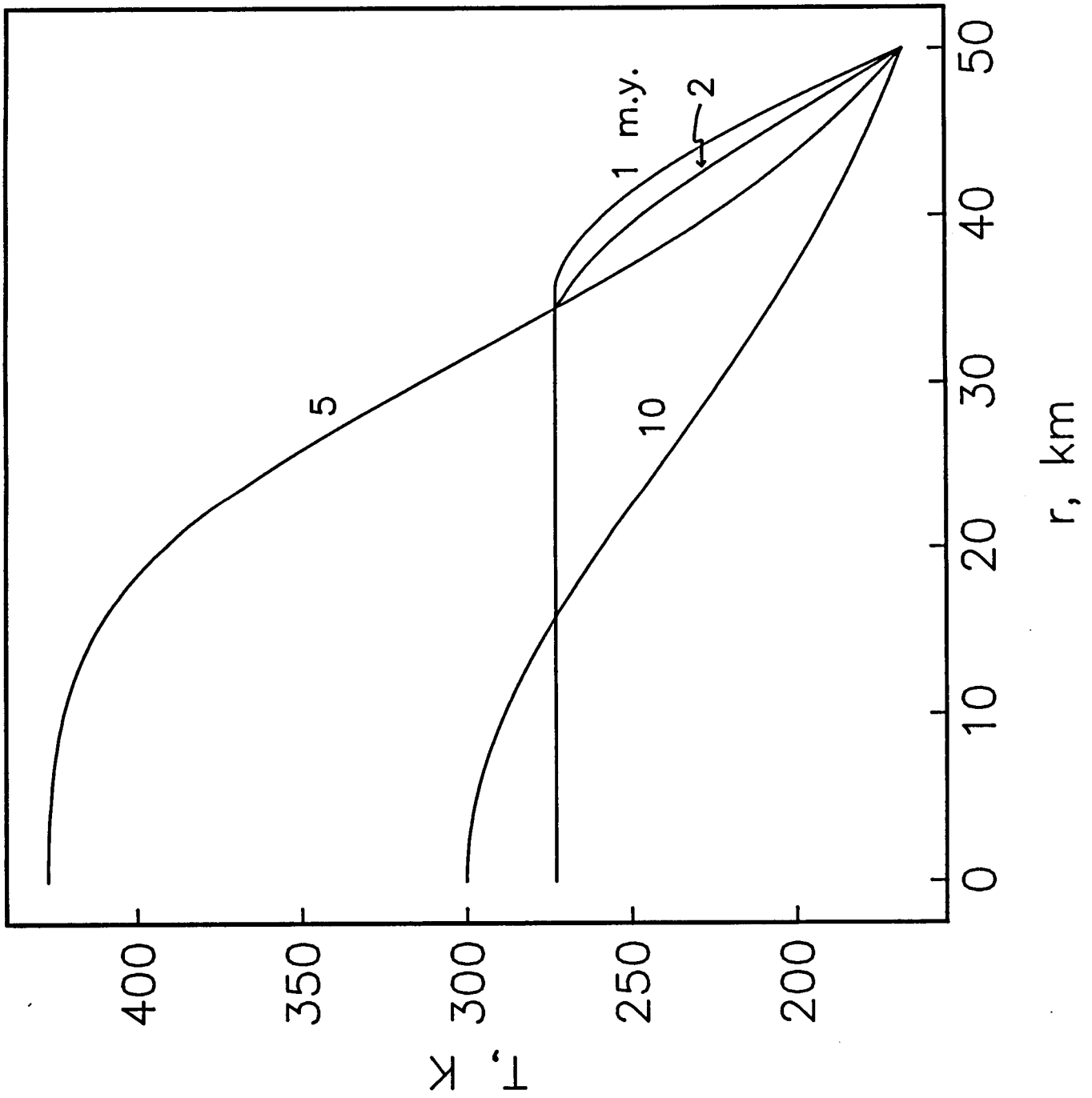


Figure 6.6a

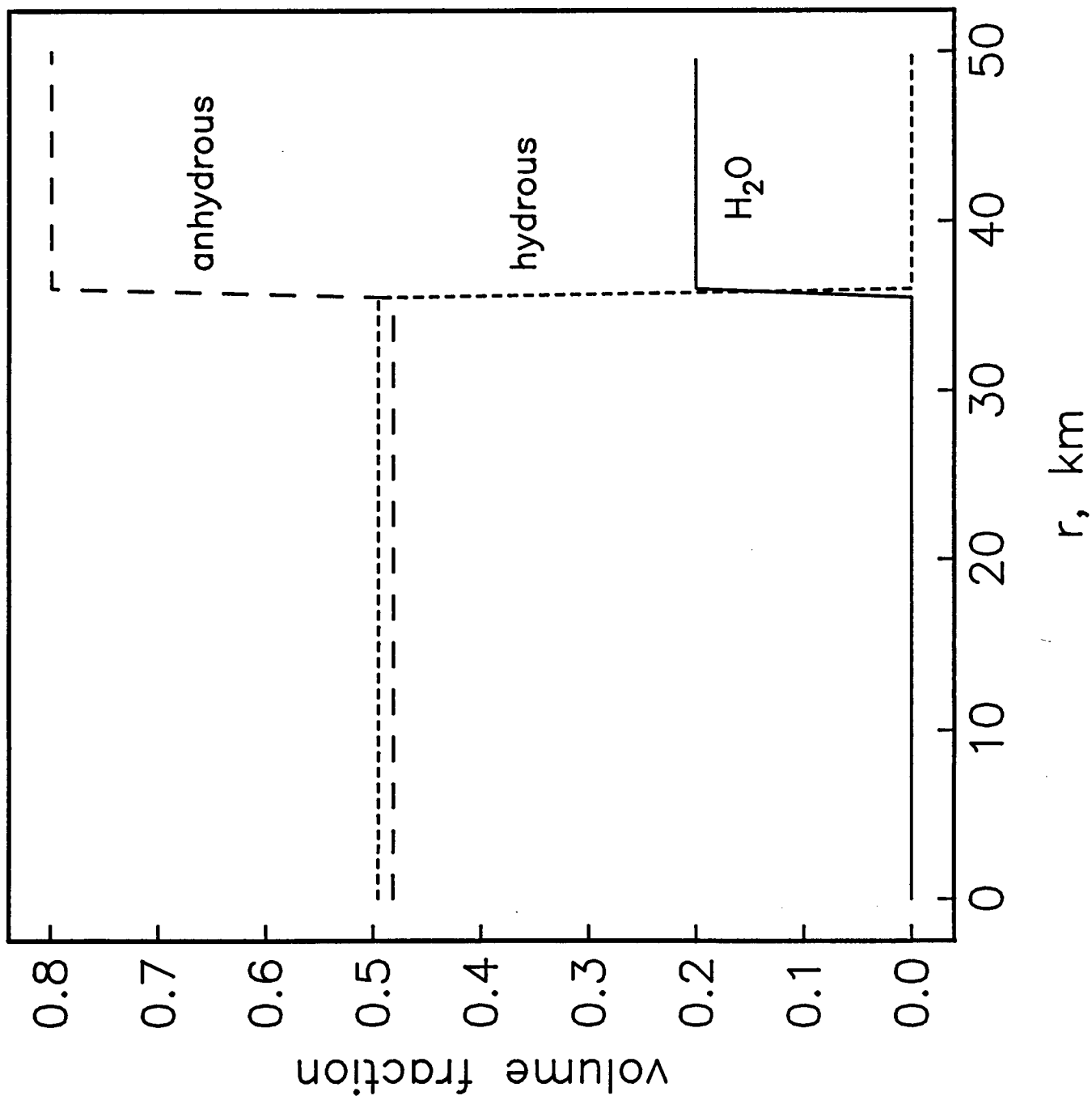


Figure 6.6b

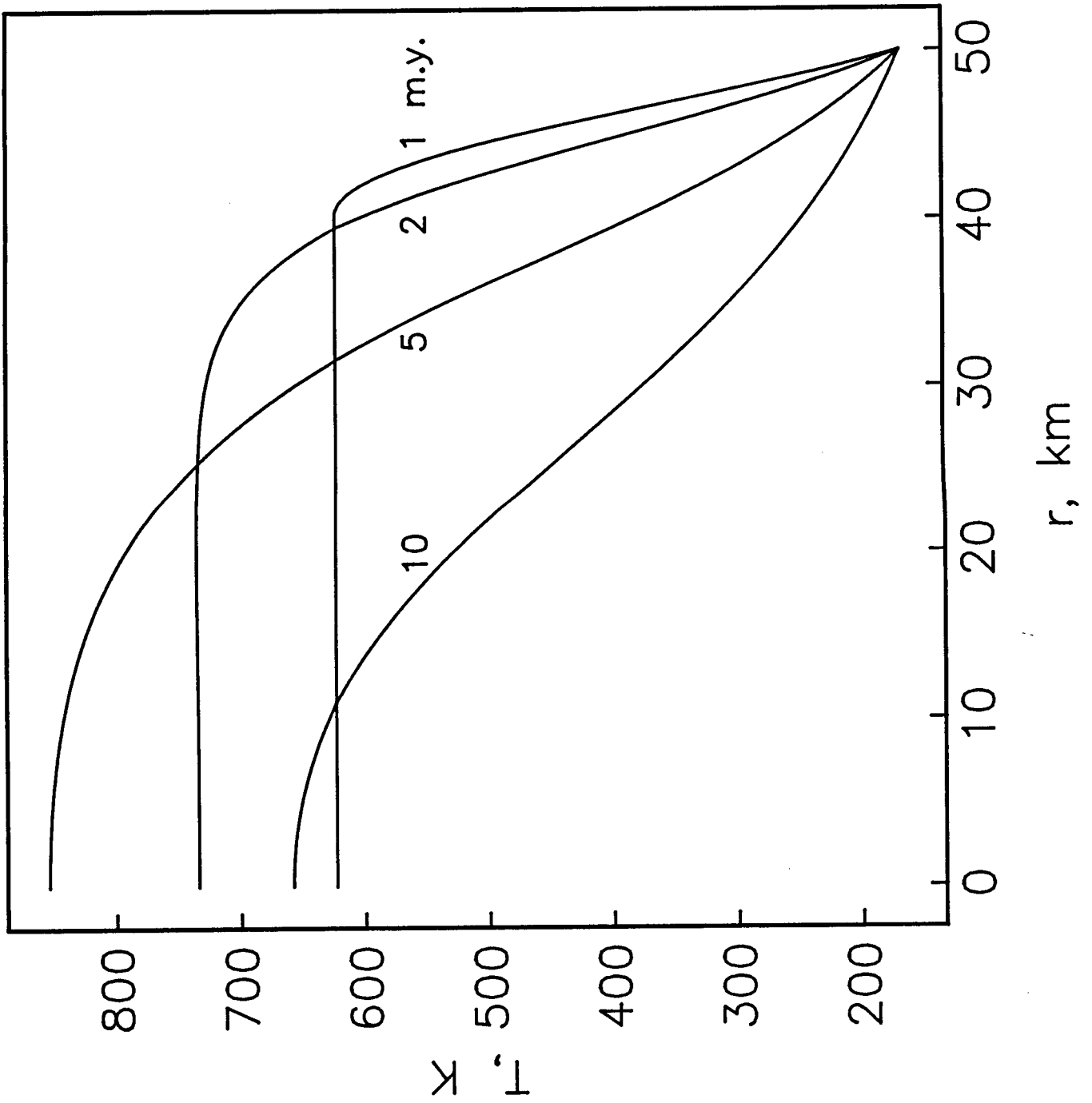


Figure 6.7a

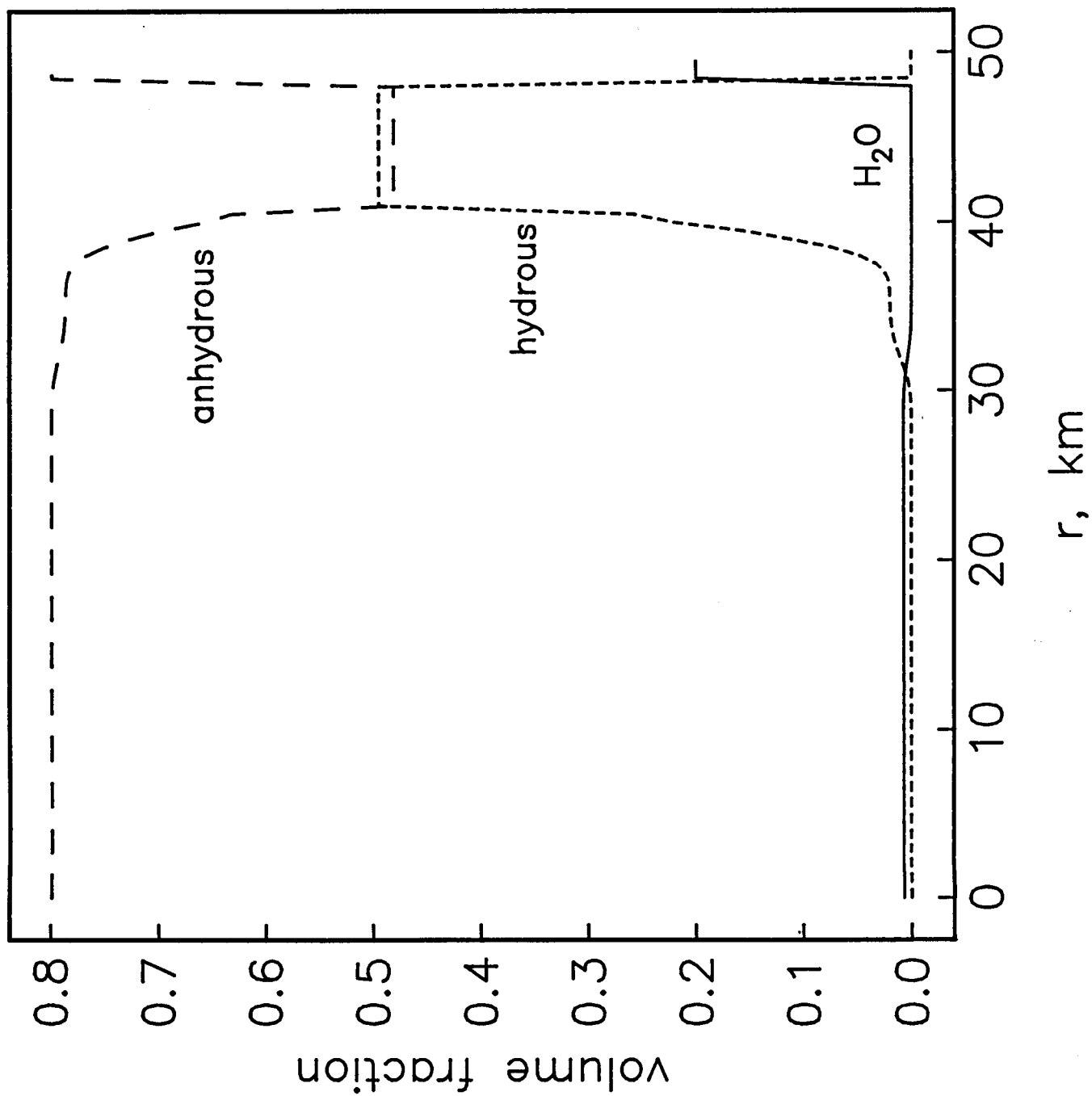


Figure 6.7b

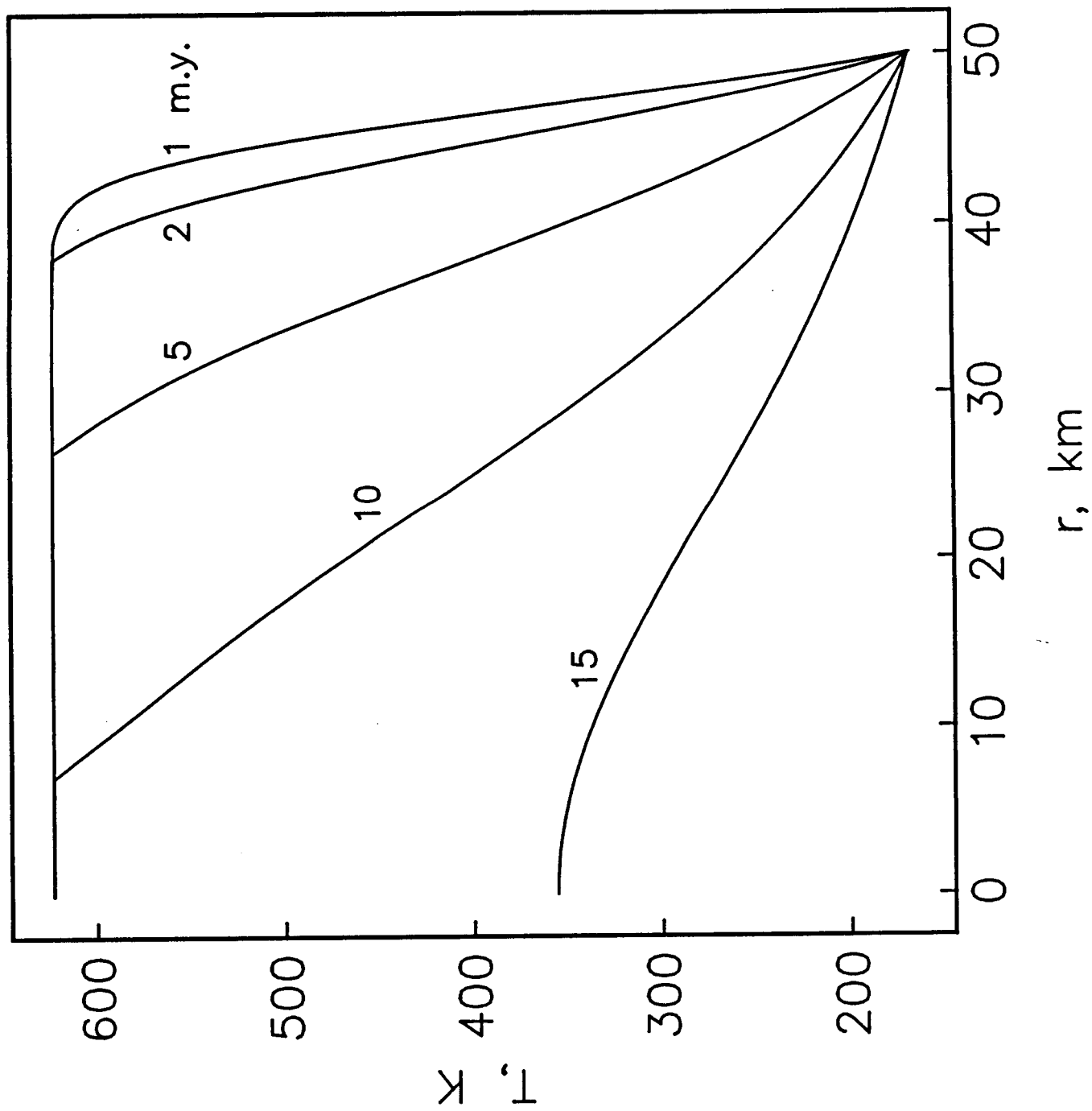


Figure 6.8

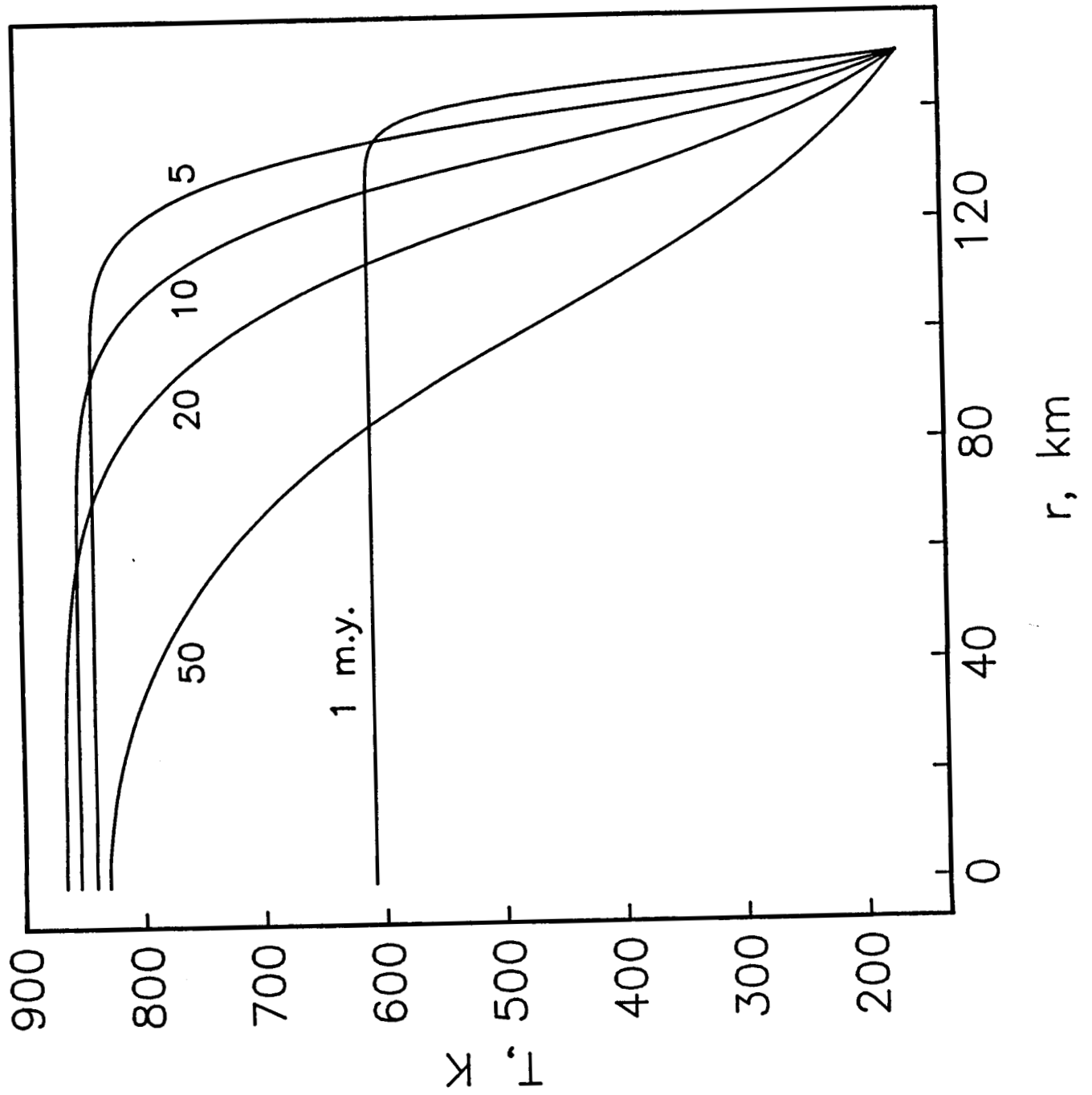


Figure 6.9a

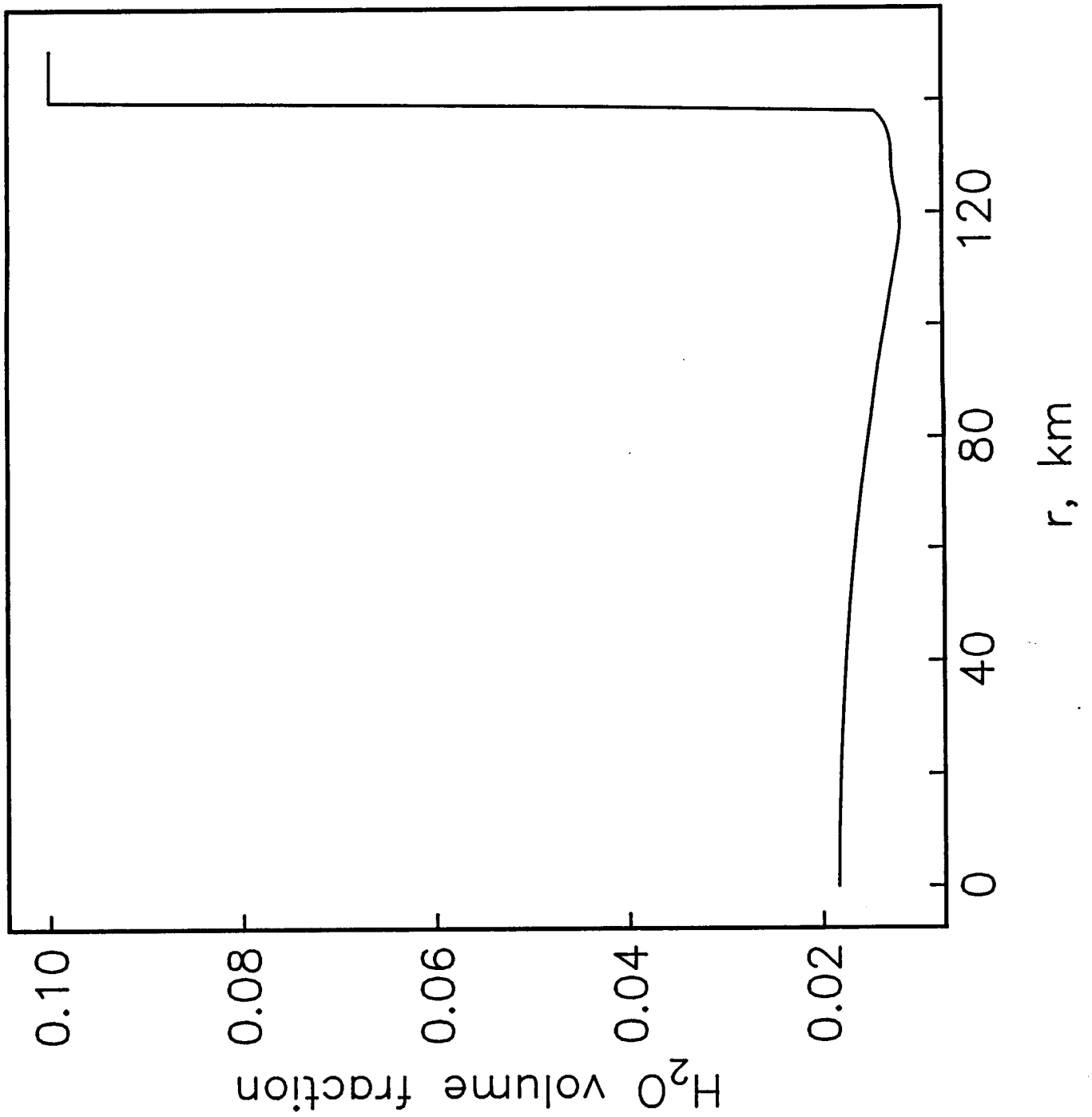


Figure 6.9b

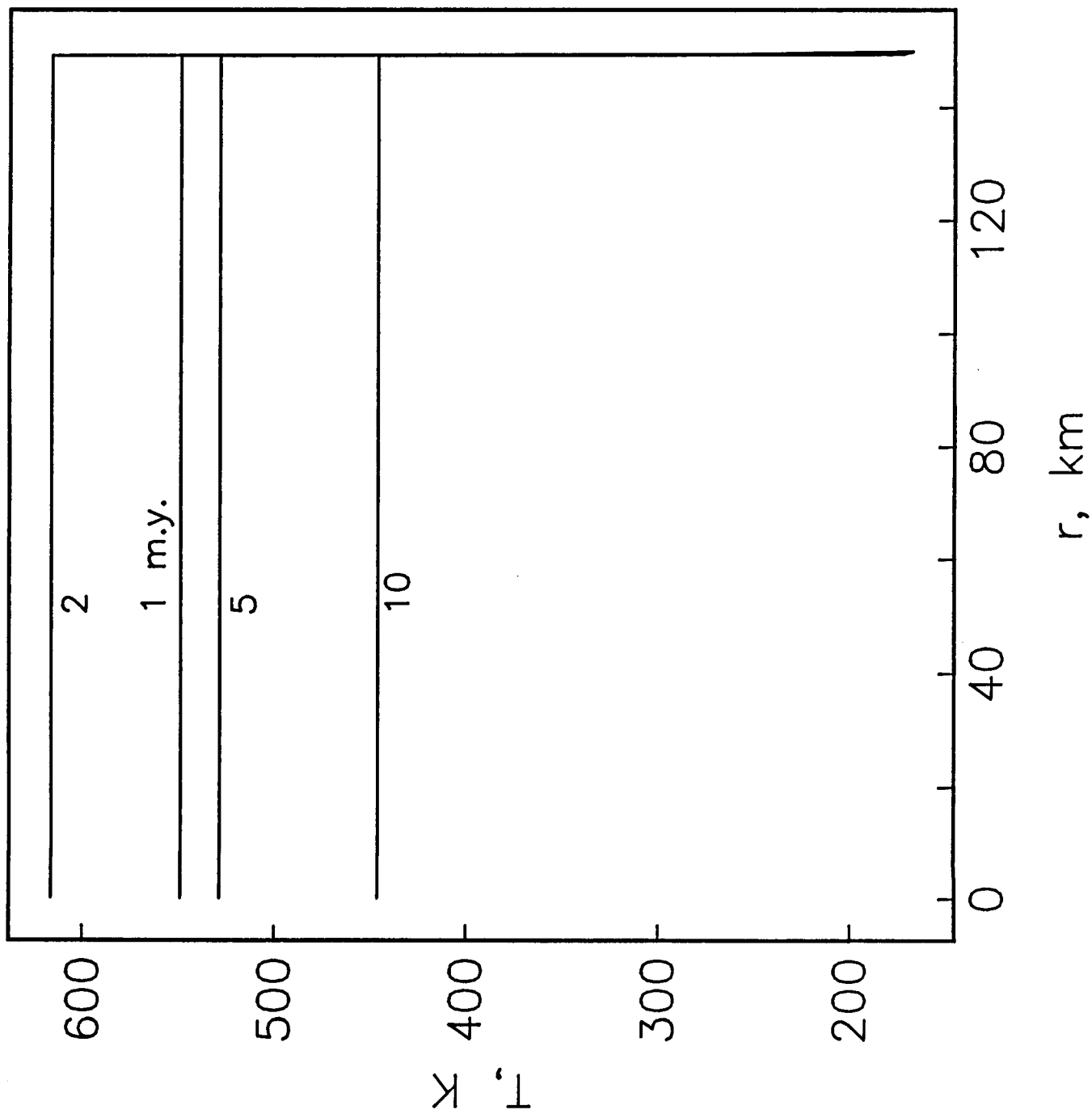


Figure 6.10

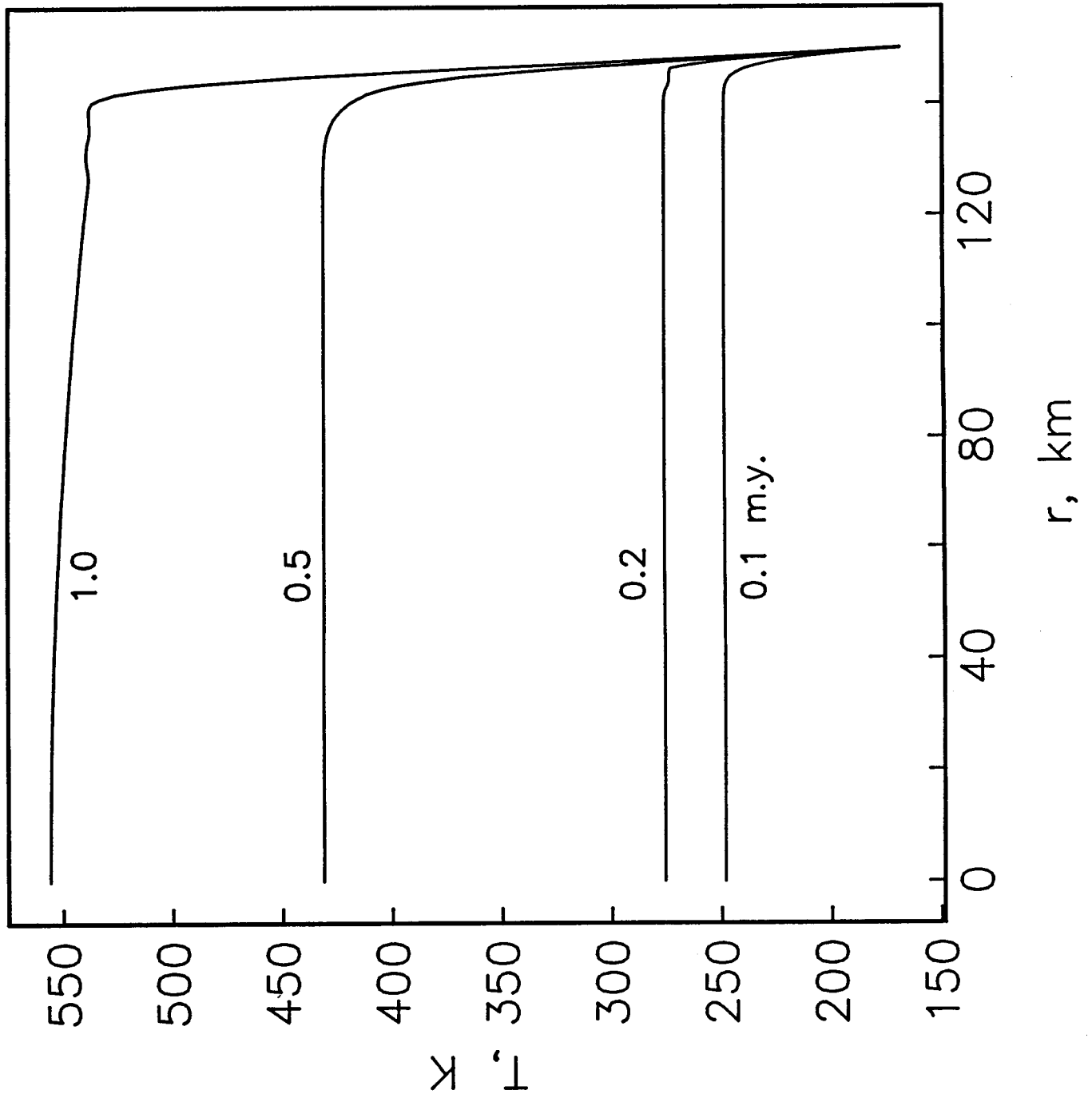


Figure 6.11a

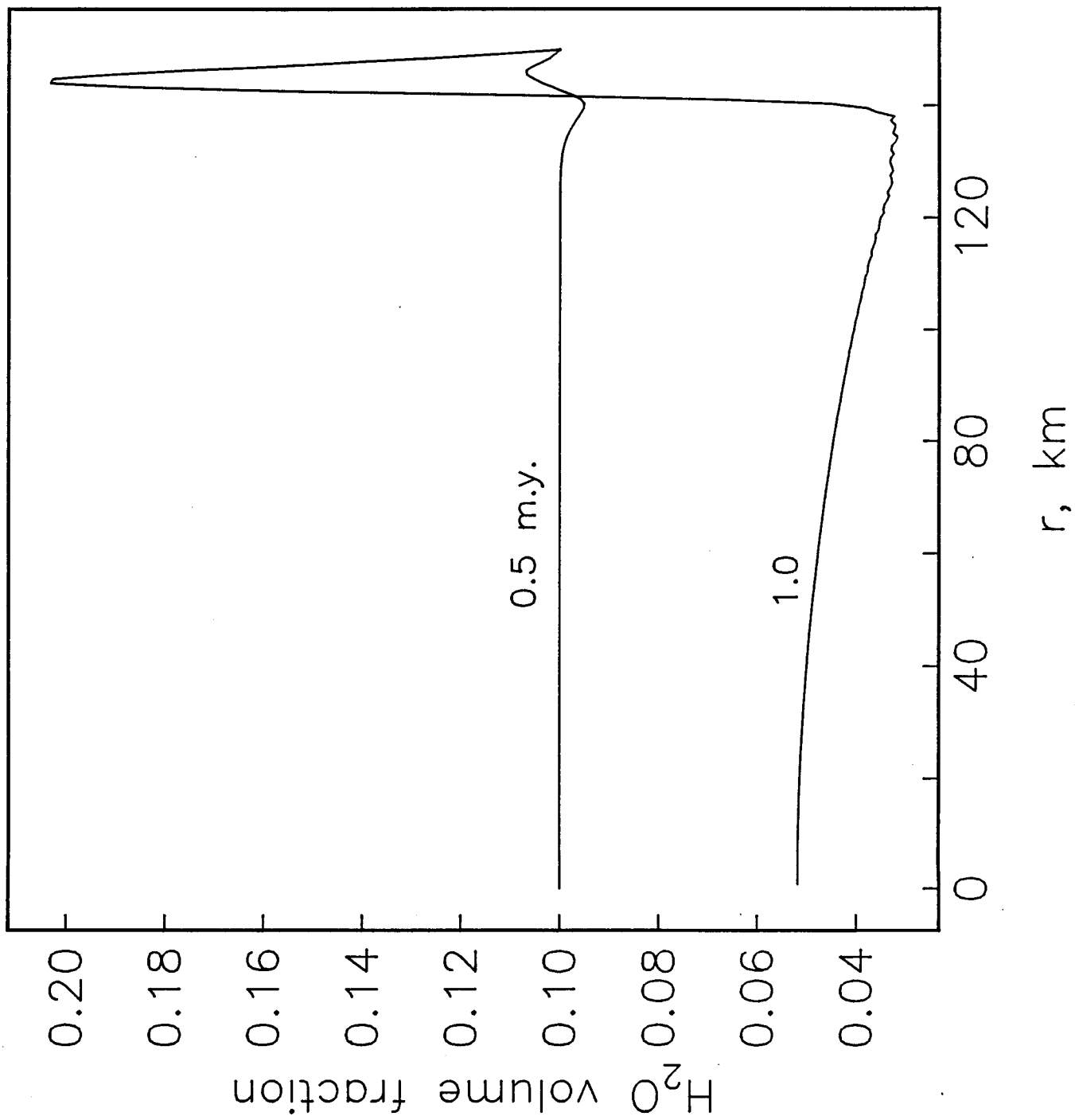


Figure 6.11b

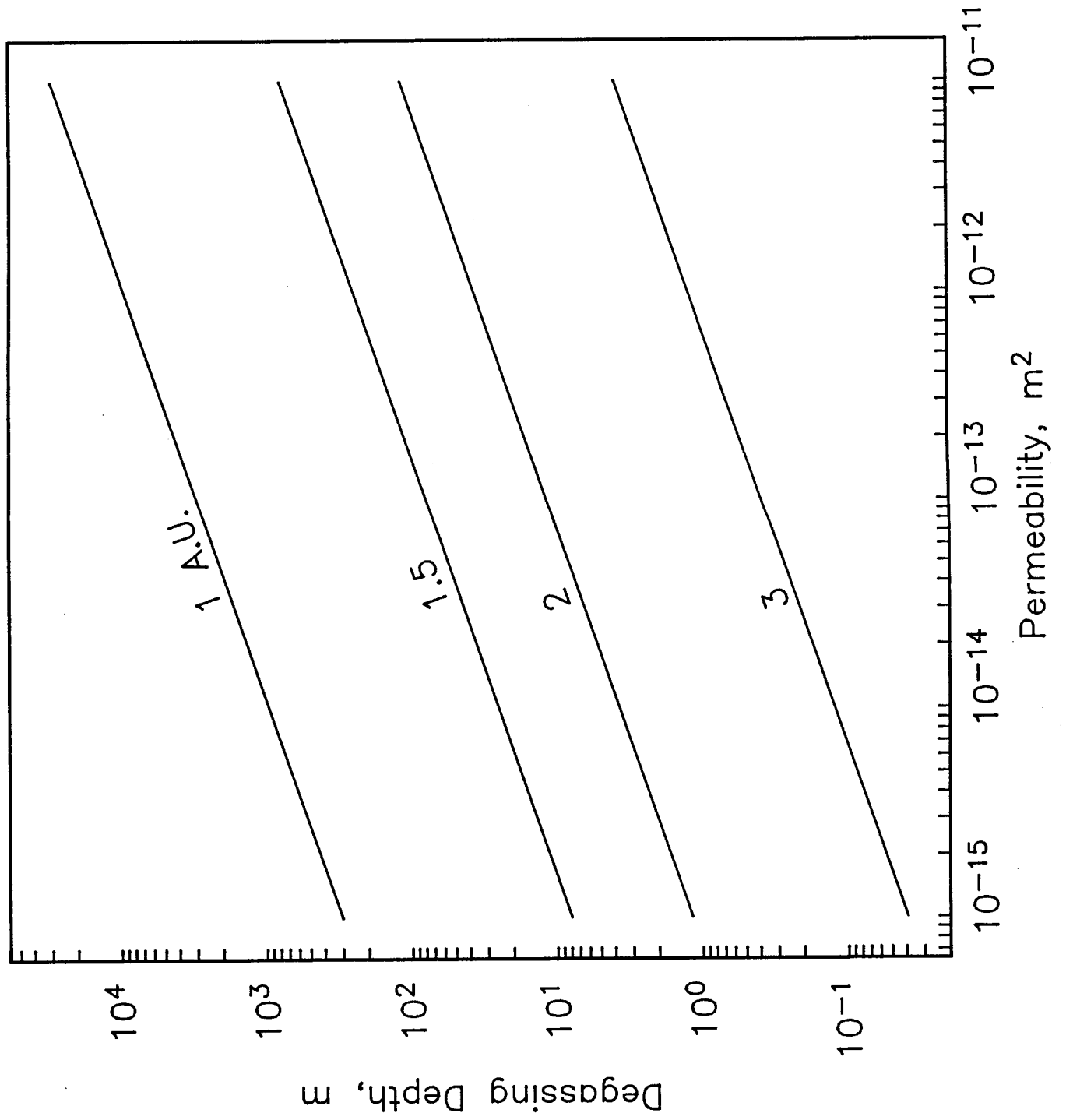


Figure 6.12a

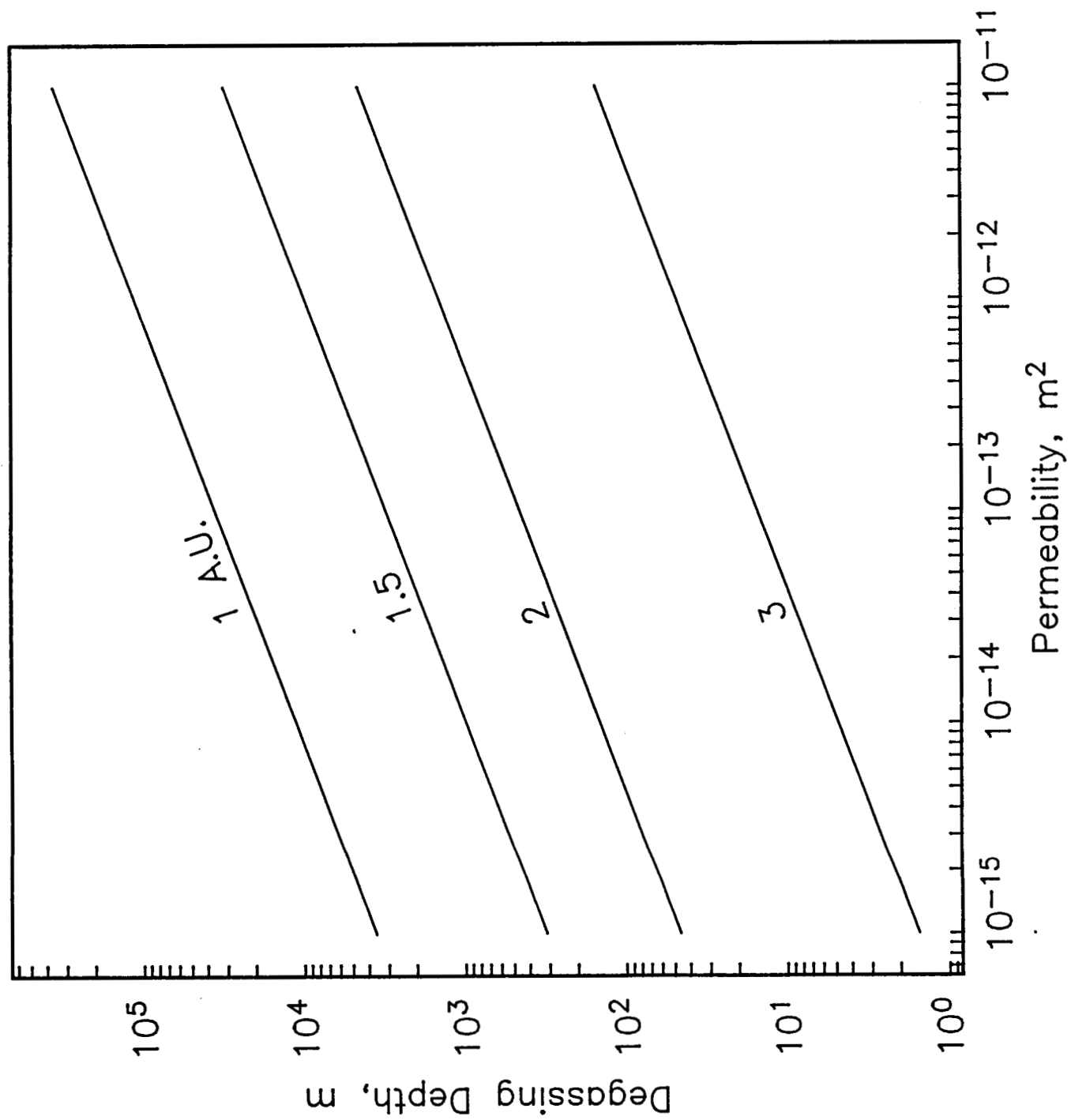


Figure 6.12b

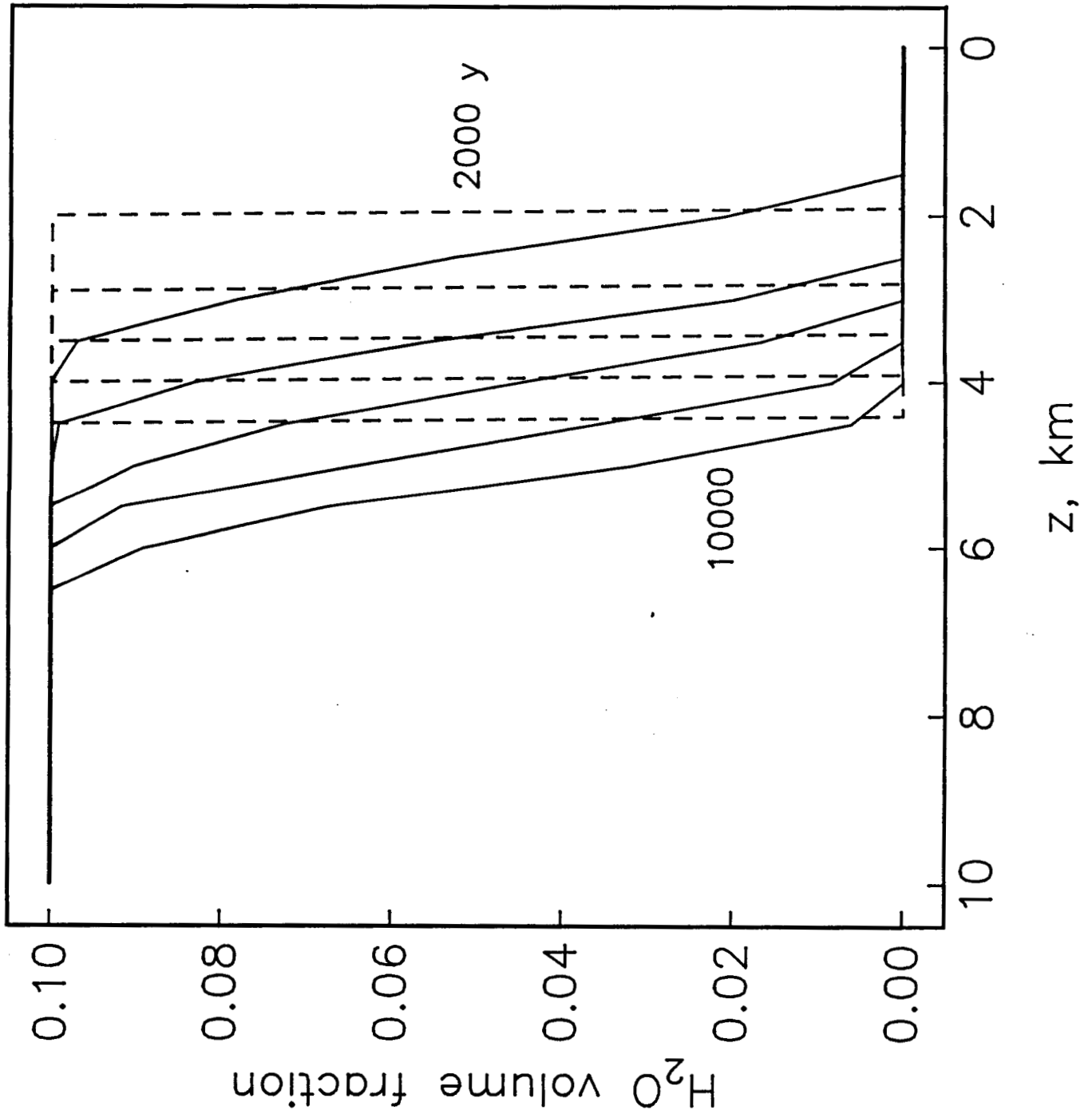


Figure 6.B1

CHAPTER 7:

CONCLUDING REMARKS

In this thesis, spacecraft measurements and laboratory analyses have been combined to infer features of the structure and evolution of the lithosphere of Venus and the parent bodies of chondritic meteorites. In Part I, limits to both the present thickness and the accumulation rate of crust on Venus have been obtained from the morphology and distribution of impact craters. Radar altimetry and imaging have been used to test hypotheses for crustal divergence. In Part II, models for the early geologic histories of both ordinary and carbonaceous chondrite parent bodies have been developed in accordance with constraints imposed by chemical, isotopic, and textural data.

The principal conclusions of Part I are

- (1) The dominant mode of lithospheric heat loss on Venus is conduction. Volcanism delivers a negligible fraction of the planetary heat loss. Lithospheric recycling cannot be ruled out but can account for no more than about one quarter of the planetary heat budget.
- (2) The mean crustal thickness throughout the lowlands and rolling plains is no more than 10-20 km. This implies either a low rate of crustal production or some form of crustal recycling.
- (3) The question of horizontal crustal divergence in Aphrodite Terra is unresolved. There is no quantitative evidence to support suggestions that individual topographic elements hundreds of kilometers in size are bilaterally symmetric on a regional scale or that the topography is consistent with a diverging and cooling thermal boundary layer. These characteristics cannot be completely excluded, but neither can they be invoked to support a rigid-plate divergence model. Detailed mapping by the *Magellan* spacecraft will resolve the geologic features needed to discriminate

between the vertical-tectonics, plate-divergence, and distributed-deformation models.

From these considerations, we may pose two alternative scenarios for the global tectonics of Venus:

- (a) Hot, buoyant lithosphere is unable to subduct and is therefore unable to drive significant horizontal motion and lithospheric divergence. Crustal production, associated with pressure-release melting at sites of lithospheric divergence, is inhibited. The crust has accumulated slowly over geologic time.
- (b) Crust and lithosphere are recycled, but at a lower rate than on Earth. The specific recycling mechanism is presently unknown.

Is Venus an active planet, truly Earth's twin? Venus must be tectonically active because the correlation of long-wavelength topography and gravity points to a strong interaction of mantle convection with the surface, and because, in the absence of dynamic support, long wavelength topographic features would be removed by viscous relaxation within a few hundred million years. The extent of igneous activity depends on the mechanism and rate of crustal recycling under scenario (a) or (b).

The principal conclusions of Part II are

- (1) Collisional fragmentation and gravitational reassembly of meteorite parent bodies during metamorphism can account for uncorrelated peak temperatures and cooling rates among ordinary chondrites. This model may be preferred over the alternative metamorphosed-planetesimal model because

there are fewer thermal and collisional restrictions. Moreover, fragmentation and reassembly provides a single mechanism to explain both narrowly-distributed and widely-scattered cooling rates among breccia clasts, by collisions during or after metamorphism, respectively.

- (2) Incorporation of ice into carbonaceous chondrite parent bodies can strongly influence the thermal evolution of these objects. If aqueous alteration occurred throughout carbonaceous chondrite parent body interiors, water may have acted as a thermal buffer, allowing aqueous alteration to replace the thermal recrystallization observed for ordinary chondrites. If aqueous alteration occurred within a surficial regolith, then water must be supplied there by direct melting of local ice (which may then undergo hydrothermal circulation), by venting of liquid or vapor along fractures caused by failure under high pore pressures, or by vapor diffusion through existing pores and cracks. Retention of H₂O on parent bodies is not limited by sublimation or by collisional comminution, but by shock vaporization. Large C-type asteroids, if representative of carbonaceous chondrite parent bodies, might have significant quantities of ice in their interiors.

These studies have addressed aspects of the different geological evolutions of the largest and smallest terrestrial objects. Study of the full range of geological diversity in the solar system offers the best promise of understanding the origin and evolution of the Earth and the future potential for human exploration and development.

Summer grass:

of stalwart warriors' splendid dreams

the aftermath.

Basho, on his visit to an old battlefield.